

FLUID DYNAMICS OF AIRFOILS WITH
MOVING SURFACE BOUNDARY-LAYER CONTROL

Farzad Mokhtarian

B.E.S.(Hons), Johns Hopkins University, 1980

S.M. (Mechanical Engineering), Massachusetts Institute of Technology, 1982

A THESIS SUBMITTED IN PARTIAL FULFILLMENT OF
THE REQUIREMENTS FOR THE DEGREE OF
DOCTOR OF PHILOSOPHY

in

The Faculty of Graduate Studies
Department of Mechanical Engineering

We accept this thesis as conforming
to the required standard

THE UNIVERSITY OF BRITISH COLUMBIA

February 1988

© Farzad Mokhtarian, 1988

In presenting this thesis in partial fulfilment of the requirements for an advanced degree at the University of British Columbia, I agree that the Library shall make it freely available for reference and study. I further agree that permission for extensive copying of this thesis for scholarly purposes may be granted by the head of my department or by his or her representatives. It is understood that copying or publication of this thesis for financial gain shall not be allowed without my written permission.

Department of Mechanical Engineering

The University of British Columbia
1956 Main Mall
Vancouver, Canada
V6T 1Y3

Date Feb. 18, 1988

ABSTRACT

The concept of moving surface boundary-layer control, as applied to the Joukowski and NACA airfoils, is investigated through a planned experimental program complemented by theoretical and flow visualization studies. The moving surface was provided by one or two rotating cylinders located at the leading edge, the trailing edge, or the top surface of the airfoil. Three carefully designed two-dimensional models, which provided a wide range of single and twin cylinder configurations, were tested at a subcritical Reynolds number ($Re = 4.62 \times 10^4$ or $Re = 2.31 \times 10^5$) in a laminar-flow tunnel over a range of angles of attack and cylinder rotational speeds. The test results suggest that the concept is indeed quite promising and can provide a substantial increase in lift and a delay in stall.

The leading-edge rotating cylinder effectively extends the lift curve without substantially affecting its slope. When used in conjunction with a second cylinder on the upper surface, further improvements in the maximum lift and stall angle are possible. The maximum coefficient of lift realized was around 2.22, approximately 2.6 times that of the base airfoil. The maximum delay in stall was to around 45° . In general, the performance improves with an increase in the ratio of cylinder surface speed (U_c) to the free stream speed (U). However, the additional benefit derived progressively diminishes with an increase in U_c/U and becomes virtually negligible for $U_c/U > 5$.

There appears to be an optimum location for the leading-edge-cylinder. Tests with the cylinder at the upper side of the leading edge gave quite promising results. Although the $C_{L,max}$ obtained was a little lower than the two-cylinder configuration (1.95 against 2.22), it offers a major advantage in terms of mechanical simplicity. Performance of the leading-edge-cylinder also depends on its geometry. A scooped configuration appears to improve performance at lower values of U_c/U ($U_c/U \leq 1$). However, at higher rates of rotation the free stream is insensitive to the cylinder geometry and there is no particular advantage in using the scooped geometry.

A rotating trailing-edge-cylinder affects the airfoil characteristics in a fundamentally different manner. In contrast to the leading-edge-cylinder, it acts as a flap by shifting the C_L vs. α plots to the left thus increasing the lift coefficient at smaller angles of attack *before* stall. For example, at $\alpha = 4^\circ$, it changed the lift coefficient from 0.35 to 1.5, an increase of 330%. Thus in conjunction with the leading-edge-

cylinder, it can provide significant improvements in lift over the entire range of small to moderately high angles of incidence ($\alpha \leq 18^\circ$).

On the theoretical side, to start with, the simple conformal transformation approach is used to obtain a closed form potential-flow solution for the leading-edge-cylinder configuration. Though highly approximate, the solution does predict correct trends and can be used at a relatively small angle of attack. This is followed by an extensive numerical study of the problem using:

- the surface singularity approach including wall confinement and separated flow effects;
- a finite-difference boundary-layer scheme to account for viscous corrections; and
- an iteration procedure to construct an equivalent airfoil, in accordance with the local displacement thickness of the boundary layer, and to arrive at an estimate for the pressure distribution.

Effect of the cylinder is considered either through the concept of slip velocity or a pair of counter-rotating vortices located below the leading edge. This significantly improves the correlation. However, discrepancies between experimental and numerical results do remain. Although the numerical model generally predicts $C_{L,max}$ with a reasonable accuracy, the stall estimate is often off because of an error in the slope of the lift curve. This is partly attributed to the spanwise flow at the model during the wind tunnel tests due to gaps in the tunnel floor and ceiling required for the connections to the externally located model support and cylinder drive motor. However, the main reason is the complex character of the unsteady flow with separation and reattachment, resulting in a bubble, which the present numerical procedure does not model adequately. It is expected that better modelling of the cylinder rotation with the slip velocity depending on a dissipation function, rotation, and angle of attack should considerably improve the situation.

Finally, a flow visualization study substantiates, rather spectacularly, effectiveness of the moving surface boundary-layer control and qualitatively confirms complex character of the flow as predicted by the experimental data.

CONTENTS

ABSTRACT	ii
LIST OF FIGURES	vi
NOMENCLATURE	xiv
ACKNOWLEDGEMENT	xix
1. INTRODUCTION	1
1.1 Preliminary Remarks	1
1.2 Scope of the Present Investigation	4
2. WIND TUNNEL TEST PROGRAM	7
2.1 Joukowski Airfoils: Models I and II	9
2.2 NACA 63-218 Modified Airfoil	21
2.3 Presentation of Results	23
3. EXPERIMENTAL RESULTS	25
3.1 Joukowski Model I	25
3.1.1 Leading-edge-cylinder	25
3.1.2 Leading-edge-scooped-cylinder	35
3.2 Joukowski Model II	45
3.2.1 Leading-edge-cylinder	45
3.2.2 Trailing-edge-cylinder	52
3.2.3 Leading and trailing-edge cylinders	59
3.2.4 Leading and upper-surface cylinders	69
3.2.5 Upper leading-edge-cylinder	80
3.2.6 Comparative performance and choice of configuration	84

3.3	NACA 63-218 Modified Airfoil	87
4.	THEORETICAL POTENTIAL FLOW APPROACHES	95
4.1	Analytical Model	95
4.2	Numerical Surface Singularity Method	108
4.2.1	Flow around a Joukowski airfoil in presence of vortices . .	113
4.2.2	Counter-rotating vortex-pair model	115
5.	VISCOUS CORRECTION SCHEME	128
5.1	Boundary Layer Calculations	128
5.2	Equivalent-Airfoil Technique	132
5.2.1	Attached-flow case	132
5.2.2	Separated-flow case	134
5.3	Results and Discussion	137
5.3.1	Modelling the effect of cylinder rotation through boundary layer modification	142
5.3.2	Cylinder rotation modelled through a pair of counter-rotating vortices	154
6.	FLOW VISUALIZATION STUDY	158
7.	CLOSING COMMENTS	164
7.1	Concluding Remarks	164
7.2	Recommendations for Future Work	168
	REFERENCES	171
	APPENDIX: THE COMPUTER PROGRAM	175

LIST OF FIGURES

2-1	A sketch of the glycerol-water solution tunnel used in the flow visualization study to establish important system parameters.	8
2-2	Pressure taps, distributed over the circumference, to provide detailed information on the surface loading. Also shown is the pressure ring assembly used for the wooden models.	10
2-3	Schematic diagram of the closed circuit wind tunnel used in the experimental study.	11
2-4	Schematic diagram of the experimental setup.	12
2-5	Details of the leading-edge rotating cylinder construction and cylinder drive mechanism.	14
2-6	Various geometries of the leading-edge-cylinder used in the wind tunnel tests.	15
2-7	Photograph of the Joukowski model I showing the leading-edge scooped cylinder in place. The nose fill-in section is shown on the side. . .	16
2-8	Photographs of the Joukowski model II showing: (a) various removable sections of the airfoil: A , nose fill-in section; B , trailing edge; C , side panel; (b) locations of the cylinders: D , location of the L.E. cylinder; E , location of the T.E. cylinder; F , locations of the upper-surface forward and rear cylinders.	18 19
2-9	Various rotating cylinder configurations possible with the Joukowski airfoil model II.	20
2-10	Schematic diagram of the leading edge construction of the Joukowski model II showing details of the pressure taps.	22
2-11	Photograph of the NACA 63-218 airfoil showing the leading edge cylinder in place.	24

3-1	Typical experimentally obtained pressure distribution plots for a conventional Joukowsky airfoil. These results serve as reference to assess the effects of airfoil modifications and cylinder rotation.	26
3-2	Effect of modification of the Joukowsky airfoil with a leading-edge-cylinder on the pressure distribution. Note, the presence of a gap significantly reduces the stall angle.	27
3-3	Effect of the gap (between the cylinder and the airfoil) on the pressure distribution of the Joukowsky airfoil before stall.	29
3-4	Effect of cylinder rotation on the pressure distribution around the Joukowsky airfoil:	
	(a) $U_c/U = 1$;	30
	(b) $U_c/U = 2$;	31
	(c) $U_c/U = 3$;	32
	(d) $U_c/U = 4$	33
3-5	Experimentally obtained pressure plots showing the delay in stall brought about by the cylinder rotation.	34
3-6	Effect of cylinder rotation on the pressure distribution over a Joukowsky airfoil showing only partially separated flow even at a relatively high angle of attack.	36
3-7	Plots showing variation of the lift coefficient with angle of attack as affected by the leading-edge-cylinder and its rotation.	37
3-8	Pressure plots for the Joukowsky airfoil with a leading-edge-scooped-cylinder. The results should be compared with those given in Figure 3-4(a).	38
3-9	Effect of the leading-edge-cylinder configurations on the pressure distribution around the Joukowsky airfoil, $U_c/U = 1$, $\alpha = 16^\circ$	40
3-10	Experimentally obtained pressure plots for the Joukowsky airfoil with a leading-edge-scooped-cylinder showing the effects of cylinder rotation and angle of attack:	

	(a) $\alpha = 18^\circ$;	41
	(b) $\alpha = 20^\circ$;	42
	(c) $\alpha = 24^\circ$	43
3-11	Plots showing improvements in the lift coefficient of a Joukowsky airfoil with various leading-edge-cylinder configurations and speeds. . .	44
3-12	Effect of Reynolds number on the lift and stall characteristics of the Joukowsky model II.	46
3-13	Experimentally obtained pressure distributions for the basic Joukowsky model II.	47
3-14	Effect the leading-edge-cylinder rotation on the lift and stall characteristics of the Joukowsky model II.	48
3-15	Effect of increasing the rate of cylinder rotation on pressure distribution around the Joukowsky model II at relatively larger angles of attack:	
	(a) $\alpha = 16^\circ$;	50
	(b) $\alpha = 20^\circ$	51
3-16	Plots showing adverse effects of increasing the gap size between the airfoil and the leading-edge-cylinder. A comparison with Figure 3-14 suggests that both $C_{L,max}$ and stall angle are significantly reduced.	53
3-17	Pressure distributions over the Joukowsky model II modified with a trailing-edge-cylinder:	
	(a) $\alpha = 0^\circ$;	54
	(b) $\alpha = 4^\circ$;	55
	(c) $\alpha = 8^\circ$;	56
	(d) $\alpha = 12^\circ$	57
3-18	Effect of the trailing-edge-cylinder rotation on the lift and stall characteristics of the Joukowsky model II.	58
3-19	Variation of C_L vs. α for a modified Joukowsky airfoil with leading and trailing-edge cylinders:	

	(a) leading-edge-cylinder rotation;	60
	(b) trailing-edge-cylinder rotation;	61
	(c) combined rotation of both the cylinders.	62
3-20	Selected pressure plots for the Joukowsky model II, modified with leading and trailing-edge cylinders, at $\alpha = 8^\circ$	64
3-21	Comparison of pressure plots for the Joukowsky model II with several combinations of leading and trailing-edge cylinder configurations:	
	(a) $\alpha = 12^\circ$;	65
	(b) $\alpha = 20^\circ$;	66
	(c) $\alpha = 24^\circ$	67
3-22	Effect of rotation of the leading and trailing-edge cylinders on the lift and stall characteristics of the Joukowsky model II.	68
3-23	A comparison between the performance of the trailing-edge and upper-surface cylinders (Joukowsky model II).	70
3-24	Typical pressure distribution plots for the Joukowsky model II with both leading-edge and rear upper-surface cylinders in operation:	
	(a) $\alpha = 16^\circ$;	72
	(b) $\alpha = 24^\circ$;	73
	(c) $\alpha = 28^\circ$	74
3-25	Typical pressure distribution results for the Joukowsky model II with leading-edge and forward upper-surface cylinders.	75
3-26	Pressure plots as affected by combinations of the leading-edge and upper-surface cylinders' rotation.	76
3-27	Lift and stall characteristics of the Joukowsky model II with the leading-edge and upper-surface cylinders:	
	(a) rear upper-surface-cylinder;	78
	(b) forward upper-surface-cylinder.	79
3-28	Experimentally obtained pressure distribution plots for the Joukowsky	

model II with the upper leading-edge-cylinder:

(a) $\alpha = 16^\circ$; 81

(b) $\alpha = 32^\circ$; 82

(c) $\alpha = 48^\circ$ 83

3-29 Lift and stall characteristics of the Joukowsky model II as affected by the upper leading-edge-cylinder rotation. Base airfoil and $U_c/U = 0$ data serve as reference to assess the effect of airfoil modification by the cylinder and its rotation. 85

3-30 Plots to assess relative influence of different configurations studied on the lift and stall characteristics. 86

3-31 Typical plots showing variation in lift coefficient with the angle of attack for the NACA 63-218 modified airfoil as affected by the leading-edge-cylinder rotation. 89

3-32 Typical experimentally obtained pressure distribution plots for NACA 63-218 airfoil modified with a leading-edge-cylinder showing the effect of cylinder rotation:

(a) $\alpha = 24^\circ$; 90

(b) $\alpha = 28^\circ$ 91

3-33 Effect of rotation rate on the lift to drag ratio of NACA 63-218 airfoil modified with a leading-edge rotating cylinder. 93

3-34 Variation of C_L vs. C_D for NACA 63-218 airfoil (modified) with a leading-edge-rotating-cylinder. 94

4-1 Analytical and numerical models. 96

4-2 The Joukowsky transformation. 99

4-3 Analytically obtained pressure plots for a symmetrical Joukowsky airfoil in presence of an external vortex located on the x-axis. 103

4-4 Analytically predicted pressure variation around a symmetrical Joukowsky airfoil section showing the effect of locating a vortex off the

	x-axis.	105
4-5	Analytical pressure distributions around a symmetrical Joukowski airfoil showing the effects of trapping a vortex below the nose at varying vertical distance from the surface.	106
4-6	Analytically obtained pressure plots for a symmetrical Joukowski airfoil showing the effects of trapping a vortex below the nose and increasing its strength.	107
4-7	Singularity representation of the airfoil and the notation for the calculation of influence coefficients.	110
4-8	Pressure distributions around a symmetrical Joukowski airfoil using the surface singularity method to simulate the leading-edge rotating cylinder with an internal vortex.	114
4-9	Numerically obtained pressure distribution around a Joukowski airfoil with a rotating cylinder forming its nose.	116
4-10	A comparison between the analytical and numerical (potential flow) methods used in modelling the leading-edge cylinder.	117
4-11	Effect of a vortex pair, located below the leading edge, on the pressure distribution of a Joukowski airfoil:	
	(a) effect of the location of the pair below the nose;	119
	(b) individual effect of the front vortex;	120
	(c) individual effect of the rear vortex.	121
4-12	Effect of the relative streamwise position of the vortices on the pressure distribution around a Joukowski airfoil.	122
4-13	Effect of increasing the strength of the vortex pair, located below the leading edge, on the pressure distribution of the Joukowski airfoil:	
	(a) vortices with the same strength;	123
	(b) front vortex of higher strength;	124
	(c) rear vortex of higher strength.	125
4-14	Streamline patterns for flow around a circular cylinder with circulation,	

	corresponding to $U_c/U = 3$, showing the detached stagnation point and the associated recirculation regions.	127
5-1	Numerical analysis procedure	133
5-2	Equivalent-airfoil models:	
	(a) attached flow;	135
	(b) separated flow.	136
5-3	Effectiveness of the numerical modelling procedures and their comparison with experimental data.	139
5-4	Variation of the lift coefficient with the angle of attack as predicted by the different models.	140
5-5	Comparison between typical potential flow and experimentally obtained pressure data for a Joukowski airfoil.	141
5-6	Models for the effect of cylinder rotation.	143
5-7	Schematic diagram of the velocity profiles around the leading edge of an airfoil illustrating the momentum injection effect due to rotation of the cylinder.	144
5-8	Typical numerical predictions of the pressure distribution using boundary-layer modification to model the cylinder rotation and their comparison with experimental results:	
	(a) $\alpha = 12^\circ, U_c/U = 1$;	146
	(b) $\alpha = 12^\circ, U_c/U = 2$;	147
	(c) $\alpha = 24^\circ, U_c/U = 2$;	148
	(d) $\alpha = 24^\circ, U_c/U = 3$;	149
	(e) $\alpha = 36^\circ, U_c/U = 4$	150
5-9	Variation of the lift coefficient with angle of attack using boundary-layer modification to model the cylinder rotation – a comparison with experimental data:	
	(a) integrated pressure data;	152

	(b) integrated pressure data with theoretical results modified at the leading edge.	153
5-10	Predicted pressure distribution using the vortex-pair modelling of the cylinder rotation and its comparison with the experimental data. .	156
5-11	Variation of the lift coefficient with angle of attack as predicted using the vortex-pair modelling of cylinder rotation and its comparison with the experimental data.	157
6-1	Typical photographs taken during the flow visualization study showing remarkable effectiveness of the moving surface boundary-layer control procedure:	
	(a) highly separated flow, at a high angle of attack, in absence of the boundary-layer control;	160
	(b) essentially attached flow established through cylinder rotation.	161
6-2	Flow visualization photographs showing the steady flow over the airfoil at various angles of attack with and without the rotation of the leading edge.	162
6-3	Flow visualization photographs showing the transition from the highly separated flow in the absence of cylinder rotation to the essentially reattached flow at $U_c/U = 6$	163

NOMENCLATURE

A	planform area, cb ; also damping-length constant defined in the eddy-viscosity formulation
a	distance of center of the circle from origin in transformed plane ζ , Figure 4-2; also length used in the calculation of influence coefficients, Figure 4-7
b	span; also length used in the calculation of influence coefficients, Figure 4-7
C	strength of doublet; also chord
C_D	drag coefficient, $D/\frac{1}{2}\rho U^2 A$
C_P	pressure coefficient, $(P - P_\infty)/\frac{1}{2}\rho U^2$
C_L	lift coefficient, $L/\frac{1}{2}\rho U^2 A$
$C_{L,max}$	maximum coefficient of lift
c_i, c_j	control points, Figure 4-7
D	drag
D_c	diameter of circular cylinder
F	complex potential
$f(x, \eta)$	dimensionless stream function, $\Psi(x, y)/(U_e \nu x)^{1/2}$
f_w	mass transfer at the wall in transformed coordinates
f', f''	derivatives of f with respect to η
f_w''	wall shear stress in transformed coordinates
K	mixing length constant
K_{ij}	matrix of influence coefficients
k	circulation due to point vortices

L	lift; also mixing length
m	source strength; also dimensionless pressure gradient parameter $(x/U_e)(dU_e/dx)$
N	number of surface elements; also mixing length constant
P	pressure
P_∞	undisturbed pressure far upstream of the model
p^+	mixing length constant
R	radius of circle in transformed plane
R_c	radius of circular cylinder
R_i	right hand side of the stream function equation
Re	Reynolds number, Uc/ν
Re_x	streamwise Reynolds number
Re_θ	Reynolds number based on momentum thickness
$r(c_i, S_j)$	straightline distance between control point c_i and midpoint of element S_j on the control surface, Figure 4-7
r_1, r_2	straightline distance between a control point and endpoints of an element on the control surface, Figure 4-7
r_o	polar coordinate in transformed plane ζ' , $\zeta'_o = r_o e^{i\theta_o}$, Figure 4-2
S	control surface, Figure 4-7
S'	point on the control surface, Figure 4-7
S_i	terms due to the source in the stream function equation
S_j	element j on the control surface, Figure 4-7
U	free stream velocity
U_c	cylinder surface velocity
U_e	external velocity

U_τ	wall velocity, $(\tau_w/\rho)^{1/2}$
u, v	x and y components of velocity, respectively
v_w	transpiration velocity, zero on a solid surface
$W(\zeta')$	complex velocity, $dF/d\zeta'$
X, Y	cartesian coordinates, Figure 4-7
X_i, Y_i	control point coordinates, Figure 4-7
X_o, Y_o	coordinates of point vortex, Figure 4-7
X_S, Y_S	surface coordinates with origin at leading edge, Figure 4-7
X_{source}, Y_{source}	coordinates of point source, Figure 4-7
x, y	cartesian coordinates
Z	complex physical plane, $X + iY$
Z_o	location of vortex in real plane Z , Figure 4-2

Greek Symbols

α	angle of attack; also universal constant, $\alpha = 0.0168$ for $Re_\theta \geq 5000$, used in the viscosity formulation
β	angle defining position of the trailing edge in transformed plane ζ
Γ	circulation around airfoil
$\gamma(S_j)$	vorticity density (circulation per unit length) of element S_j
γ_j	circulation per unit length of the j th element; also local surface velocity
γ_{tr}	intermittency factor that accounts for the transition between laminar and turbulent regions
δ	angle defining position of a circle in the transformed plane, Fig-

	ure 4-2; also boundary-layer thickness
δ^*	boundary-layer displacement thickness
Δ	element half-length, Figure 4-7
ϵ^+	eddy viscosity, ϵ/ν
$(\epsilon^+)_i$	inner region eddy viscosity
$(\epsilon^+)_o$	outer region eddy viscosity
ζ, ζ'	transformed planes, Figure 4-2
ζ'_o	location of vortex in transformed plane $\zeta', \zeta'_o = r_o e^{i\theta_o}$, Figure 4-2
η	transformed cross-stream coordinate in the Falkner-Skan transformation, $(U_e/\nu x)^{1/2} y$
η_∞	transformed boundary-layer thickness
θ	polar coordinate in transformed plane; also boundary-layer momentum thickness
θ_o	polar coordinate in transformed plane $\zeta', \zeta'_o = r_o e^{i\theta_o}$, Figure 4-2
μ	dynamic viscosity
ν	kinematic viscosity
ρ	fluid density
τ_w	shear stress at wall
Φ	velocity potential
Ψ	stream function
Ψ_k	stream function for component k

Subscripts

l.e.	leading-edge-cylinder
t.e.	trailing-edge-cylinder
f	forward upper-surface-cylinder
r	rear upper-surface-cylinder
u.l.e.	upper leading-edge-cylinder

ACKNOWLEDGEMENT

I would like to express my sincere thanks to Professor V.J. Modi, my advisor, for his support, counsel, and understanding throughout my stay at the University of British Columbia.

Thanks are also due to Dr. T. Yokomizo, Professor of mechanical engineering at the Kanto Gakuin University, Yokohama, Japan, for permitting the use of his excellent flow visualization facility and assistance in photography.

The research work was supported by the Natural Sciences and Engineering Council of Canada, Grant No. A-2181.

The models were fabricated in the Mechanical Engineering workshop. Assistance of Mr. Ed Abell, Senior Technician, in design and construction of the models is gratefully acknowledged.

Many thanks to all my friends in the Rusty Hut for their constructive comments, criticism, and help.

1. INTRODUCTION

1.1 Preliminary Remarks

Ever since the introduction of the boundary-layer concept by Prandtl, there has been a constant challenge faced by scientists and engineers to minimize its adverse effects and control it to advantage. Methods such as suction, blowing, vortex generators, turbulence promoters, etc., have been investigated at length and employed in practice with a varying degree of success. A vast body of literature accumulated over years has been reviewed rather effectively by several authors including Goldstein [1], Lachmann [2], Rosenhead [3], Schlichting [4], Chang [5] and others. However the use of moving wall for boundary layer control has received relatively less attention.

Irrespective of the method used, the main objective of a control procedure is to prevent or at least delay the separation of boundary layer from the wall. A moving surface attempts to accomplish this in two ways:

- it retards the initial growth of the boundary layer by minimizing relative motion between the surface and the free stream;
- it injects momentum into the existing boundary layer.

Newton was probably the first one to observe the effect of moving wall boundary-layer control on the trajectory of a spinning ball [6], without any appreciation as to the basis of the effect. Almost 200 years later Magnus [7] studied lift generated by circulation and utilized the effect to construct a ship with a vertical rotating cylinder replacing the sail. Swanson [8] and Iverson [9] have presented excellent reviews of literature on the Magnus effect. As early as in 1910, Prandtl [10] himself demonstrated his “ship of zero resistance” through flow around two counter-rotating cylinders, while Flettner [11] applied the principle to ship propulsion in

1924 when he fitted large vertical rotating cylinders on the deck of the "Buchau". Later, in 1934, Goldstein [1] illustrated the principle of boundary layer control using a rotating cylinder at the leading edge of a flat plate. However, the most practical application of moving wall for boundary layer control was demonstrated by Favre [12]. Using an airfoil with upper surface formed by a belt moving over two rollers, he was able to delay separation until the angle of attack reached 55° where the maximum lift coefficient of 3.5 was realized.

After a lull of more than twenty years (1938–1960), during which the tempo of research activity as indicated by important contributions in the field remained dormant, there appeared some signs of renewed interest in this form of boundary layer control. Alvarez–Calderon and Arnold [13] carried out tests on a rotating cylinder flap to evolve a high lift airfoil for STOL type aircraft. The system was flight tested on a single engine high wing research aircraft designed by Aeronautics Division of the Universidad Nacional de Ingenieria in Lima, Peru [14]. Around the same time Brooks [15] presented his preliminary results of tests on a hydrofoil with a rotating cylinder at the leading or trailing edge. For the leading–edge configuration only a small increase in lift was observed. However, for the trailing–edge case a substantial gain in lift resulted. Motivation for the test program was to assess improvement in fin performance for torpedo control. Along the same line, Steele and Harding [16] studied the application of rotating cylinders to improve ship manoeuvrability. Extensive force measurements and flow visualization experiments were conducted using a water tunnel and a large circulating water channel. Three different configurations of rudder were used with the rotating cylinder:

- a) in isolation;
- b) at the leading edge of a rudder; and
- c) combined with a flap–rudder, the cylinder being at the leading edge of the flap.

From the overall consideration of hydrodynamic performance, mechanical complexity, and power consumption the configuration in (b) was preferred. An application to a 250,000 *ton* tanker showed the power requirement for a 1 *m* diameter cylinder rotating at 350 *rpm* to be around 400 *kW*.

Of some interest is the North American Rockwell designed OV-10A aircraft which was flight tested by NASA's Ames Research Center [17–19]. Cylinders, located at the leading edges of the flaps, are made to rotate at high speed with the flaps in lowered position. The main objective of the test program was to assess handling qualities of the propeller-powered STOL type aircraft at higher lift coefficients. The aircraft was flown at speeds of 29–31 *m/sec*, along approaches up to -8° , which corresponded to a lift coefficient of about 4.3. In the pilot's opinion any further reductions in approach speed were limited by the lateral-directional stability and control characteristics. Excellent photographs of the airplane on ground (showing the cylinders in position) and in flight have been published in the *Aviation Week and Space Technology* [20].

Efforts so far, though useful to an extent, were generally aimed at specific configurations and lacked approach to the problem at a fundamental level in an organized fashion. From this point of view, Tennant's contribution to the field is significant. In 1971 Tennant presented an interesting analysis for the two-dimensional moving wall diffuser with a step change in area [21, 22]. The diffuser incorporated rotating cylinders to form a part of its wall at the station of the area change. Preliminary experiments were also conducted for an area ratio up to 1 : 2.5, which showed no separation for appropriate moving surface to diffuser inlet velocity ratio. Tennant et al. [23] have also conducted tests with a wedge shaped flap having a rotating cylinder as the leading edge. Flap deflection was limited to 15° and the critical cylinder velocity necessary to suppress separation was determined. Effects of increase in gap size (between the cylinder and the flap surface) were also assessed. No effort was made to observe the influence of an increase in cylinder surface veloc-

ity beyond $U_c/U = 1.2$. More recently Tennant et al. [24] have reported circulation control for a symmetrical airfoil with a rotating cylinder forming its trailing edge. For zero angle of attack, the lift coefficient of 1.2 was attained with $U_c/U = 3$. Also of interest is their study concerning the boundary-layer growth on moving surfaces accounting for gap effects [25, 26].

With reference to V/STOL application the preliminary experimental study by Modi et al. [27] with NACA 63-218 (modified) airfoil used in the Canadair CL-84 must be mentioned. The test program was divided into three stages:

- a) the airfoil with its leading edge formed by a circular cylinder;
- b) the airfoil with its leading edge formed by a rotating cylinder and provided with a plain unslotted flap; and
- c) the airfoil with a slotted flap, leading edges of both formed by circular cylinders.

The results suggested that the moving surface can provide quite effective boundary-layer control. It can lead to a significant increase in the maximum lift coefficient and stall angle. A rotating cylinder at the leading edge of an airfoil seems to provide the maximum benefit. In general, the rear cylinder did not contribute substantially to the improvement in performance, at least in the configuration tested. In fact, in certain situations, due to presence of an additional gap, it affected the performance adversely.

1.2 Scope of the Present Investigation

The investigation reported here builds upon this body of literature. It studies fluid dynamics of an airfoil with the moving surface boundary-layer control using experimental, analytical, and numerical procedures.

To begin with, an extensive wind tunnel test program is undertaken to assess effectiveness of the moving surface boundary-layer control. The information also

serves as reference to evaluate validity of the theoretical results. The experimental study uses three distinct models as follows:

- i)* a symmetrical Joukowsky model with its nose replaced by three different configurations of rotating cylinders:
 - a) solid circular cylinder,
 - b) a scooped cylinder,
 - c) reversed scooped cylinder;
- ii)* a multi-section design, based also on the same symmetrical Joukowsky shape, which allows the use of one or more rotating cylinders at various possible locations around the airfoil such as:
 - a) the leading edge,
 - b) the trailing edge,
 - c) the upper surface,
 - d) any combination of the above;
- iii)* a NACA 63-218 modified airfoil model, with a rotating cylinder replacing its nose. As mentioned earlier, the airfoil was used by Canadair in its CL-84 tilt wing V/STOL design study.

Next, the simple conformal transformation approach is used to obtain preliminary qualitative information on the character of the flow. The attractive feature here is a closed form potential flow solution which permits ready parametric analysis. Of course, the solution is expected to be highly approximate as it does not account for viscosity and boundary-layer separation. However, at small angles of attack, the procedure may provide useful information.

This is followed by a more elaborate numerical procedure which approaches the problem in several stages representing increasing order of complexity. It consists

of:

- i)* a surface singularity approach incorporating wall confinement and separated flow effects. This involves replacement of the airfoil and wind tunnel wall surfaces with vorticity distribution in conjunction with appropriate constraint relations, and inclusion of a source within the contour of the airfoil to model the wake;
- ii)* a finite-difference boundary-layer scheme to account for viscous corrections. The scheme uses potential flow pressure distribution results to calculate the boundary-layer growth on the airfoil top and bottom surfaces until the point of separation;
- iii)* a procedure which uses the results of (*ii*) to construct an equivalent airfoil, by displacing the airfoil surface in accordance with the local displacement thickness of the boundary layer. Iteration between the potential flow method and the boundary layer scheme leads to a final pressure distribution.

An extensive flow visualization study complements the experimental and numerical results. The thesis ends with some concluding comments and thoughts on extension of the work.

2. WIND TUNNEL TEST PROGRAM

Before embarking upon an extensive wind tunnel test program it was thought appropriate to undertake a preliminary flow visualization study to obtain some appreciation as to the character of the flow and to help establish, qualitatively, relative merit of the system parameters involved (such as gap size, velocity ratio, cylinder surface roughness, etc.). This in turn helped design the models and plan the aerodynamic tests. The flow visualization experiments were carried out in a glycerol-water solution tunnel having a test-section of $20.32\text{ cm} \times 20.32\text{ cm} \times 2.44\text{ m}$ and capable of producing Reynolds number in the range 60 – 10,000 (Figure 2-1). Deflection annular vanes together with several sections of honeycombs, brass screens and nylon wool gave exceptionally flat velocity profiles. The tunnel is powered by a centrifugal pump (Aurora type GAPB, 200 gal/min, 7.6 m head, 1750 rpm) driven by a three horsepower variable speed d.c. motor. A heat exchanger in the return circuit maintained temperature variation of the working fluid within $0.1\text{ }^{\circ}\text{C}$. The dyed solution, of the same density as the working fluid, was injected upstream of the specially constructed model with rotating cylinders powered by an externally located drive system. The dye injection probe consisted of seven #23 syringe needles (0.38 mm diameter) placed 0.5 – 1 cm apart on a streamlined support. The rate of injection was controlled with brass needle valves.

The results suggested that the cylinder rotation had a substantial effect on the character of the flow field. In general, with an increase in speed, the streaklines on the top surface tended to move closer to the airfoil surface resulting in a smaller wake. The same tendency persisted even at a higher angle of attack when the airfoil would normally stall.

The tests pointed to the size of the gap and the ratio of the cylinder surface velocity to the free-stream velocity as the two significant parameters governing the

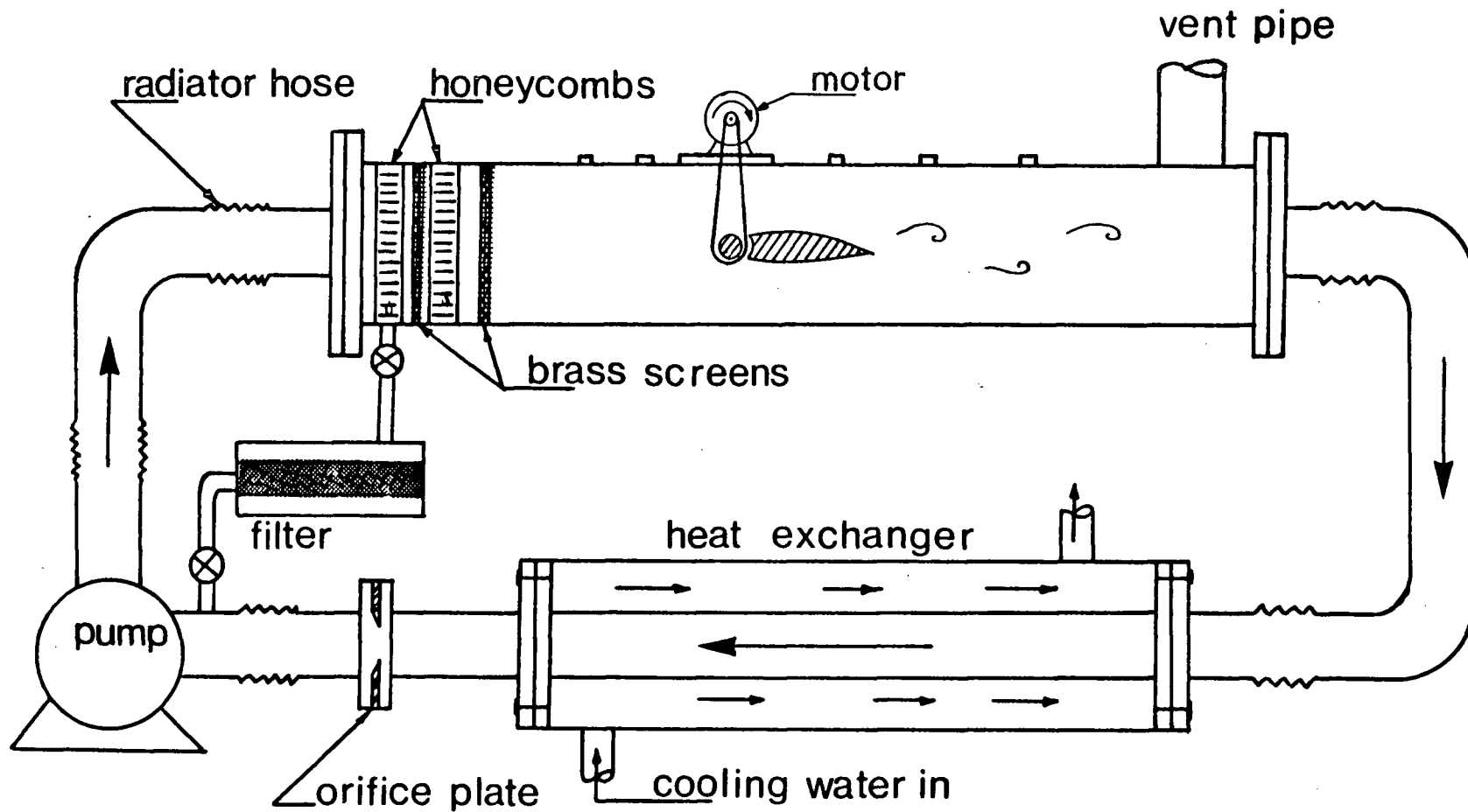


Figure 2-1 A sketch of the glycerol-water solution tunnel used in the flow visualization study to establish important system parameters.

beneficial effect of the rotation. With the gap size $> 5 \text{ mm}$ the effect of cylinder rotation reduced to almost negligible. Furthermore beyond $U_c/U > 5$, again the improvement in the flow pattern seemed only marginal. The information proved useful in planning the design of aerodynamic models for wind tunnel tests.

The wind tunnel models, approximately 0.38 m along chord and 0.68 m long, spanned the tunnel test-section, $0.91 \times 0.68 \times 2.6 \text{ m}$, to create essentially two-dimensional condition. The models were provided with pressure taps, suitably distributed over the circumference, to yield detailed information concerning the surface loading (Figure 2-2). A given model was supported by an Aerolab six component strain gauge balance and tested in a low speed, low turbulence, return type wind tunnel where the air speed can be varied from $1\text{--}50 \text{ m/sec}$ with a turbulence level of less than 0.1% . A Betz micromanometer with an accuracy of 0.2 mm of water was used to measure pressure differential across the contraction section of $7:1$ ratio. The rectangular test section ($0.91 \times 0.68 \text{ m}$) is provided with 45° corner fillets which vary from $15.25 \times 15.25 \text{ cm}$ to $12 \times 12 \text{ cm}$ to partly compensate for the boundary layer growth. The spatial variation of velocity in the test section is less than 0.25% . A schematic diagram of the tunnel is shown in Figure 2-3 with the test arrangement and associated instrumentation schematically indicated in Figure 2-4.

The tests were carried out with a systematic variation of the angle of attack and the cylinder rotational speed. The pressure plots were integrated in each case to obtain the lift coefficient. The lift was also measured independently using a strain gauge balance to assess two-dimensional character of the test arrangement.

2.1 Joukowski Airfoil Models I and II

For the first set of wind tunnel tests a symmetrical Joukowski airfoil model, of 15% maximum thickness to chord ratio, modified with a leading-edge cylinder was constructed. Radius of the cylinder was so selected as to match average curvature

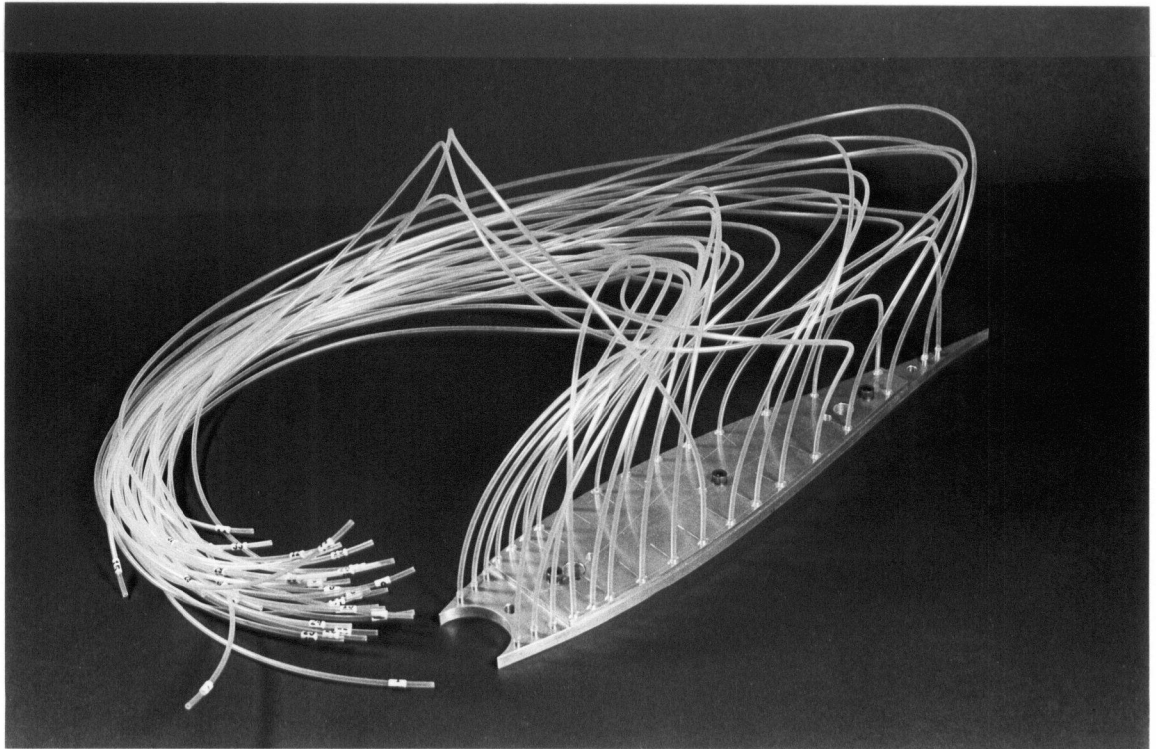
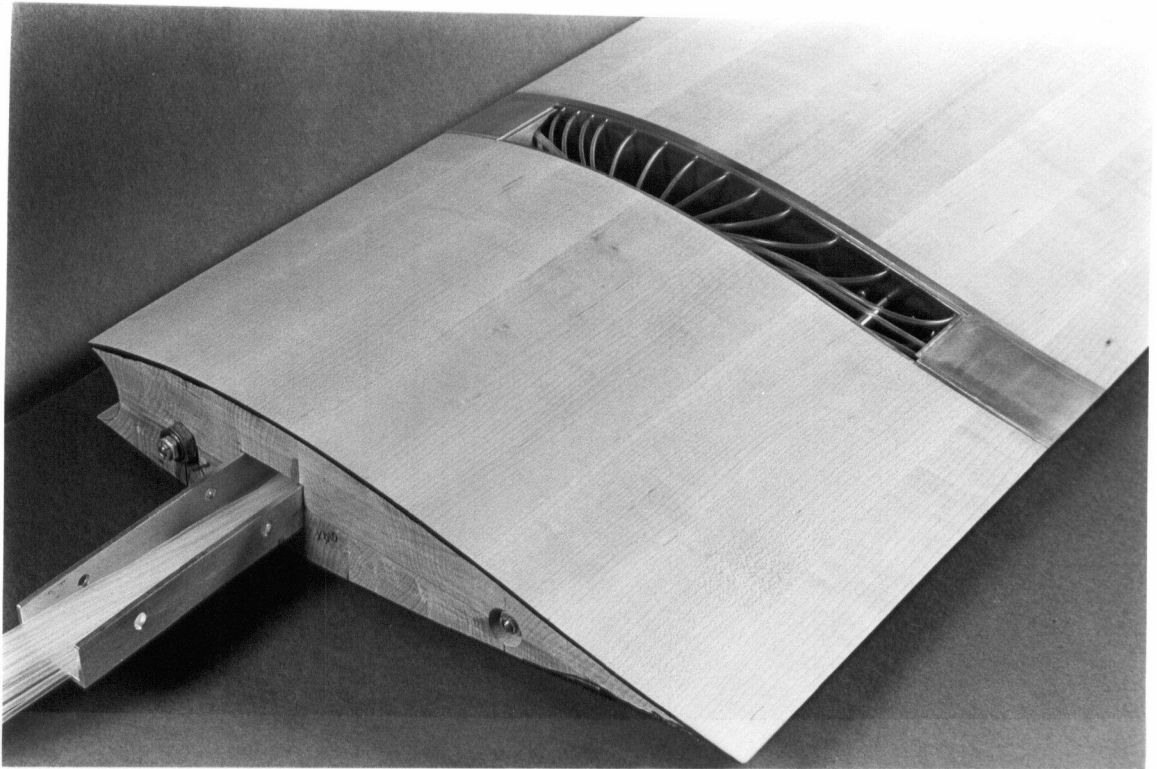


Figure 2-2 Pressure taps, distributed over the circumference, to provide detailed information on the surface loading. Also shown is the pressure ring assembly used for the wooden models.

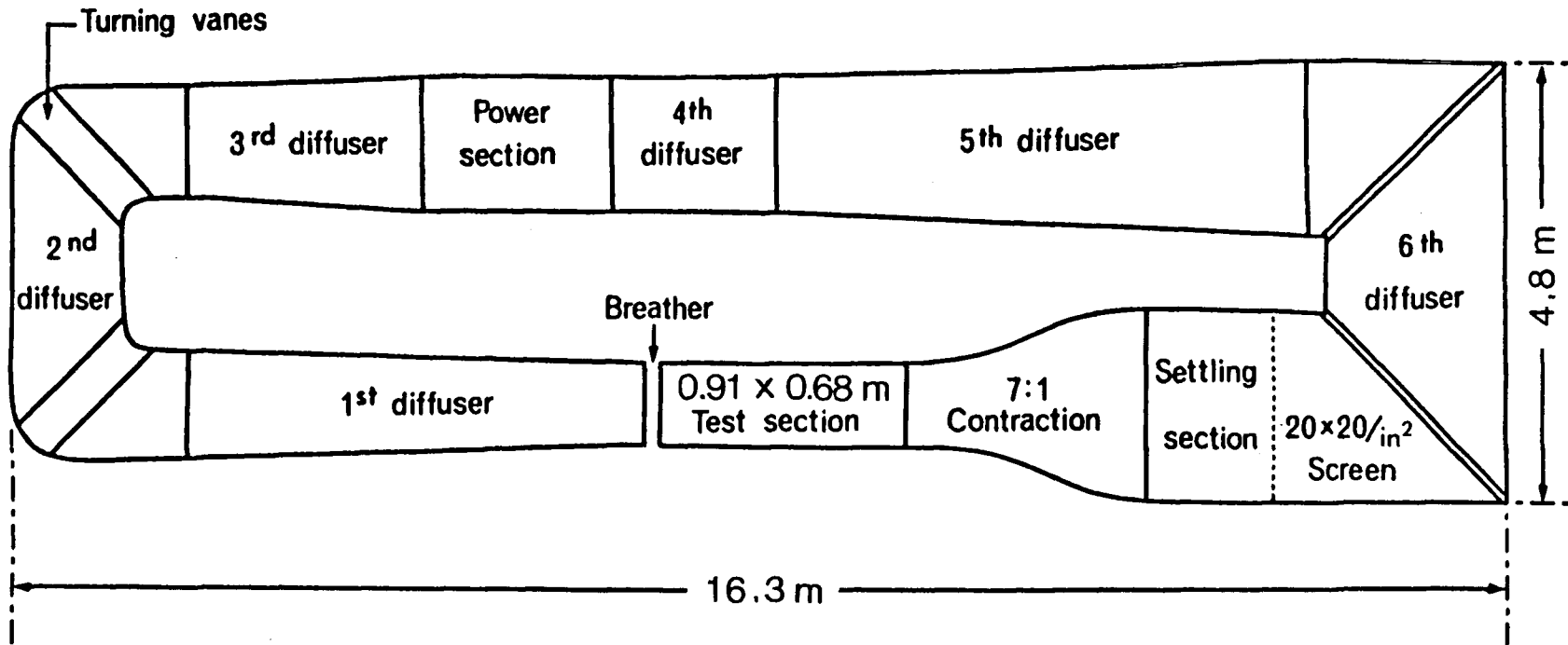


Figure 2-3 Schematic diagram of the wind tunnel used for the experimental study.

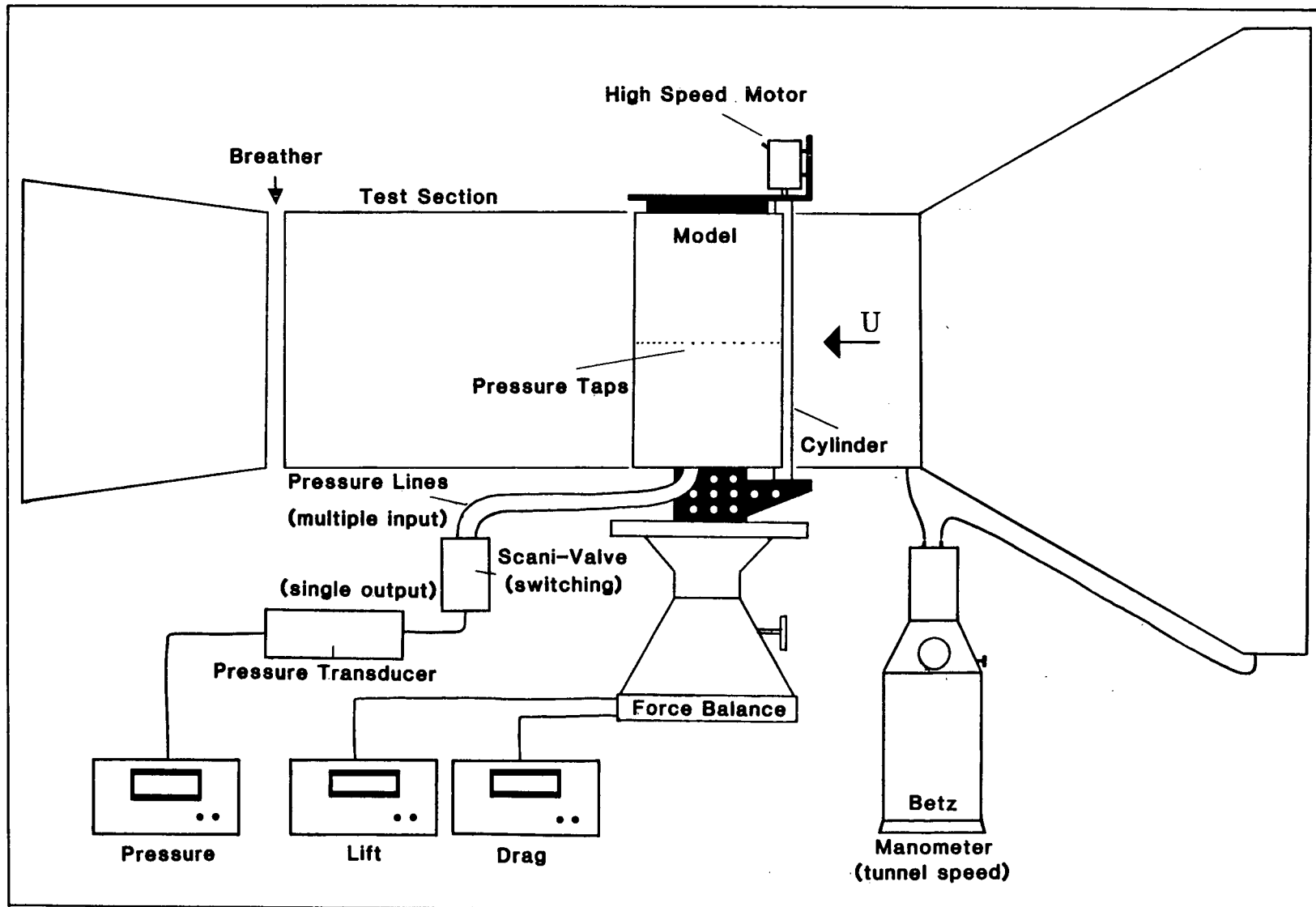


Figure 2-4 Schematic diagram of the experimental setup.

of the leading edge. Details of the leading edge geometry and the cylinder drive mechanism are shown in Figure 2-5. Primarily made of wood, the model carried a central aluminum pressure ring provided with 37 pressure taps distributed over the circumference with the exception of the leading edge. The rotating nose section was not provided with pressure taps in this set of experiments due to practical difficulty in locating the taps over the surface of a rotating cylinder. However, it was possible to replace the rotating cylinder with a nose fill-in section, provided with 5 pressure taps, to obtain local pressure information at the nose in absence of the cylinder rotation.

The three distinct configurations used in the experiments, including:

- (a) a solid smooth cylinder;
- (b) a scooped cylinder; and
- (c) a reversed scooped cylinder;

are shown in Figure 2-6. The cylinders were designed for clockwise rotation to inject momentum into the upper-surface boundary layer. Configuration (b) was designed as a "air scoop" to enhance cylinder's effect in displacing the air. It would slow down the flow over the lower surface and redirect more flow over the upper surface. Configuration (c), on the other hand, was designed as a vortex generator.

The rotating cylinder was mounted between two high speed bearings, housed in the brackets at either end of the model. It was driven by a 1/4 *h.p.*, 3.8 A Variac controlled motor, located outside the tunnel, through a standard Fenner Coupling (Figure 2-5). During a typical experiment, depending on the air speed in the tunnel and the ratio U_c/U , the cylinder rotation rate could reach as high as 17,000 *rpm* (with the solid cylinder).

A photograph of the model is presented in Figure 2-7. The leading-edge-cylinder drive assembly can be clearly seen here with the scooped cylinder in place. Also shown on the side of the model is the nose fill-in section mentioned above.

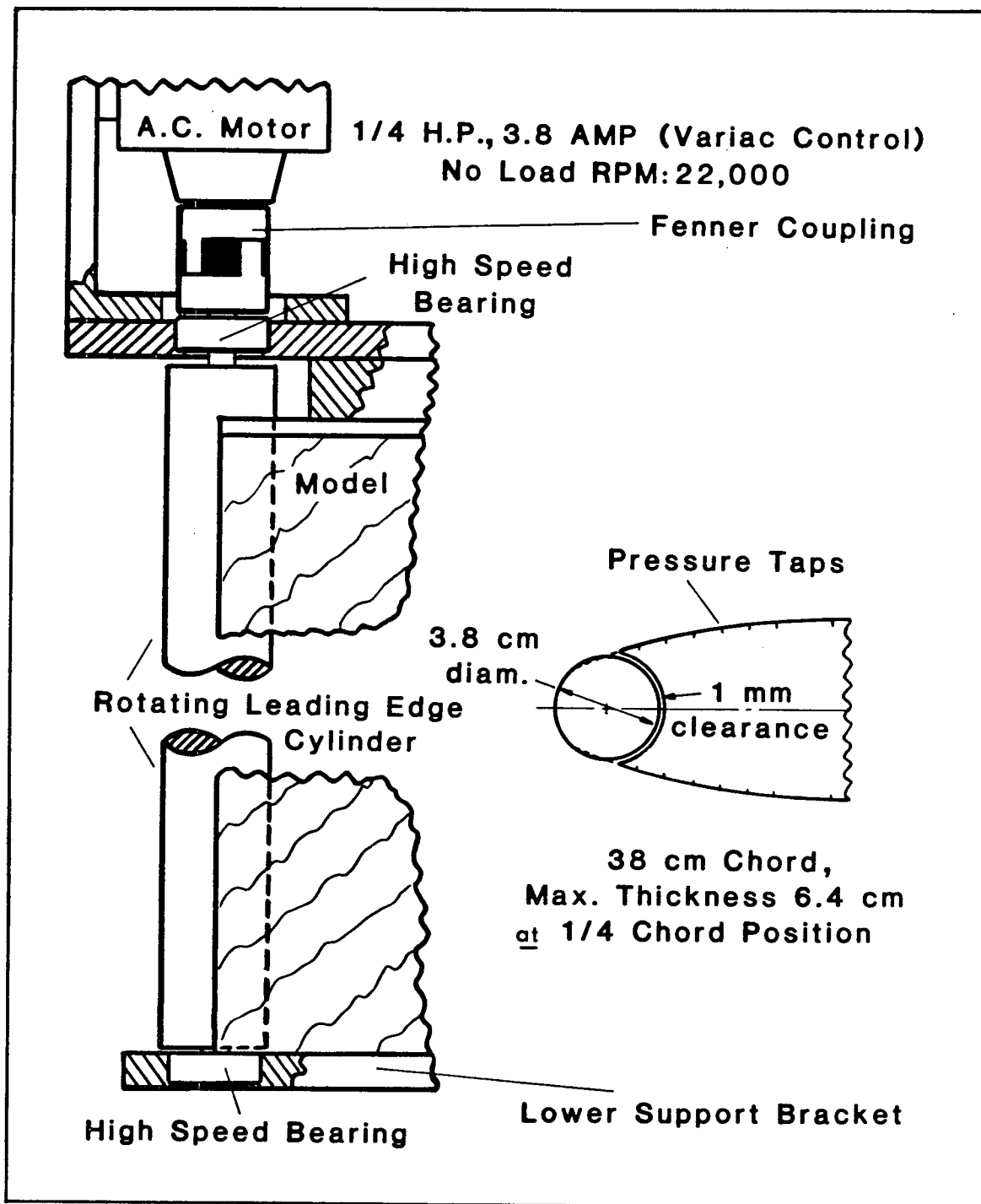


Figure 2-5 Detailed schematic of the leading edge rotating cylinder and cylinder drive mechanism.

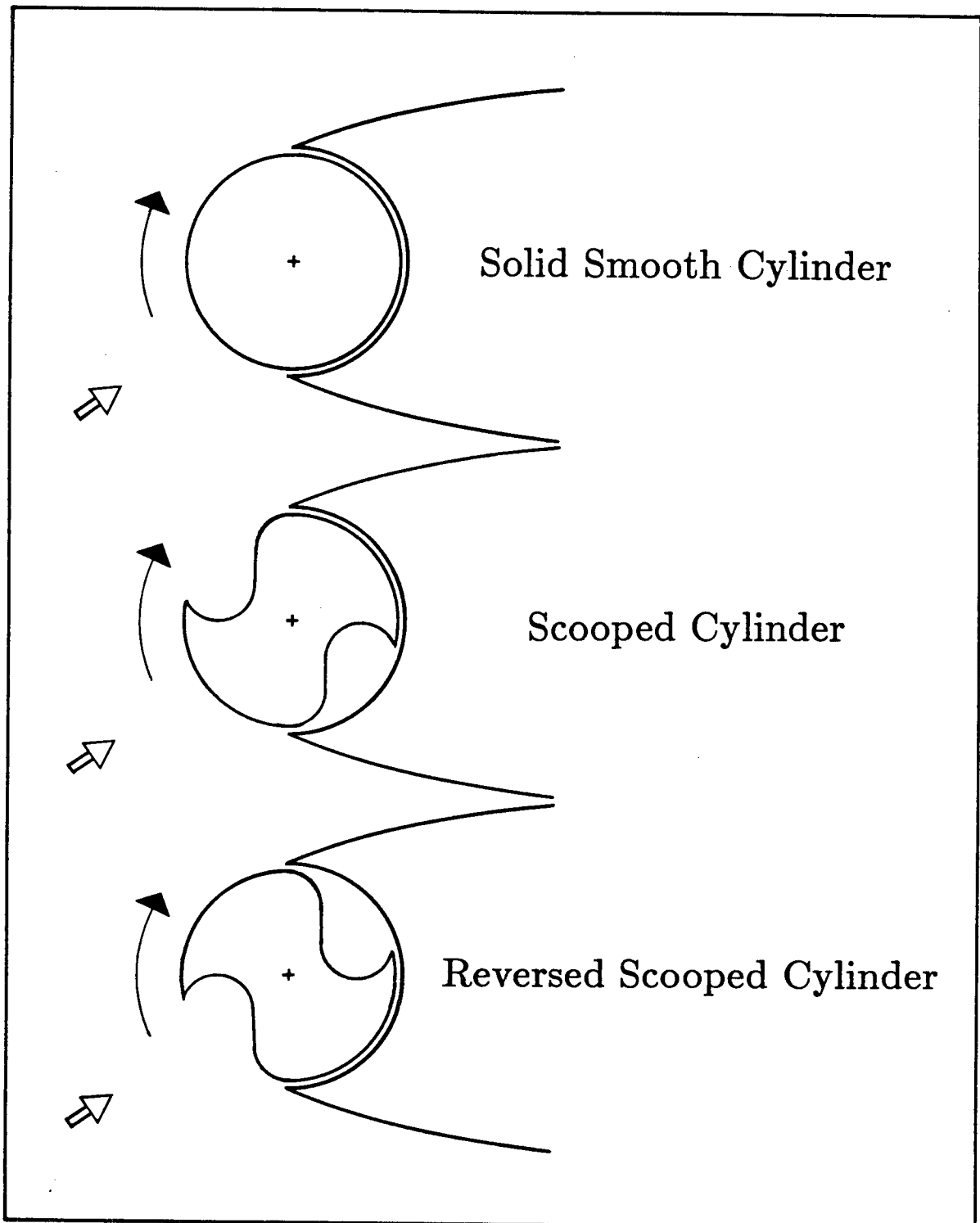


Figure 2-6 Various geometries of the leading-edge-cylinder used in the experiments.

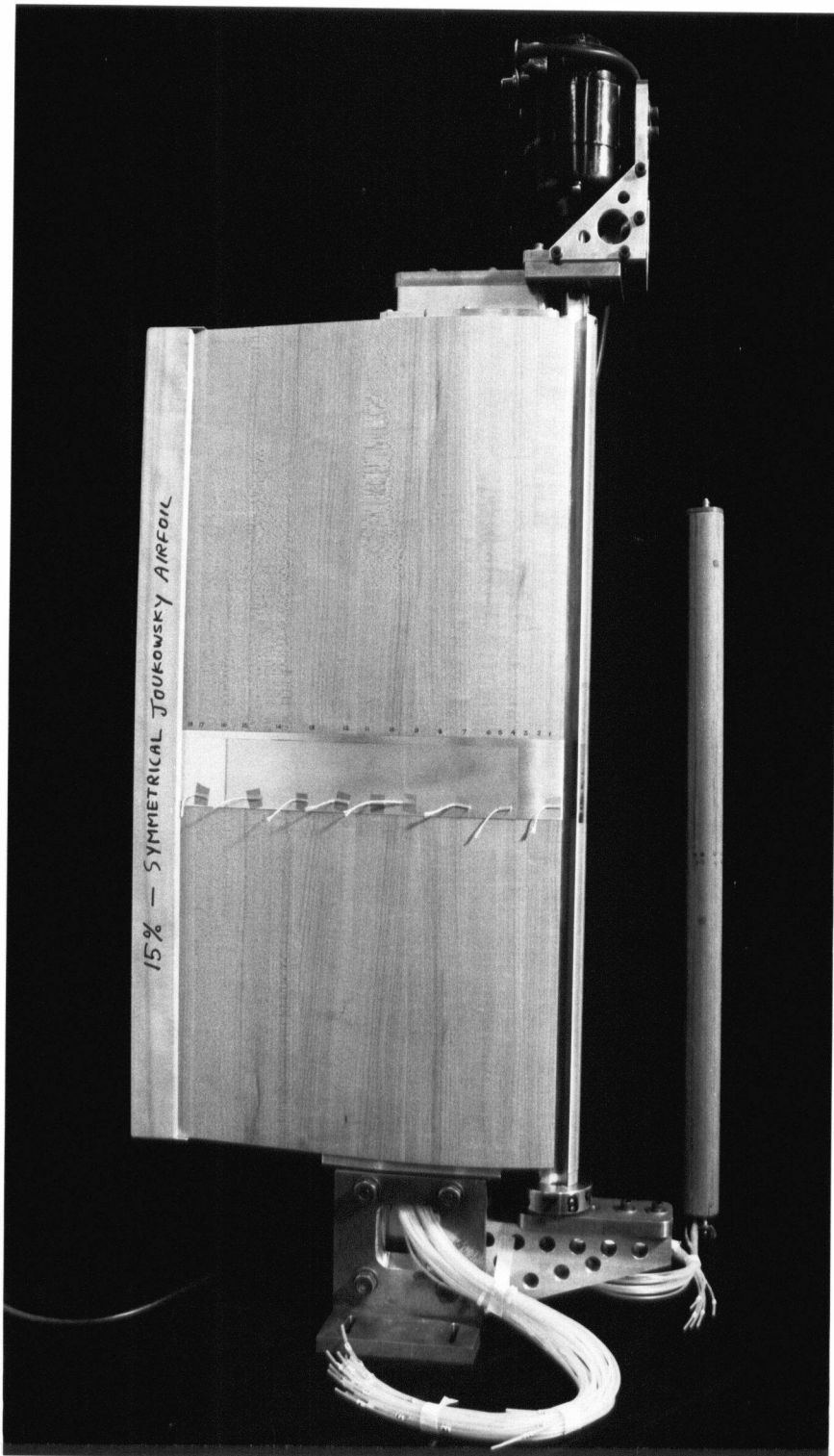


Figure 2-7 Photograph of the Joukowski model I showing the scooped leading-edge-cylinder in place. Also shown, on the side, is the nose fill-in section.

The tests were carried out over a range of cylinder rotational speeds ($U_c/U = 0, 1, 2, 3, 4$ for the solid cylinder and $U_c/U = 1/8, 1/4, 1/2, 1$ for the scooped cylinders) and angles of attack at a Reynolds number of 2.3×10^5 .

To provide greater flexibility in locating the cylinder on the airfoil and permit testing of multicylinder configurations, a new sectional model of the same basic Joukowsky shape was constructed. The model consists of an aluminum skin wrapped around an aluminum and steel frame with various sections of the surface removable, as required, to accommodate cylinders. Photographs of the model in Figure 2-8 show details of the construction including the removable sections and possible locations of the rotating cylinders. The nose fill-in section (A) replaced the leading-edge-cylinder when it was not used as a rotating element. The trailing-edge section (B) of the model was removed while using the trailing-edge-cylinder at location E. Note, the effective chord of the airfoil is reduced in this case. Also, the side panel (C) was removed to house the upper-surface-cylinders at locations F.

The possible locations of the cylinders used in the experimental program are shown in Figure 2-9. The actual configurations tested were:

- a) the leading-edge-cylinder;
- b) the trailing-edge-cylinder;
- c) leading and trailing-edge-cylinders;
- d) the upper-surface rear or forward cylinder;
- e) the upper-surface rear or forward cylinder in conjunction with the leading-edge-cylinder; and
- f) the upper leading-edge-cylinder.

For the upper leading-edge-cylinder configuration a different nose section (also shown in Figure 2-9) was constructed.

The model was provided with a total of 44 pressure taps, distributed over the

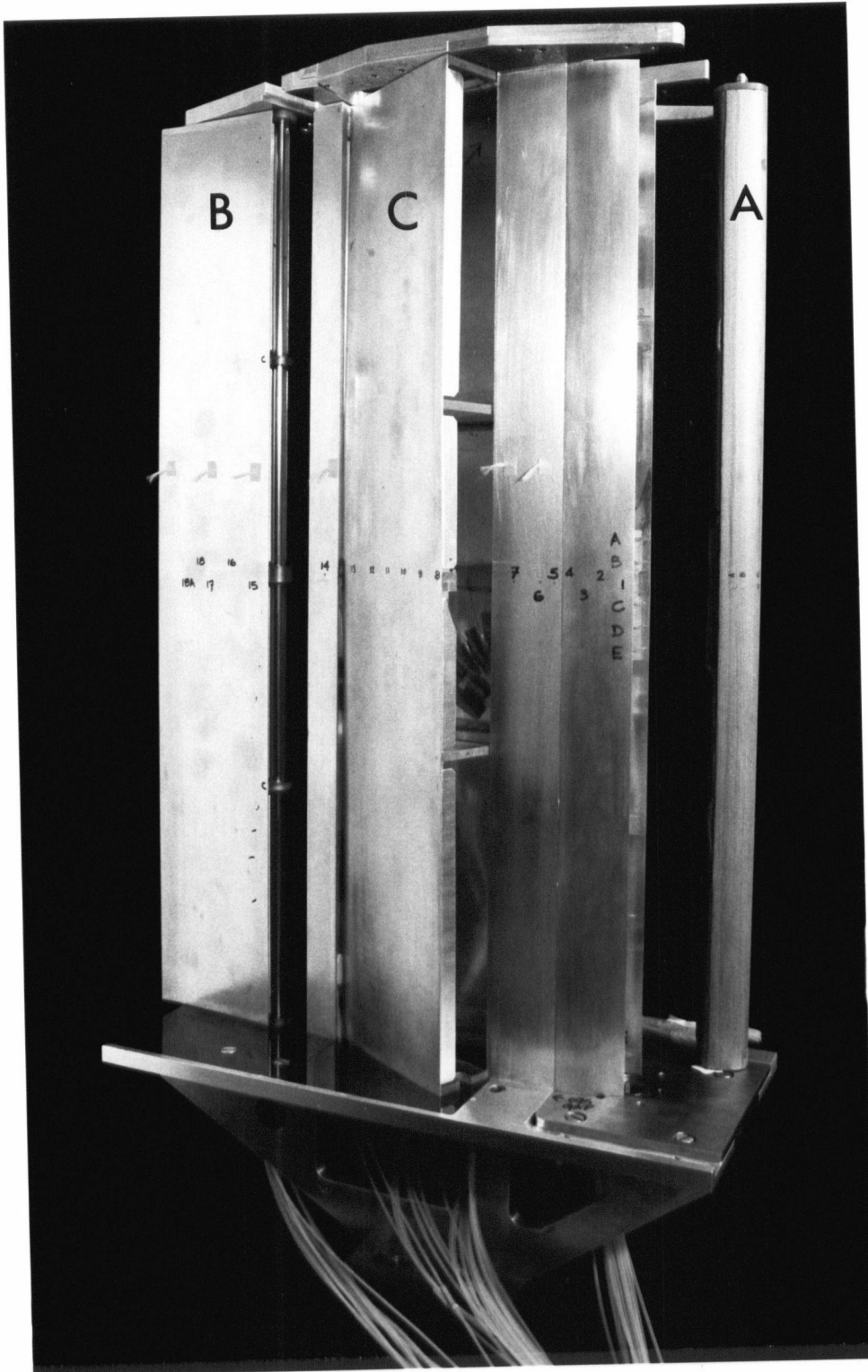


Figure 2-8 Photographs of the Joukowsky model II showing:
(a) various removable sections of the airfoil: **A**, nose fill-in section; **B**, trailing edge; **C**, side panel;



Figure 2-8 Photographs of the Joukowski model II showing:
(b) locations of the cylinders: **D**, location of the L.E. cylinder; **E**, location of the T.E. cylinder; **F**, locations of the upper-surface front and rear cylinders.

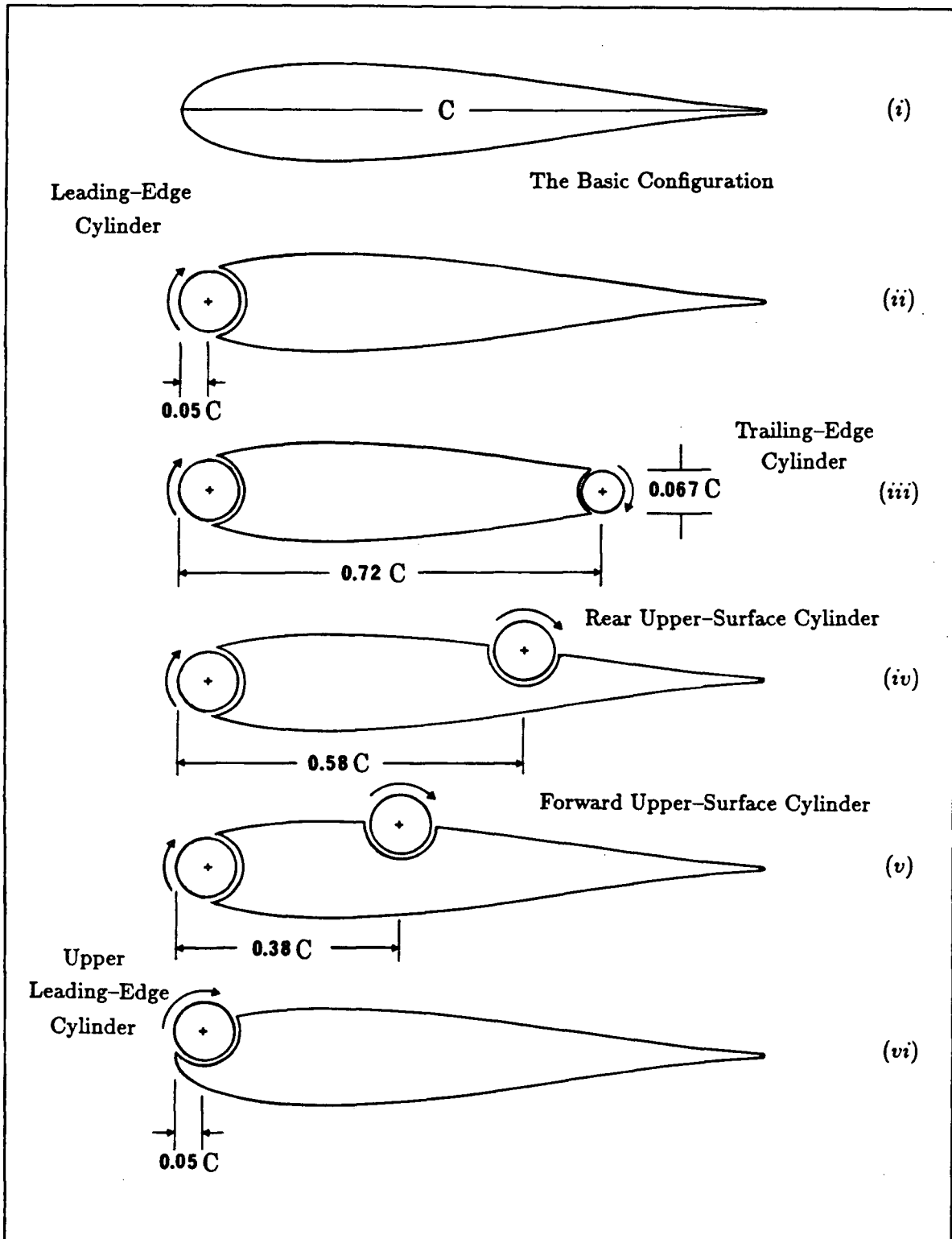


Figure 2.9 Various rotating cylinder configurations possible with the Joukowski airfoil model II.

circumference, to yield detailed information about the surface loading. However, once a section of the model was removed to accommodate a cylinder, the pressure taps in that section were lost. Although the pressure information over the small region represented by the upper cylinder is not of particular significance, the corresponding data at the leading edge of the airfoil is crucial since it represents a high suction region. Its measurement presented a challenging task. Locating pressure taps on the surface of the cylinder, typically rotating in the range of 2000 to 7000 *rpm* offers enormous practical difficulty. The problem was resolved by measuring the pressure in the immediate vicinity of the cylinder rather than on the surface itself.

This was achieved by keeping the pressure taps stationary while the cylinder rotated. By locating the tap in a narrow ring, the width of which represented only a very small fraction of that of the cylinder, it was possible to ensure the continuity of flow over the entire surface and obtain an estimate of the surrounding pressure. The leading-edge-cylinder was provided with a groove to house the "pressure rings" while maintaining the cylinder surface uniform. Figure 2-10 shows details of the leading edge geometry and position of the pressure taps.

Tests with the Joukowski model II were conducted over an extended range of angles of attack and cylinder rotational speeds, corresponding to $U_c/U = 0, 1, 2, 3, 4, 5$, at a Reynolds number of 4.62×10^4 . The choice of the lower Reynolds number in this case was dictated by vibration problems with multicylinder configurations operating at high rotational speeds.

2.2 NACA 63-218 Modified Airfoil Model

The Joukowski cross-section, though convenient for analysis, is not suitable for practical application because of the cusp and relatively poor aerodynamic characteristics. It was, therefore, thought appropriate to apply the moving surface boundary layer control concept to a more practical configuration. To that end,

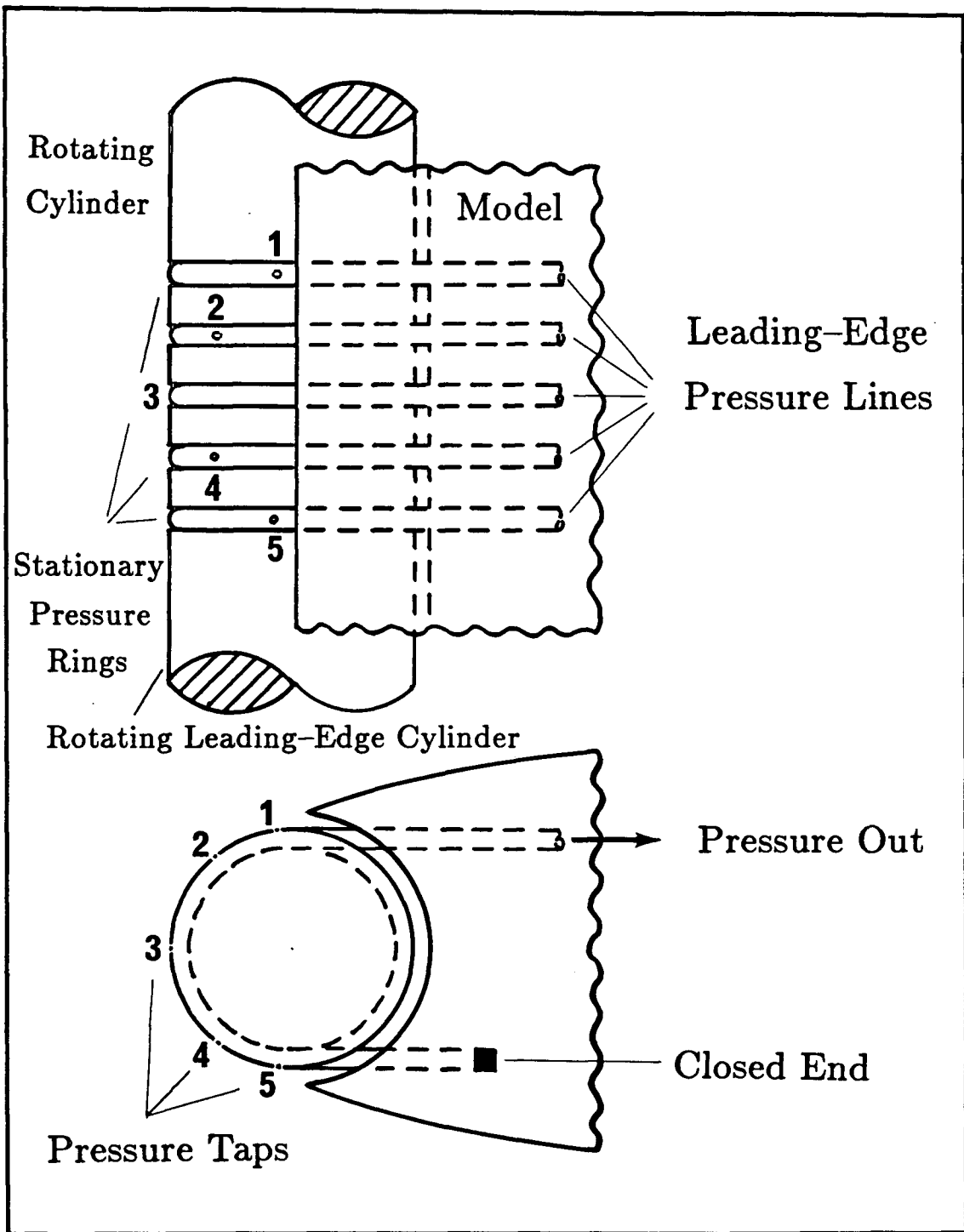


Figure 2-10 Schematic diagram of the leading edge construction of the Joukowski model II showing the details of the pressure taps.

the NACA 63-218 (modified) section, which was used in the Canadair CL-84 (a twin propeller V/STOL design), was selected. Availability of some preliminary lift information for the section in presence of a leading-edge cylinder [27] was also a factor in its choice.

A model was constructed with a leading-edge-cylinder (Figure 2-11), as that had shown to be a relatively more effective element. The trailing-edge and upper-surface cylinder tests were not deemed necessary here as the earlier results had already established trends as to their relative contributions. The objective was not to compile an extensive set of results but to confirm effectiveness of the concept with reference to a more practical airfoil section.

As before, the tests were carried out with a systematic variation of the angle of attack and the cylinder rotational speed ($U_c/U = 0, 1, 2, 3$) at a Reynolds number of 2.3×10^5 .

2.3 Presentation of Results

The relatively large angles of attack used in the experiments result in a considerable blockage of the wind tunnel test-section, from 21% at $\alpha = 30^\circ$ to 30% at $\alpha = 45^\circ$. The wall confinement leads to an increase in local wind speed, at the location of the model, thus resulting in an increase in aerodynamic forces. Several approximate correction procedures have been reported in literature to account for this effect. However, these procedures are mostly applicable to streamlined bodies with attached flow. A satisfactory procedure applicable to bluff bodies with *large* blockage is still not available.

With rotation of the cylinder(s), the problem is further complicated. As shown by the pressure data and confirmed by the flow visualization, the unsteady flow can be separating and reattaching over a large portion of the top surface. In absence of any reliable procedure to account for wall confinement effects in the present situation, the results are purposely presented in the uncorrected form.



Figure 2-11 Photograph of the NACA 63-218 airfoil showing the leading-edge-cylinder in place.

3. EXPERIMENTAL RESULTS AND DISCUSSION

3.1 Joukowski Model I

The symmetrical Joukowski airfoil model I was tested systematically at a Reynolds number of 2.31×10^5 over a range of angles of attack and cylinder speeds. The pressure plots were integrated for each case to obtain the corresponding lift coefficient. The amount of information obtained is rather extensive and only a few of the typical results useful in establishing trends are recorded here.

Figure 3-1, which serves as a reference, shows pressure distribution on the surface of a conventional Joukowski airfoil, i.e., without rotating cylinder replacing its nose. Due to practical difficulty in locating pressure taps in the cusp region there is an apparent discontinuity in the pressure plots near the trailing edge. However, the region has little importance in the present discussion. It is apparent that the airfoil, in absence of any modification to its nose geometry, stalls at an angle of attack somewhere between 16° – 18° .

3.1.1 Leading-edge-cylinder

Figure 3-2, which also serves as a reference, shows the adverse effect of replacing the nose by a nonrotating cylinder ($U_c/U = 0$). Again the discontinuity in the pressure plots near the leading edge is due to practical difficulty in measurement of pressure at the surface of the cylinder (this problem was subsequently resolved for the Joukowski model II tests). However, since in the subcritical flow regime, the peak negative pressure on the surface of a circular cylinder occurs at around 70° , location of the first pressure tap (top and bottom surfaces) would come quite close to it. Note, although the nose geometry is altered only slightly, now we have a two-element airfoil with a gap between the cylinder surface and the rest of the

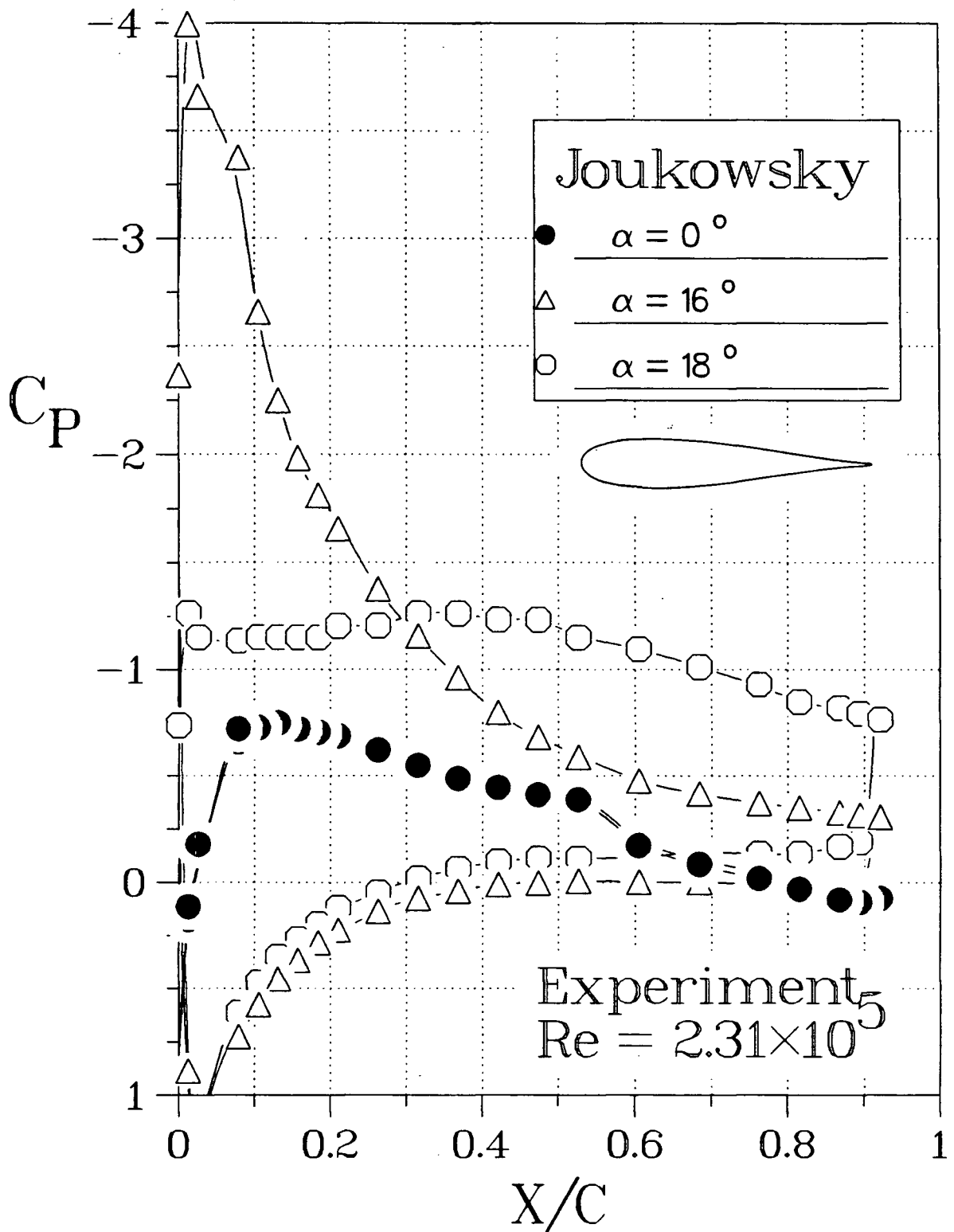


Figure 3-1 Typical experimentally obtained pressure distribution plots for a conventional Joukowski airfoil. These results serve as reference to assess the effects of airfoil modifications and cylinder rotation.

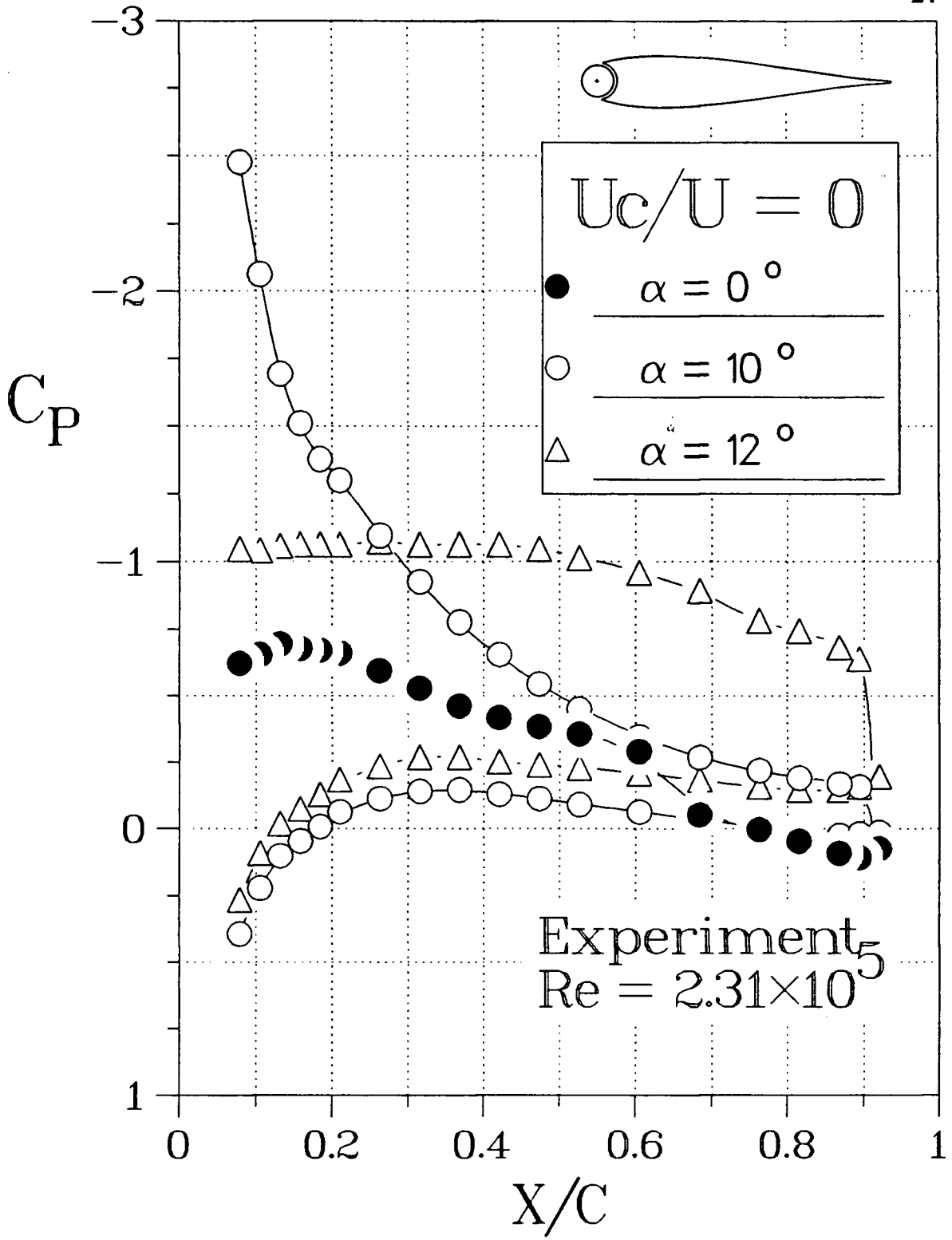


Figure 3-2 Effect of modification of the Joukowski airfoil with a leading-edge-cylinder on the pressure distribution. Note, the presence of a gap significantly reduces the stall angle.

airfoil. This discontinuity in the wall with a sharp corner protruding into the thin boundary layer causes it to grow faster and separate earlier thus reducing the stall angle which is now between 10° – 12° .

The pressure distribution plots before stall, however, did not show any significant deviation from the no-gap case except very close to the gap where presence of the sharp corner produced a slightly higher suction (Figure 3-3). There seems to be little indication of any appreciable flow leakage from the bottom to the top surface through the cylinder-airfoil interface. The effect of the gap is, therefore, confined to causing stall at a lower angle of attack in this case.

Figure 3-4 shows the effect of cylinder rotation on the pressure distribution and the onset of stall. Four cases of $U_c/U = 1, 2, 3, 4$ are considered for which Figure 3-2 serves as a reference. The plots bring to light several interesting points of information:

- In general, effect of the leading edge rotating cylinder is to increase the peak negative pressure. However, the relative increase is less at higher U_c/U .
- With an increase in cylinder surface velocity to free stream velocity ratio, the stall angle corresponding to complete separation (i.e., no reattachment) is delayed. Note, without rotation the separation (on the top surface) occurs at around 12° ; however, with rotation a part of the surface always has an attached flow up to $x/c \approx 0.25$.
- With higher rates of rotation the onset of flow separation occurs at a higher angle of attack and there is a tendency for the boundary-layer to reattach towards the trailing edge as best evident in Figure 3-4(d).
- One would expect the cylinder rotation to increase $C_{L,max}$ due to the delayed stall and give a higher C_L/C_D at any given angle of attack.

Figure 3-5 clearly shows the delay in stall brought about by the cylinder rotation. For $\alpha = 12^\circ$ the airfoil is stalled in absence of the cylinder rotation, however,

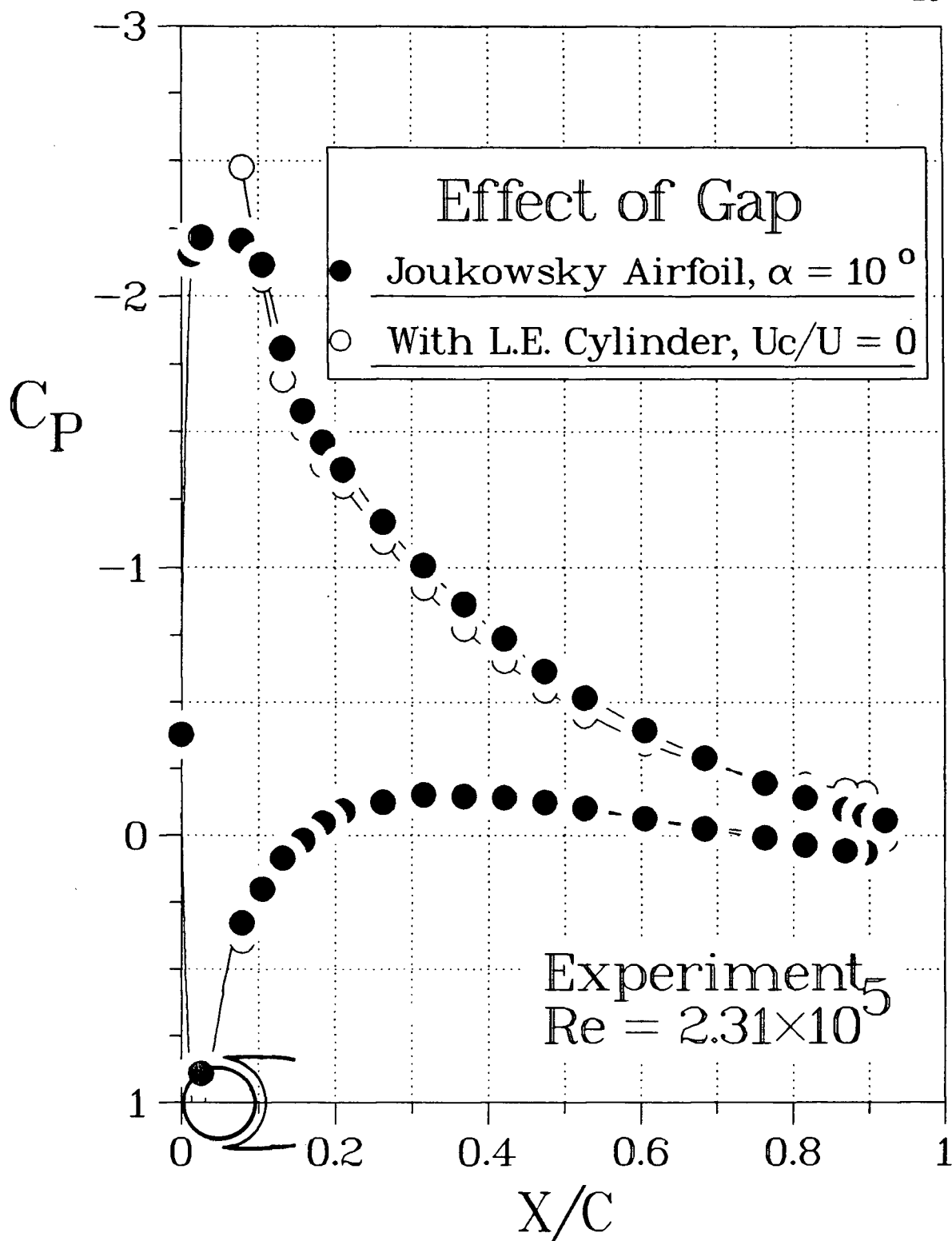


Figure 3-3 Effect of the gap (between the cylinder and the airfoil) on the pressure distribution of the Joukowski airfoil before stall.

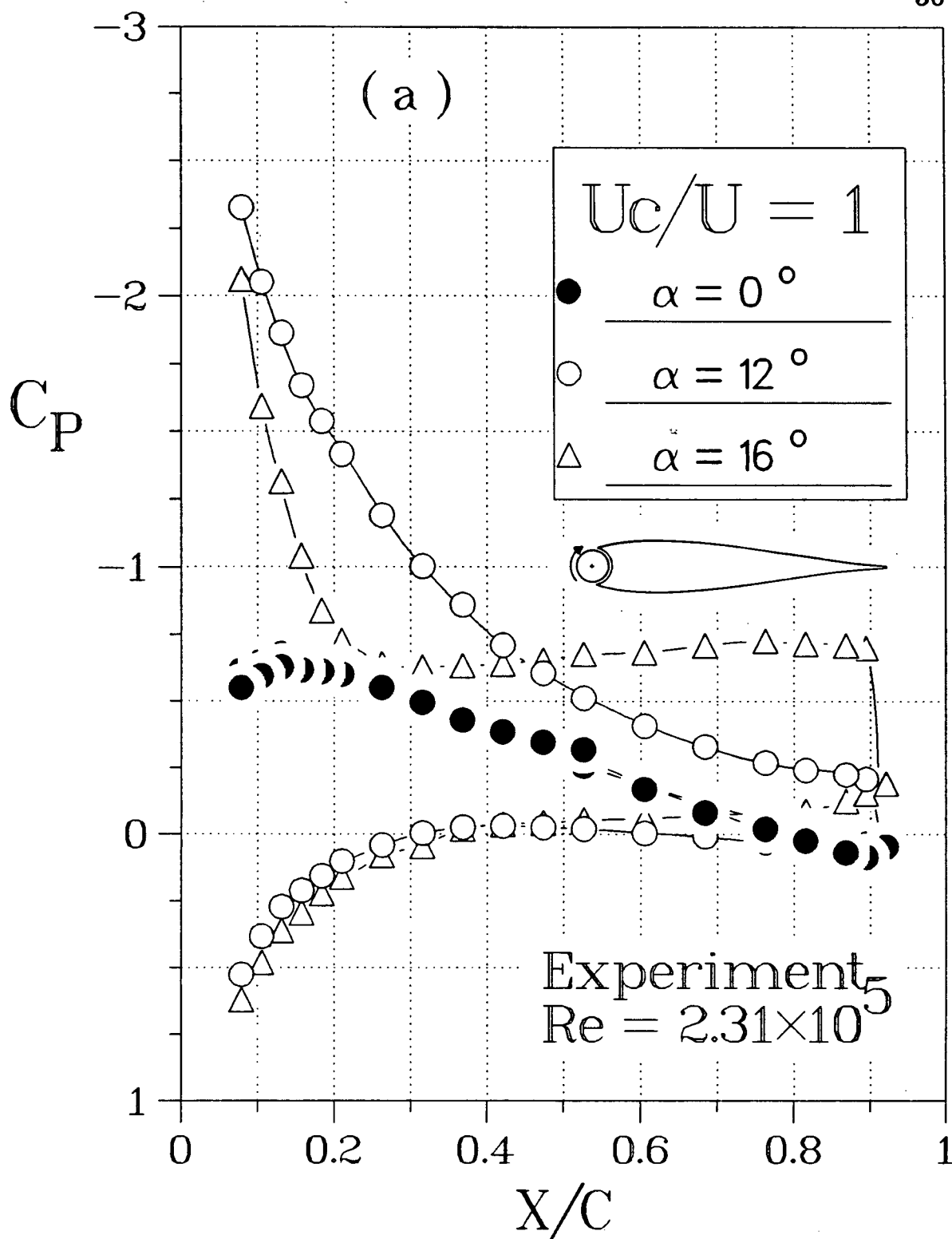


Figure 3-4 Effect of cylinder rotation on the pressure distribution around the Joukowski airfoil: (a) $U_c/U = 1$;

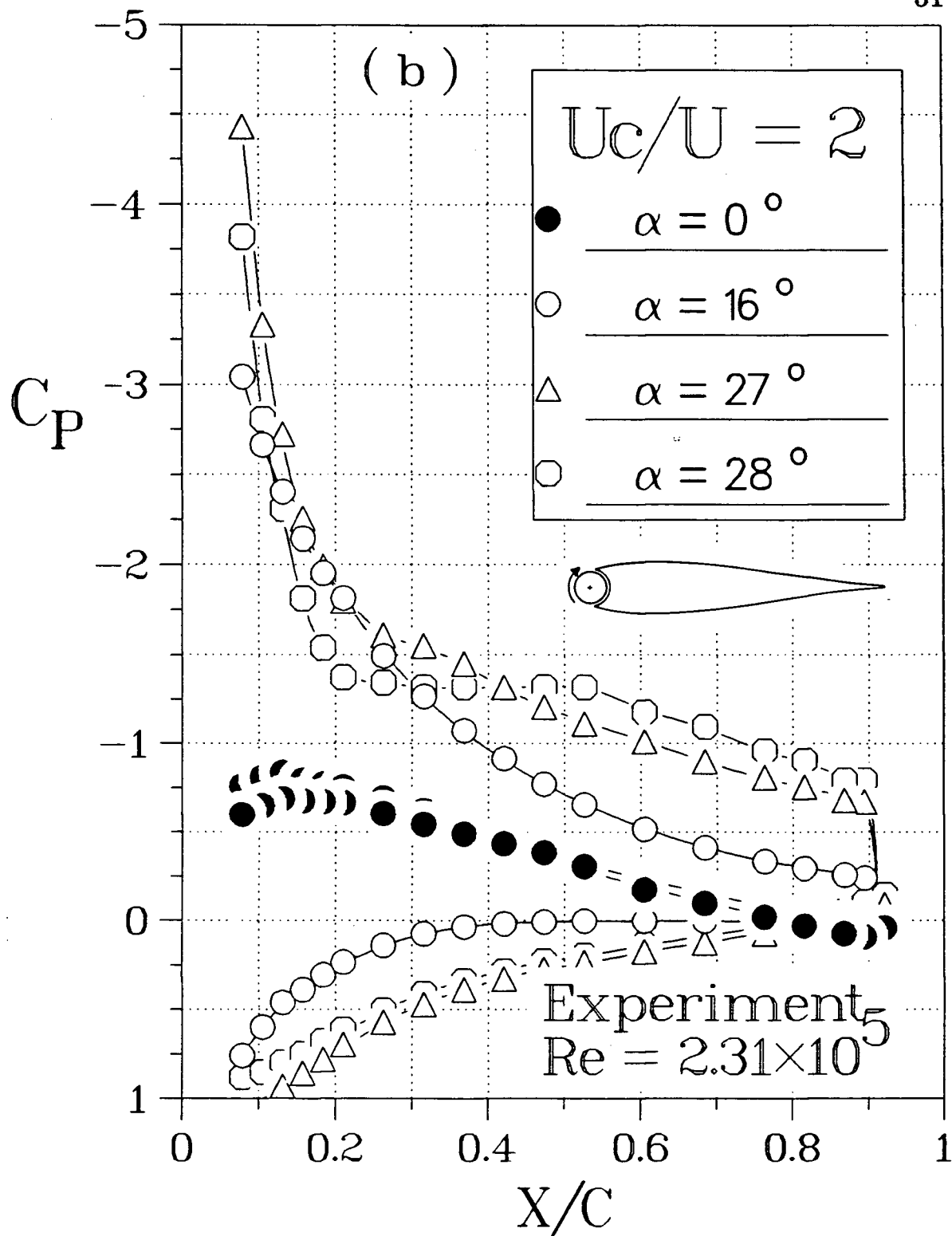


Figure 3-4 Effects of cylinder rotation on the pressure distribution around the Joukowski airfoil: (b) $U_c/U = 2$;

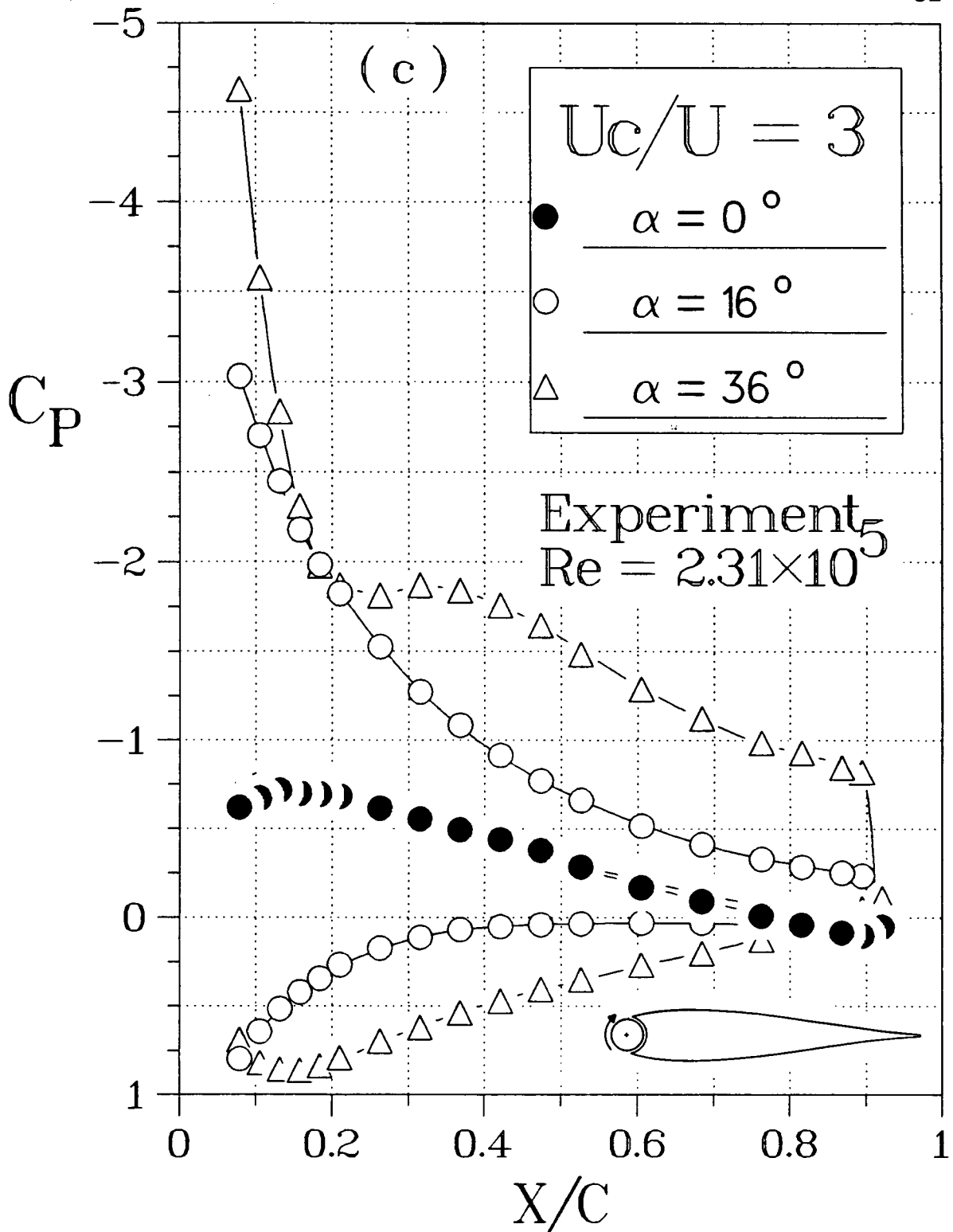


Figure 3-4 Effects of cylinder rotation on the pressure distribution around the Joukowski airfoil: (c) $U_c/U = 3$;

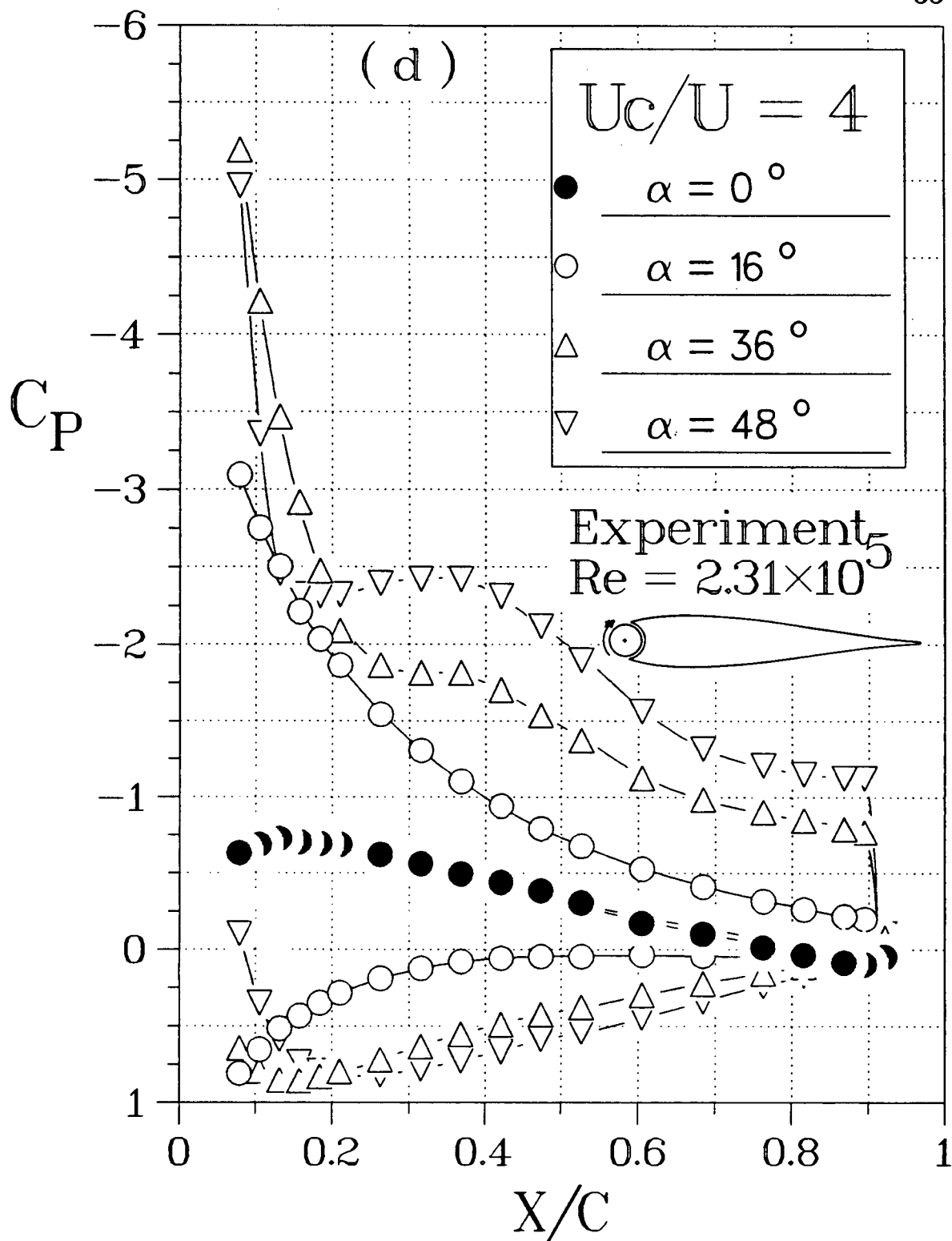


Figure 3-4 Effects of cylinder rotation on the pressure distribution around the Joukowski airfoil: (d) $U_c/U = 4$.

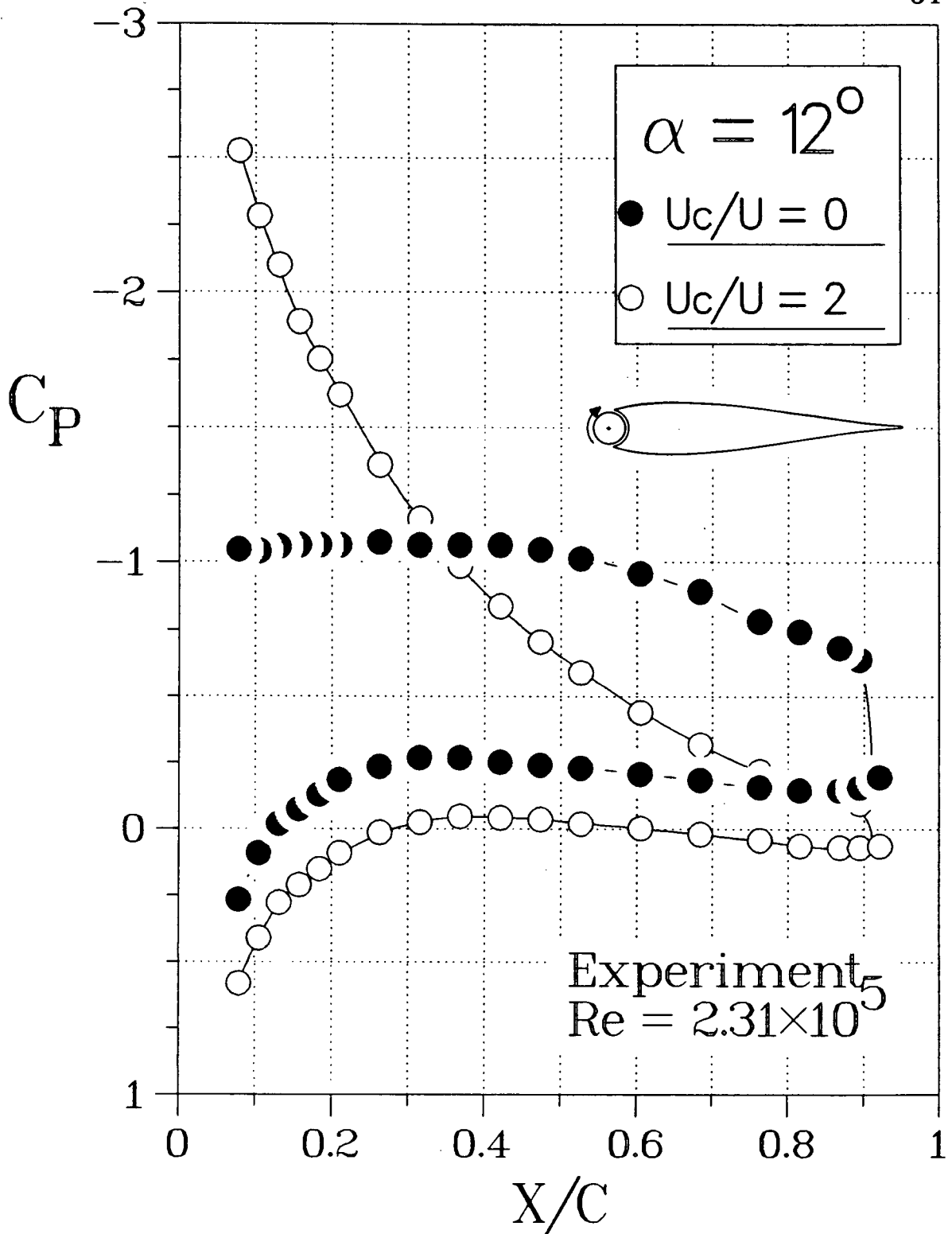


Figure 3-5 Experimentally obtained pressure plots showing the delay in stall brought about by the cylinder rotation.

with $U_c/U = 2$ the flow reattaches thus avoiding stall and the associated pressure collapse. Note, however, that at a sufficiently high angle of attack (say $\alpha = 32^\circ$, Figure 3-6), irrespective of the level of cylinder rotation, it is not possible to achieve completely attached flow over the top surface. Hence the pressure distribution over the bottom surface remains essentially the same. Further increase in the angle of attack only leads to an increase in the peak negative pressure at the leading edge.

The corresponding lift data for different rates of rotation of the cylinder are summarized in Figure 3-7. The basic (i.e., unmodified) Joukowski airfoil has a maximum lift coefficient of around 1.1. However, with modification, bluntness of the cylinder and the associated gap cause the $C_{L,max}$ to diminish. Note, the slope of the lift curve remains virtually unaffected. In absence of the cylinder rotation the modified airfoil stalls at around 12° giving uniform pressure distribution on the top surface as seen before (Figure 3-5). The stall sets in rather abruptly as shown by a sudden drop in lift. However, with the cylinder rotation, a large well developed suction peak at the leading edge of the wing suggests a delay in the stall. In fact the data show the stall to occur around 32° ($U_c/U = 4$) with an increase in the lift coefficient by about 68%. Note that an increase in cylinder speed beyond $U_c/U = 3$ improves the situation only marginally suggesting the existence of a critical speed ratio beyond which momentum injection through a moving surface appears to have little effect. Note also that the effect of rotation is to extend the lift curve without affecting its slope, and flatten the stall peak.

3.1.2 Leading-edge-scooped-cylinder

Typical pressure distribution plots for the Joukowski model with the leading-edge scooped cylinder rotating at $U_c/U = 1$ are shown in Figure 3-8. The plots, compared to those of Figure 3-4(a), show an improvement (in terms of larger suction and delayed separation) suggesting higher effectiveness of the scooped cylinder.

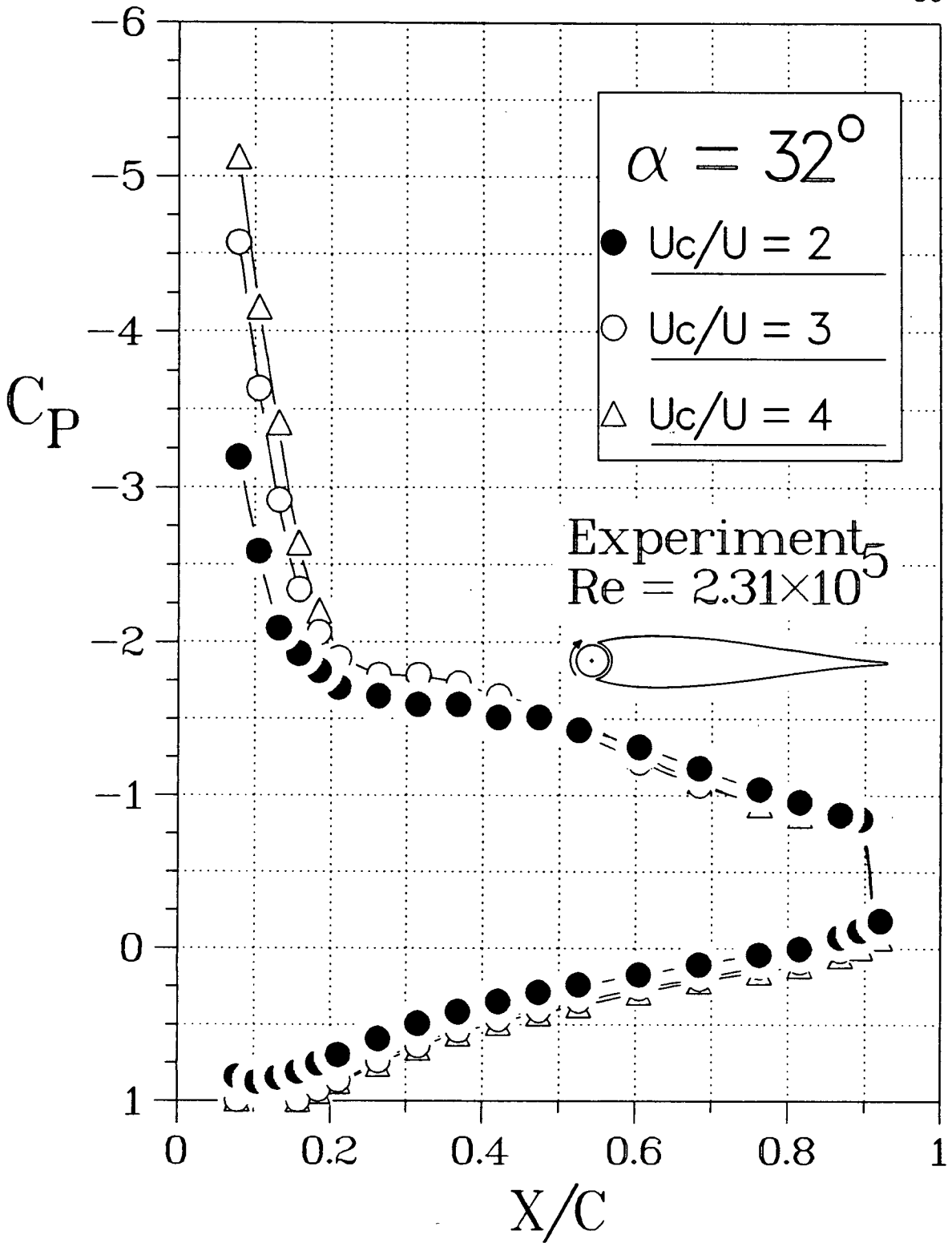


Figure 3-6 Effect of cylinder rotation on the pressure distribution over a Joukowski airfoil showing only partially separated flow even at a relatively high angle of attack.

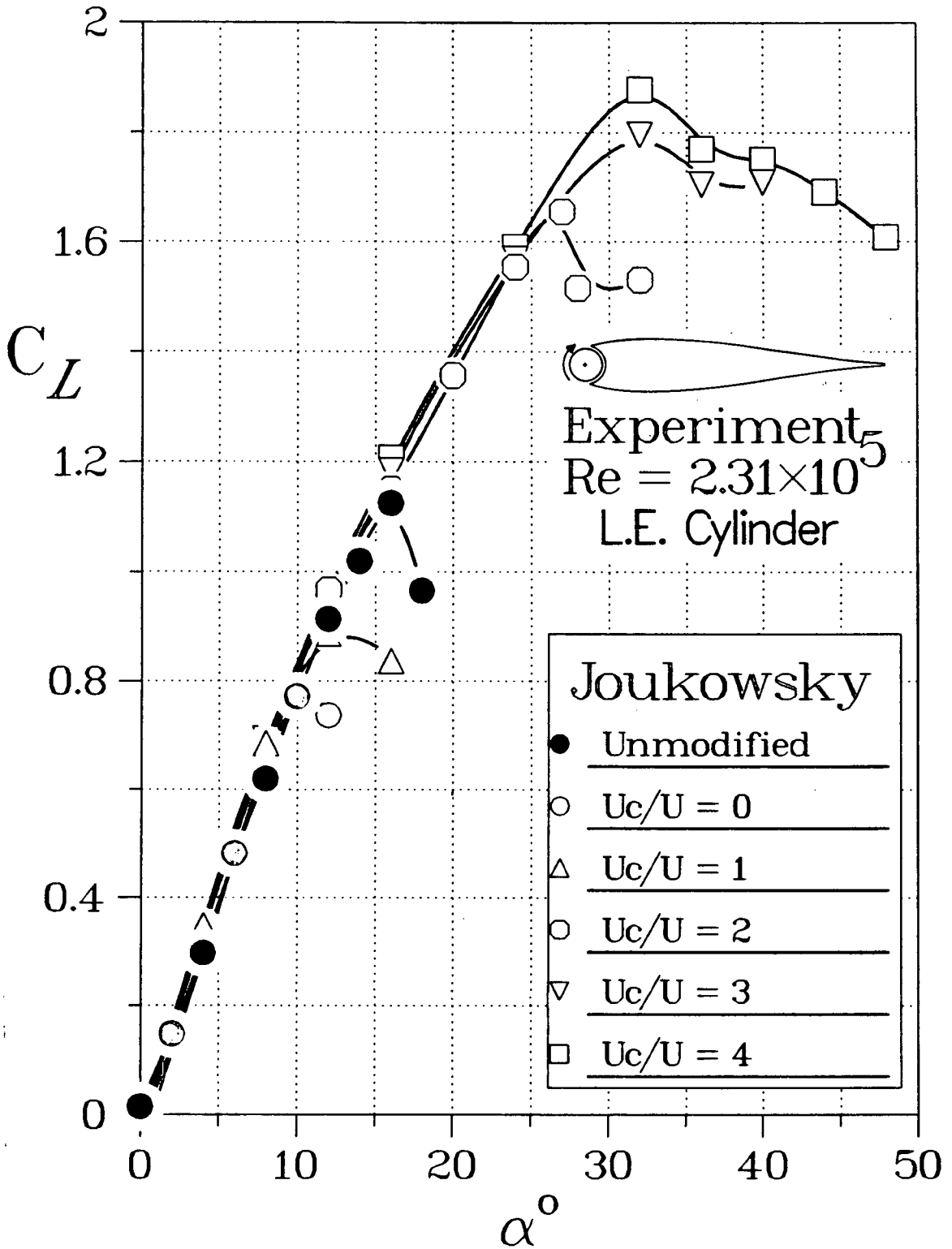


Figure 3-7 Plots showing variation of the lift coefficient with angle of attack as affected by the leading-edge cylinder and its rotation.

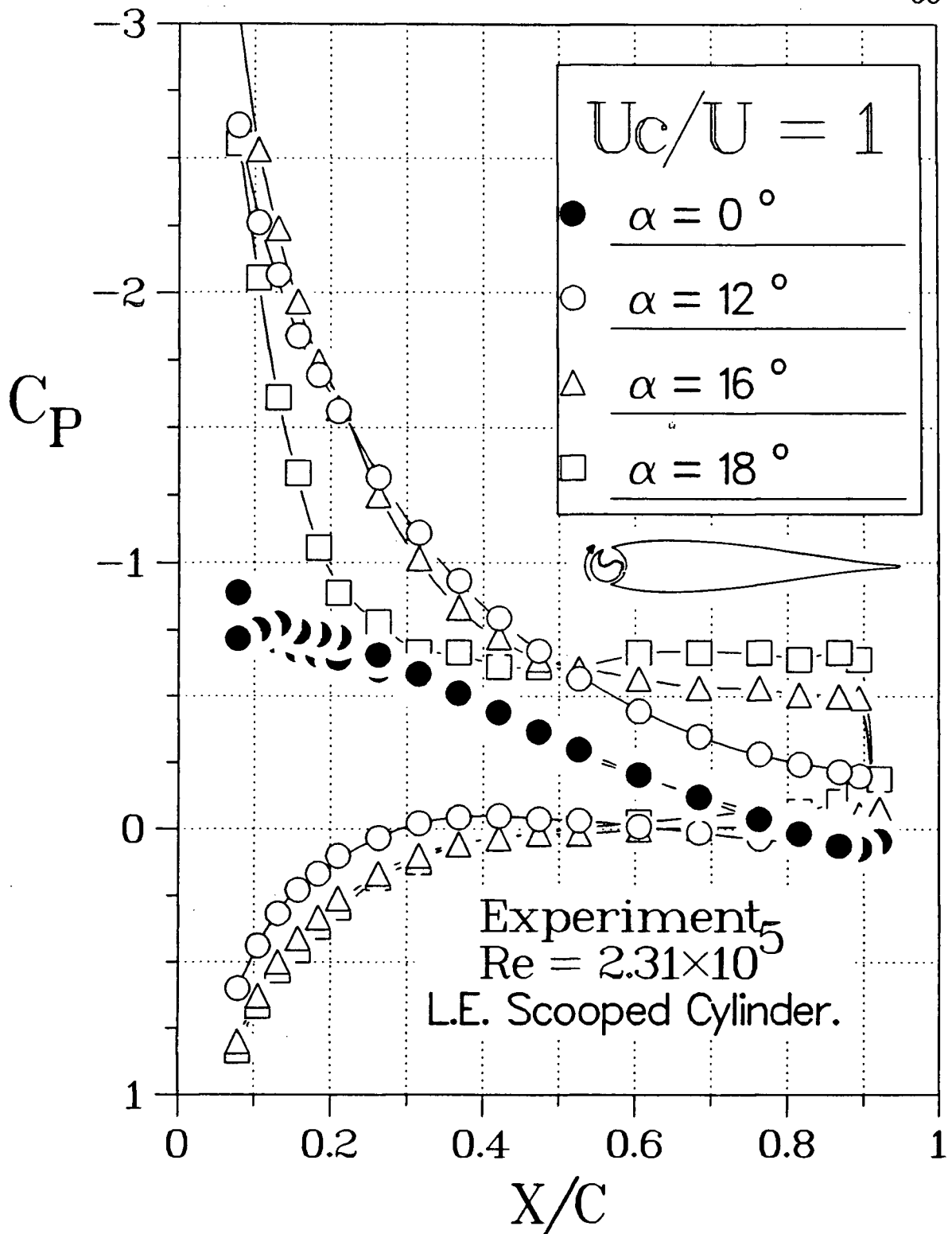


Figure 3-8 Pressure plot for the Joukowski airfoil with a leading-edge-scooped-cylinder. The results should be compared with those given in Figure 3-4(a).

The flow is now completely attached at $\alpha = 16^\circ$ with a much higher suction peak at the leading edge than that with the solid cylinder.

The rotating air-scoop appears to, in effect, slow down the flow over the lower surface and redirect more air over the upper surface. Reversing the scoop should therefore have the opposite effect. This is precisely the case as shown in Figure 3-9. The partially separated flow with the solid cylinder is reattached when the normal scoop configuration is used but completely detaches with the reversed scoop.

At higher rates of rotation the scooped cylinder appears to the flow as effectively solid and there is no particular advantage in having the scoop. On the other hand, slower speeds of rotation appear to enhance the effect of the scoop (Figure 3-10). For example, even at the cylinder rotation speed as low as $U_c/U = 0.125$ (the lowest speed used in the test program) the flow remains completely attached at $\alpha = 24^\circ$ (Figure 3-10c). This is in contrast to the separated flow at $\alpha = 16^\circ$ with the normal cylinder rotating at $U_c/U = 1$ (Figure 3-4).

The corresponding lift data are summarized in Figure 3-11. Typical results for normal solid cylinder at $U_c/U = 1$ are also included to facilitate comparison. A slight shift of the lift plots to the left suggests a small increase in circulation due to the scooped geometry. The main advantage of the scooped geometry is that it can provide the same beneficial effect of the normal rotating cylinder but at a much lower speed. The concept appears promising and needs to be explored further.

It may be of interest to point out that the experiments with the scooped cylinder were extremely difficult to conduct primarily due to the demanding balancing requirement. Even a small unbalance caused during machining of the 68 *cm* long cylinder was sufficient to cause vibration, particularly at higher speeds, which had to be controlled as the gap-size is only 1 *mm*. Thus the tolerance on machining and balancing was rather exacting.

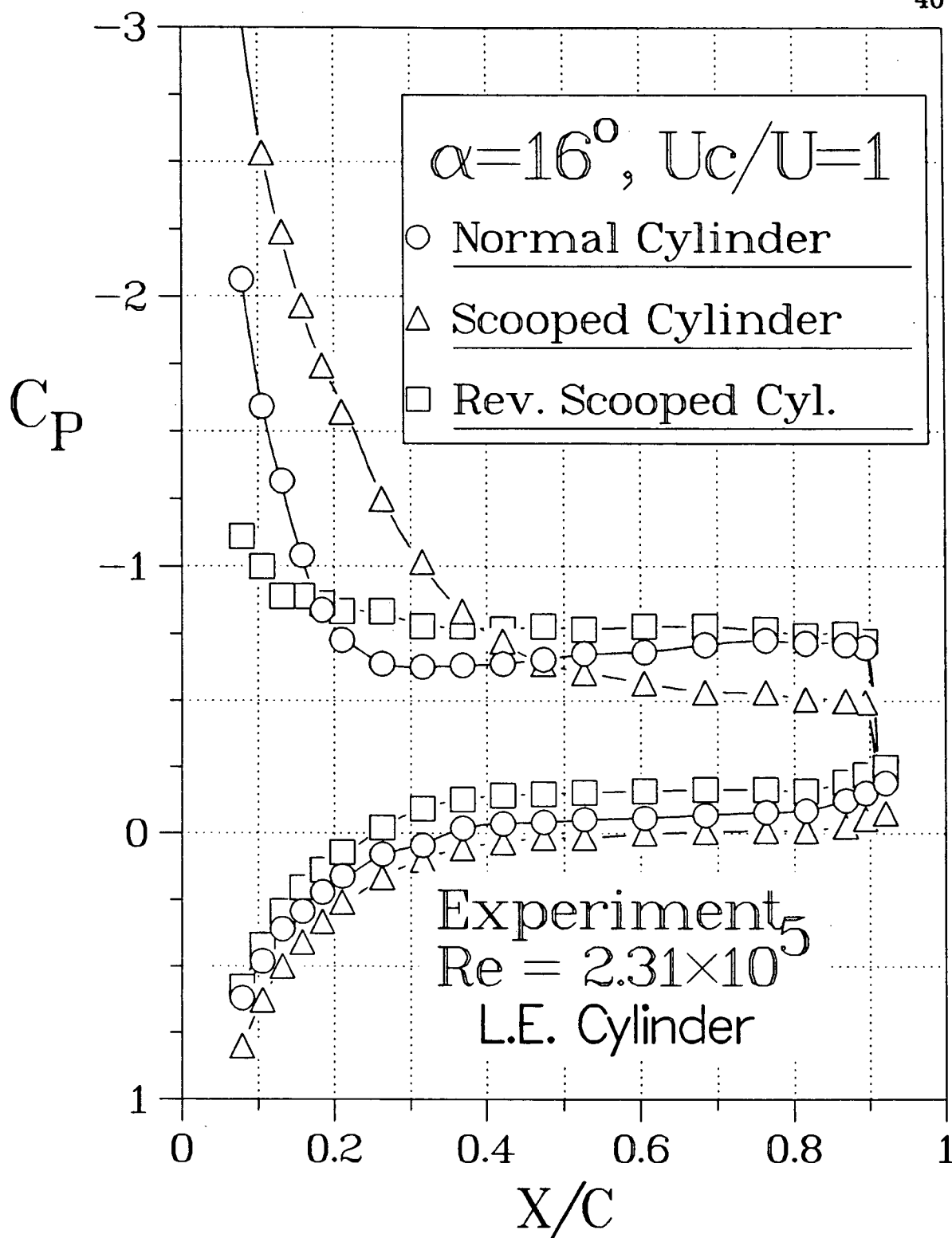


Figure 3-9 Effect of the leading-edge-cylinder configuration on the pressure distribution around the Joukowski airfoil, $U_c/U = 1$, $\alpha = 16^\circ$.

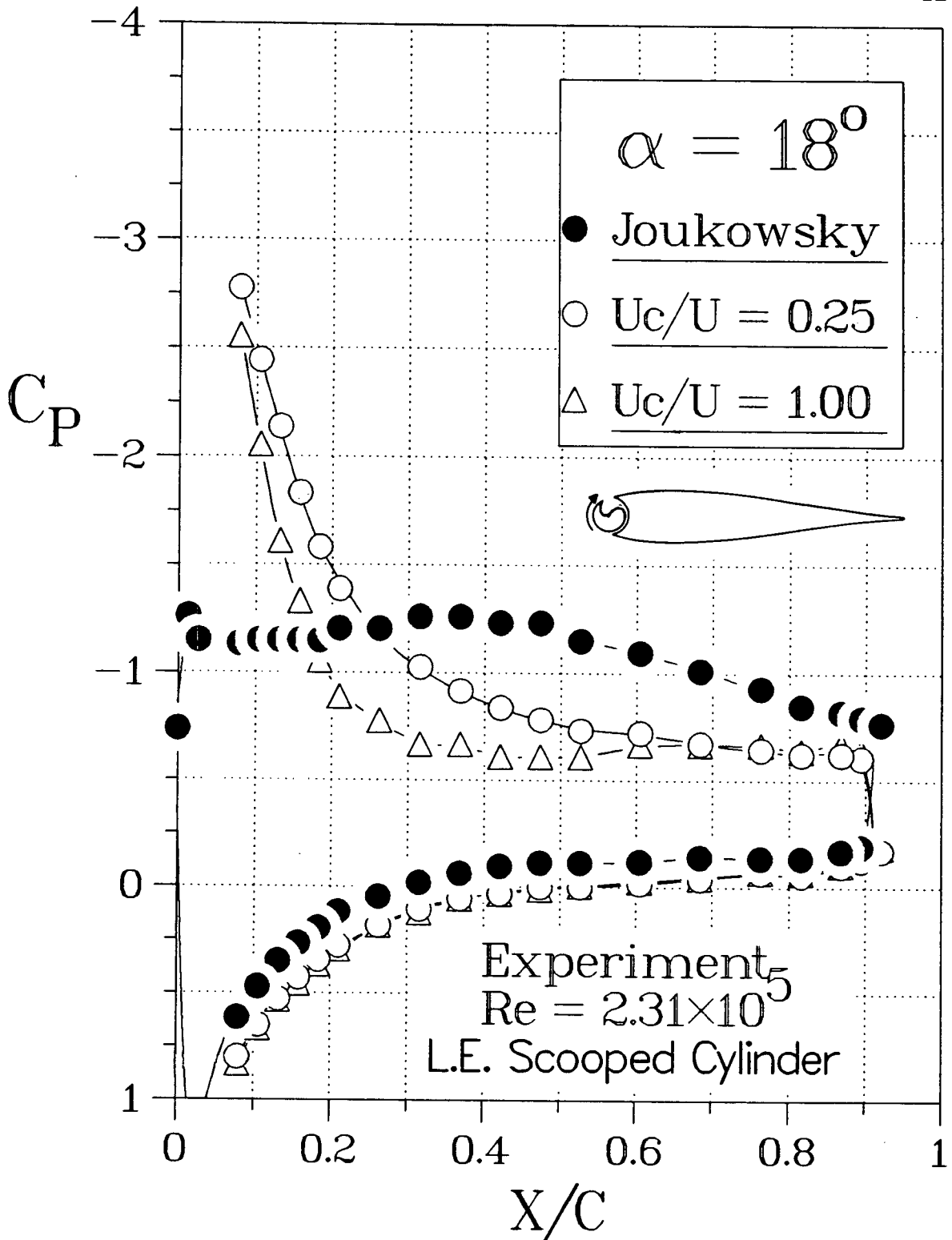


Figure 3-10 Experimentally obtained pressure plots for the Joukowski airfoil with a leading-edge-scooped-cylinder showing the effects of cylinder rotation and angle of attack: (a) $\alpha = 18^\circ$;

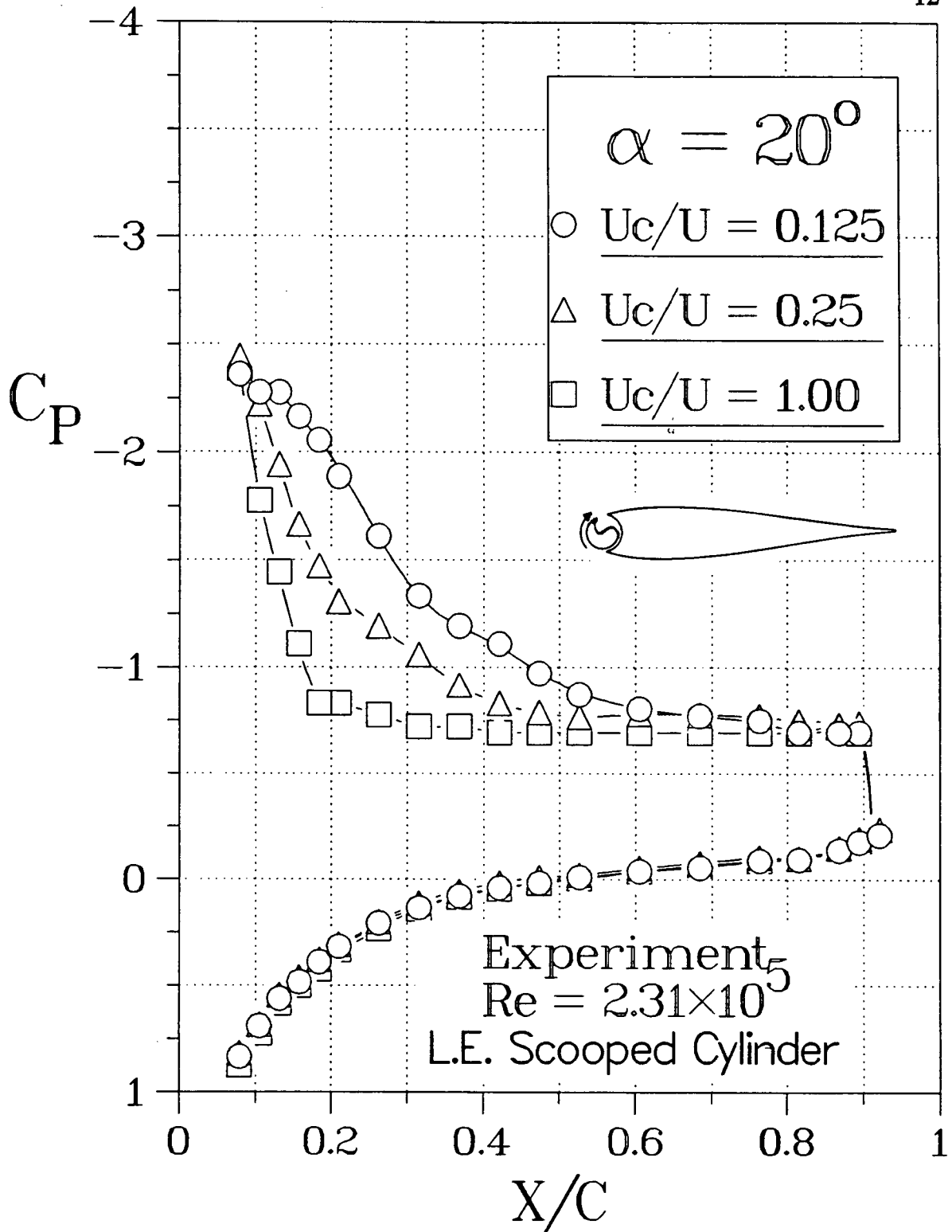


Figure 3-10 Experimentally obtained pressure plots for the Joukowski airfoil with a leading-edge-scooped-cylinder showing the effects of cylinder rotation and angle of attack: (b) $\alpha = 20^\circ$;

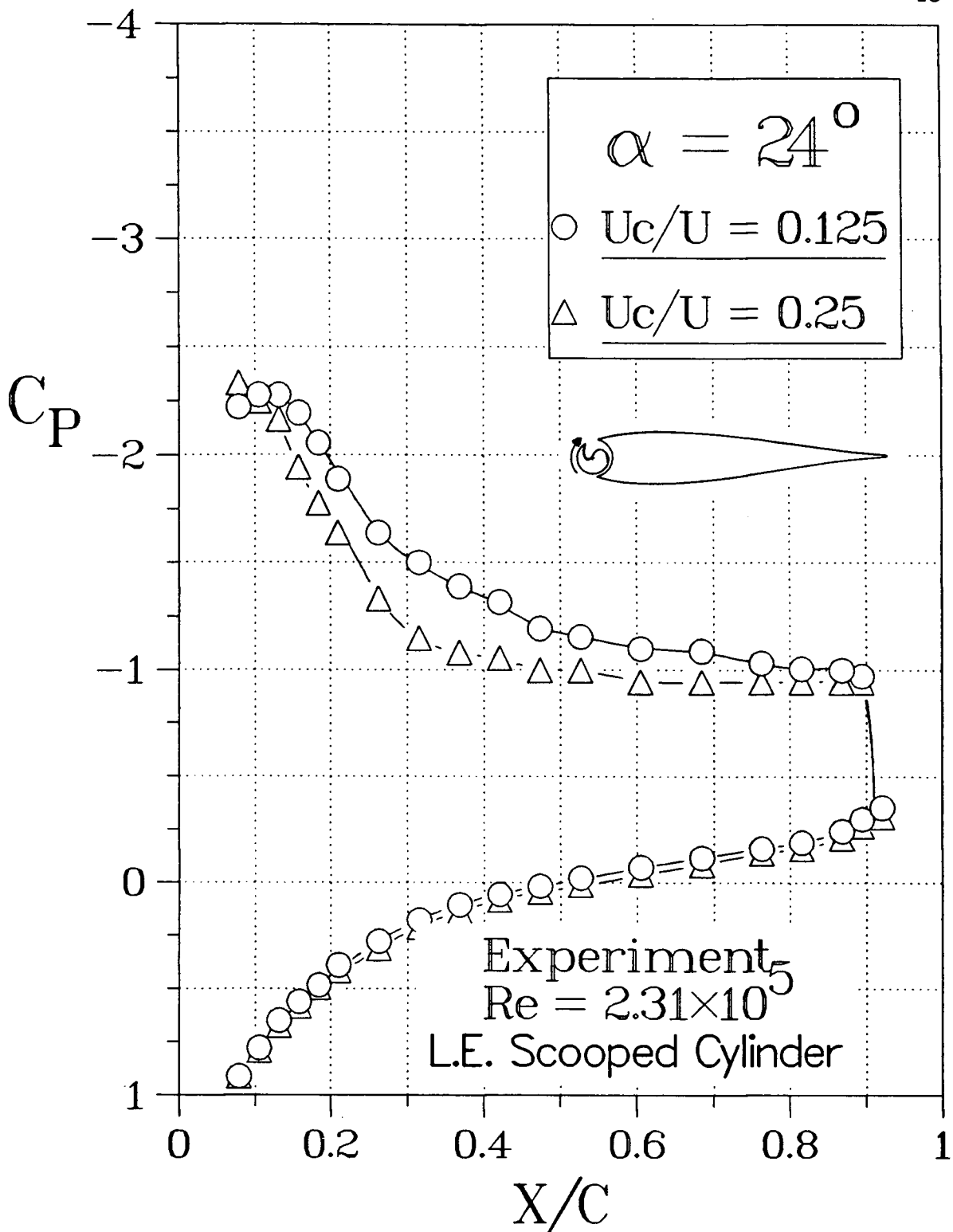


Figure 3-10 Experimentally obtained pressure plots for the Joukowski airfoil with a leading-edge-scooped-cylinder showing the effects of cylinder rotation and angle of attack: (c) $\alpha = 24^\circ$.

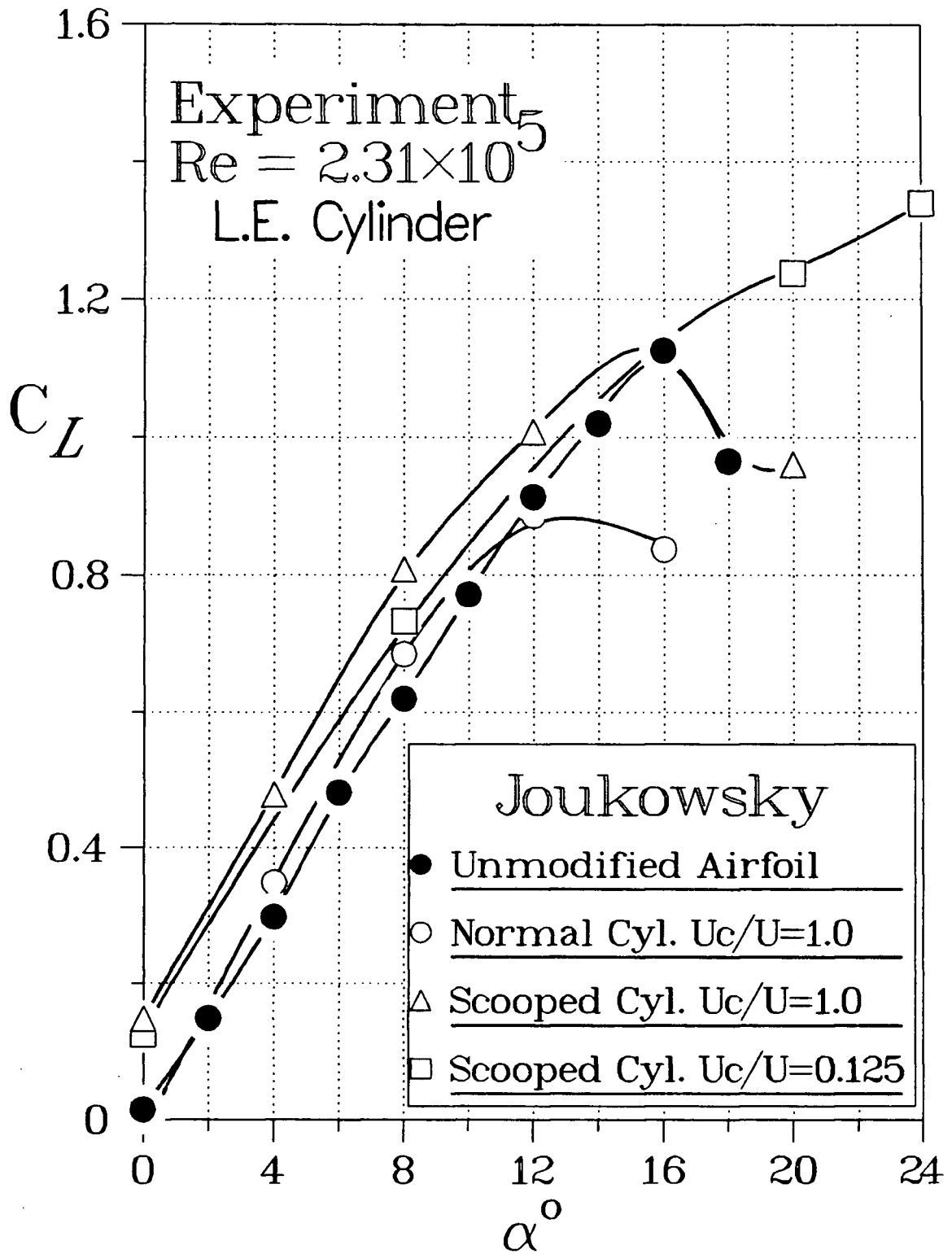


Figure 3-11 Plots showing improvements in the lift coefficient of a Joukowski airfoil with various leading-edge-cylinder configurations and speeds.

3.2 Joukowsky Model II

As mentioned before, the second model provided a flexibility in terms of location of the cylinder. The Reynolds number used here was slightly lower (4.62×10^4) than that employed in the previous set of tests. Its choice was primarily governed by the mechanical consideration of the cylinder vibration at higher rotational speeds, which in turn affects the ratio U_c/U . Besides homogeneity of the cylinder mass distribution and bearing condition, nature of the model affected the level of vibration. In terms of construction, the second model was quite complex as it provided four different positions for the cylinder. Furthermore, now it was possible to rotate two cylinders simultaneously which further raised the possibility of vibration.

The effect of Reynolds number on the lift and stall characteristics of this Joukowsky airfoil model is shown in Figure 3-12. At the lower Reynolds number, the airfoil has a slightly lower maximum lift and stalls at around 10° .

The pressure distribution data for this "base airfoil" (in absence of the modifications imposed by the leading edge, trailing edge, and upper-surface-cylinders) are presented in Figure 3-13. The leading edge was now formed by a snugly fitting plug (the nose fill-in section, Figure 2-8a). As before, this set of results serve as reference to assess the effect of rotating cylinders in different locations. The lower stall angle and consequent decrease in the maximum lift coefficient of this airfoil, as compared to the Joukowsky model I (Figure 3-1), are mainly due to the multi-section design of the model, resulting in surface discontinuities, as well as the lower Reynolds number used in this set of experiments.

3.2.1 Leading-edge-cylinder

Figure 3-14 summarizes the effects of modification of the airfoil with the leading-edge-cylinder and the cylinder rotation. The base airfoil has a maximum lift coefficient of about 0.82 at an angle of attack of 10° . There is a penalty associated

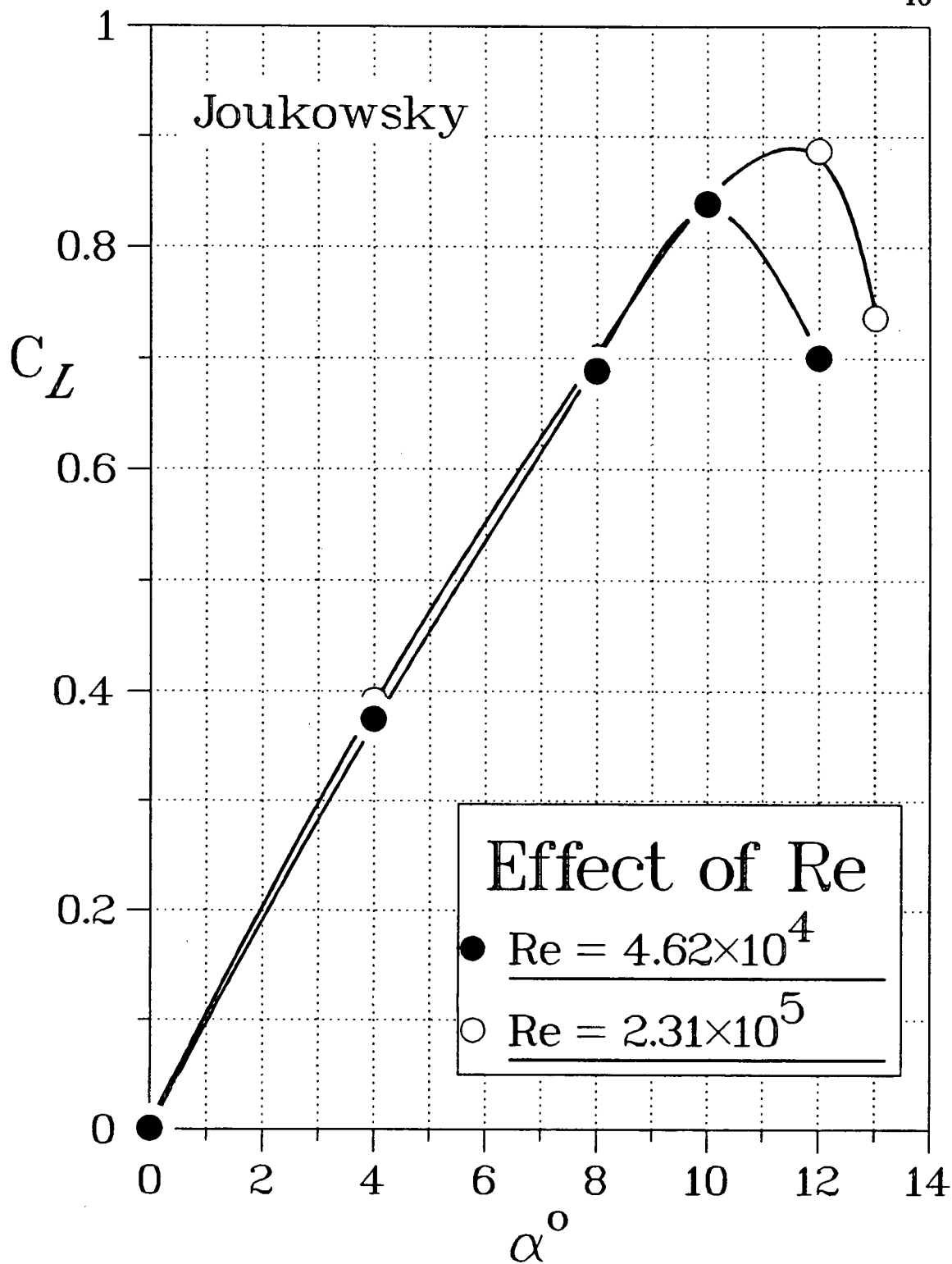


Figure 3-12 Effect of Reynolds number on the lift and stall characteristics of the Joukowsky model II.

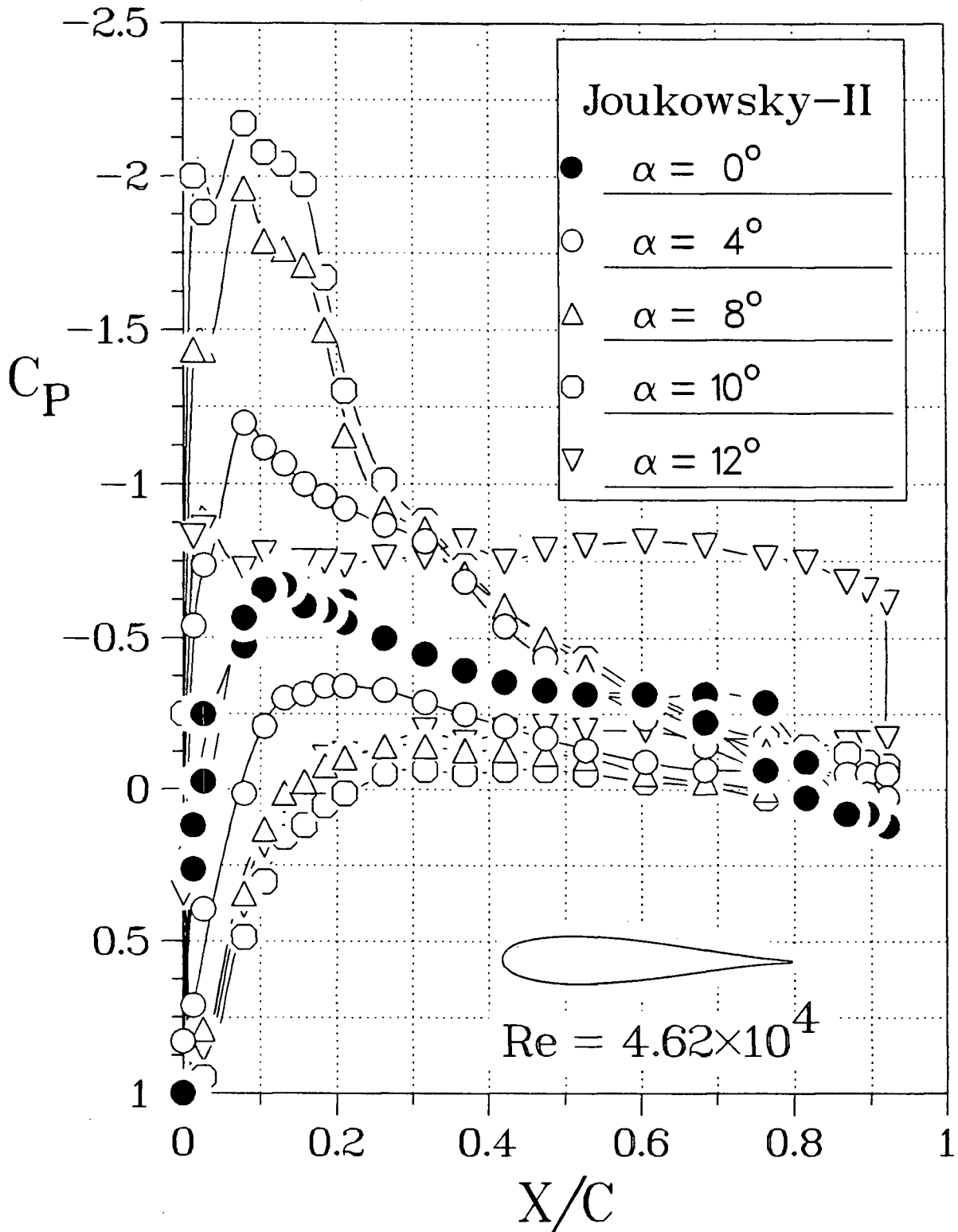


Figure 3-13 Experimentally obtained pressure distributions for the basic Joukowski model II.

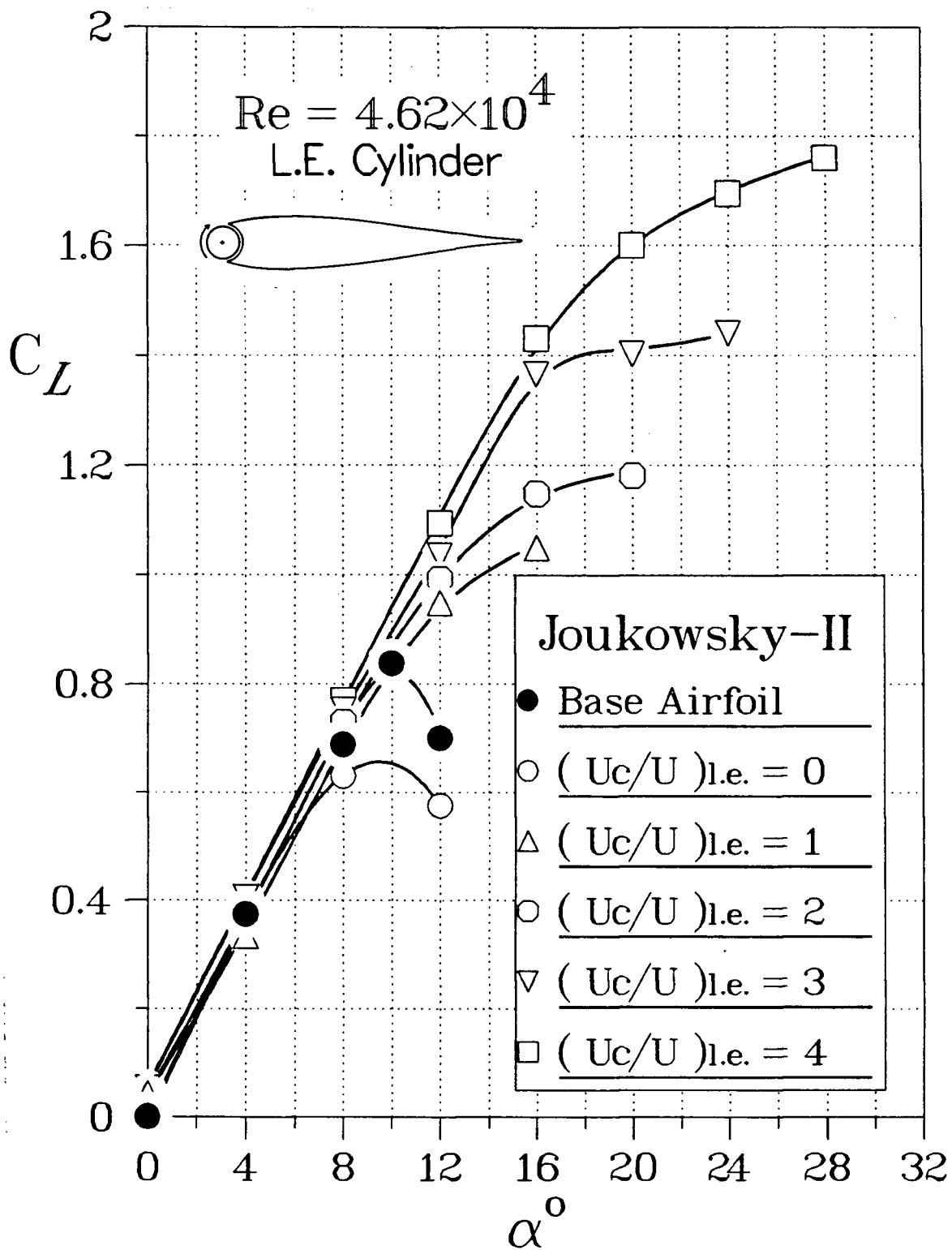


Figure 3-14 Effect of the leading-edge-cylinder rotation on the lift and stall characteristics of the Joukowsky model II.

with the modified nose geometry as discussed earlier, as well as due to the gap, but even at the lowest rate of rotation of the cylinder ($U_c/U = 1$) the lift and stall characteristics are significantly improved. The airfoil exhibits a desirable flattening of the lift curve at stall. The maximum lift coefficient measured with $U_c/U = 4$ was around 1.8 at $\alpha = 28^\circ$ which is almost 2.2 times the lift coefficient of the base airfoil.

Selected pressure plots at relatively larger angles are presented in Figure 3-15 to assist in more careful examination of the local flow field. As the angle of attack of the airfoil is increased, the flow starts to separate from the upper surface closer to the leading edge. At $\alpha = 16^\circ$, for example, the cylinder rotating at $U_c/U = 1$ only keeps the flow attached at the leading edge. As the rate of rotation is increased, however, the size of the separation region is reduced and at the higher rates of rotation, the flow is again completely attached. Similar trends are present at $\alpha = 20^\circ$ (Figure 3-15b). Note, the point of separation on the upper surface clearly moving back with increasing rotation. The flow separates at around $X/C = 15\%$ with $U_c/U = 2$, around $X/C = 50\%$ when U_c/U is increased to 3, and at the trailing edge with the highest U_c/U used. The flow visualization study discussed later substantiated this general behavior rather dramatically.

Effect of the modified nose geometry and the gap associated with the leading-edge-cylinder was discussed earlier (section 3.1.1). Essentially, it leads to an earlier stall. The pressure distribution plots before stall show little indication of any appreciable flow leakage from the bottom to the top surface through the cylinder-airfoil interface. This is specially true at higher angles of attack where the stagnation point, located off the lower surface, moves downstream of the gap thereby isolating it from the high pressure region. Associated with the gap, nevertheless, is a sharp corner which protrudes into the upper surface boundary-layer causing it to grow and separate much faster. A large gap would appear to the flow as a step from the cylinder to the airfoil surface and result in a large separation bubble thus causing

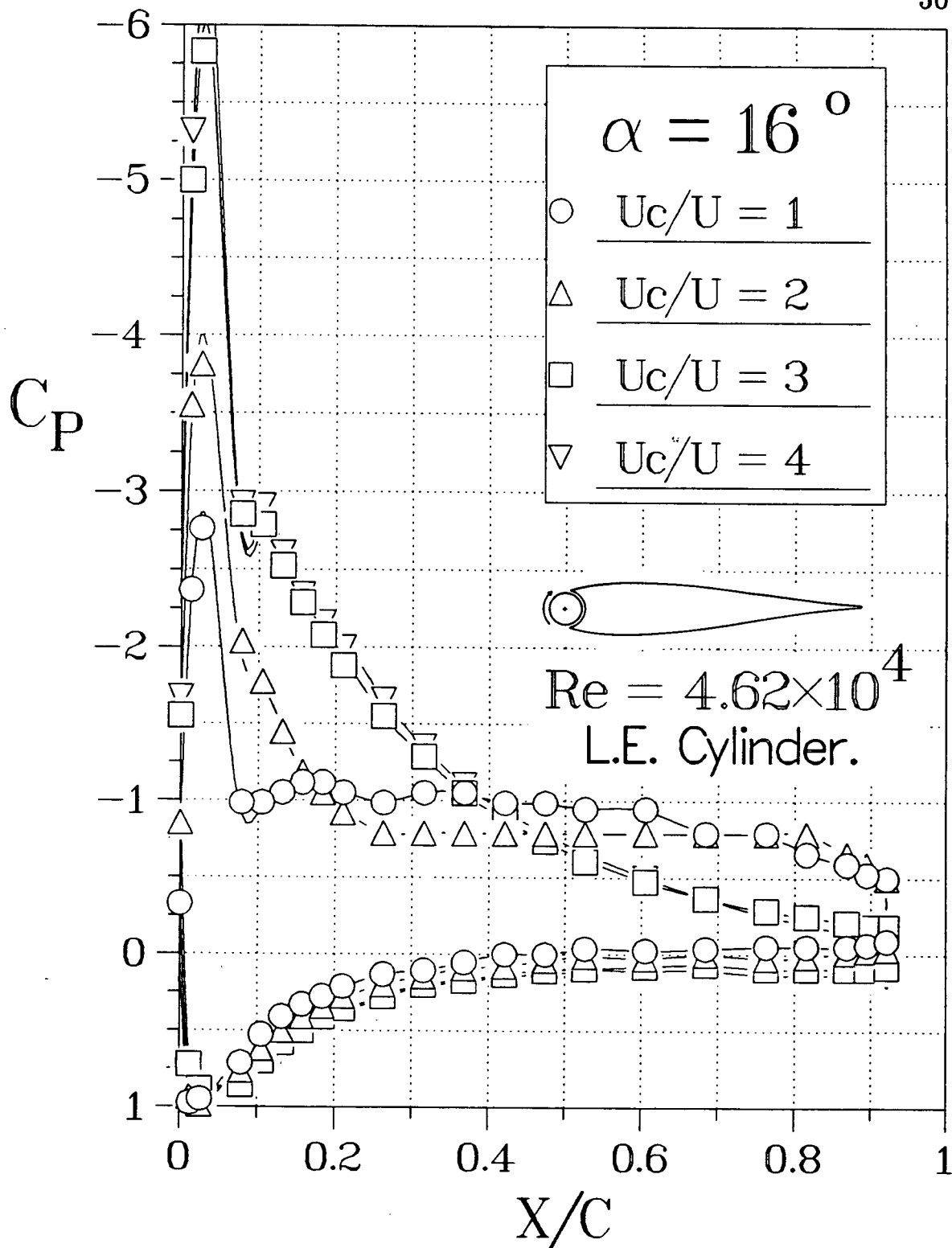


Figure 3-15 Effect of increasing the rate of cylinder rotation on pressure distribution around the Joukowski model II at relatively larger angles of attack:
 (a) $\alpha = 16^\circ$;

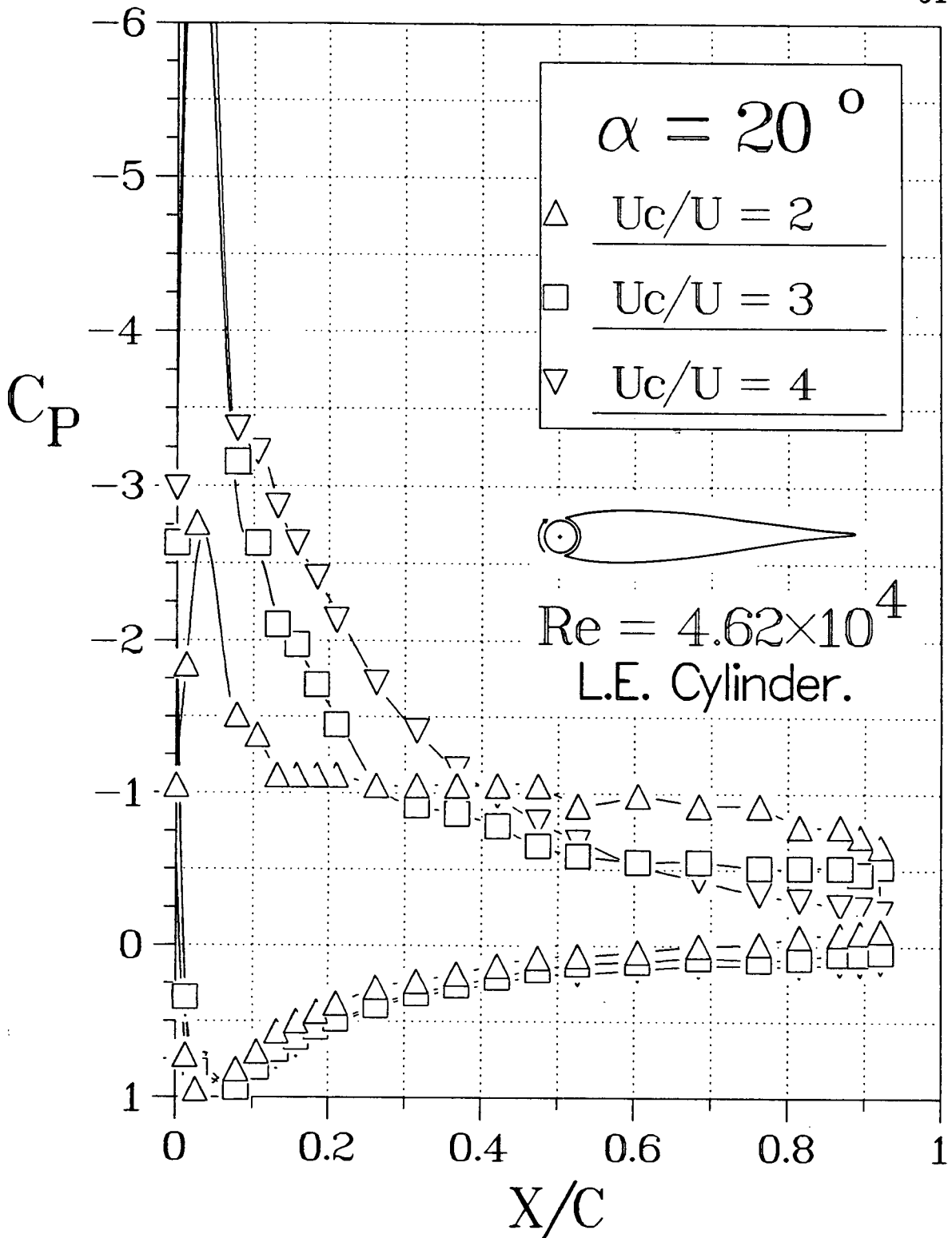


Figure 3-15 Effect of increasing the rate of cylinder rotation on pressure distribution around the Joukowski model II at relatively larger angles of attack: (b) $\alpha = 20^\circ$.

a decrease in lift of the airfoil as well as the effectiveness of cylinder rotation.

The Joukowski model II was tested with a larger gap (5 mm) between the leading-edge cylinder and the airfoil. The results, summarized in Figure 3-16, show little difference due to the size of the gap without cylinder rotation (compare results for $U_c/U = 0$ in Figure 3-14). However, effectiveness of the cylinder rotation is drastically reduced.

3.2.2 Trailing-edge-cylinder

The Joukowski model II was next tested with the trailing-edge cylinder. Unlike the leading edge configuration, the cylinder at the trailing edge changes the basic geometry substantially (Figure 2-9). The trailing edge of the airfoil beyond $\approx 72\%$ chord is removed to accommodate the cylinder. The resulting chord is approximately 28% shorter than that of the base airfoil, and the model has a blunt trailing edge in the form of a cylinder.

Only a representative set of pressure plots for this model are presented in Figure 3-17. In absence of the cylinder rotation, the pressure distribution over the airfoil is not changed substantially compared to that for the model with the trailing edge (Figure 3-17b). With rotation of the trailing edge cylinder, the suction over the upper surface as well as compression on the lower surface increase. The effect is particularly noticeable with the higher rate of cylinder rotation and at the lower angles of attack (Figure 3-17 a, b). The relative improvement decreases at the larger angles but is still quite evident at and beyond the stall (Figure 3-17 c, d).

This, in turn, results in a large improvement in the lift coefficient as shown in Figure 3-18. For example, rotating the trailing-edge-cylinder at $U_c/U = 4$ results in an increase in lift by about 330% at $\alpha = 4^\circ$ (about 130% at $\alpha = 8^\circ$). In contrast to the leading-edge-cylinder, however, this configuration does not extend the stall beyond that of the base configuration. As can be expected, the trailing-edge-cylinder essentially behaves as a flap shifting the plots to the left.

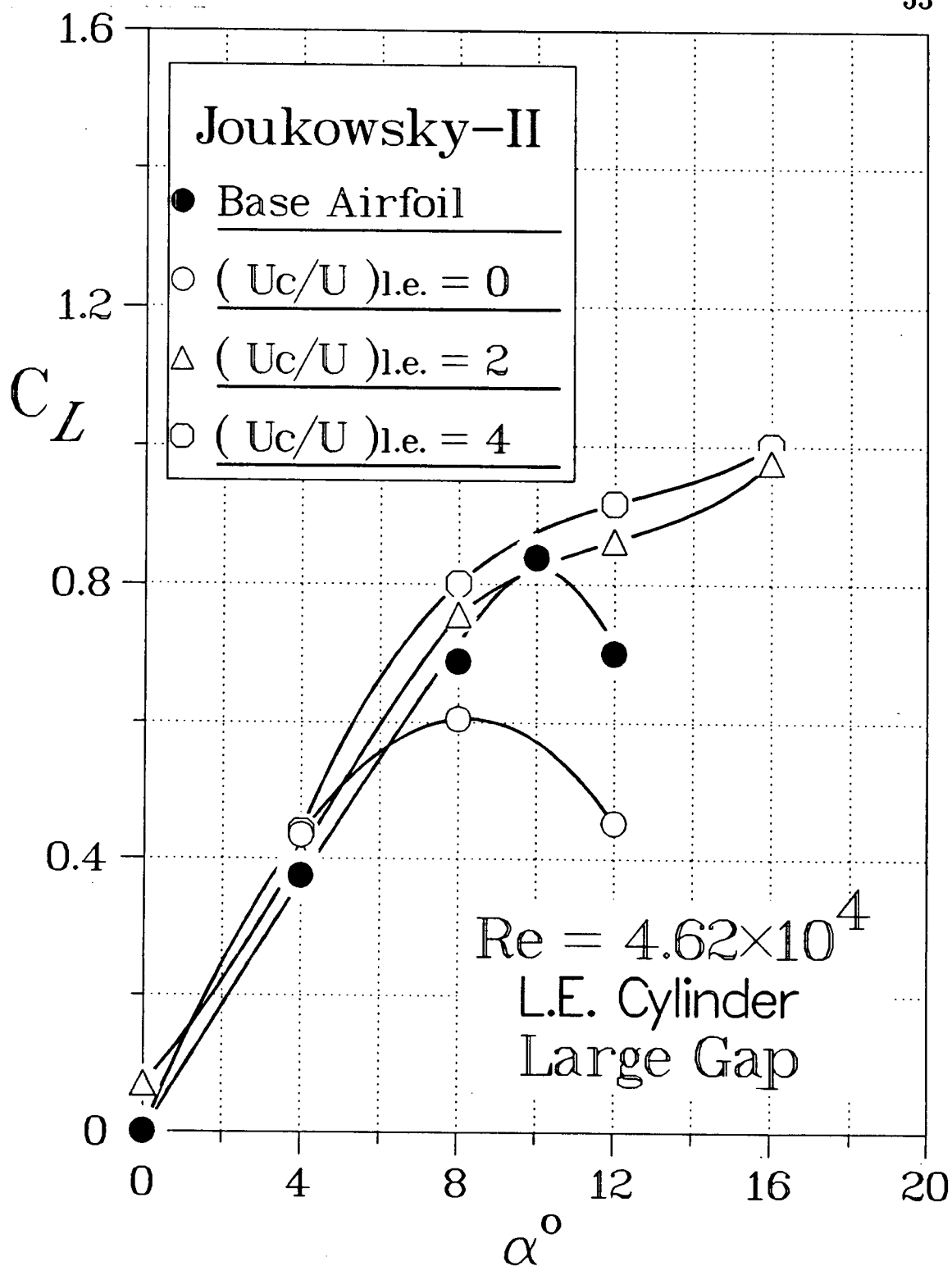


Figure 3-16 Plots showing adverse effect of increasing the gap size between the airfoil and the leading-edge-cylinder. A comparison with Figure 3-14 suggests that both $C_{L,max}$ and stall angle are significantly reduced.

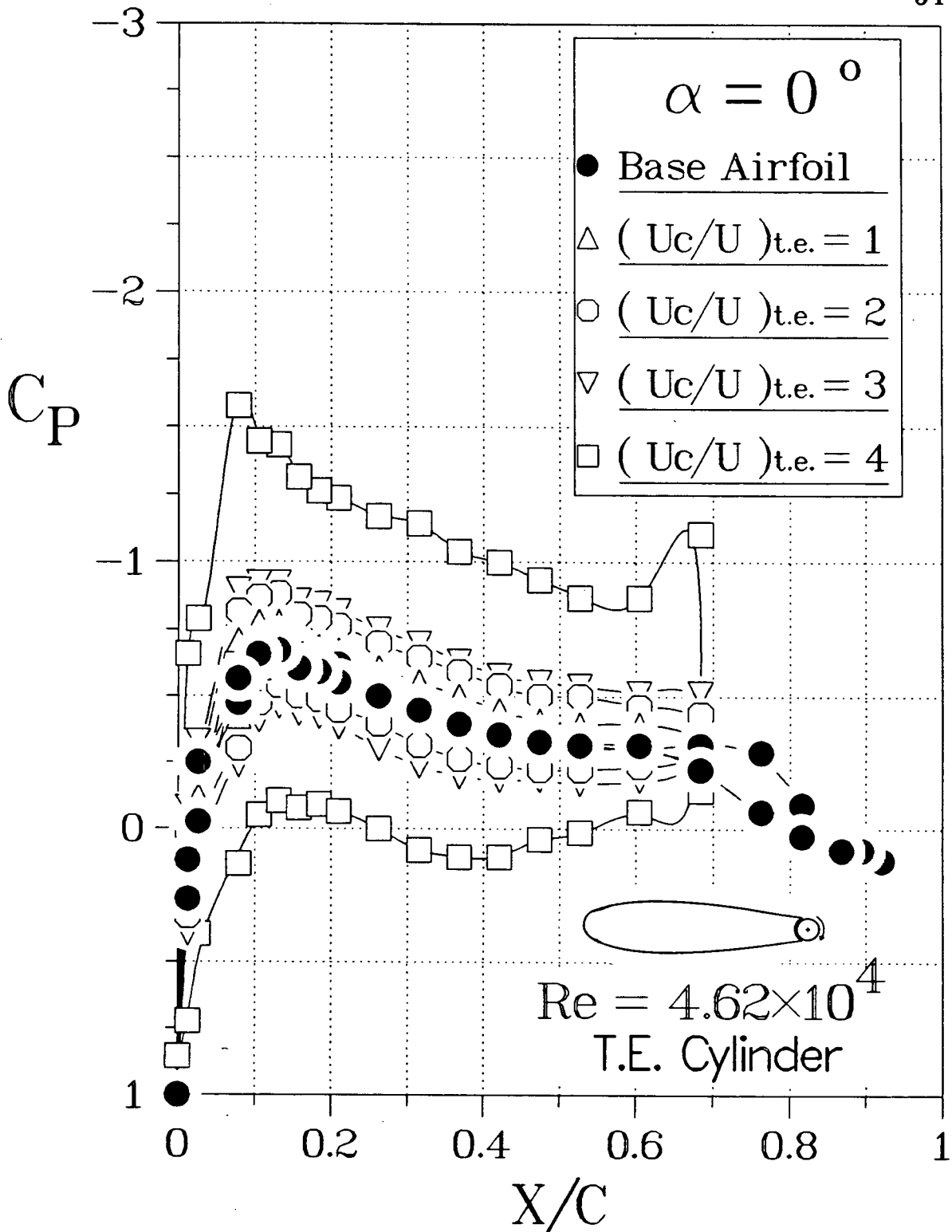


Figure 3-17 Pressure distributions over the Joukowski model II modified with a trailing-edge cylinder: (a) $\alpha = 0^\circ$;

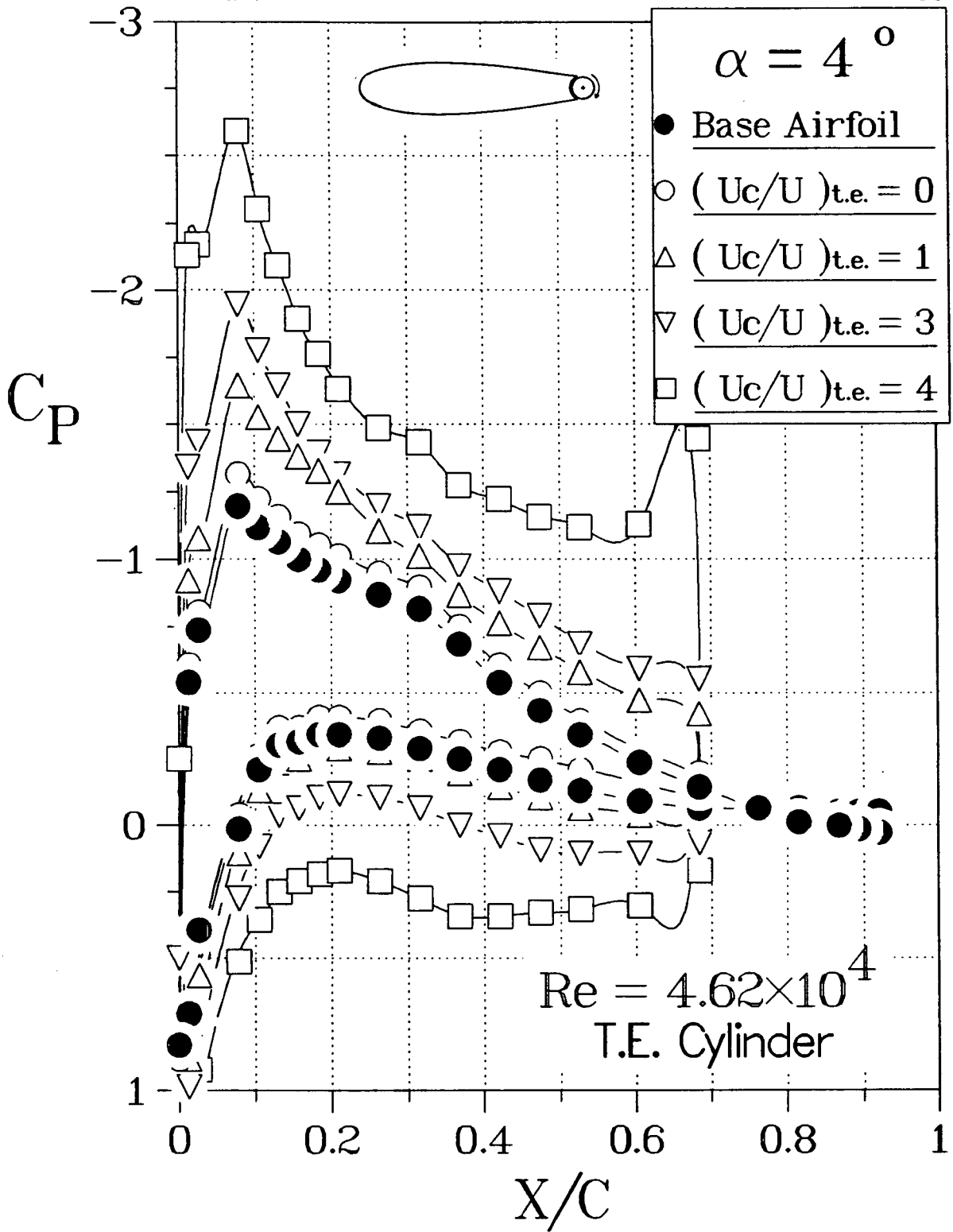


Figure 3-17 Pressure distributions over the Joukowski model II modified with a trailing-edge-cylinder: (b) $\alpha = 4^\circ$;

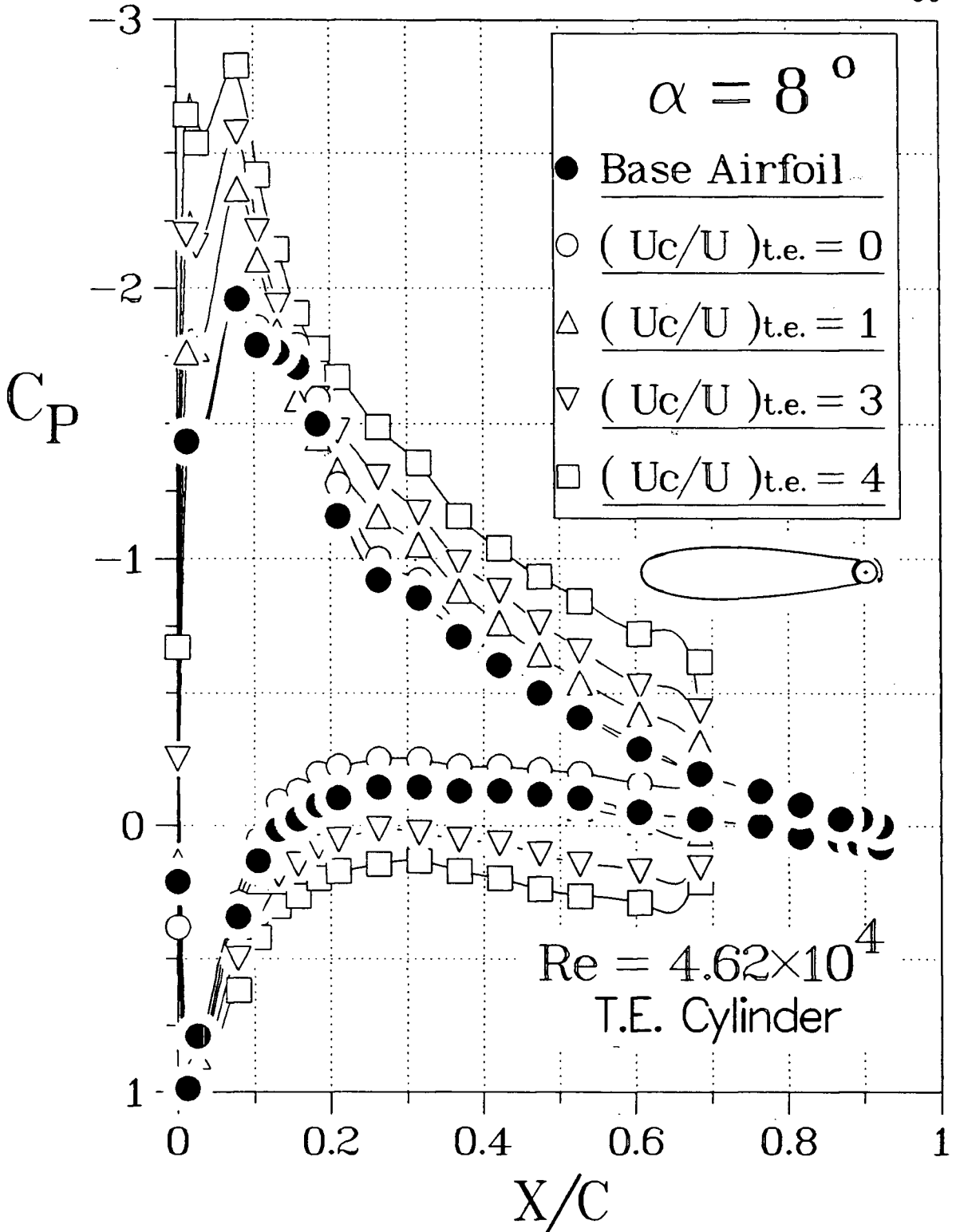


Figure 3-17 Pressure distributions over the Joukowski model II modified with a trailing-edge-cylinder: (c) $\alpha = 8^\circ$;

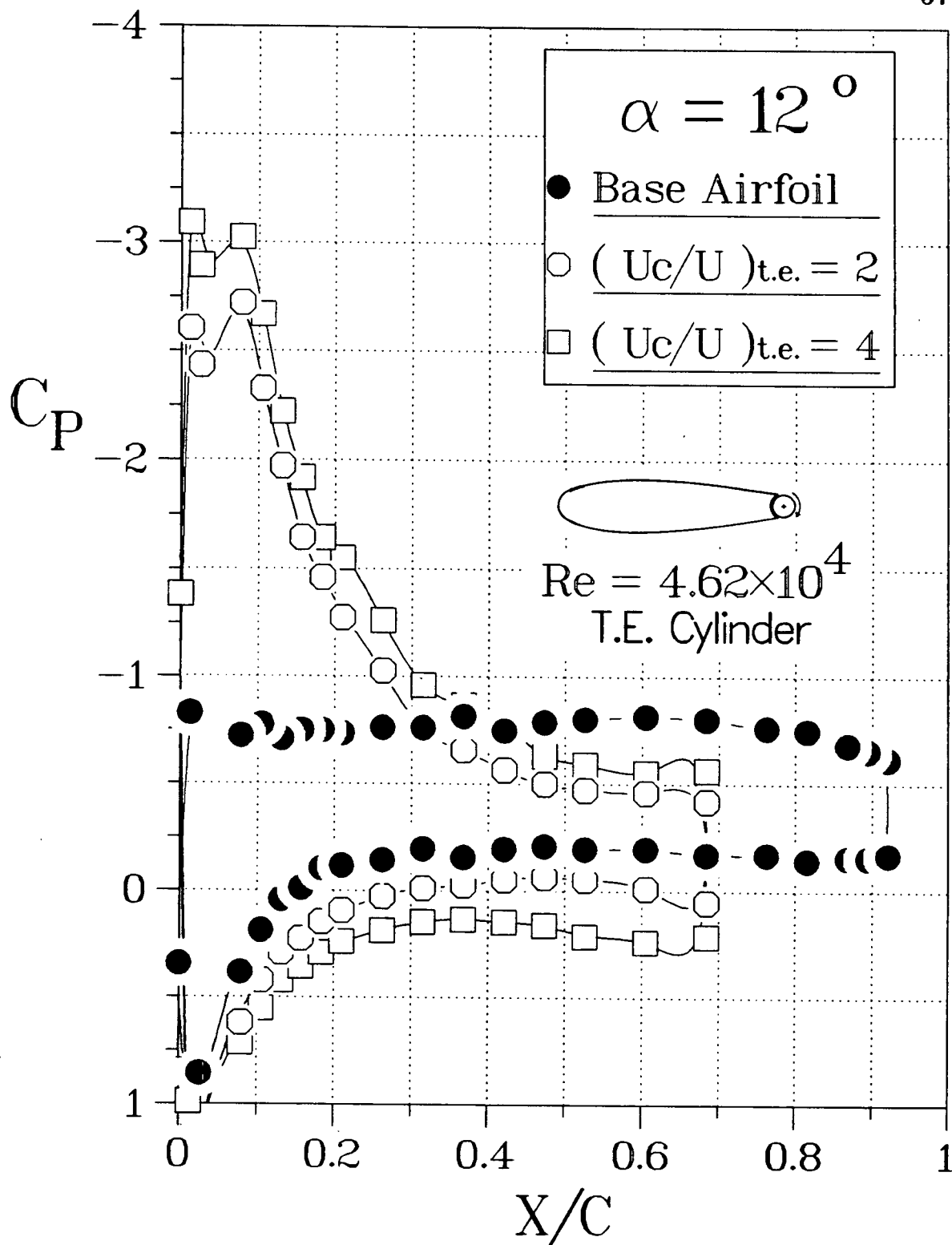


Figure 3-17 Pressure distributions over the Joukowski model II modified with a trailing-edge cylinder: (d) $\alpha = 12^\circ$.

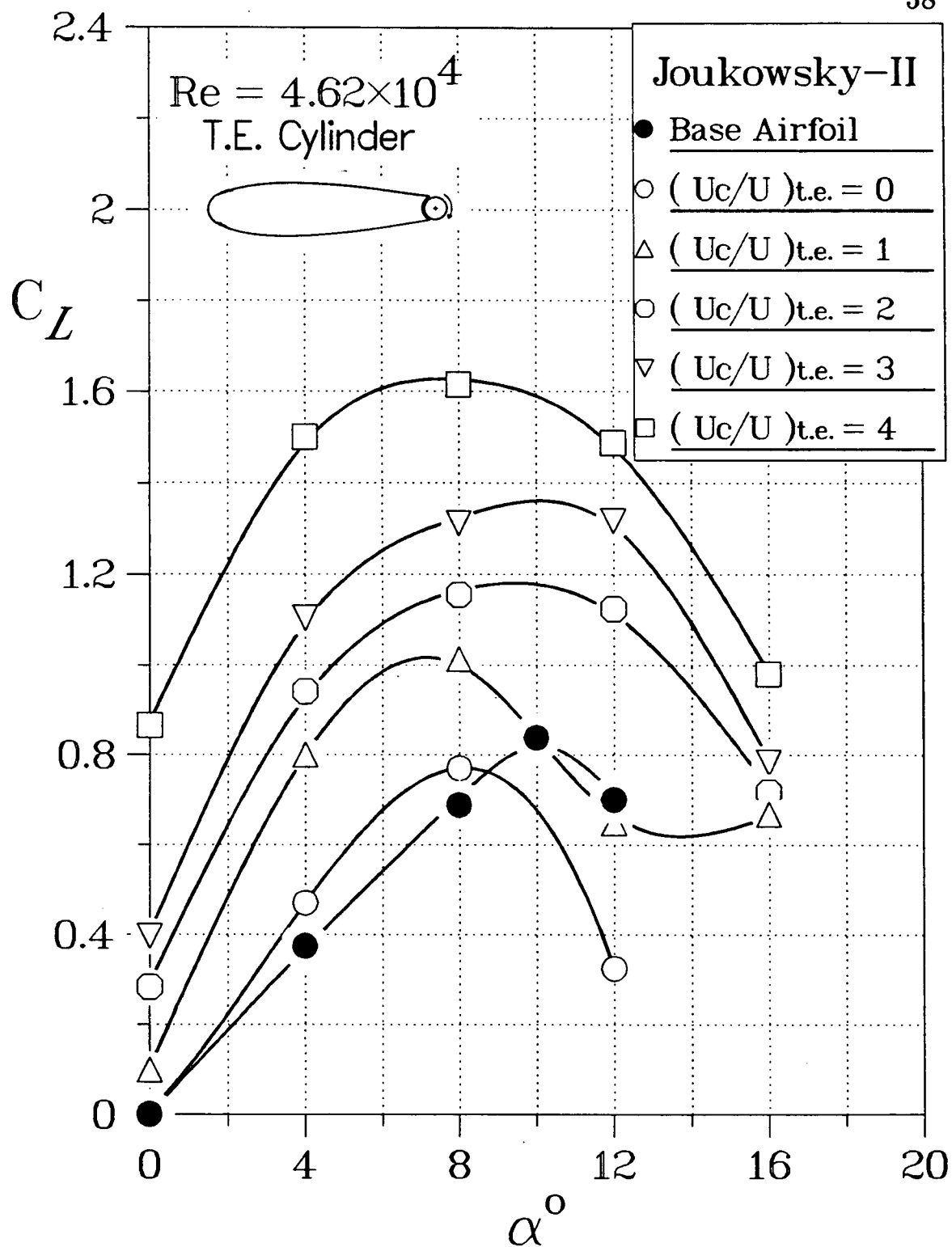


Figure 3-18 Effect of the trailing-edge-cylinder rotation on the lift and stall characteristics of the Joukowsky model II.

3.2.3 Leading and trailing-edge cylinders

The use of a leading-edge-cylinder was shown to extend the lift curve, thus substantially increasing the maximum lift coefficient and delaying stall (Figure 3-14). On the other hand, the trailing-edge-cylinder rotation resulted in an improvement in the lift coefficient, at a given angle of attack, before stall (Figure 3-19). In order to combine these effects, therefore, the base configuration was modified to include both the leading and trailing-edge cylinders (Figure 2-9, configuration *iii*). This phase of the test program examines the effect of individual and combined cylinder rotations.

The effect of rotating the leading-edge-cylinder, with the trailing-edge-cylinder stationary, is summarized in Figure 3.19(a). Although the leading edge cylinder rotation still appears to be quite effective in improving the lift and stall characteristics of the base configuration, there is a substantial penalty associated with the removal of the sharp trailing edge and replacing it with a cylinder (compare results with those of Figure 3-7). Moreover, due to the modified nose geometry and the presence of a gap associated with the use of a leading-edge-cylinder, performance of the trailing-edge-cylinder itself is also affected. Although Figure 3-19(b) shows a significant increase in $C_{L,max}$ as a result of the trailing-edge-cylinder rotation, the improvement is considerably less than that obtained previously (Figure 3-18).

It is, however, the combined effects of both the cylinders that is of interest here. The results, shown in Figure 3-19(c), suggest some benefit due to rotation of the two cylinders together. Although the increase in $C_{L,max}$ is rather modest (from 1.75 to 2.22, around 27%) and it fails to delay the stall further, compared to the leading-edge-cylinder case (sharp trailing edge, Figure 3-14), the lift coefficient at a given α is indeed increased significantly, as expected, due to the leftward shift of the plots (compare Figures 3-19a and 3-19c). As pointed out before, this is due

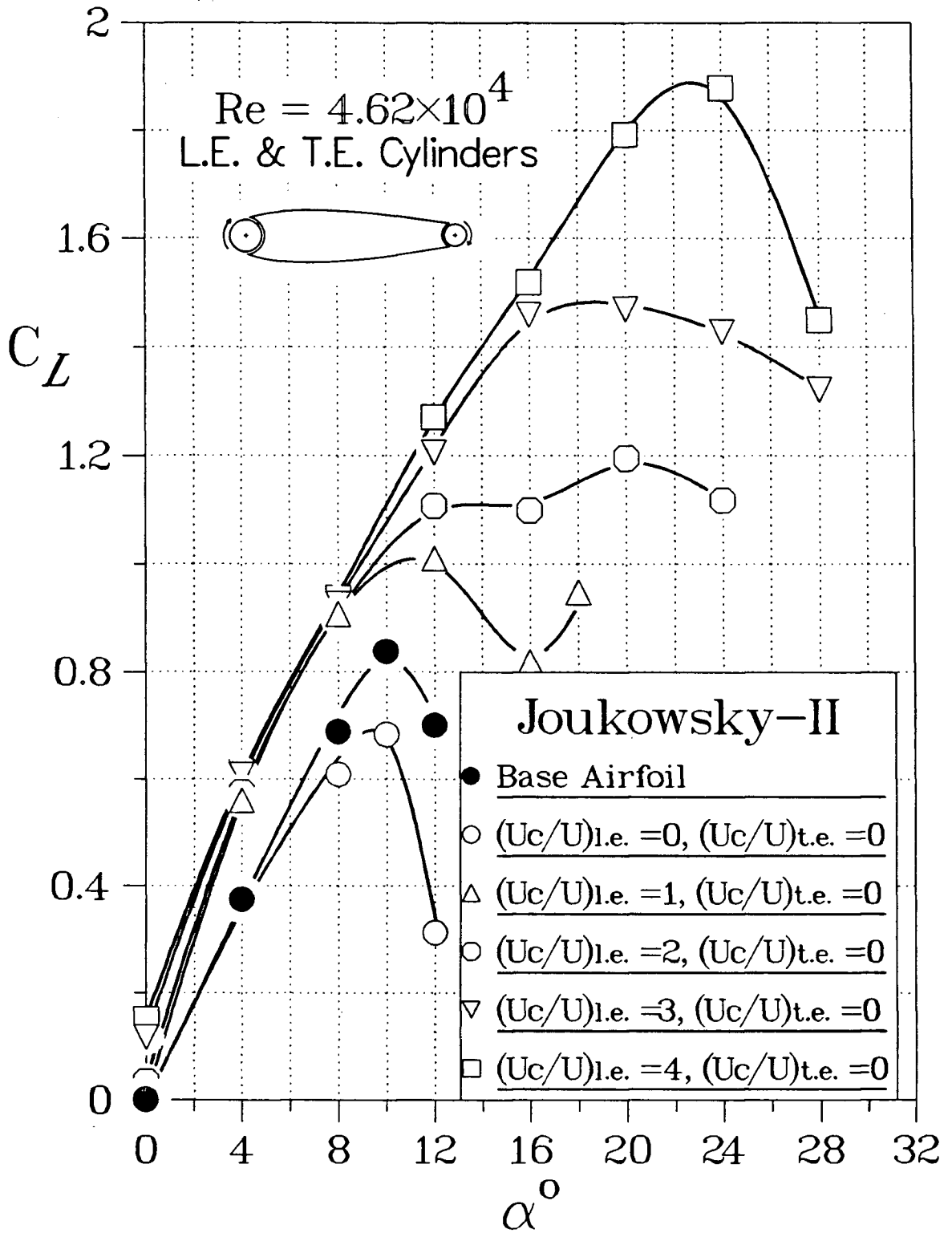


Figure 3-19 Variation of C_L vs. α for a modified Joukowski airfoil with leading and trailing edge cylinders: (a) leading-edge-cylinder rotation;

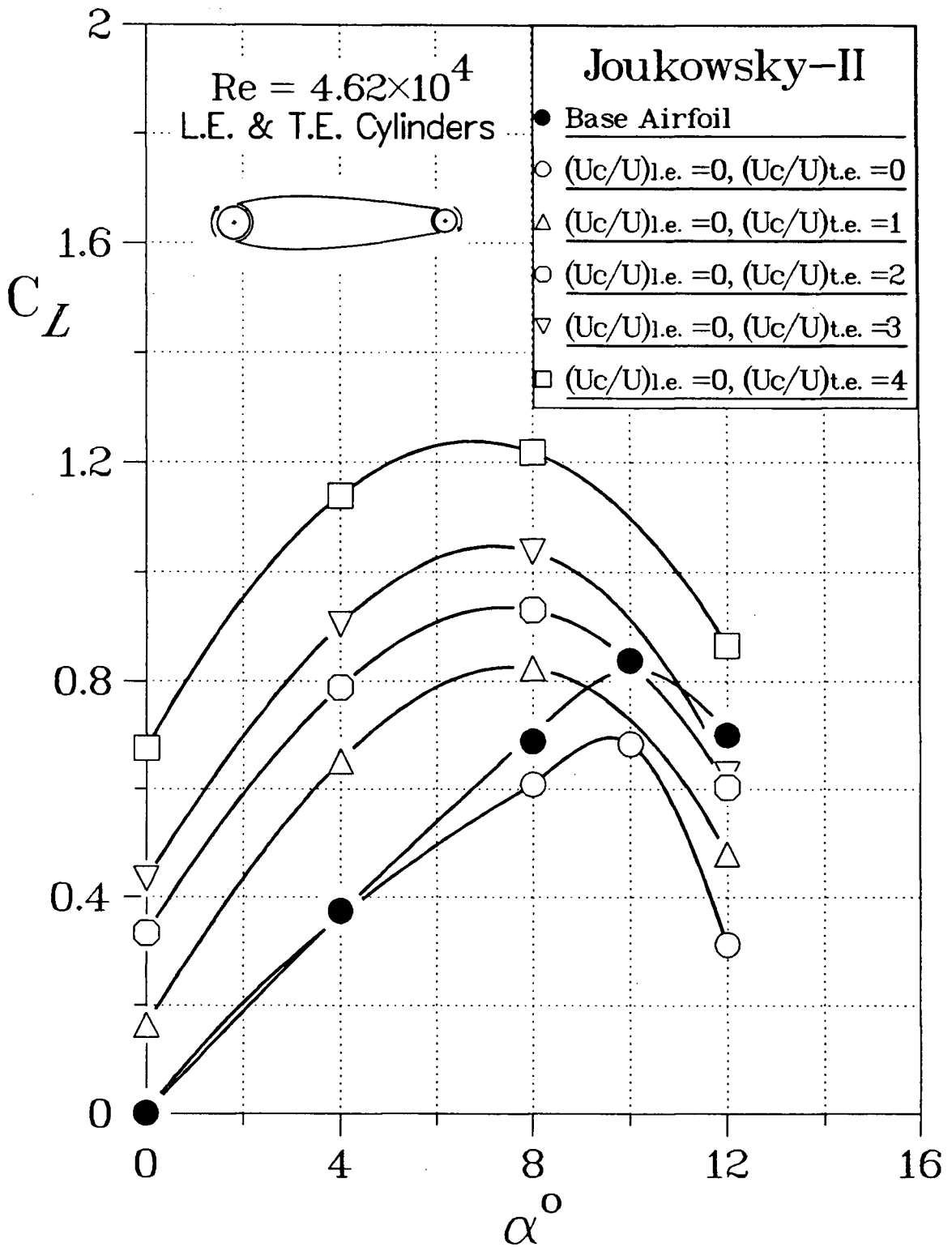


Figure 3-19 Variation of C_L vs. α for a modified Joukowsky airfoil with leading and trailing edge cylinders: (b) trailing-edge-cylinder rotation;

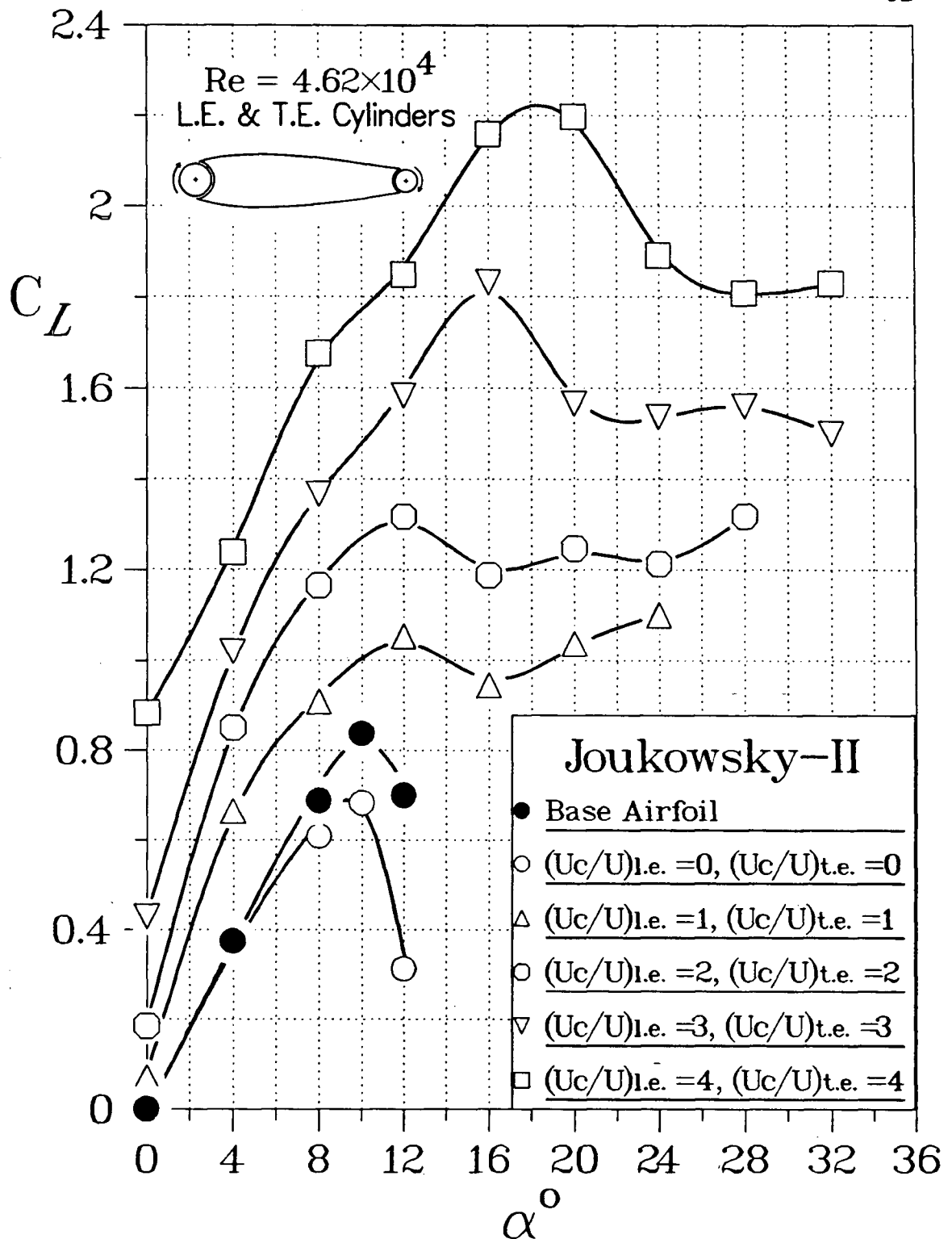


Figure 3-19 Variation of C_L vs. α for a modified Joukowsky airfoil with leading and trailing edge cylinders: (c) combined rotation of both the cylinders.

to the added circulation contributed by the trailing edge cylinder. For example $C_L = 0.7$ at $\alpha = 8^\circ$ and $(U_c/U)_{l.e.} = 3$ (Figure 3-14) while for the same angle of attack and $(U_c/U)_{l.e.} = (U_c/U)_{t.e.} = 3$ the corresponding $C_L \approx 1.38$, an increase of around 97%. Similarly, $C_L \approx 1.43$ for $\alpha = 16^\circ$ and $(U_c/U)_{l.e.} = 4$. On the other hand, with both the cylinders rotating at $U_c/U = 4$ the lift coefficient is around 2.15, a further gain of about 50%. Note, this value of the maximum lift coefficient represents an increase of 160% with respect to the reference configuration ($C_{L,max}$ of about 2.22 vs. 0.85, Figure 3-19).

A typical set of corresponding pressure plots are given in Figure 3-20. At $\alpha = 8^\circ$ a substantial increase in lift with cylinder rotation is quite evident. The suction peak over the leading edge associated with the rotation of the leading-edge-cylinder, as well as an increase in suction over the upper surface and in compression on the lower surface due to rotation of the trailing-edge-cylinder, can be observed quite clearly.

The pressure data are also compared with those for the leading-edge-cylinder configuration, with and without the sharp trailing edge, in Figure 3-21. At $\alpha = 12^\circ$ (Figure 3-21a) the adverse effect of replacing the sharp trailing edge with a cylinder is still quite small and rotation of the trailing-edge-cylinder results in an increased lift. The penalty becomes more evident, however, as the angle of attack is further increased. The rotation of the cylinder becomes less effective at $\alpha = 20^\circ$ (Figure 3-21b), and at $\alpha = 24^\circ$, the flow separates earlier than that in the leading-edge-cylinder case (Figure 3-21c). Thus the higher lift coefficients obtained, at low to moderately high angles of attack, are at the cost of lower maximum lift coefficient and stall angle.

To better appreciate the overall effect of this twin cylinder configuration, the results are summarized in Figure 3-22. The base data correspond to the Joukowski model II with the leading edge fill-in section (no gap) and the sharp trailing edge. Modifying the configuration with the leading and trailing edge cylinders adversely

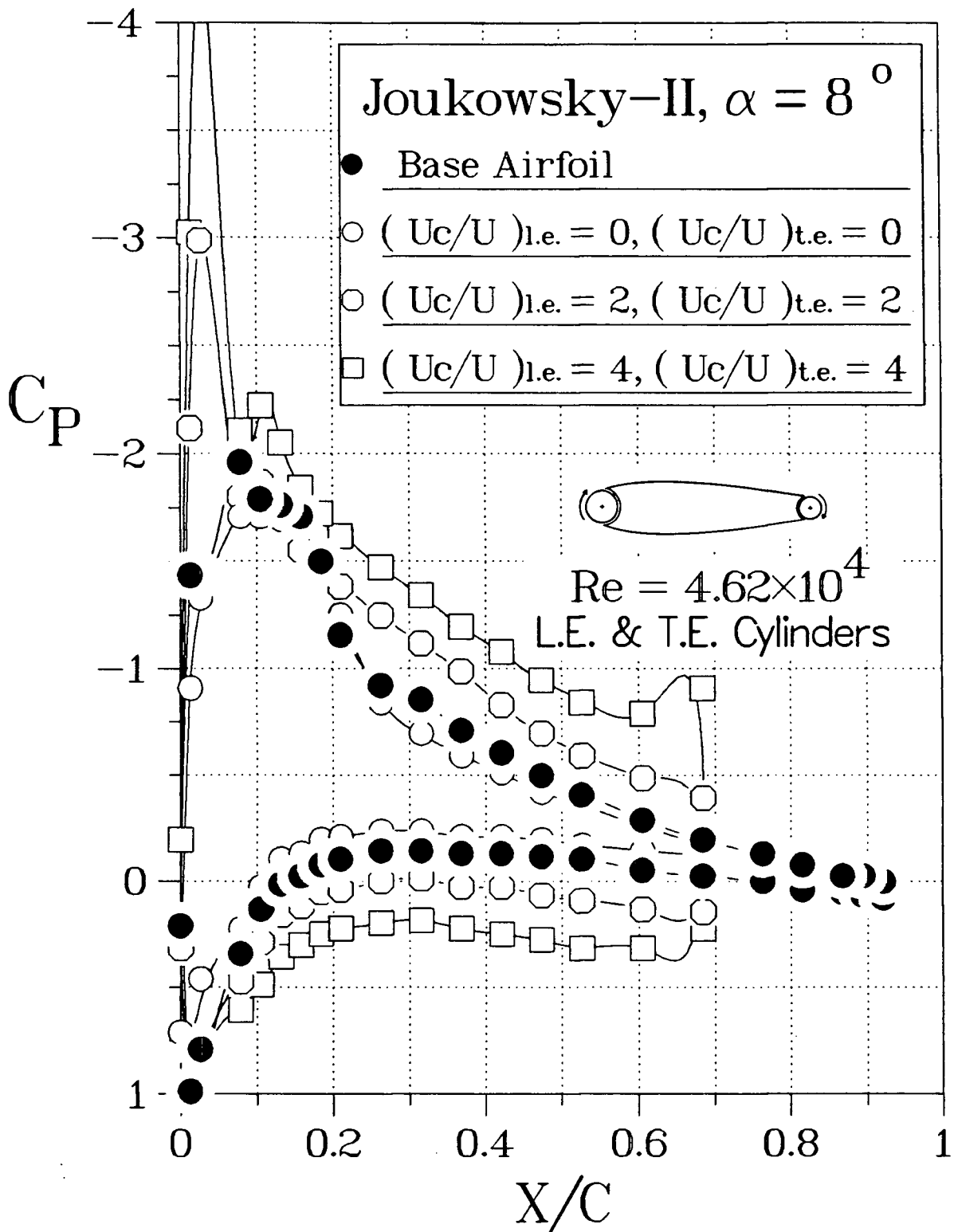


Figure 3-20 Selected pressure plots for the Joukowski model II, modified with leading and trailing edge cylinders, at $\alpha = 8^\circ$.

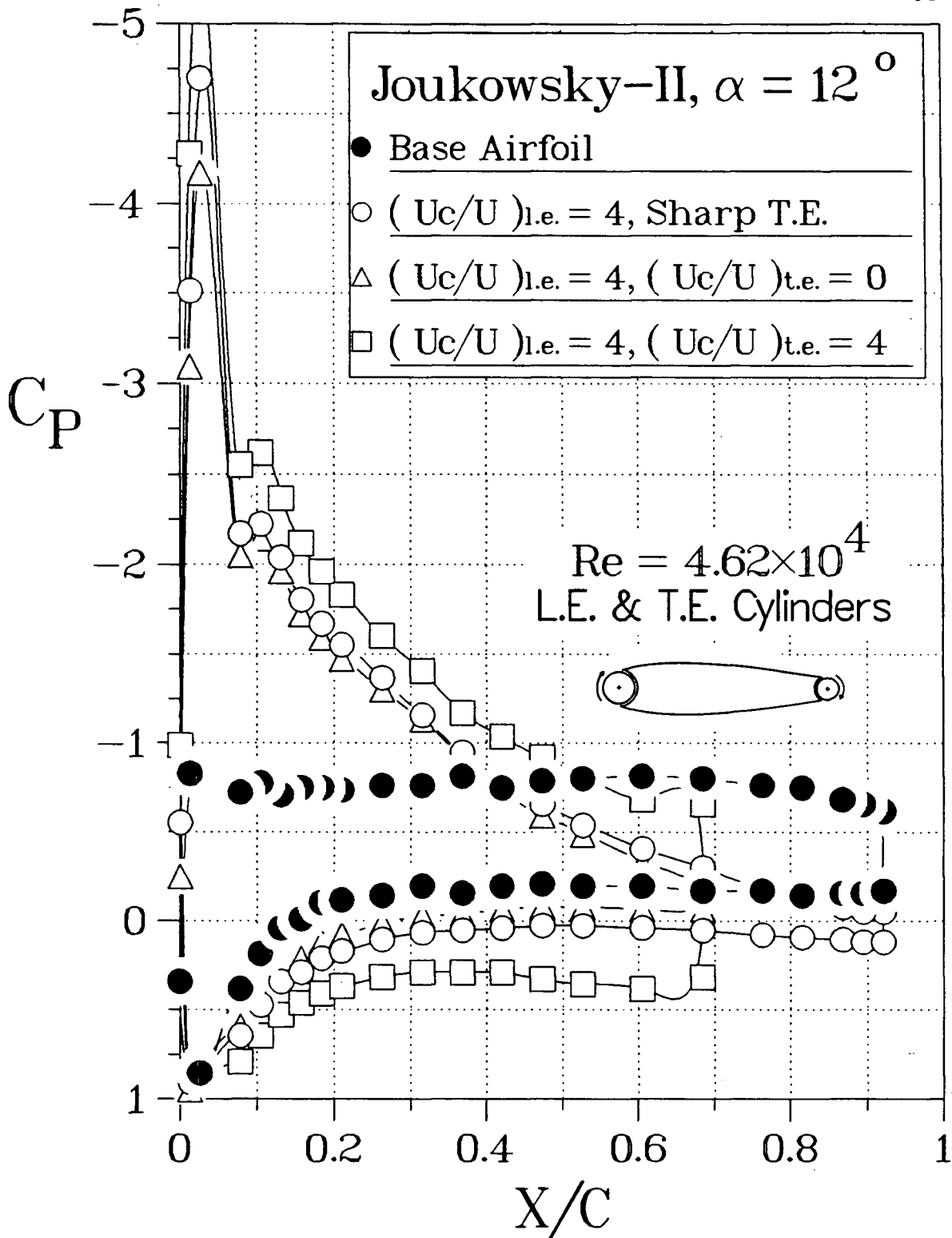


Figure 3-21 Comparison of pressure plots for the Joukowski model II with several combinations of leading and trailing edge cylinder configurations:

(a) $\alpha = 12^\circ$;

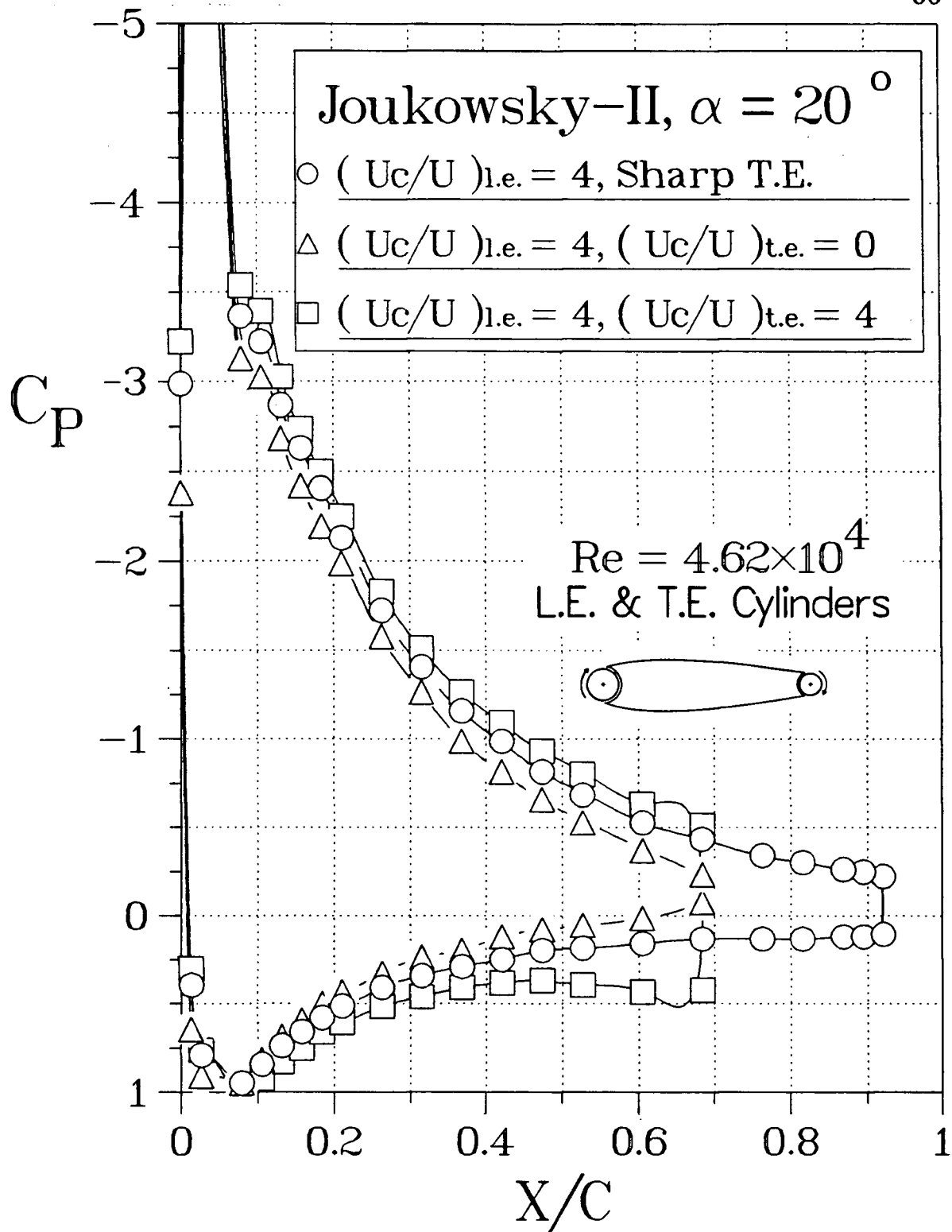


Figure 3-21 Comparison of pressure plots for the Joukowski model II with several combinations of leading and trailing edge cylinder configurations: (b) $\alpha = 20^\circ$;

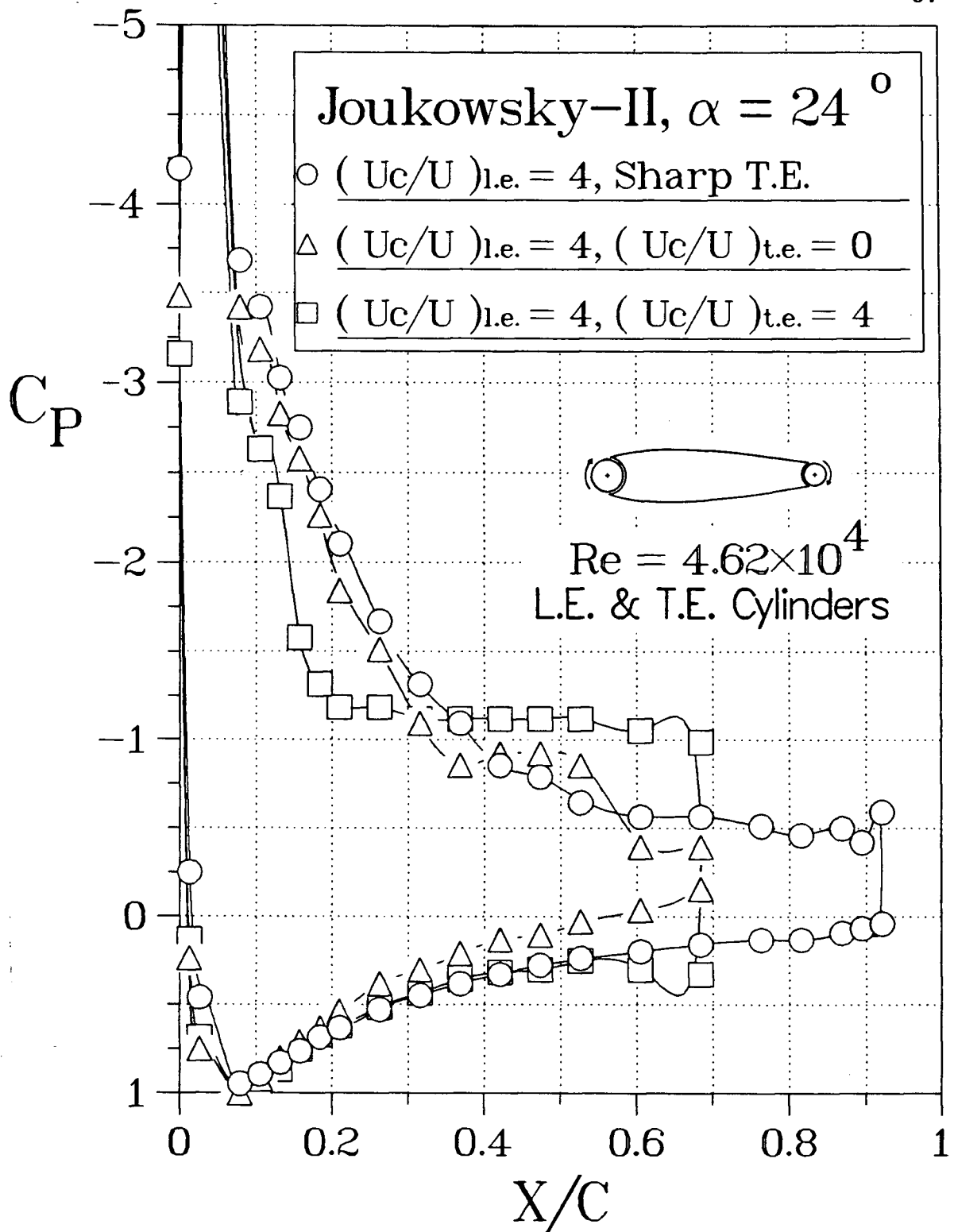


Figure 3-21 Comparison of pressure plots for the Joukowski model II with several combinations of leading and trailing edge cylinder configurations: (c) $\alpha = 24^\circ$.

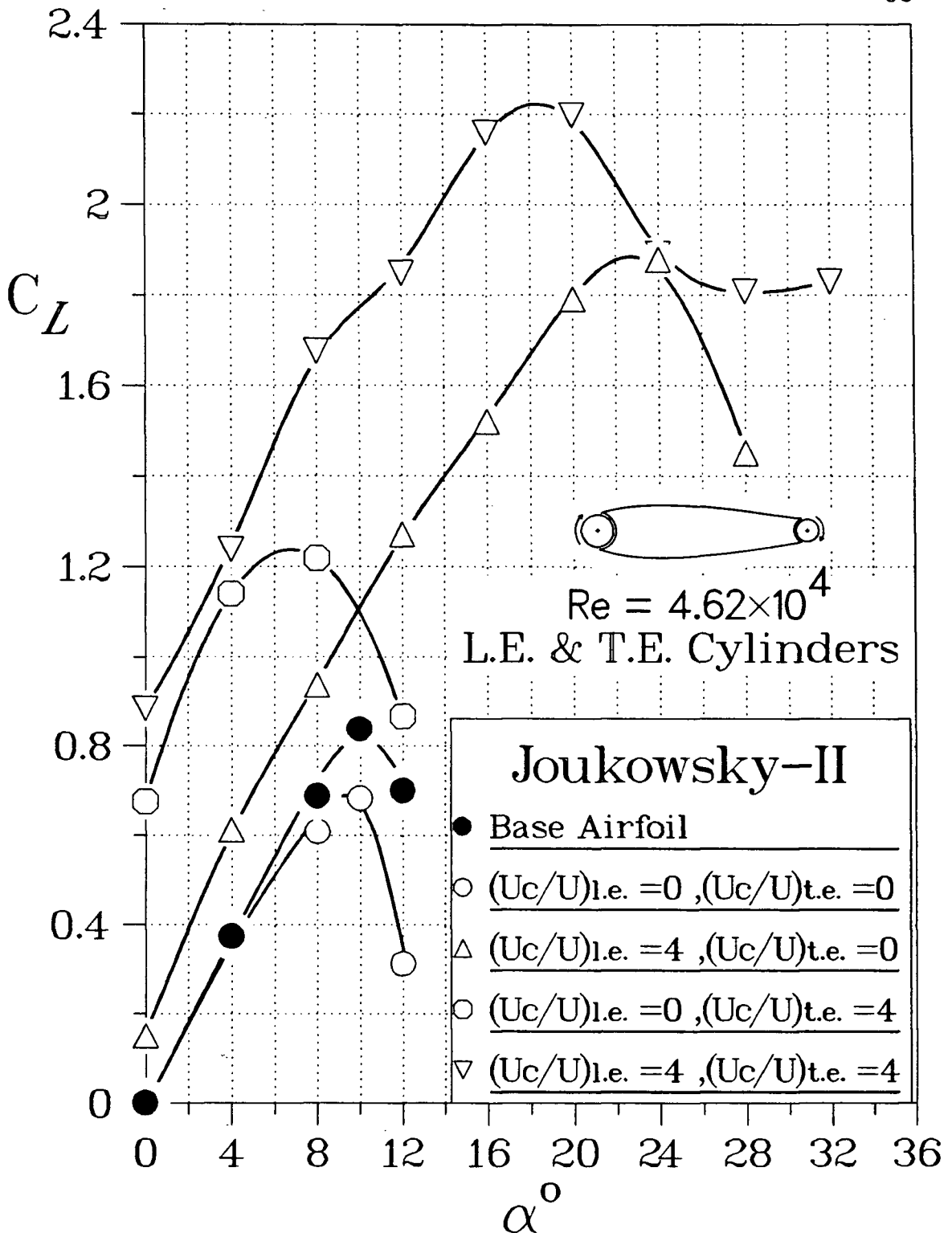


Figure 3-22 Effect of rotation of the leading and trailing edge cylinders on the lift and stall characteristics of the Joukowsky airfoil model II.

affects the $C_{L,max}$ which now reduces from around 0.85 to ≈ 0.7 . The trailing-edge-cylinder rotating at $(U_c/U)_{t.e.} = 4$ not only makes up for the loss but actually increases C_L , particularly at $\alpha \leq 8^\circ$. However, the stall angle is reduced from around 10° to 7° due to leftward movement of the curve caused by an increase in circulation. The leading-edge-cylinder rotating at $(U_c/U)_{l.e.} = 4$, with the trailing-edge-cylinder stationary, significantly increases the $C_{L,max}$ to around 1.85 with the stall delayed to 23° , an increase of about 120% with respect to the base configuration ($\approx 180\%$ with reference to the modified configuration). With both the cylinders rotating at $U_c/U = 4$ there is a further increase in $C_{L,max}$ and a substantial increase in lift for $\alpha \leq 18^\circ$, the new stall angle.

Note, the C_L values for this leading and trailing edge twin cylinder case are much higher than those given by the leading-edge-cylinder at lower angles of attack (Figure 3-14). The α_{stall} for this configuration, which is now around 18° , is still lower than the corresponding stall angle of the leading-edge-cylinder alone with the sharp trailing edge.

3.2.4 Leading and upper-surface cylinders

The forward and rear upper-surface-cylinders, located at 38% and 58% chord respectively, were considered independently and with either of them operating in conjunction with the leading-edge-cylinder. In absence of rotation, their protrusion into the upper-surface flow had an adverse effect on the aerodynamic characteristics of the model. The flow separated at the location of the cylinder resulting in a lower lift and increased drag. Even at the highest rate of rotation the improvement in the lift performance was below that achieved by the trailing-edge-cylinder (Figure 3-23, $\alpha < 10^\circ$). However, at each of the locations, the upper-surface-cylinder was successful in attaining a higher $C_{L,max}$ and delaying the stall. In this respect, the forward upper-surface-cylinder was particularly effective.

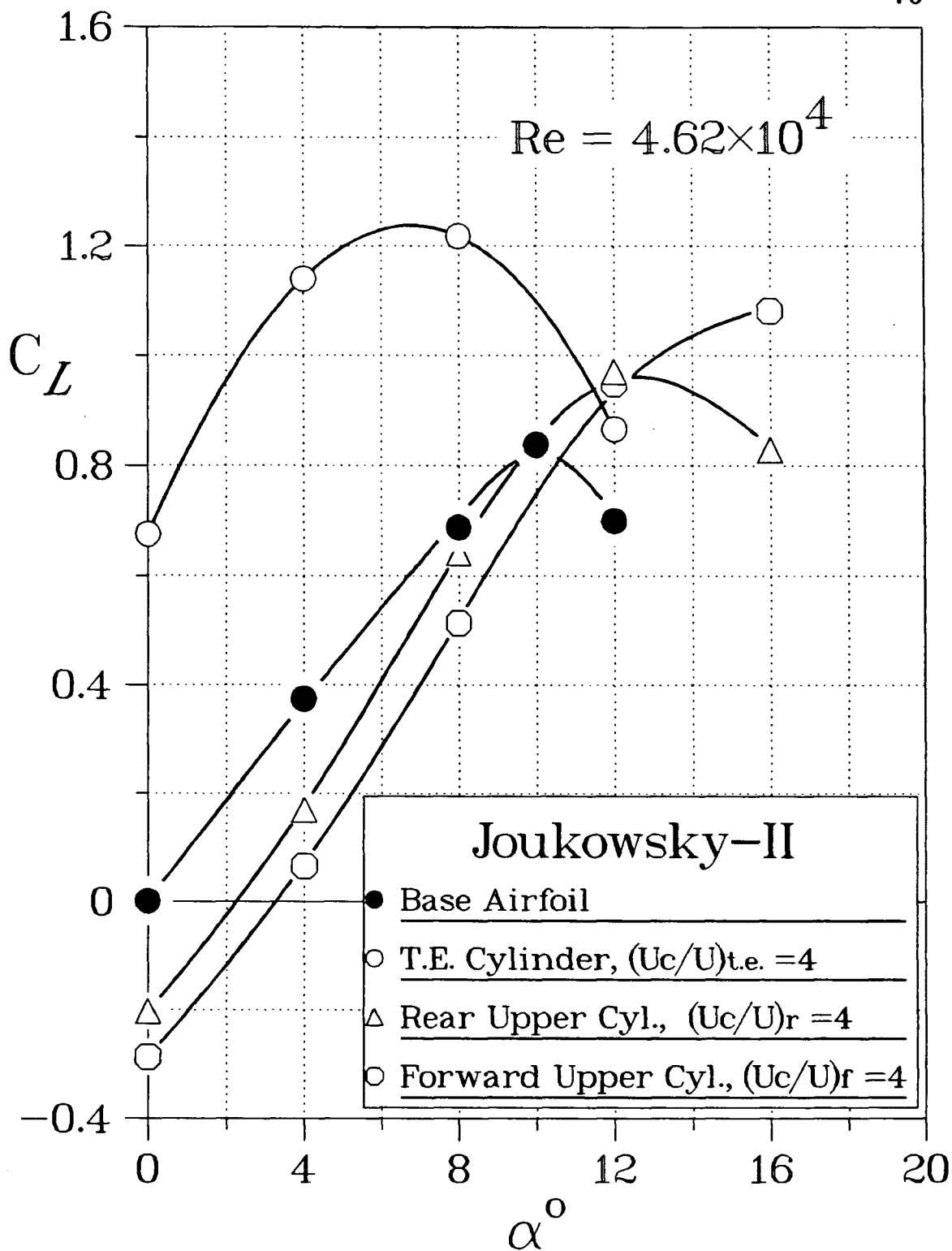


Figure 3-23 A comparison between the performance of the trailing-edge and upper-surface cylinders (Joukowsky model II).

Typical pressure distribution data for the rear upper-surface-cylinder in a combined configuration with the leading-edge-cylinder are shown in Figure 3-24 at medium to moderately high angles of attack. Contribution of the individual cylinder rotation is particularly noticeable at the lower rates of rotation. For example, $U_c/U = 1$ at $\alpha = 16^\circ$ (Figure 3-24a) results in attached flow at the leading edge primarily due to rotation of the leading-edge-cylinder. The flow separates, however, further downstream (near $X/C \approx 0.1$) due to a large adverse pressure gradient. The rear upper-surface-cylinder rotation causes the flow to reattach, but it separates again at the trailing edge. Increasing the cylinder rotation rate to $U_c/U = 2$ prevents the initial separation of the flow behind the leading edge and the flow remains attached over a substantial portion of the top surface. Finally, with the highest rate of rotation, there is a further recovery of the pressure with a significantly higher base value.

At $\alpha = 24^\circ$ (Figure 3-24b), the flow is separated over most of the airfoil with cylinders rotating at $U_c/U = 2$. The size of the separated region decreases significantly with a further increase in the speed, particularly at $U_c/U = 4$. As the angle of attack is increased to $\alpha = 28^\circ$ (Figure 3-24c), even the highest rate of rotation leaves a large separated region.

Similar general trends were observed for the forward upper-surface-cylinder at $\alpha = 28^\circ$ as shown in Figure 3-25. The two cylinders in this configuration are closer together. Although their combined contributions show a larger pressure recovery near the trailing edge compared to the rear cylinder case (Figure 3-24c), the size of the separated region is also increased.

Figure 3-26 attempts to summarize salient effects of the leading-edge and upper-surface cylinder rotations at a relatively high angle of attack of $\alpha = 32^\circ$. The rotation of the leading-edge-cylinder alone gives attached flow at the leading edge only, leaving the flow separated over most of the airfoil. Adding rotation of the rear upper-surface-cylinder does not change the situation substantially. Only

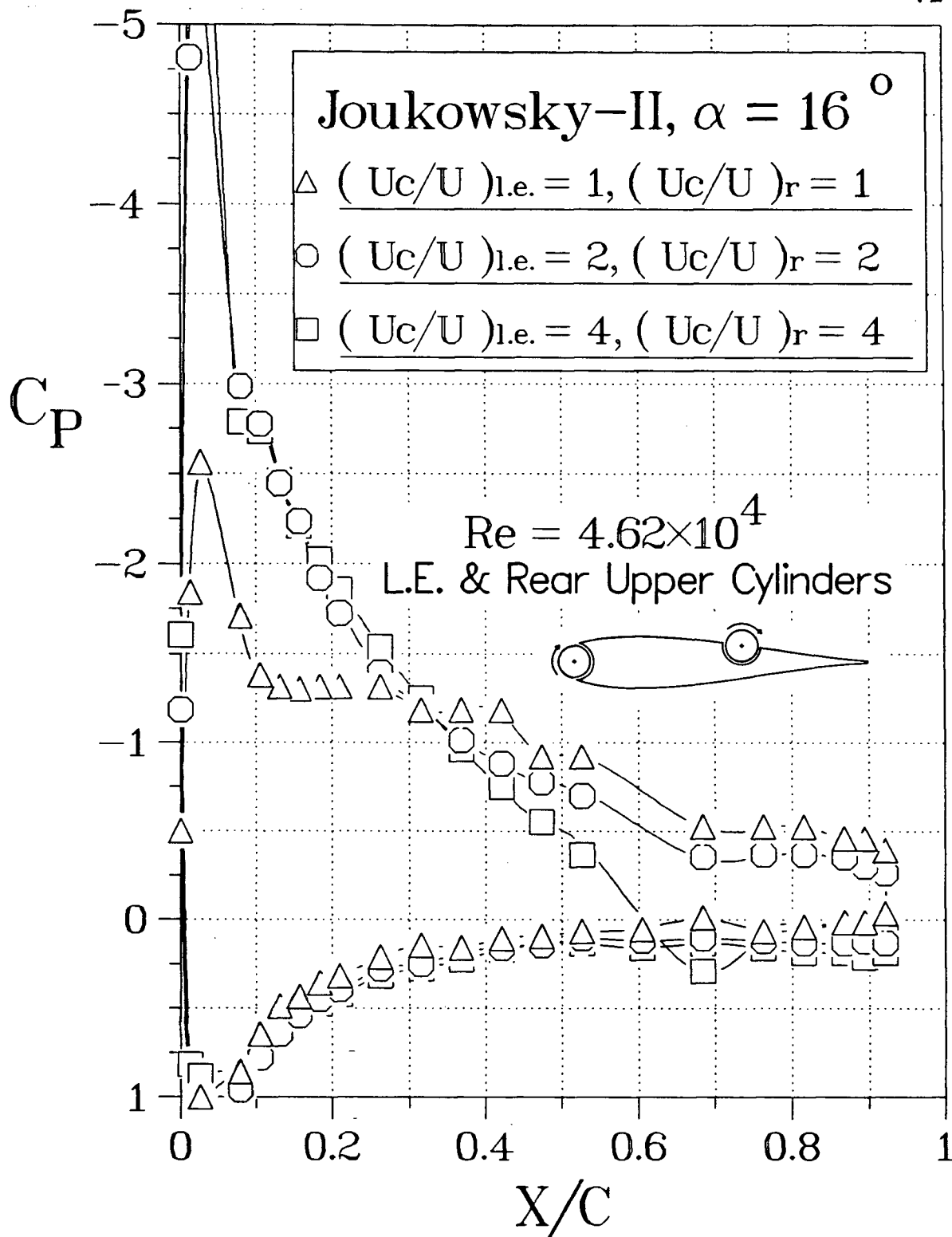


Figure 3-24 Typical pressure distribution plots for the Joukowsky model II with both leading-edge and rear upper-surface cylinders in operation: (a) $\alpha = 16^\circ$;

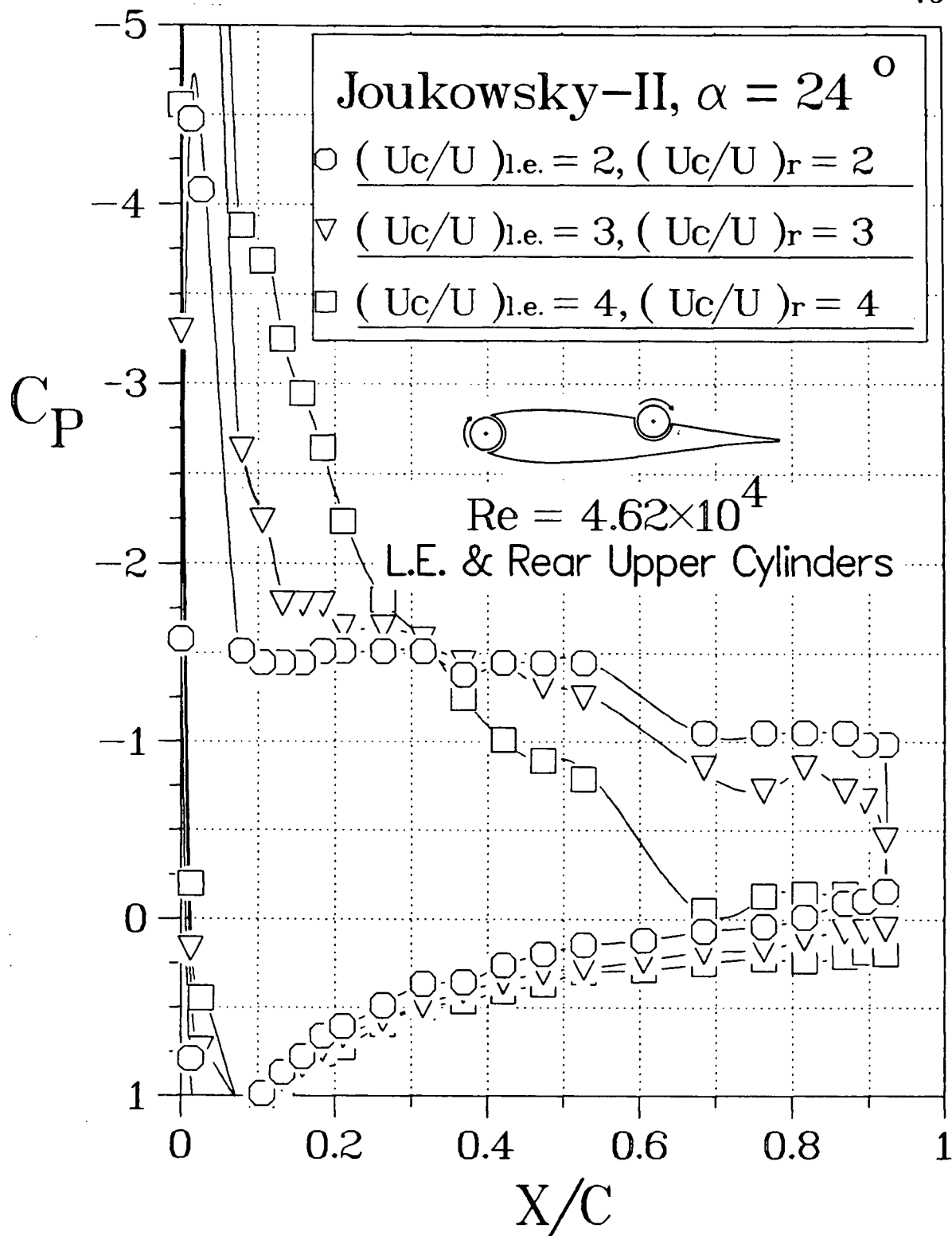


Figure 3-24 Typical pressure distribution plots for the Joukowski model II with both leading-edge and rear upper-surface cylinders in operation: (b) $\alpha = 24^\circ$;

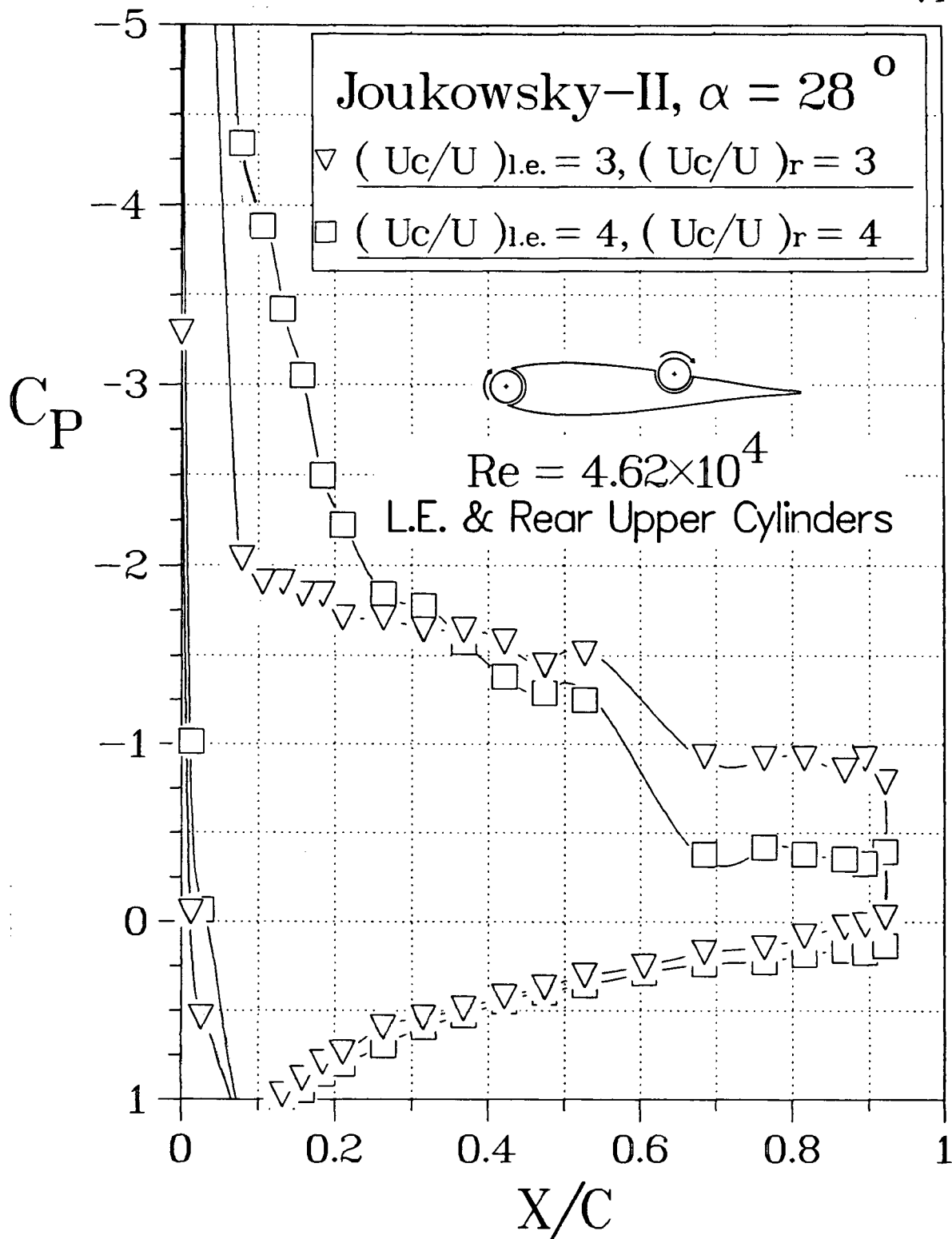


Figure 3-24 Typical pressure distribution plots for the Joukowski model II with both leading-edge and rear upper-surface cylinders in operation: (c) $\alpha = 28^\circ$.

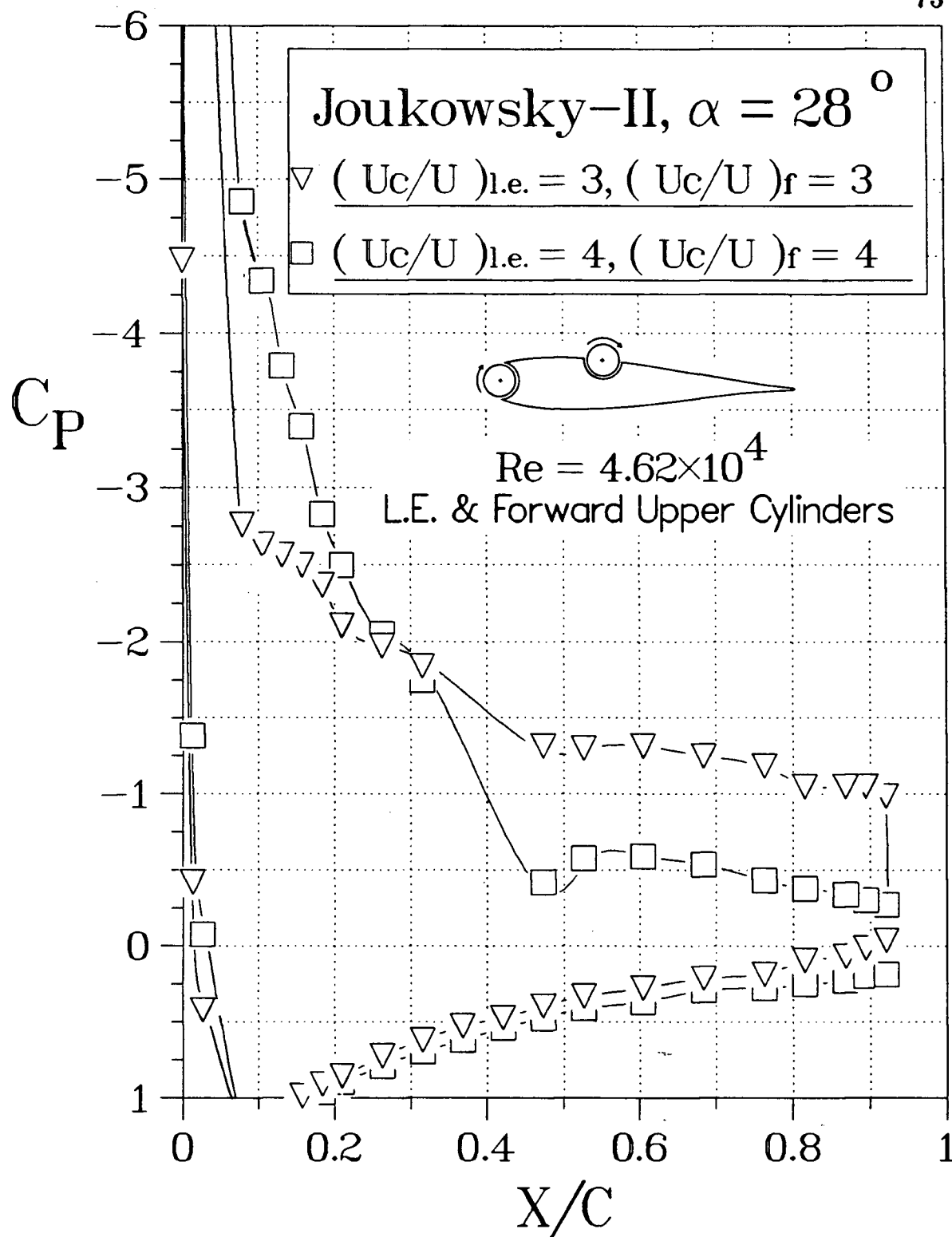


Figure 3-25 Typical pressure distribution results for the Joukowski model II with leading-edge and forward upper-surface cylinders, $\alpha = 28^\circ$.

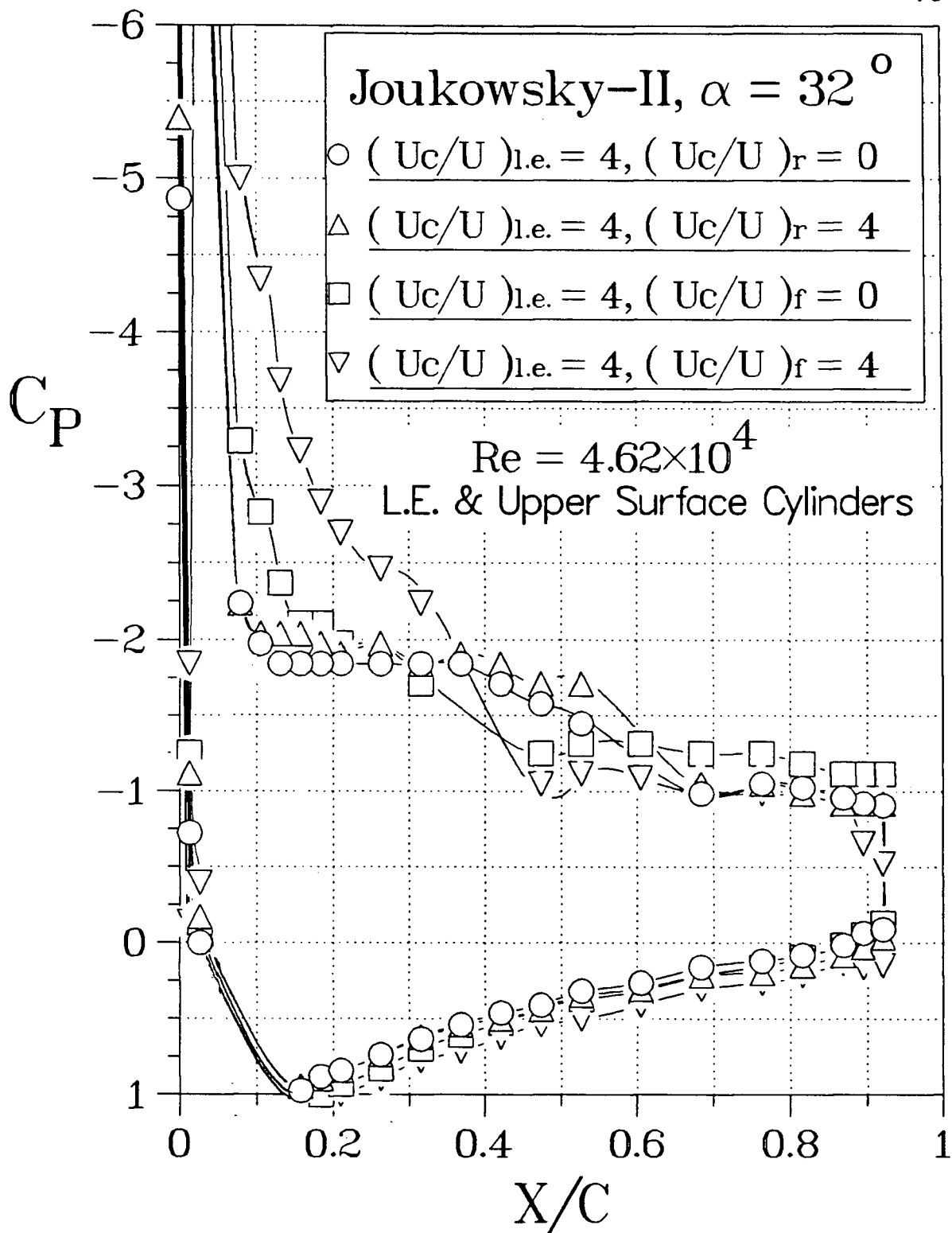


Figure 3-26 Pressure plots as affected by combinations of the leading-edge and upper-surface cylinders' rotation.

the combined effects of both the leading-edge and forward upper-surface cylinders decrease the adverse pressure gradient enough for the flow to remain attached up to around $X/C \approx 0.5$. The flow then separates in the form of a bubble with reattachment close to the trailing edge.

Influence of the leading-edge-cylinder operating in conjunction with the forward or rear upper-surface-cylinder can be better appreciated through the lift plots presented in Figure 3-27. Performance of the original base airfoil (with sharp trailing edge and nose insert) as well as effect of its modifications through introduction of the cylinders are indicated to assess beneficial contribution of the cylinder rotation.

At the outset it is apparent that the change in geometry of the base airfoil and the presence of a gap affects both the $C_{L,max}$ as well as the stall angle. However, as can be expected in light of the leading-edge-cylinder data presented earlier in Figure 3-14, $(U_c/U)_{l.e.} = 1$ with $(U_c/U)_r = 1$ or $(U_c/U)_f = 1$ more than compensated for this initial loss giving $C_{L,max}$ of around 1.2 and 1.3, respectively (not shown to avoid overcrowding of data). Note, the upper-surface-cylinders, rear or forward, while operating individually are also able to make up for the loss (introduced by the airfoil modification), but they must rotate at a much higher speed. With both the leading edge and upper-surface-cylinder rotating at $U_c/U = 4$, the stall is delayed to around 28° with a $C_{L,max}$ of around 1.95, an increase of 130% over the base airfoil data (Figure 3-27a). Rotation of the forward upper-surface-cylinder appears to be relatively more effective. With $(U_c/U)_{l.e.} = (U_c/U)_f = 4$, additional improvement in performance is apparent with the stall angle now around 36° and a corresponding $C_{L,max}$ of 2.22, an increase of around 160% (Figure 3-27b). The pressure recovery results observed earlier in Figure 3-26 also suggest favorable drag characteristics.

To summarize, a rotating leading-edge-cylinder results in a large suction peak at the nose. However, depending on the angle of attack, the adverse pressure gradient still causes the flow to separate downstream. The use of a second cylinder

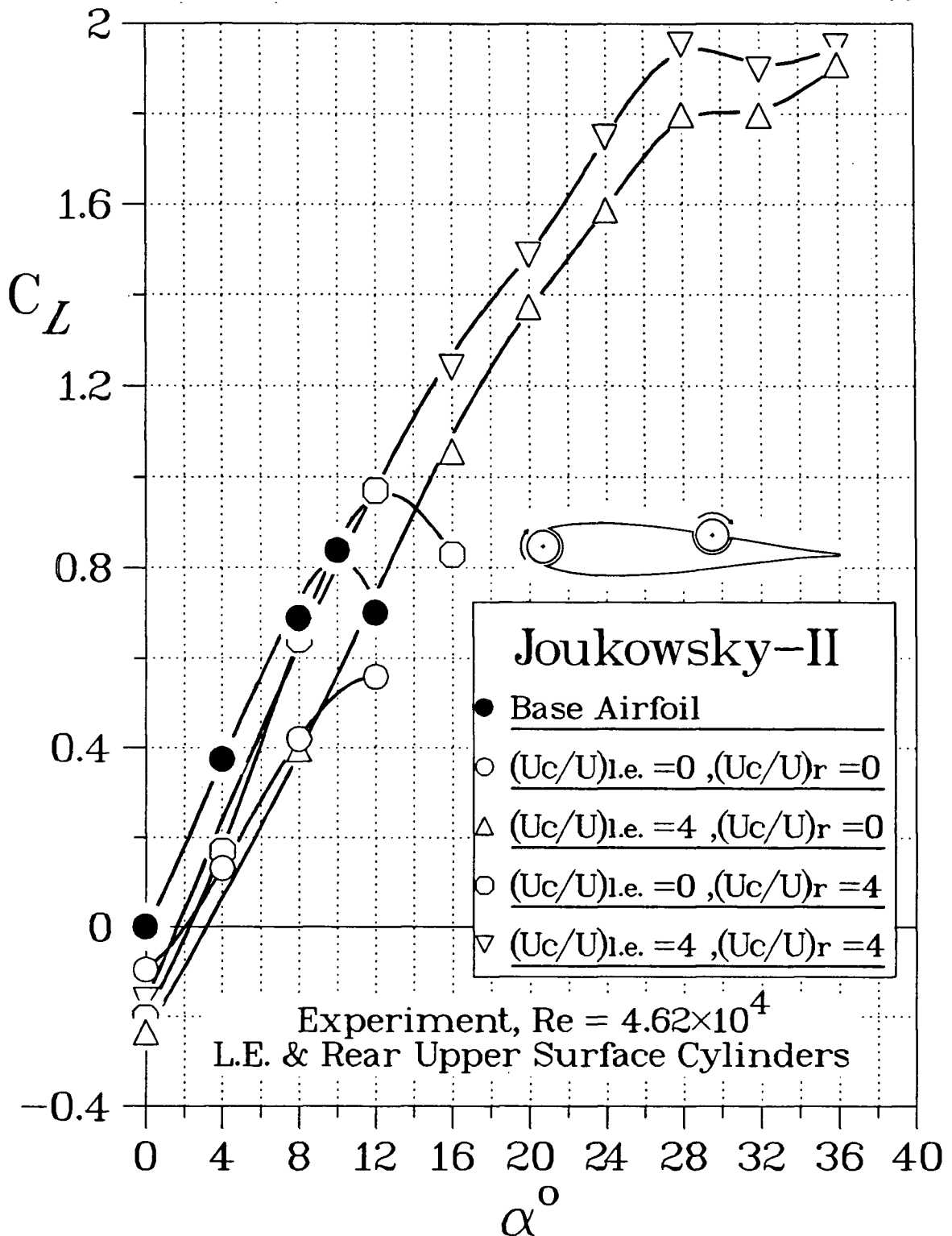


Figure 3-27 Lift and stall characteristics of the Joukowski model II with the leading-edge and upper-surface cylinders: (a) rear upper-surface-cylinder;

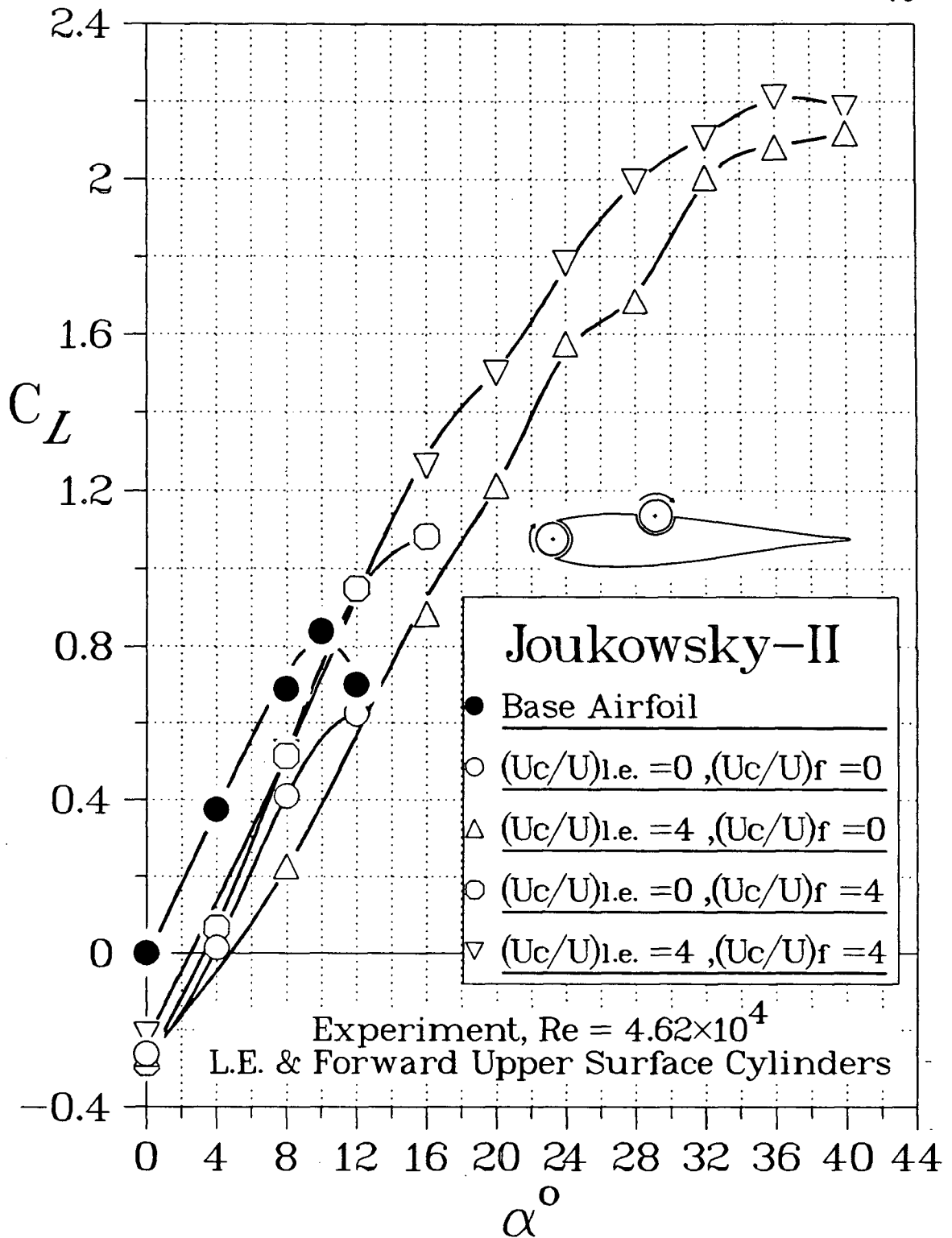


Figure 3-27 Lift and stall characteristics of the Joukowski model II with the leading edge and upper-surface cylinders: (b) forward upper-surface-cylinder.

on the upper surface helps to reduce the separated region. As far as the location of the upper cylinder is concerned, it is likely to be more effective in the front where the adverse pressure gradient is quite significant.

3.2.5 Upper leading-edge-cylinder

Effectiveness of the combination of leading-edge and forward upper-surface cylinders suggested a possibility of replacing the two by a single cylinder as shown in Figure 2-9 (configuration *vi*). This avoids the practical complications associated with construction, installation, and operation of two rotating cylinders.

The configuration, with a cylinder located at approximately 5% of the chord, was tested at cylinder speeds in the range of U_c/U upto 4. The results showed attached flow for angles of attack of as high as 48° . Several typical pressure plots as affected by the angle of attack and cylinder rotation are presented in Figure 3-28.

At $\alpha = 16^\circ$ all but the lowest speed of the cylinder rotation keep the flow attached over the top surface. As the rate of rotation is increased, the suction over the upper surface is generally increased except immediately behind the cylinder where a dip in the pressure profile becomes apparent at $U_c/U > 3$. This is due to the fact that the surface of the cylinder is higher than that of the airfoil and the rotating cylinder is transferring momentum to the airfoil surface in this region. The discontinuity in the pressure plots near the leading edge is again due to difficulty in locating pressure taps close to and on the surface of the cylinder. Although the missing data are important for accurate calculation of the lift coefficient, this does not obscure the the effects of cylinder rotation discussed presently.

At $\alpha = 32^\circ$, the airfoil has stalled even with $U_c/U = 2$. Only the higher speeds of the cylinder ($U_c/U \geq 3$) are capable of keeping the upper-surface flow attached.

Finally, even at a very high incidence of $\alpha = 48^\circ$, it is remarkable that the

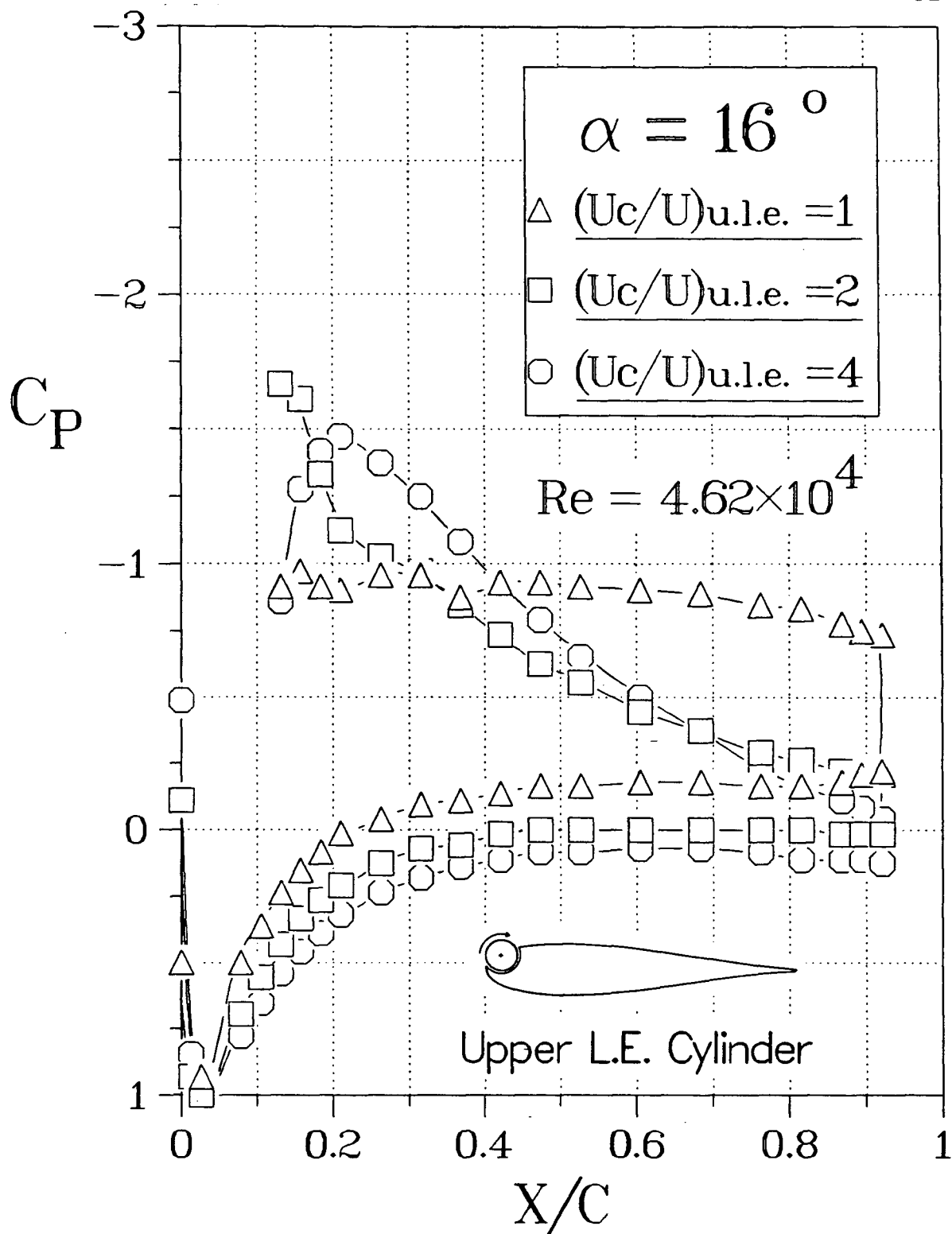


Figure 3-28 Experimentally obtained pressure distribution plots for the Joukowski model II with the upper leading-edge-cylinder: (a) $\alpha = 16^\circ$;

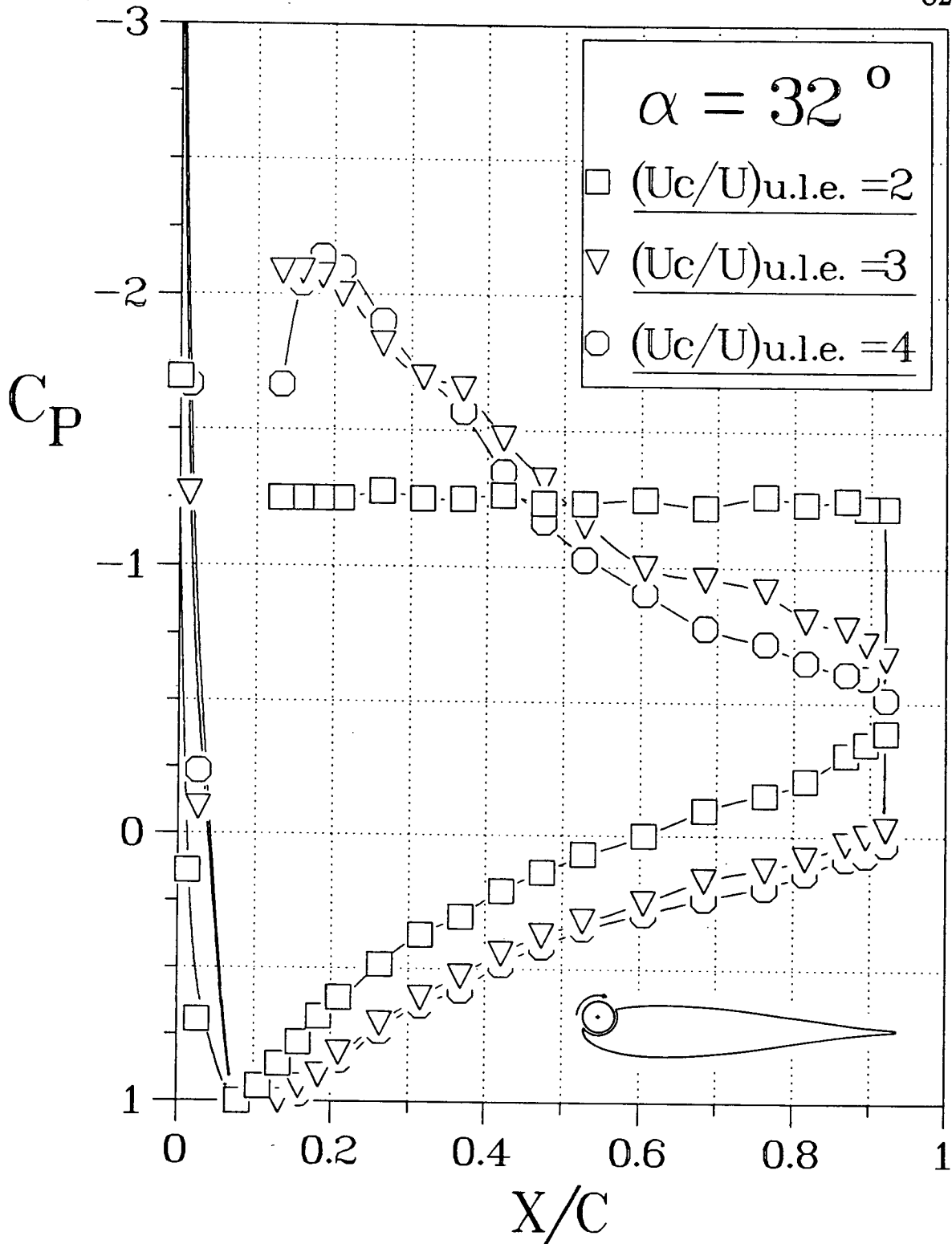


Figure 3-28 Experimentally obtained pressure distribution plots for the Joukowski model II with the upper leading-edge-cylinder: (b) $\alpha = 32^\circ$;

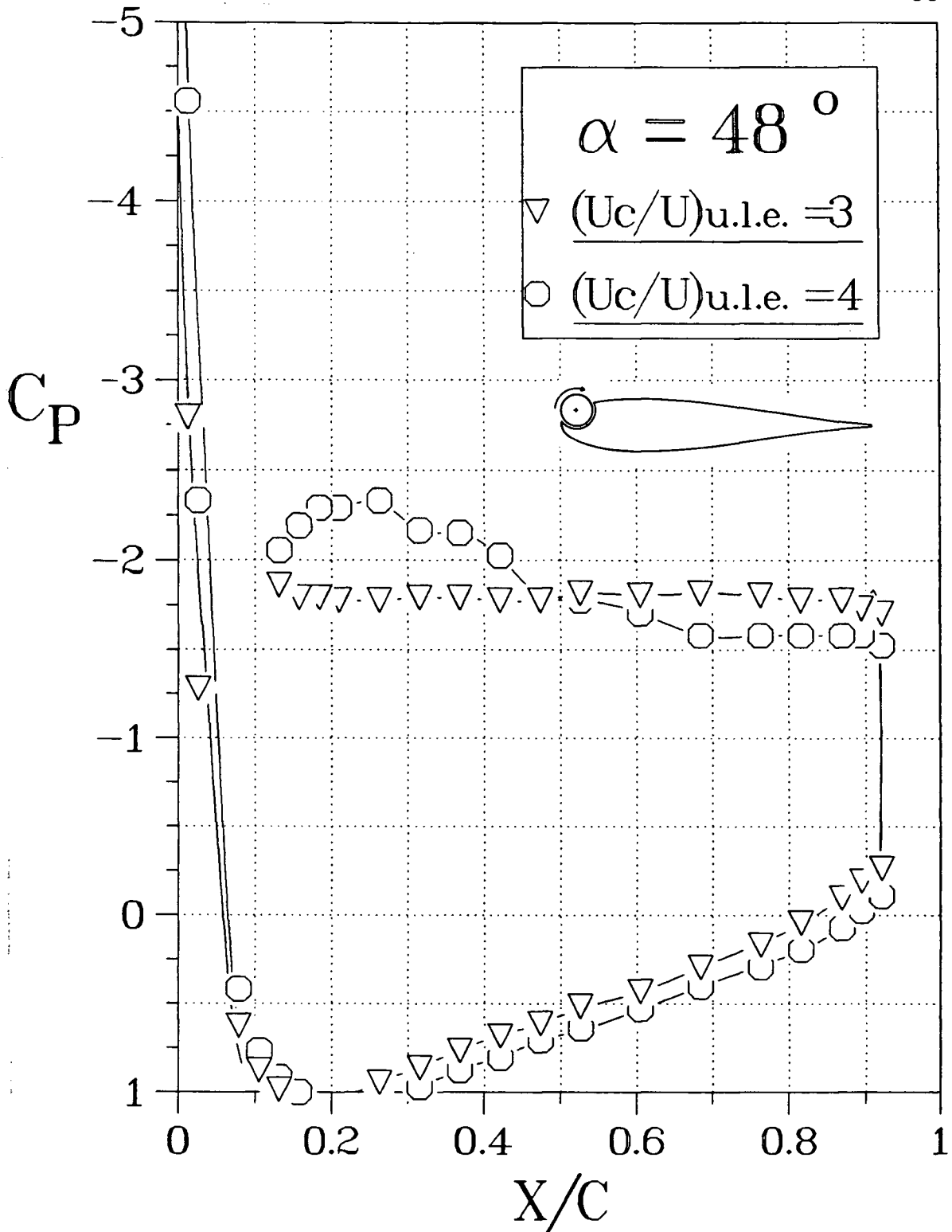


Figure 3-28 Experimentally obtained pressure distribution plots for the Joukowski model II with the upper leading-edge-cylinder: (c) $\alpha = 48^\circ$.

cylinder rotation at $U_c/U = 4$ is able to maintain partially attached flow over the upper surface. There is, as can be expected, however, an associated drag penalty as evident by the lack of any significant pressure recovery near the trailing edge.

The pressure profiles were integrated to yield the coefficients of lift plotted in Figure 3-29. These values, however, are likely to be underestimated due to a lack of high suction data over the rotating cylinder. In absence of measured information, the pressure was conservatively approximated to remain locally constant, over the region with missing pressure taps, at the minimum observed value.

Compared to the leading-edge-cylinder study reported earlier (section 3.2.1, Figure 3-14), where for $U_c/U = 4$, $C_{L,max} \approx 1.75$ and $\alpha_{stall} \approx 28^\circ$, now we have $C_{L,max} \approx 1.95$ with $\alpha_{stall} \approx 48^\circ$. This clearly suggests that location of the cylinder near the leading edge can significantly affect the airfoil performance. Thus there is room for a systematic study to arrive at an optimum location.

Even compared to the results obtained using the leading-edge-cylinder together with the forward upper-surface-cylinder (Figure 3-27b), performance of the present single cylinder configuration appears attractive. Although the $C_{L,max}$ is slightly lower (down from 2.22 to 1.95) the stall is delayed from around 36° to 48° . However, the main advantage would be the mechanical simplicity of working with one cylinder.

3.2.6 Comparative performance and choice of configuration

With a vast amount of data obtained through a planned experimental program using the configurations presented in Figure 2-9, it would now be useful to compare their distinctive features to help establish relative merits. Figure 3-30 attempts to achieve this objective. Results of the standard Joukowski airfoil (symmetrical, 15% thickness, model II), with its $C_{L,max} = 0.85$ and $\alpha_{stall} = 10^\circ$, serve as reference for all the cases presented.

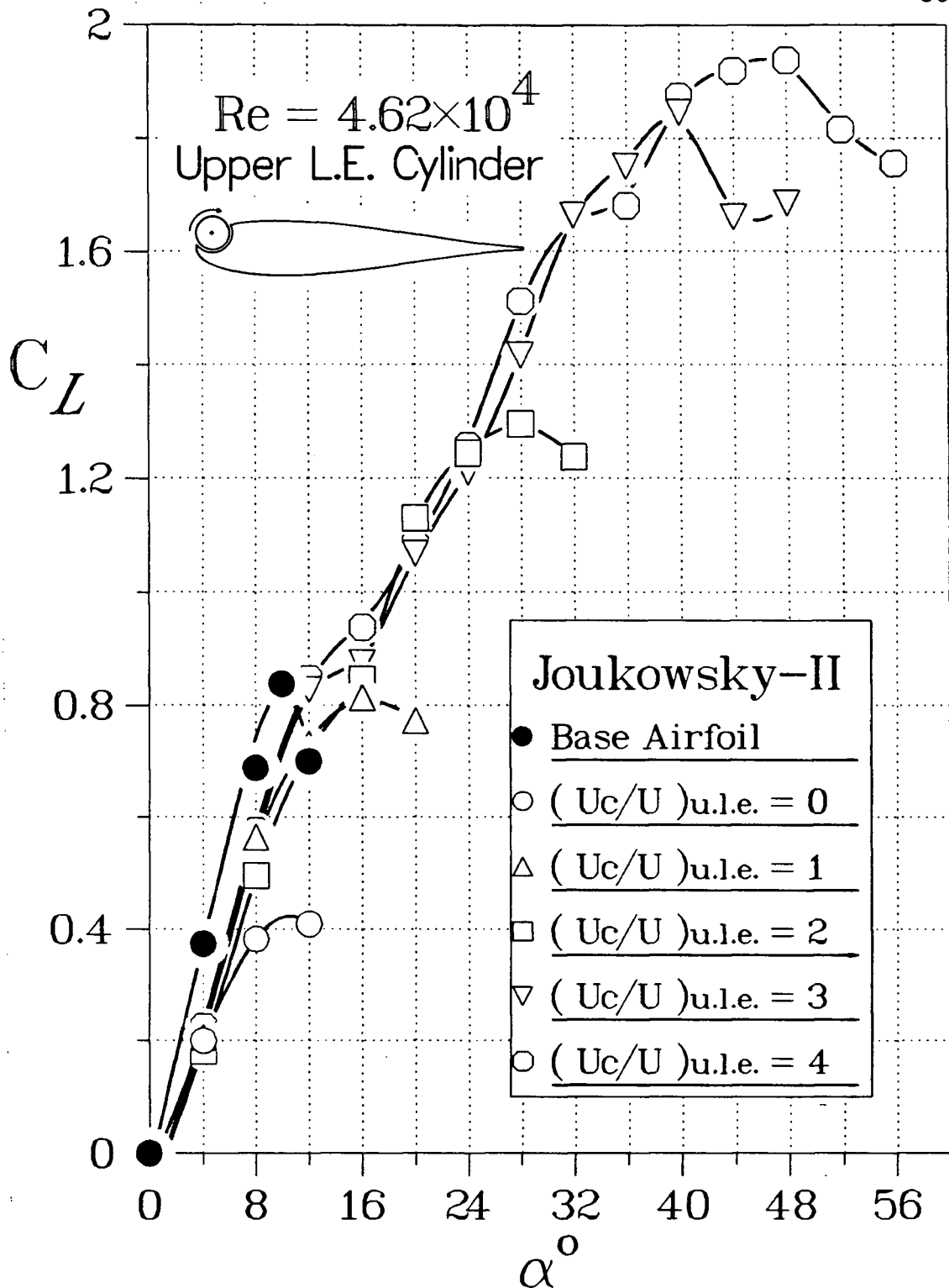


Figure 3-29 Lift and stall characteristics of the Joukowsky model II as affected by the upper leading-edge-cylinder rotation. Base airfoil and $U_c/U = 0$ data serve as reference to assess the effect of airfoil modification by the cylinder and its rotation.

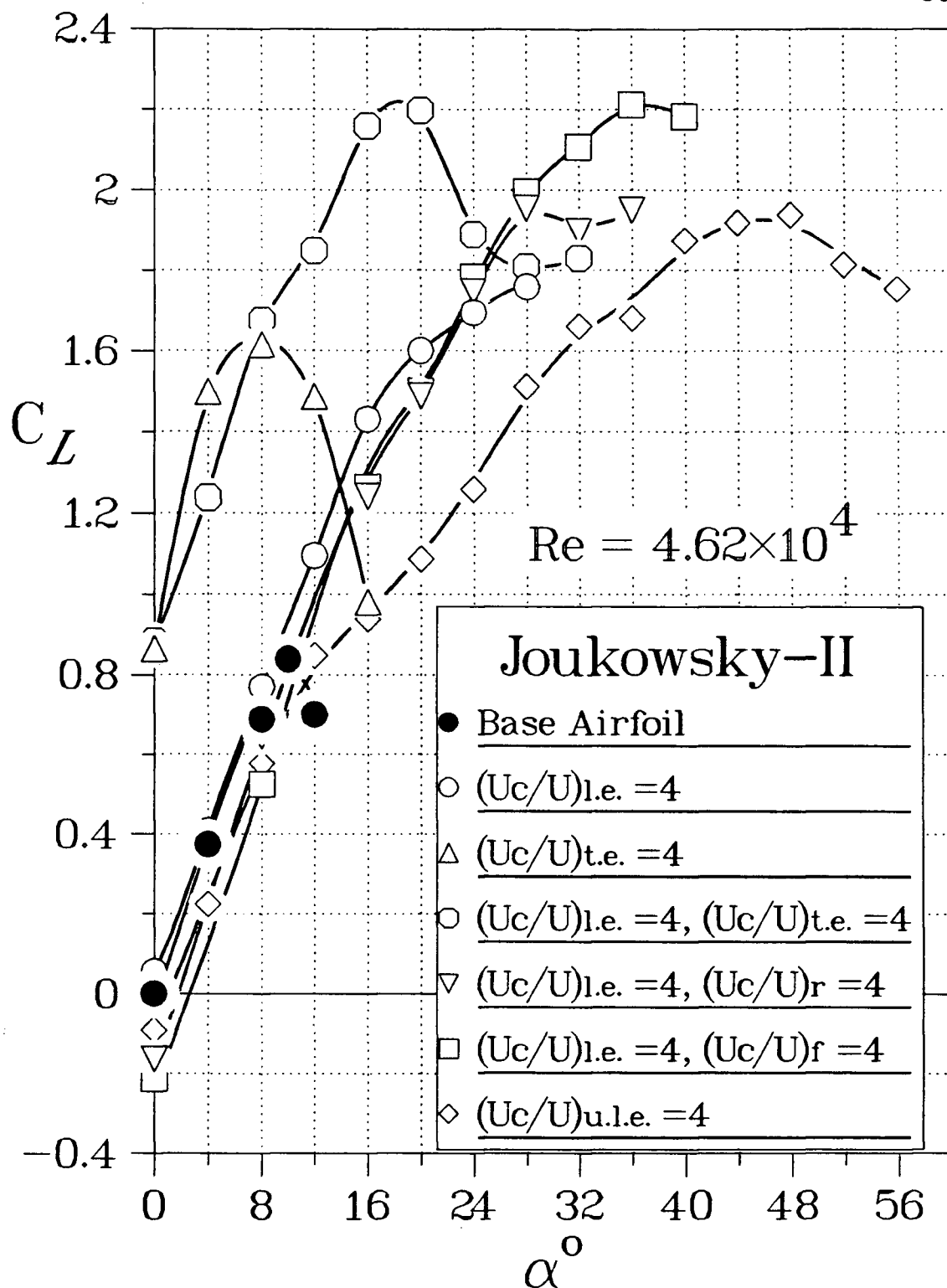


Figure 3-30 Plots to assess relative influence of different configurations studied on the lift and stall characteristics.

The leading-edge-cylinder is quite effective in extending the lift curve, without changing its slope, thus substantially increasing the maximum lift coefficient (1.75) and delaying the stall angle (28°). Further improvements in the maximum lift coefficient and stall angle are possible when the leading-edge-cylinder is used in conjunction with an upper-surface-cylinder. This configuration also results in a lower drag due to a large recovery of pressure near the trailing edge, at moderately high angles of attack. The $C_{L,max}$ realized with the leading-edge and forward upper-surface cylinders, was about 2.22 ($\alpha = 36^\circ$), approximately 2.6 times that of the base configuration.

A rotating cylinder on the upper side of the leading edge also proves very effective. Although the maximum coefficient of lift realized with its rotation is slightly lower (≈ 1.95), it does have a major advantage in terms of mechanical simplicity. Note, now the lift curve has a lower slope and is not an extension of the base airfoil lift curve. Hence the lift at a given α is relatively lower, however, the stall is delayed to around 48° .

On the other hand, to improve lift over the range of low to medium angles of attack ($\alpha \leq 20^\circ$), the trailing-edge-cylinder proves much more effective, particularly in conjunction with the leading-edge-cylinder. The suction over the airfoil upper surface as well as the compression on the lower surface are increased dramatically with the higher rates of rotation of this cylinder, resulting in a substantial increase in lift ($\approx 160\%$).

Thus, depending on the intended objective in terms of desired $C_{L,max}$ and stall angle, one can select an appropriate configuration to initiate a preliminary design.

3.3 NACA 63-218 modified airfoil

Wind tunnel experiments with the NACA 63-218 modified airfoil showed

aerodynamic coefficients to be essentially independent of the Reynolds number in the range $Re = 10^5$ to 2.5×10^5 . In general the results were obtained for five values of the speed ratio ($U_c/U = 0, 1, 2, 3, 4$) and over a range of the angle of attack extending beyond the stall value. However, in presenting the data certain runs are purposely omitted for clarity.

The first logical step would be to record aerodynamic characteristics of the basic airfoil to assess deterioration in performance caused by a bluff cylinder, with a gap, replacing its nose. One can then evaluate the influence of the rotating cylinder as reflected on the boundary-layer control. This is shown in Figure 3-31.

The basic airfoil (without cylinder) has a maximum lift coefficient of around 1.3. However, bluntness of the cylinder and the associated gap cause the slope of the lift curve as well as $C_{L,max}$ to diminish. In absence of the cylinder rotation the airfoil stalls at around 12° giving uniform pressure distribution on the top surface. The stall sets in rather abruptly as shown by a sudden drop in the lift. However, with the cylinder rotation, a large well developed suction peak was observed at the leading edge of the wing suggesting a delay in the stall. In fact, the balance data show the stall to occur around 45° ($U_c/U = 3$) with an increase in the lift coefficient of around 200%. An increase in cylinder speed beyond $U_c/U = 3$ improved the situation only marginally suggesting the existence of a critical speed ratio beyond which momentum injection into the boundary layer through a moving surface appears to have little effect. Note also that the effect of cylinder rotation is to extend the lift curve without substantially affecting its slope, as before (Figures 3-7, 3-14), and it also flattens the stall peak.

Typical pressure distribution plots showing the effectiveness of the cylinder rotation are plotted in Figure 3-32. At $\alpha = 24^\circ$, even the lowest cylinder speed is sufficient to prevent separation and only minor improvements in lift and drag can be realized with increasing speeds. Note a slight increase in suction behind the leading edge and the effect on the pressure recovery at the trailing edge. There is

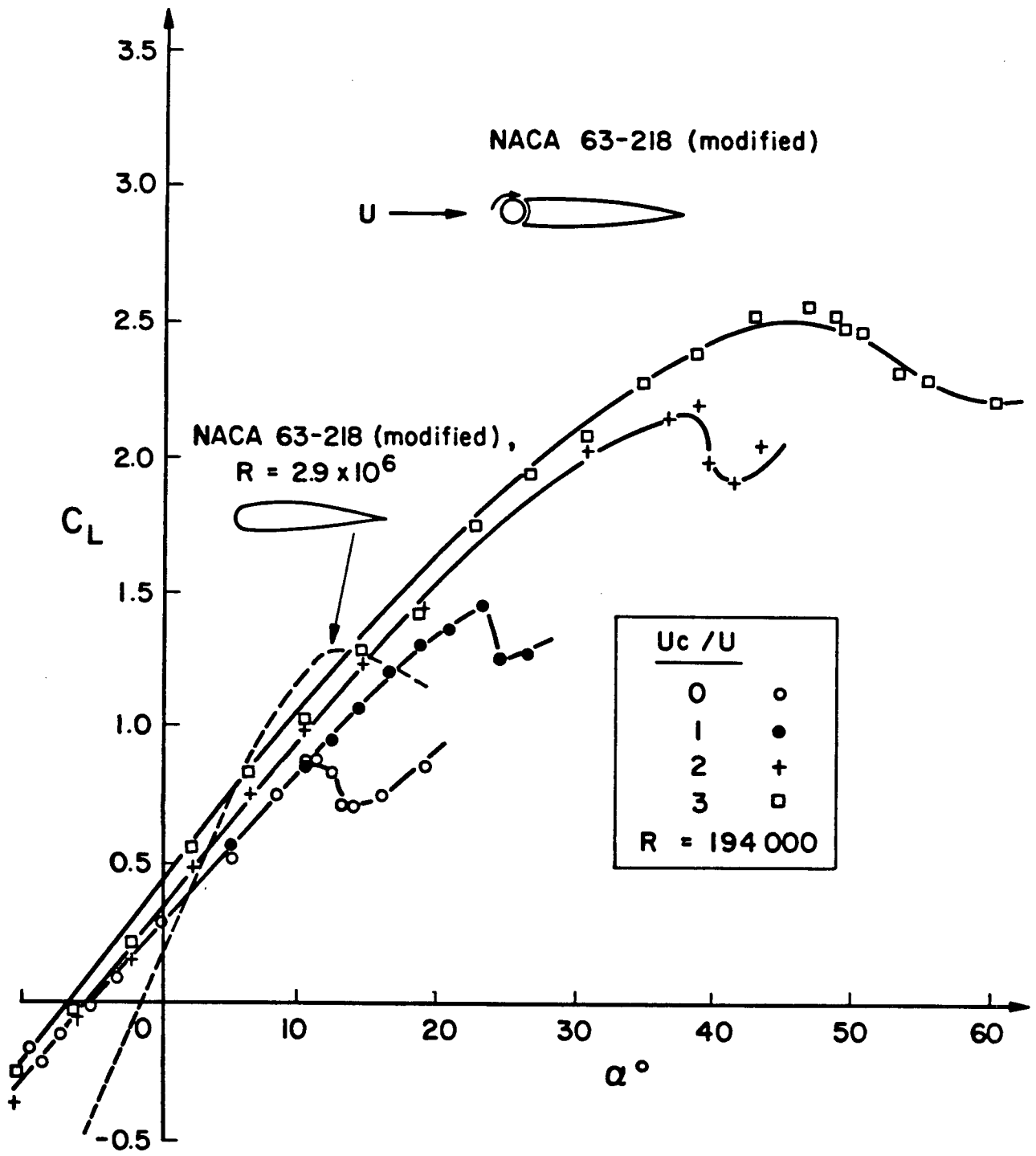


Figure 3-31 Typical plots showing variation in the lift coefficient with angle of attack for NACA 63-218 modified airfoil as affected by the leading-edge-cylinder rotation.

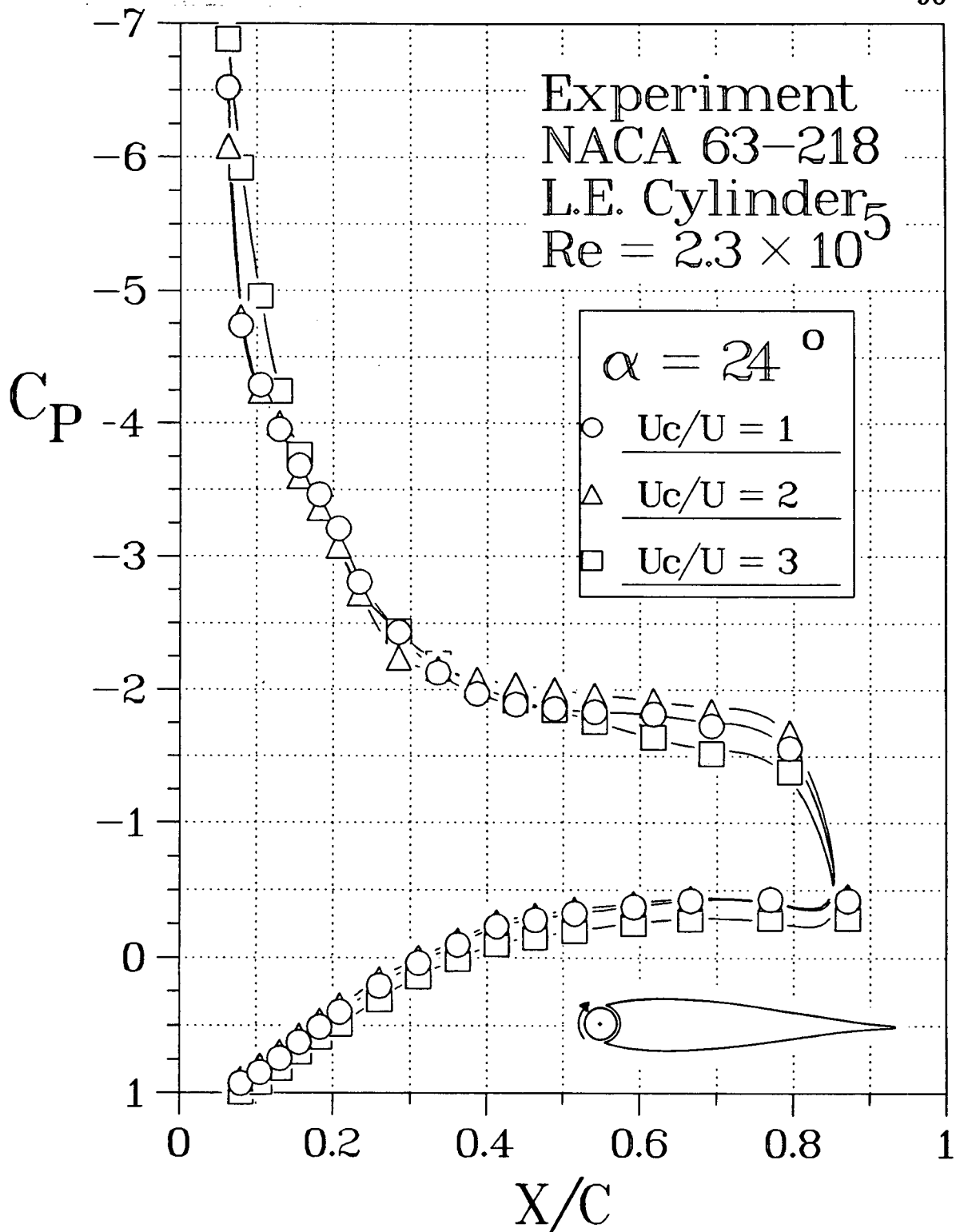


Figure 3-32 Typical experimentally obtained pressure distribution plots for NACA 63-218 airfoil modified with a leading-edge-cylinder showing the effect of cylinder rotation: (a) $\alpha = 24^\circ$;

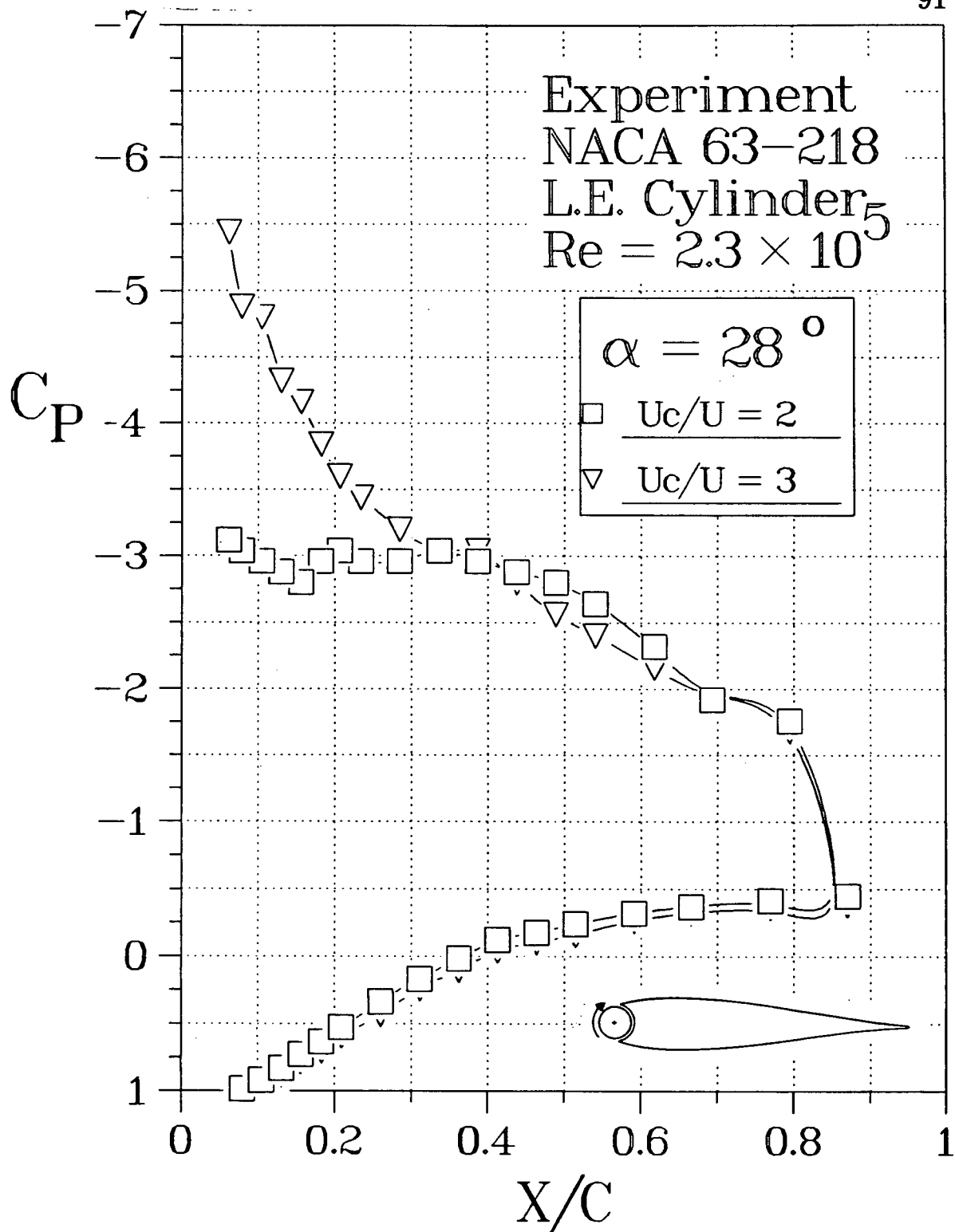


Figure 3-32 Typical experimentally obtained pressure distribution plots for NACA 63-218 airfoil modified with a leading-edge cylinder showing the effect of cylinder rotation: (b) $\alpha = 28^\circ$.

also a small increase in lift with rotation because of the increasing suction over the cylinder. This, however, is not reflected in the plots due to the lack of pressure taps on the surface of the cylinder but is recorded by the balance (Figure 3-31).

At $\alpha = 28^\circ$, Figure 3-32(b), rotation of the cylinder at $U_c/U = 1$ is no longer effective and the pressure profile shows partial separation (followed by reattachment as indicated by the pressure recovery) even at $U_c/U = 2$. The flow, however, reattaches towards the trailing edge and the lift continues to increase (Figure 3-31). At a higher rate of rotation ($U_c/U = 3$) the pressure peak is reinstated near the leading edge.

From design considerations and for better indication as to the overall effectiveness of this concept one should also look at the associated drag penalty, i.e., the ratio of lift to drag. This is shown in Figure 3-33. Substantial improvement at all angles of attack is quite evident. However, for $U_c/U > 2$ any additional gain appears to be only marginal in this particular case. The corresponding C_L vs. C_D plot is perhaps more useful (Figure 3-34). Note, for a given C_L , the drag coefficient diminishes with an increase in the cylinder rotation rate.

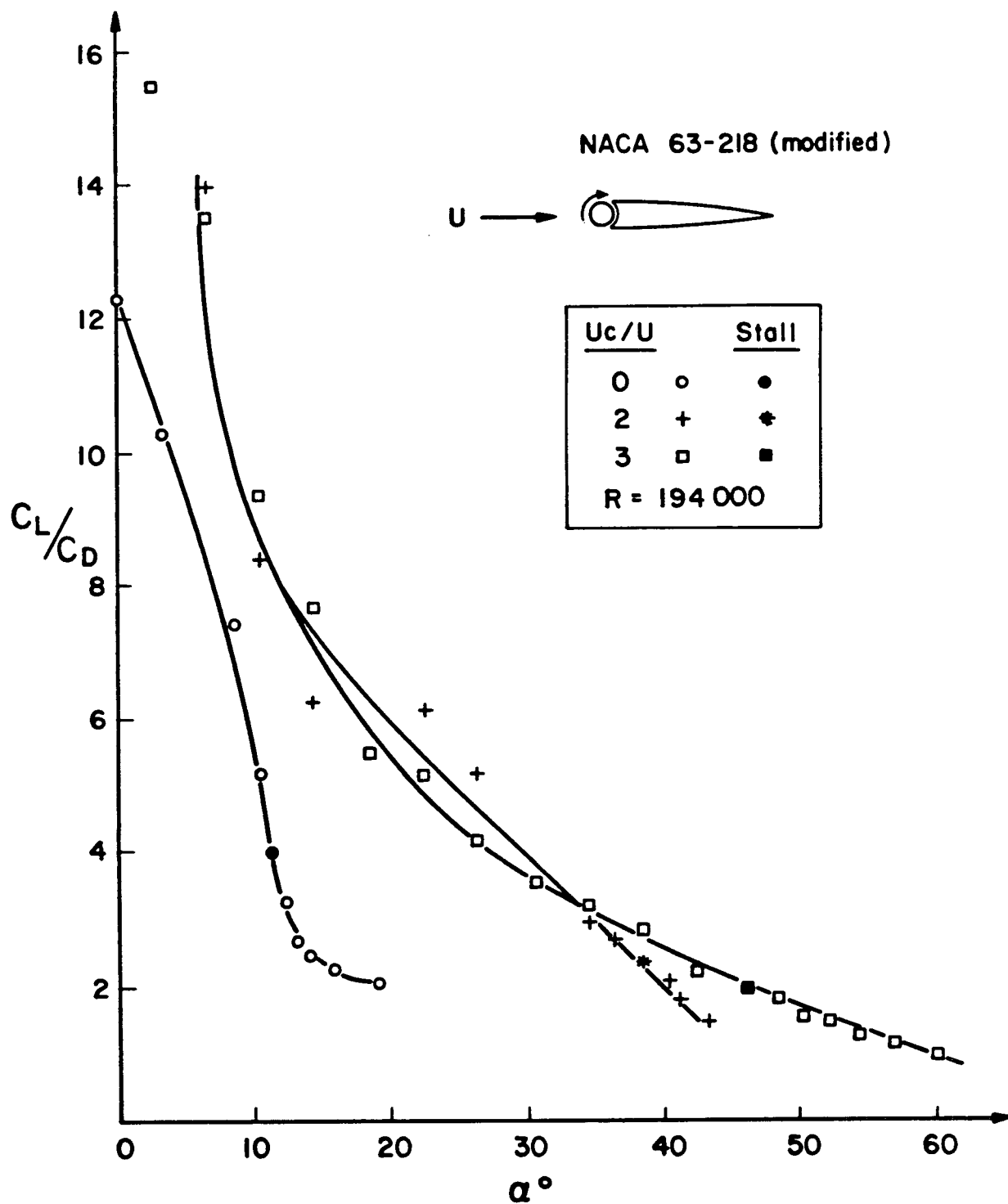


Figure 3-33 Effect of rotation rate on the lift to drag ratio of NACA 63-218 airfoil modified with a leading-edge rotating cylinder.

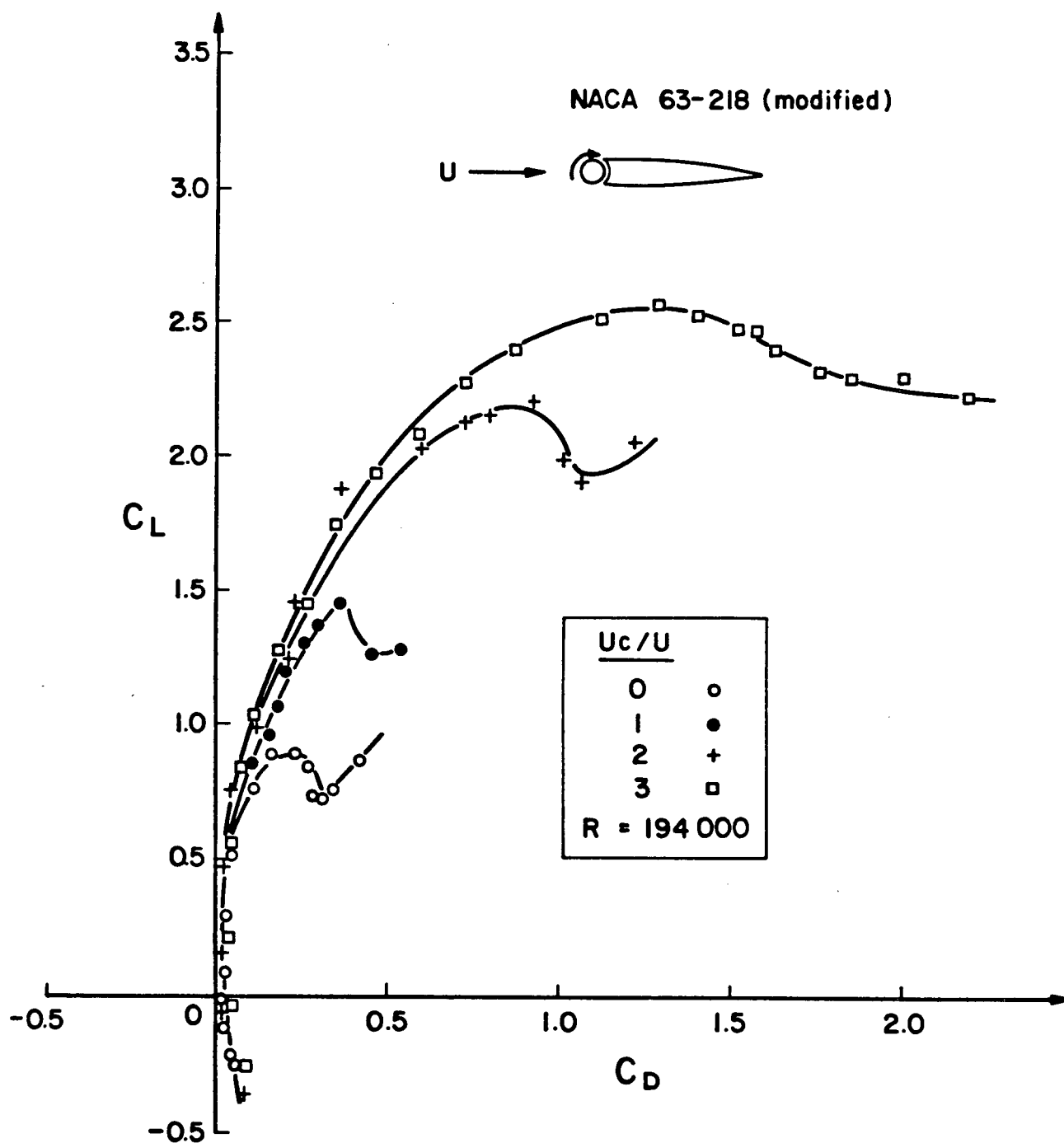


Figure 3-34 Variation of C_L vs. C_D for NACA 63-218 airfoil (modified) with a leading-edge rotating cylinder.

4. THEORETICAL POTENTIAL FLOW APPROACHES

Complex character of the flow suggests a need for an elaborate modelling procedure that can account for viscous effects. The complications introduced by separation and reattachment of the flow would, ideally, require an approach to the the problem through the full Navier–Stokes equations and their numerical solution consistent with the boundary conditions.

The prohibitive cost and the possible loss of appreciation for the physical process, usually associated with the use of such elaborate modelling packages, led to the search for simpler approaches. The main objective of the project was to explore effectiveness of the moving–surface boundary–layer control experimentally and develop mathematical tools that may help predict trends. With this as background, the attention was turned to relatively simple but promising analytical and numerical procedures that can meet this objective.

The mathematical models used in this theoretical stage of the investigation are shown in Figure 4-1.

4.1 Analytical Model

In a potential flow analysis, due to the absence of viscosity, rotating cylinders can not be treated as boundary–layer control devices but rather should be viewed as a means of circulation control for airfoils. Since their effect in increasing the circulation around an airfoil is similar to that of a vortex, the simple analytical model of flow about an airfoil in the presence of an arbitrarily fixed vortex is used as a first approximation to the actual case.

The recent work of Huang and Chow [28] investigates the possibility of trapping a free vortex in the vicinity of a Joukowski airfoil for lift augmentation. It is found that very high lift forces can be generated by a stationary vortex captured

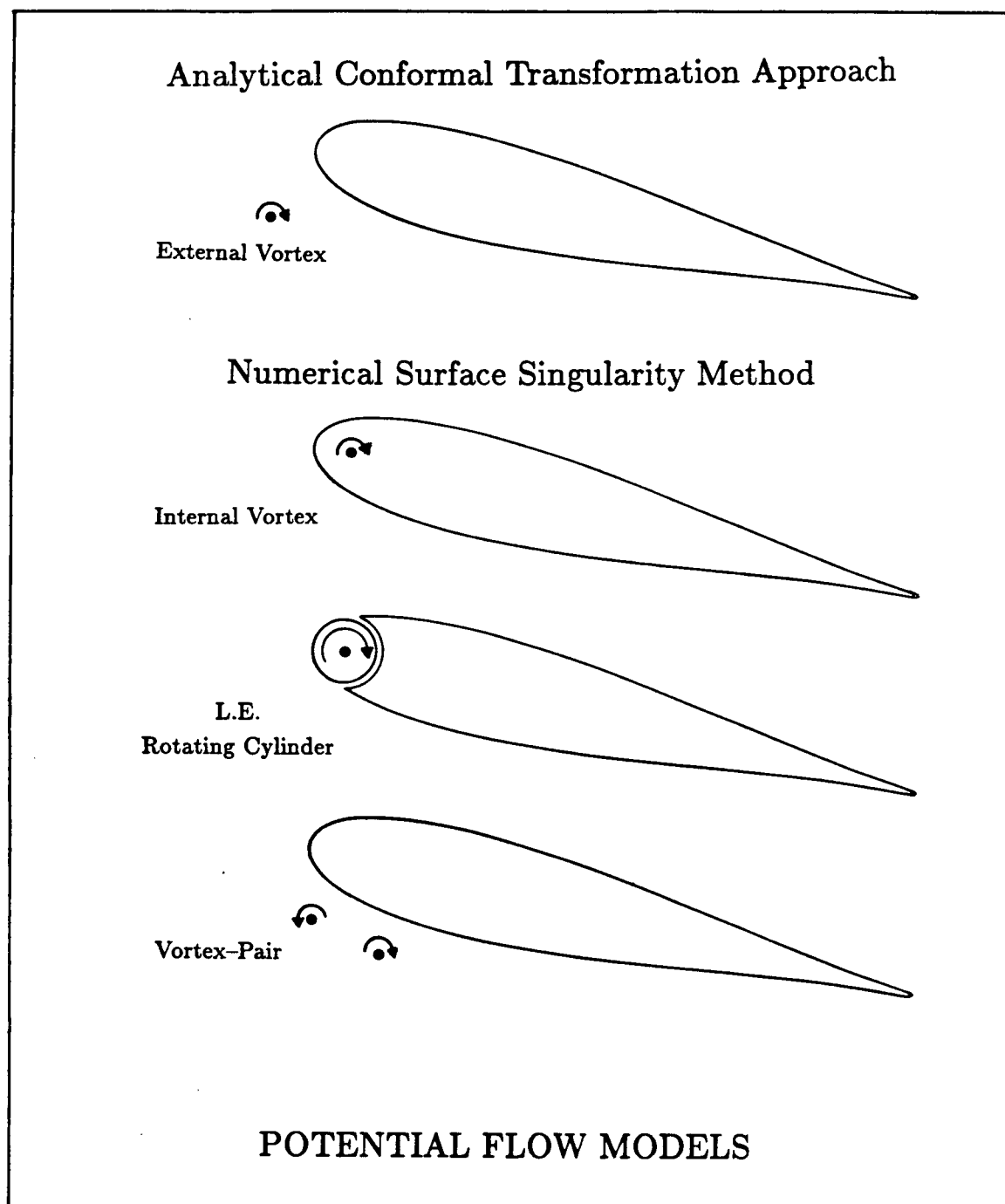


Figure 4-1 Analytical and numerical models.

above the leading edge, but the vortex is always unstable in the sense that it will move away after being displaced from its equilibrium position. Through the use of special devices, such as a leading edge flap, a vortex can be trapped below or above the leading edge of the airfoil resulting in the desired effect.

The authors also investigated the effect of relative motion of the vortex with respect to the airfoil [29]. Their results suggest that by moving the vortex towards or away from the wing in a proper manner, additional lift may be generated. Alternatively, by increasing the strength of a vortex when it is appropriately located with respect to the airfoil, the lift so produced can be several times higher than that generated by a constant-strength vortex of comparable circulation.

For an airfoil moving at a speed U through an incompressible fluid of density ρ , a circulation Γ is created in order to satisfy the Kutta condition at the sharp trailing edge. When a vortex of circulation k is placed above the airfoil, it produces a reversed fluid motion on the upper surface, so that a stagnation point would appear there if the same circulation were maintained around the airfoil. However, to remove the infinite velocity situation at the sharp trailing edge, additional circulation $\Delta\Gamma$ is required to shift the stagnation point back to the trailing edge so that the Kutta condition is fulfilled again. A vortex of circulation $-\Delta\Gamma$ is shed in the wake. The wing has thus gained a circulation of $\Delta\Gamma + k$.

The basis of the Joukowski airfoil analysis through a conformal transformation is well established. Here the major difference would arise due to introduction of a vortex and its location in the physical plane Z . Due to the classical character of the analysis, only more important aspects are touched upon here.

A circle of radius R centered at the origin of the ζ' -plane is transformed into a Joukowski airfoil in the Z -plane by a translation in the ζ -plane and the transformation

$$Z = \zeta + \frac{1}{\zeta} .$$

The shape of the airfoil is controlled by varying the parameters of the intermediate transformation defined by

$$\zeta = \zeta' + ae^{i(\pi-\delta)} .$$

Under these transformations (Figure 4-2), free stream velocity U at an angle α with the horizontal axis maps into a uniform flow of the same speed without changing its orientation. Similarly a vortex of circulation k at ζ'_0 maps into a vortex of the same strength at Z_0 .

Let $F = \Phi + i\Psi$ be the complex potential of the flow where Φ is the velocity potential and Ψ , the stream function. The complex potential in the ζ' -plane consists of the contributions from the uniform flow, the vortex and its image in the circle, and the circulation about the center of the circle,

$$F(\zeta') = Ue^{-i\alpha} \left[\zeta' + \frac{R^2}{\zeta'} e^{i2\alpha} \right] + \frac{ik}{2\pi} \left[\ln(\zeta' - \zeta'_0) - \ln\left(\zeta' - \frac{R^2}{\bar{\zeta}'_0}\right) \right] + \frac{i}{2\pi} (\Gamma + k) \ln \zeta' ,$$

where the bar denotes the complex conjugate.

The complex velocity of the flow can now be written as

$$W(\zeta') = Ue^{-i\alpha} \left[1 - \frac{R^2}{\zeta'^2} e^{i2\alpha} \right] + \frac{ik}{2\pi} \left[\frac{1}{\zeta' - \zeta'_0} - \frac{1}{\zeta' - \frac{R^2}{\bar{\zeta}'_0}} \right] + \frac{i}{2\pi} \frac{(\Gamma + k)}{\zeta'} .$$

The Kutta condition requires the velocity to be finite at the trailing edge. This is achieved by setting $W(\zeta') = 0$ at $\zeta = 1$ or $\zeta' = Re^{-i\beta}$. Introducing this relation into the above equation and using $\zeta'_0 = r_0 e^{i\theta_0}$ for the location of the vortex yields, after some manipulation,

$$\frac{i}{2\pi} (\Gamma + k) = 2iRU \sin(\alpha + \beta) - RB \frac{ik}{2\pi} ,$$

where

$$B = \frac{r_0^2 - R^2}{R [2Rr_0 \cos(\theta_0 + \beta) - R^2 - r_0^2]} .$$

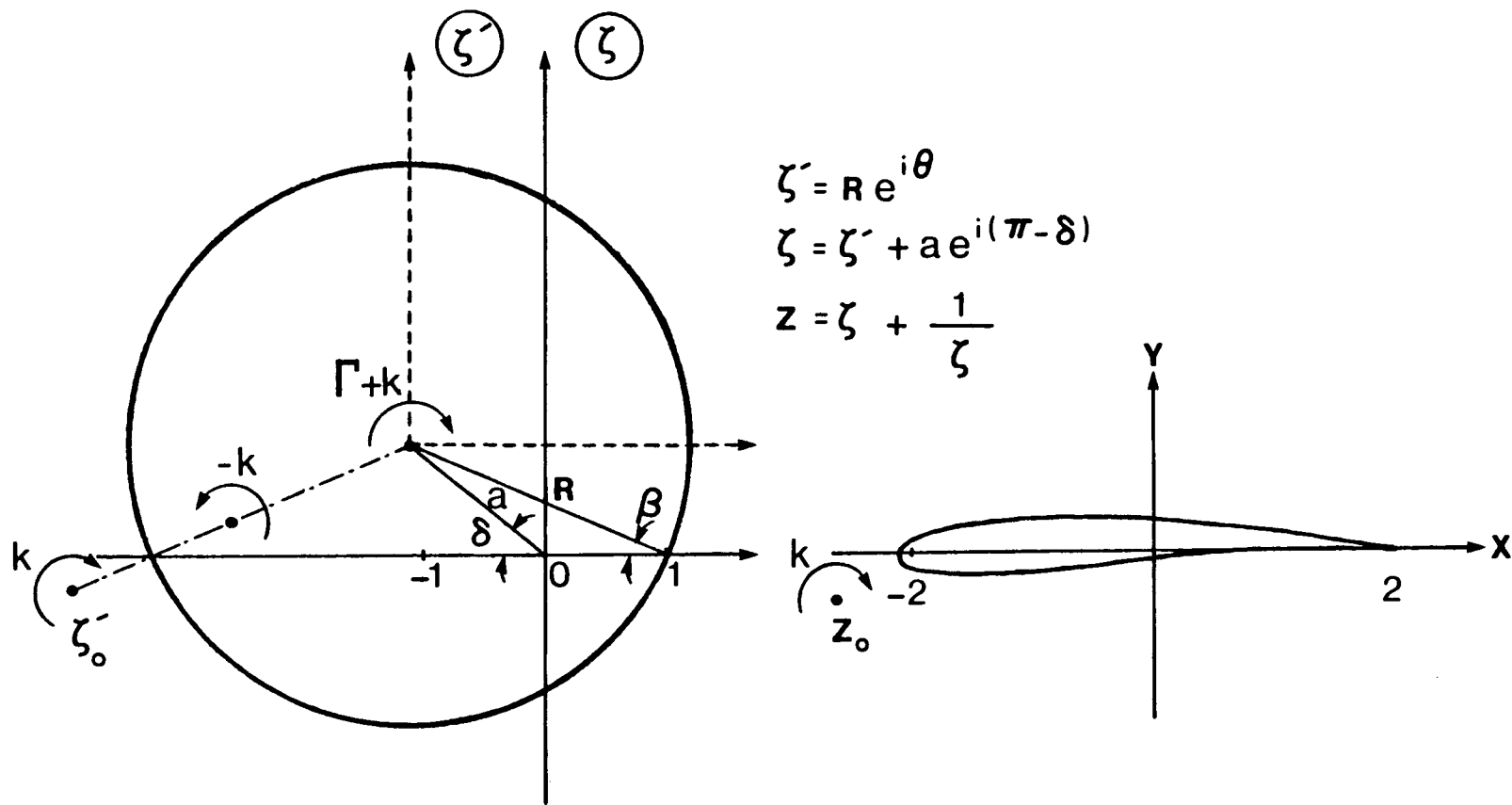


Figure 4-2 The Joukowski transformation.

The complex velocity now takes the form

$$W(\zeta') = Ue^{-i\alpha} \left[1 - \frac{R^2}{\zeta'^2} e^{i2\alpha} \right] + \frac{ik}{2} \left[\frac{1}{\zeta' - \zeta'_o} - \frac{1}{\zeta' - \frac{R^2}{\zeta'_o}} \right] + \frac{2iRU \sin(\alpha + \beta)}{\zeta'} - \frac{RB}{\zeta'} \frac{ik}{2\pi}.$$

In order to gain some appreciation as to the magnitude of circulation, k , an analogy is made with a rotating cylinder as follows. The amount of circulation around a circular cylinder of diameter D_c rotating with a surface velocity U_c is given by

$$k = \pi D_c U_c,$$

therefore, from now on the circulation will be specified in terms of the ratio of cylinder surface velocity to the uniform free stream velocity, U_c/U .

The fluid velocity on the circle is obtained by setting $\zeta' = Re^{i\theta}$ and the corresponding velocity on the airfoil can finally be derived using the relation

$$\frac{dF}{dZ} = \frac{dF}{d\zeta'} \frac{d\zeta'}{d\zeta} \frac{d\zeta}{dZ} = \frac{dF}{d\zeta'} = \frac{W(\zeta')}{\frac{dZ}{d\zeta}},$$

where $\frac{dZ}{d\zeta} = 1 - 1/\zeta^2$. The pressure coefficient, defined by

$$C_p = \frac{|W(\zeta')|^2}{U^2 \left| \frac{dZ}{d\zeta} \right|^2},$$

is obtained for this case as

$$C_p = 1 - \frac{2 \sin(\alpha + \beta) - 2 \sin(\alpha - \theta) + \frac{1}{2} D_c \frac{U_c}{U} \left[\frac{r_o^2 - R^2}{R[2Rr_o \cos(\theta_o - \theta) - R^2 - r_o^2]} \right] - \frac{1}{2} B D_c \frac{U_c}{U}}{\left| 1 - \frac{1}{\zeta^2} \right|^2}.$$

Note that if the vortex is chosen infinitely close to the circle in the ζ' -plane so that $\zeta'_o \simeq Re^{i\theta_o}$, the vortex and its image in the circle form a doublet at that location and the complex potential becomes,

$$F(\zeta') = Ue^{-i\alpha} \left[\zeta' + \frac{R}{\zeta'} e^{i2\alpha} \right] + iC \frac{1}{\zeta' - \zeta'_o} + \frac{i}{2\pi} (\Gamma + k) \ln \zeta',$$

where C , the strength of the doublet, can be related to the circulation k . For this case, the Kutta condition at the trailing edge results in the relation,

$$\left[Ue^{-i\alpha} \left[1 - \frac{R^2}{\zeta'^2} e^{i2\alpha} \right] - \frac{iC}{(\zeta' - Re^{i\theta_0})^2} + \frac{i}{2\pi} \frac{\Gamma + k}{\zeta'} \right]_{\zeta'=Re^{-i\beta}} = 0.$$

After some manipulation, the above condition can be rewritten as

$$\frac{i(\Gamma + k)}{2\pi R} = 2iU \sin(\alpha + \beta) + \frac{iC}{R^2} \frac{\cos \theta_0 - i \sin \theta_0}{2[\cos(\theta_0 + \beta) - 1]},$$

which can only be satisfied if:

$$\frac{\Gamma + k}{2\pi R} = 2iU \sin(\alpha + \beta) + \frac{iC}{2R^2} \frac{\cos \theta_0}{[\cos(\theta_0 + \beta) - 1]}; \quad (i)$$

and

$$\sin \theta_0 = 0; \quad \text{i.e., } \theta_0 = 0 \text{ or } \pi. \quad (ii)$$

Condition (i) sets the amount of circulation around the airfoil and condition (ii) fixes the location of the vortex doublet which satisfies the Kutta condition at the trailing edge. With the simplification of $\sin \theta_0 = 0$, condition (i) reduces to

$$\frac{\Gamma + k}{2\pi R} = 2U \sin(\alpha + \beta) + \frac{C}{2R^2(\cos \beta + 1)}.$$

Since, in the absence of the vortex doublet, the circulation around a Joukowski airfoil is given by

$$\Gamma = 4\pi R U \sin(\alpha + \beta),$$

the additional circulation, k , due to the vortex doublet is

$$\frac{k}{2\pi R} = \frac{C}{2R^2(1 + \cos \beta)}.$$

Setting $k = \pi D_c U_c$ as before gives the strength of the doublet in terms of the cylinder surface velocity as

$$C = R(1 + \cos \beta) D_c U_c,$$

and the total amount of circulation becomes

$$\frac{\Gamma + k}{2\pi R} = 2U \sin(\alpha + \beta) + \frac{D_c U_c}{2R}.$$

The complex velocity for this case has the form

$$W(\zeta') = U e^{-i\alpha} \left[1 - \frac{R^2}{\zeta'^2} e^{i2\alpha} \right] - \frac{iR(1 + \cos \beta) D_c U_c}{(\zeta' + R)^2} + \frac{i}{\zeta'} \left[2RU \sin(\alpha + \beta) + \frac{D_c U_c}{2} \right],$$

with the pressure distribution, obtained in the same way as before,

$$C_p = 1 - \frac{\left[2 \sin(\alpha + \beta) - 2 \sin(\alpha - \theta) + \frac{1}{2R} D_c \frac{U_c}{U} \left(1 - \frac{1 + \cos \beta}{1 + \cos \theta} \right) \right]^2}{\left| 1 - \frac{1}{\zeta'^2} \right|^2}.$$

Although the above analysis is applied to a Joukowski airfoil in this case, any arbitrary airfoil can be treated using similar approaches as described by Theodorsen [30] and Halsey [31].

The analytically predicted pressure distribution plots, obtained through application of the conformal transformation approach to a symmetrical Joukowski section, in the presence of an external vortex are shown in Figure 4-3. The strength of the vortex is reflected in the parameter U_c/U (cylinder surface speed to free stream speed ratio) using the analogy discussed earlier. The “No Vortex” case, included as reference, shows the pressure distribution over the upper and lower surfaces (at $\alpha = 0^\circ$) to be identical since the airfoil is symmetrical. The vortex is located on the x-axis in front of the leading edge of the airfoil and is progressively moved closer. The results show a large increase in suction on the upper surface close to the leading edge accompanied by an increase in compression on the lower surface. As the vortex gets closer to the leading edge, the suction peak value becomes higher and tends to infinity in the limit. This is due to the infinite velocity at the core of the potential vortex doublet in the flow model.

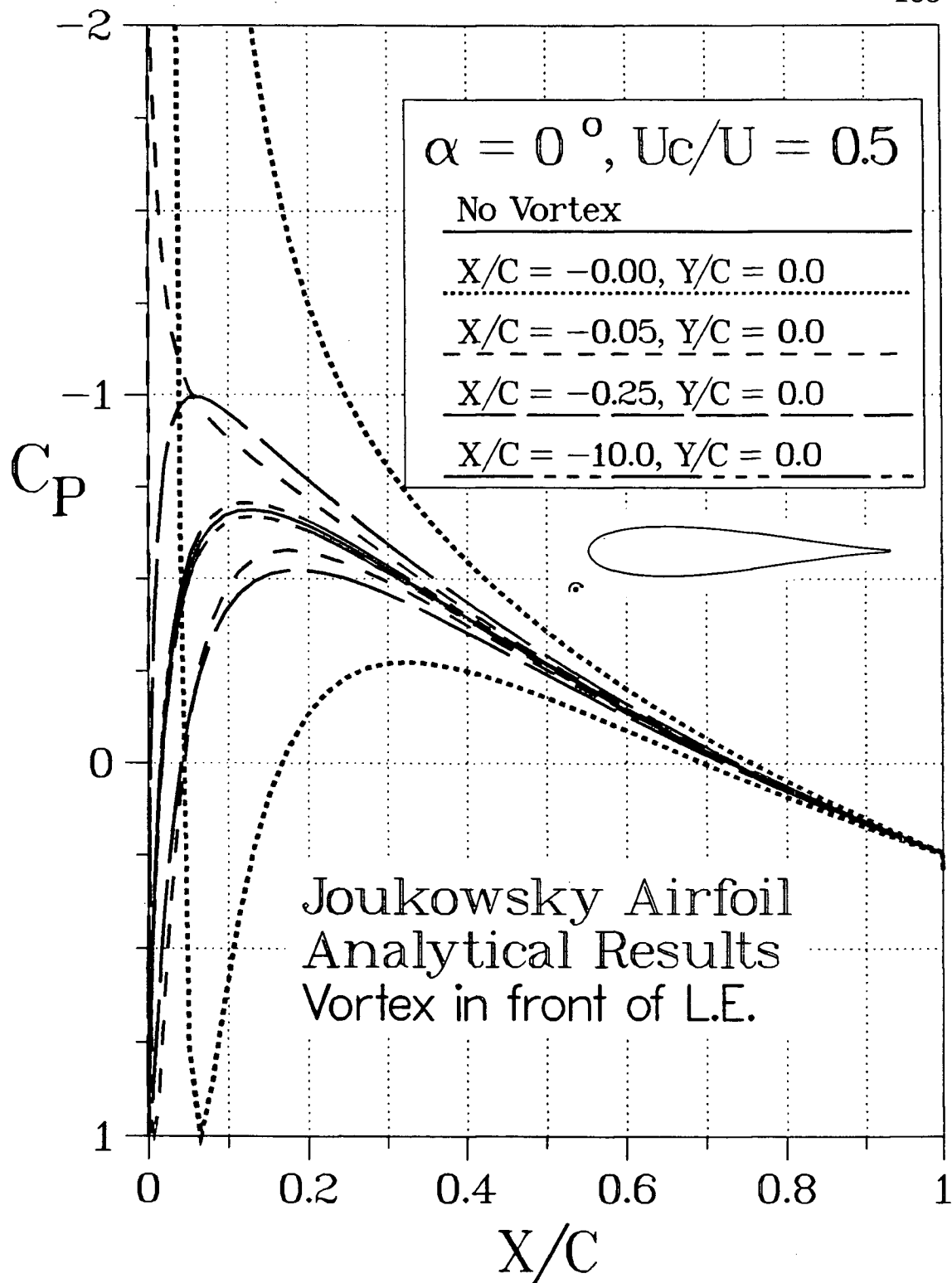


Figure 4-3 Analytically obtained pressure plots around a symmetrical Joukowski airfoil in presence of an external vortex, located on the x-axis.

The effect of locating the vortex off the x -axis is shown in Figure 4-4. Through the use of a leading edge flap, a vortex can be trapped below the nose leading to an increase in the lift of the airfoil. The vortex is first considered on the x -axis in front of the leading edge at $X/C = -0.125$. The resulting pressure distribution at an angle of attack of 4° , compared to that in the absence of the vortex, shows a sharp increase in the negative pressure peak over the leading edge as already discussed. The vortex is then located below the nose at the same distance from the leading edge. The increase in suction over the nose due to this configuration is relatively small but is accompanied by a larger increase in compression on the lower surface. The stagnation point moves a little downstream on the compression surface suggesting reorientation of the streamlines and an increase in the effective angle of attack.

The vertical offset of the vortex, located below the nose, also affects the pressure distribution as demonstrated in Figure 4-5. Although the pressure peak over the leading edge is hardly changed, the location of the stagnation point on the lower surface moves downstream as the vortex approaches the airfoil surface.

The effect of an increase in the vortex strength (equivalent to an increase in speed of rotation of the nose cylinder) is to raise the suction on the top surface and compression on the bottom surface with their effects propagating downstream, along with the position of the stagnation point (Figure 4-6).

Though severely handicapped by the potential flow assumption, the closed form conformal transformation based analysis seems to suggest, at least qualitatively, a significant increase in lift due to a rotating cylinder forming the nose of a Joukowski airfoil. The trends predicted by such a simple analysis, however, are substantiated by the experimental data.

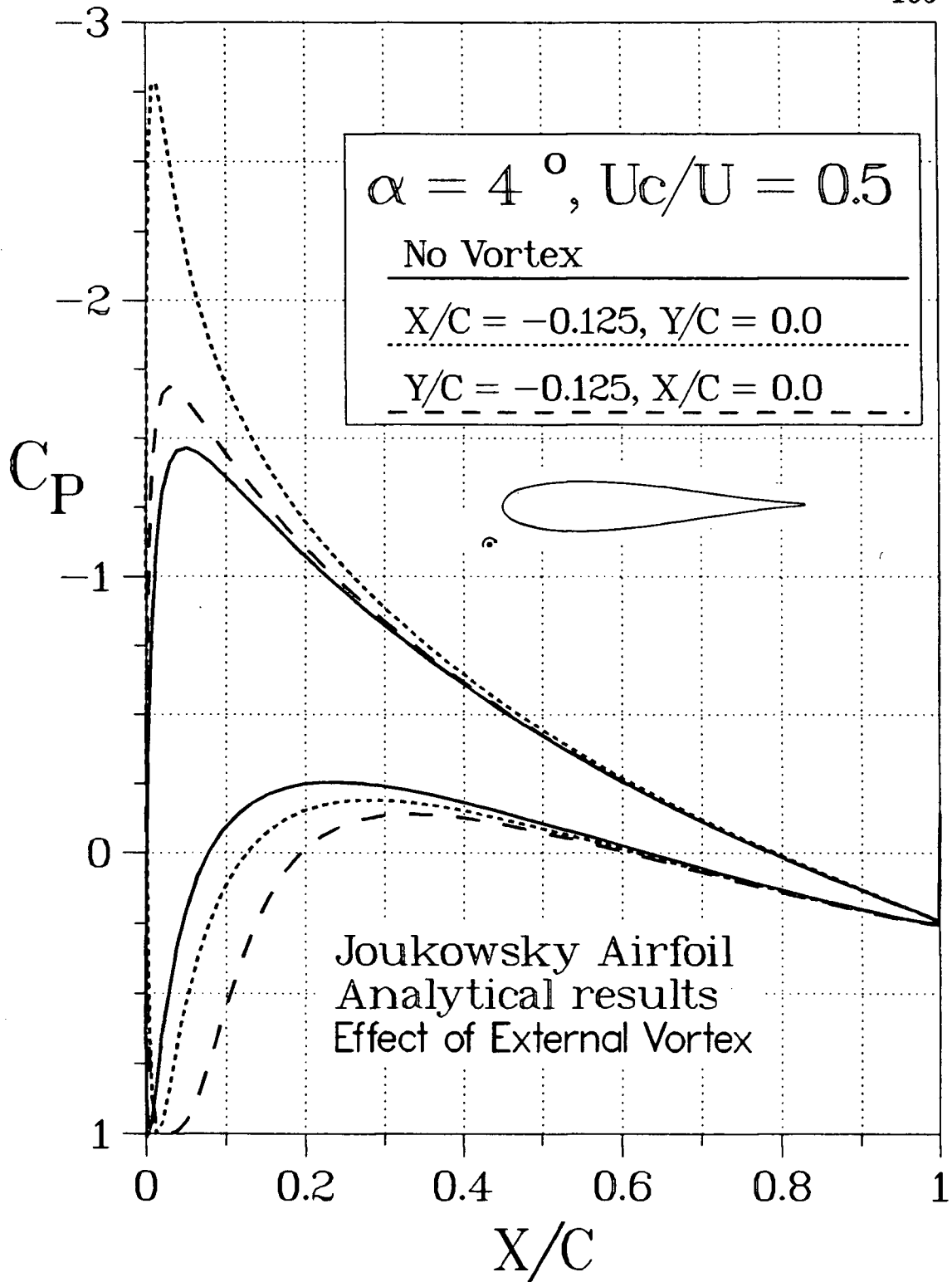


Figure 4-4 Analytically predicted pressure variation around a symmetrical Joukowski airfoil showing the effect of locating a vortex off the x-axis.

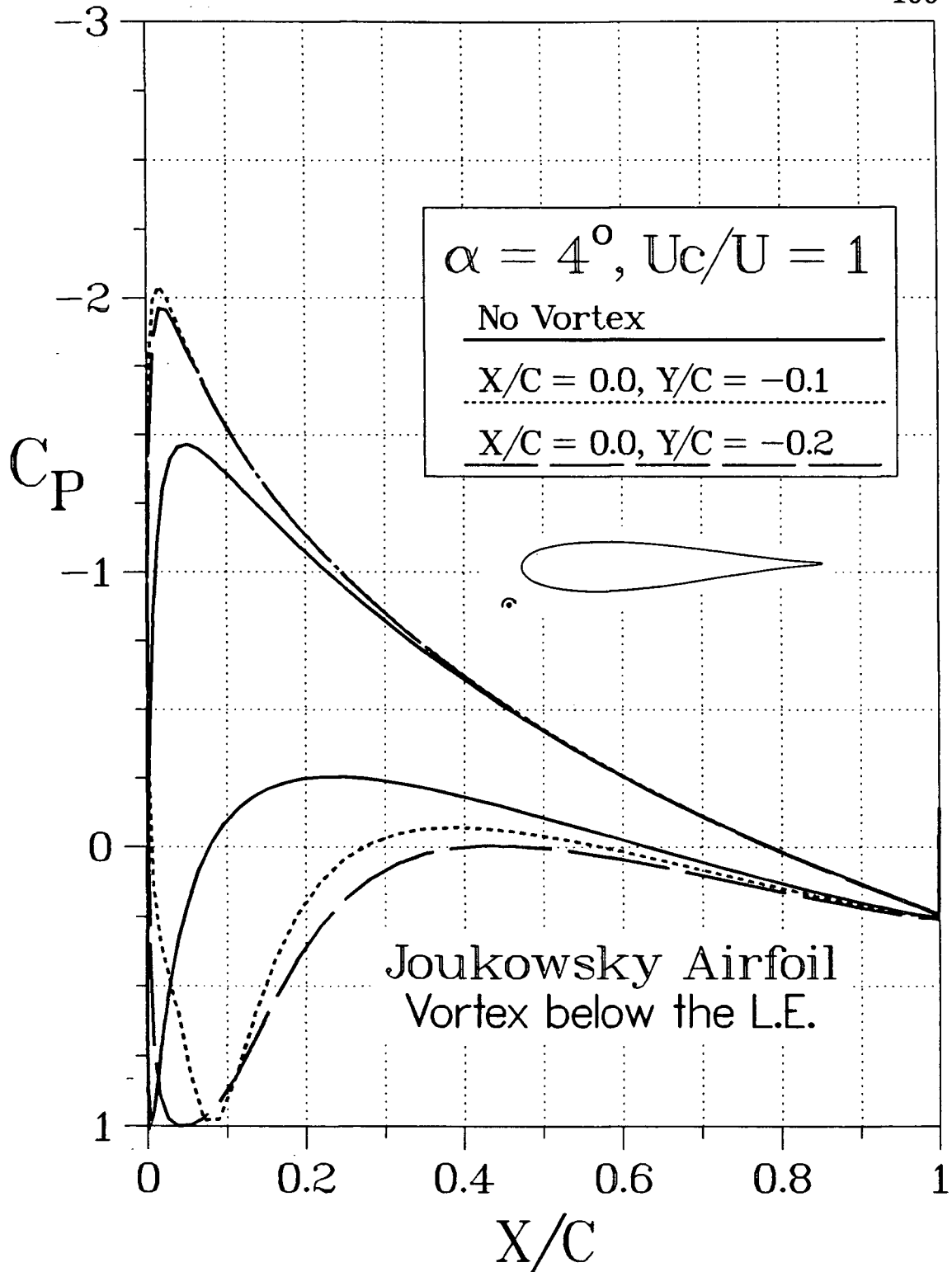


Figure 4-5 Analytical pressure distributions around a symmetrical Joukowski airfoil showing the effects of trapping a vortex below the nose at varying vertical distance from the surface.

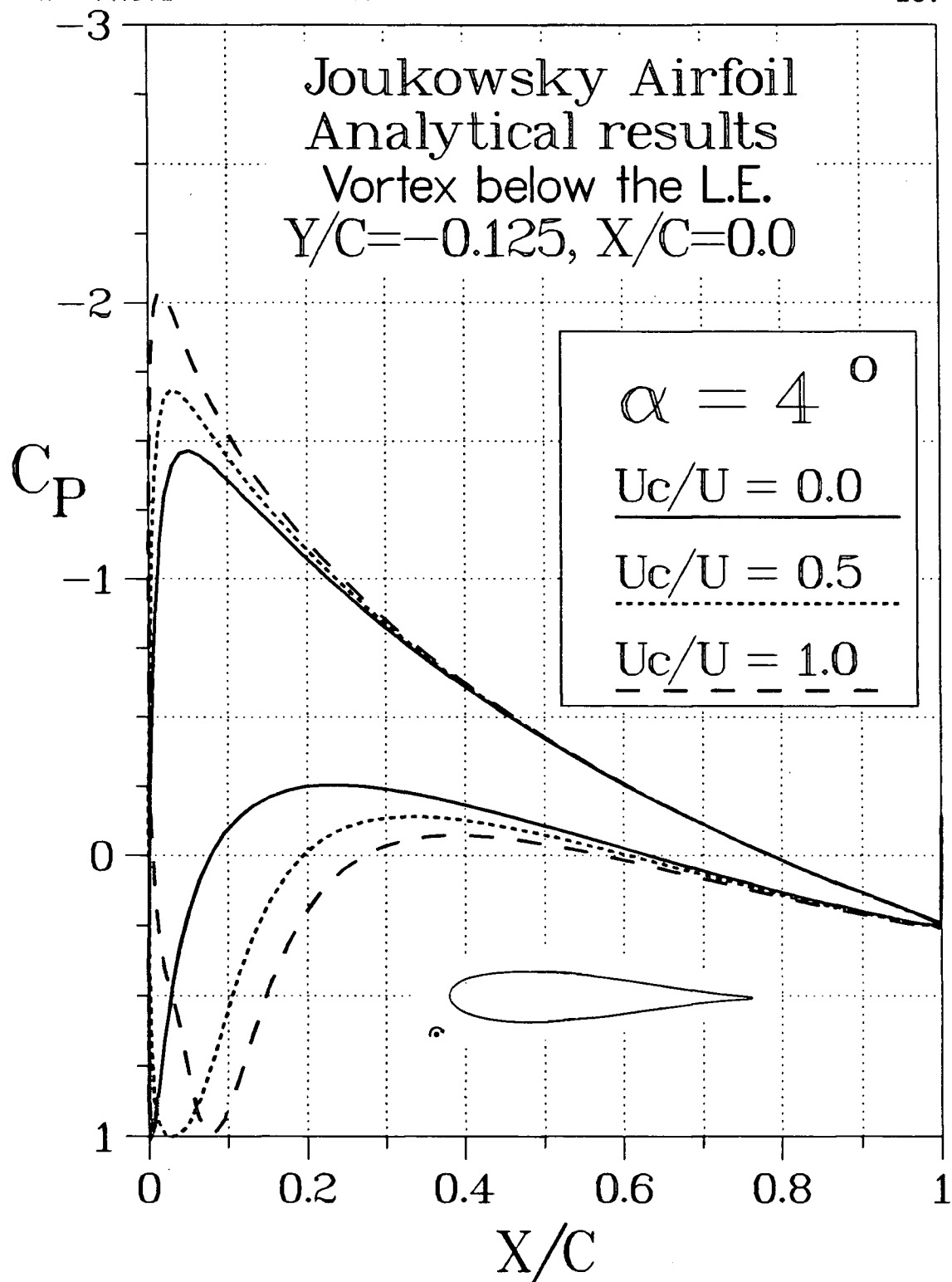


Figure 4-6 Analytically obtained pressure plots around a symmetrical Joukowsky airfoil showing the effects of trapping a vortex below the nose and increasing vortex strength.

4.2 Numerical Surface Singularity Method

In the numerical approach to the problem, a surface singularity, potential flow model involving distribution of vorticity on the airfoil surface and boundary conditions specified in terms of the stream function was used. The method, described in detail by Kennedy [32] in his Ph.D. dissertation is thought to be the simplest available. Although the viscosity effects are ignored, it provides a fairly accurate estimate of the flow around the section.

For flow over an airfoil section there can be no normal velocity at the solid surface, hence it represents a streamline of the flow. The stream function is a constant on the surface of the airfoil section. It consists of contributions from the uniform stream at an angle of attack α and distributed point vortices on the airfoil surface,

$$\Psi = Y_S \cos \alpha - X_S \sin \alpha - \frac{1}{2\pi} \int_{S'} \gamma(S') \ln r(S, S') dS' = \text{Constant} ,$$

where Ψ is the stream function for the airfoil, and an arbitrary point on the surface S is designated S' . The distances are nondimensionalized with respect to the chord length C , the velocities by U and the stream functions using the product UC . The airfoil surface is divided into N small elements. On each of these there is a control point, c_i , located at (X_i, Y_i) , where the above boundary condition is required to be satisfied. Each element j has a vorticity of density $\gamma(S_j)$ distributed on its surface (Figure 4-7). The integral over the whole surface is then replaced by a summation of N integrals over the N surface elements,

$$\Psi + \sum_{j=1}^N \frac{1}{2\pi} \int_{S_j} \gamma(S_j) \ln r(c_i, S_j) dS_j = Y_i \cos \alpha - X_i \sin \alpha .$$

At this point it is necessary to make some assumptions about the section geometry, the location of the control points, and the form of $\gamma(S_j)$ over each element j . The

simplest approximation is to assume that the elements are straight lines, with the control point at the midpoint of the element, and that $\gamma(S_j)$ is a constant (γ_j) over each element. This yields the system of equations,

$$\Psi + \sum_{j=1}^N K_{ij} \gamma_j = Y_i \cos \alpha - X_i \sin \alpha, \quad i = 1, \dots, N,$$

where K_{ij} is a coefficient representing the influence of element j on control point i , and is purely a function of the coordinates of the surface elements and the angle of attack. It can be determined by evaluating the integral in the stream function equation (using the notation of Figure 4-7) as

$$K_{ij} = \frac{1}{4\pi} \left[(b + \Delta) \ln(r_1^2) - (b - \Delta) \ln(r_2^2) + 2a \tan^{-1} \left(\frac{2a\Delta}{a^2 + b^2 - \Delta^2} \right) - 4\Delta \right].$$

In cases where $a^2 + b^2 - \Delta^2 \leq 0$, the relation

$$\tan^{-1} \left(\frac{2a\Delta}{a^2 + b^2 - \Delta^2} \right) = \tan^{-1} \left(\frac{b + \Delta}{a} \right) - \tan^{-1} \left(\frac{b - \Delta}{a} \right)$$

helps determine which value of the *arctangent* should be used.

To satisfy the condition that the flow leaves the trailing edge smoothly (the Kutta condition), an extra control point is introduced a short distance downstream of the trailing edge. This provides an additional equation

$$\Psi + \sum_{j=1}^N K_{N+1,j} \gamma_j = Y_{N+1} \cos \alpha - X_{N+1} \sin \alpha,$$

thus reducing the problem of potential flow over an airfoil section to the solution of $N + 1$ simultaneous equations. The velocity in the interior of the closed airfoil section is zero and discontinuity in the tangential velocity across a vortex sheet is equal to the density of the vortex sheet. Thus by solving the above equations, one directly obtains the surface velocities, γ_j , on the airfoil elements.

The procedure can easily account for one or more vortices at any location in

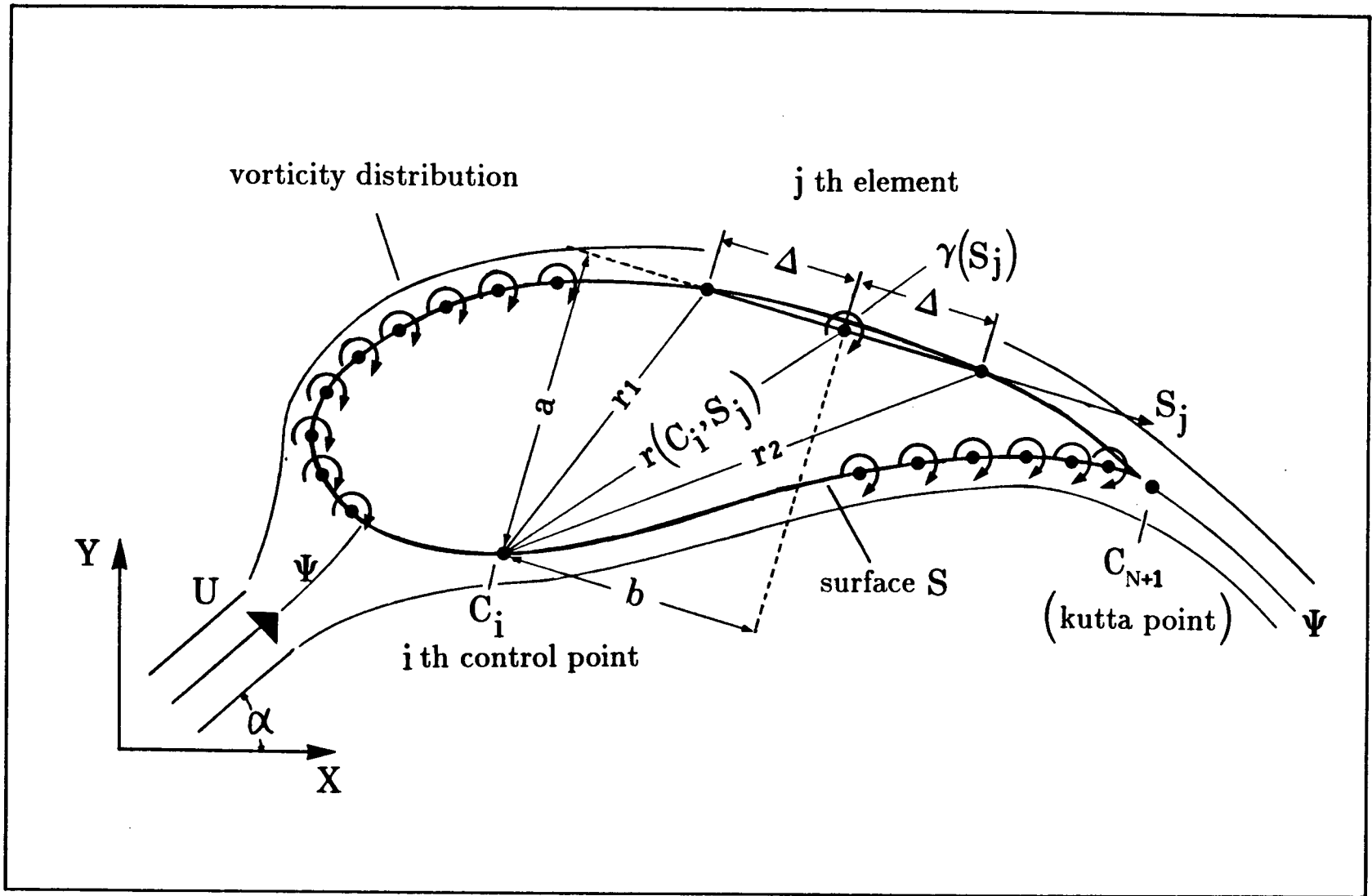


Figure 4-7 Singularity representation of the airfoil and the notation for the calculation of influence coefficients.

the field. The stream function for a point vortex of known strength, k (positive in the clockwise sense), located at (X_o, Y_o) is simply added to the right hand side of the above equation,

$$\Psi + \sum_{j=1}^N K_{ij} \gamma_j = Y_i \cos \alpha - X_i \sin \alpha + \frac{k}{2\pi} \ln r_i, \quad i = 1, \dots, N,$$

where

$$r_i = \sqrt{(X_i - X_o)^2 + (Y_i - Y_o)^2}.$$

This method is extended to permit the analysis of an airfoil with finite thickness trailing edge. The vortex sheet defining the airfoil surface is open at the trailing edge in this case. A source singularity of unknown strength is now required within the contour of the body to model the flow in the wake which theoretically extends to infinity. Including the stream function for the source in the previous equation gives

$$\Psi + \sum_{j=1}^N K_{ij} \gamma_j + \frac{m}{2\pi} \tan^{-1} \left(\frac{Y_i - Y_{source}}{X_i - X_{source}} \right) = Y_i \cos \alpha - X_i \sin \alpha + \frac{k}{2\pi} \ln r_i, \quad i = 1, \dots, N,$$

where m is the unknown source strength. The use of a second Kutta condition similar to the first one is now required to generate the extra equation needed to solve for the strength of the source. Since the velocity in the interior of the wing is not zero in this case, the local vortex sheet densities, γ_j , are no longer the surface velocities at the airfoil components. The tangential velocities are governed by the combined contributions from the surface vorticity distribution, the uniform flow, the point source inside the contour, and the external vortex, and can easily be calculated [33].

The above system of equations can be written in matrix form as

$$\begin{pmatrix} K_{ij} \end{pmatrix} \begin{pmatrix} \gamma_j \end{pmatrix} + \begin{pmatrix} S_i \end{pmatrix} m + \begin{pmatrix} 1 \\ \vdots \\ 1 \end{pmatrix} \Psi = \begin{pmatrix} R_i \end{pmatrix}, \quad i, j = 1, \dots, N,$$

where R_i denotes the right-hand side of the stream function equation:

$$R_i = Y_i \cos \alpha - X_i \sin \alpha + \frac{k}{2\pi} \ln r_i ;$$

and

$$S_i = \frac{1}{2\pi} \tan^{-1} \left(\frac{Y_i - Y_{source}}{X_i - X_{source}} \right) .$$

With the inclusion of the Kutta conditions, the system becomes

$$\begin{pmatrix} K_{1,1} & \dots & K_{1,N} & 1 & S_1 \\ \vdots & \ddots & \vdots & \vdots & \vdots \\ K_{N,1} & \dots & K_{N,N} & 1 & S_N \\ K_{N+1,1} & \dots & K_{N+1,N} & 1 & S_{N+1} \\ K_{N+2,1} & \dots & K_{N+2,N} & 1 & S_{N+2} \end{pmatrix} \begin{pmatrix} \gamma_1 \\ \vdots \\ \gamma_N \\ \Psi \\ m \end{pmatrix} = \begin{pmatrix} R_1 \\ \vdots \\ R_N \\ R_{N+1} \\ R_{N+2} \end{pmatrix} .$$

Extension of this method to the case of multicomponent configurations gives rise to a different stream function for each component thus requiring corresponding Kutta conditions. It can also be applied to a configuration of an airfoil section between two walls but the stream functions for the wall components have to be treated as known quantities since the flow rate between the walls is given. These known stream functions can be moved to the right hand side of the equations and the unnecessary Kutta conditions removed. Also, the angle of attack modifications to the airfoil surface must be applied before the coefficient matrices can be calculated, i.e., the airfoil must be rotated to the appropriate angle of incidence within the

tunnel walls. In this case the system of equations can be written as:

$$\left[\begin{array}{c} \left(\begin{array}{c} K11 \\ \text{kutta 1} \\ \text{kutta 2} \end{array} \right) \left(\begin{array}{c} 1 \\ \vdots \\ 1 \end{array} \right) \left(\begin{array}{c} S1 \\ S1_{N+1} \\ S1_{N+2} \end{array} \right) \left(\begin{array}{c} K12 \\ \text{kutta 1} \\ \text{kutta 2} \end{array} \right) \left(\begin{array}{c} K13 \\ \text{kutta 1} \\ \text{kutta 2} \end{array} \right) \\ \left(\begin{array}{c} K21 \\ \vdots \\ 0 \end{array} \right) \left(\begin{array}{c} 0 \\ \vdots \\ 0 \end{array} \right) \left(\begin{array}{c} S2 \\ S2 \\ S2 \end{array} \right) \left(\begin{array}{c} K22 \\ \text{kutta 1} \\ \text{kutta 2} \end{array} \right) \left(\begin{array}{c} K23 \\ \text{kutta 1} \\ \text{kutta 2} \end{array} \right) \\ \left(\begin{array}{c} K31 \\ \vdots \\ 0 \end{array} \right) \left(\begin{array}{c} 0 \\ \vdots \\ 0 \end{array} \right) \left(\begin{array}{c} S3 \\ S3 \\ S3 \end{array} \right) \left(\begin{array}{c} K32 \\ \text{kutta 1} \\ \text{kutta 2} \end{array} \right) \left(\begin{array}{c} K33 \\ \text{kutta 1} \\ \text{kutta 2} \end{array} \right) \end{array} \right] \left[\begin{array}{c} \left(\begin{array}{c} \gamma1 \\ \Psi1 \\ m \end{array} \right) \\ \left(\begin{array}{c} \gamma2 \\ \vdots \\ \vdots \end{array} \right) \\ \left(\begin{array}{c} \gamma3 \\ \vdots \\ \vdots \end{array} \right) \end{array} \right] = \left[\begin{array}{c} \left(\begin{array}{c} R1 \\ R1_{N+1} \\ R1_{N+2} \end{array} \right) \\ \left(\begin{array}{c} R2 - \Psi2 \\ \vdots \\ \vdots \end{array} \right) \\ \left(\begin{array}{c} R3 - \Psi3 \\ \vdots \\ \vdots \end{array} \right) \end{array} \right].$$

Here ($K11$) is the coefficient matrix calculated for the airfoil section, ($K22$) and ($K33$) are the coefficient matrices calculated for the wall components, and ($K12$), ($K13$), etc., represent the relations between the corresponding components.

The system of equations is then solved by Gaussian elimination procedure.

4.2.1 Flow around a Joukowski airfoil in presence of vortices

The numerical surface singularity approach was applied to the same symmetrical Joukowski airfoil as used in the case of the analytical conformal transformation procedure, thus facilitating comparison of results. The leading edge rotating cylinder was simulated with an internal vortex located at the center of the leading edge. Figure 4-8 presents typical pressure distribution plots at $\alpha = 4^\circ$ showing the effect of the leading edge vortex strength corresponding to an increase in the cylinder velocity. The results suggest a significant rise in suction over the leading edge accompanied by a slight increase in compression on the lower surface due to the stagnation point moving downstream.

Numerical analysis of a two-component Joukowski airfoil, with the rotating cylinder also modelled by the surface singularity approach, resulted in the informa-

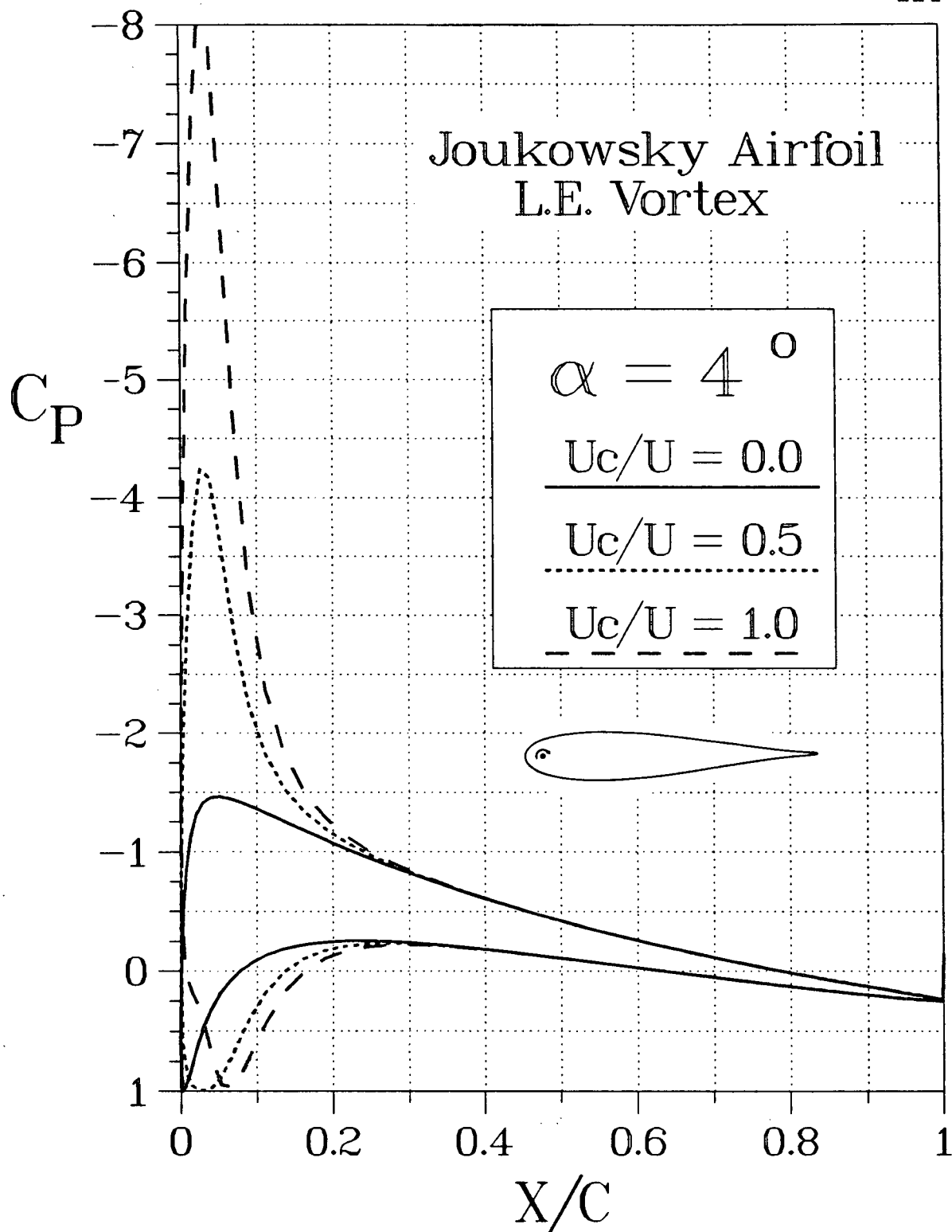


Figure 4-8 Pressure distributions around a symmetrical Joukowsky airfoil using the surface singularity method to simulate the leading-edge rotating cylinder with an internal vortex.

tion presented in Figure 4-9. The pressure plots show essentially the same trend as the leading-edge vortex case. However, the peak suction value is slightly lower and confined to the area just over the cylinder.

Modelling the effect of the rotating cylinder with an internal nose vortex predicts a qualitatively correct increase in the negative pressure peak over the leading edge (refer to the experimental data obtained with the Joukowsky airfoil model II). The exaggerated magnitude of this rise in pressure is, of course, expected due to the potential flow nature of the model. The model also correctly predicts a change in the location of the stagnation point on the lower surface due to cylinder rotation.

A typical comparison between numerically obtained results of the leading-edge-cylinder using an internal nose vortex and the corresponding analytical result of the vortex doublet are presented in Figure 4-10. It is interesting to note, though not surprising, that the correlation between the analytical and numerical predictions (both suffering from the potential flow assumption) is rather good. Although this does not help in correctly predicting the flow field, it is indeed reassuring that reliable trends can be obtained.

4.2.2 Counter-rotating vortex-pair model

At higher angles of attack ($\alpha > 16^\circ$), the large unfavorable pressure gradient behind the leading edge causes the immediate separation of the boundary layer from the upper surface. If the effect of the leading-edge-cylinder is to control the boundary layer, i.e., to suppress or at least delay separation, the corresponding flow model should reflect this as a favorable change in the pressure gradient.

To that end, a model of counter-rotating vortex-pair, located below the leading edge, is considered. With vortices of equal strength, in magnitude, no additional circulation is introduced in the flow. However, the location of the leading edge suction peak (and the associated pressure gradient) is directly affected by the relative position of the vortices, with respect to each other and the airfoil, as well

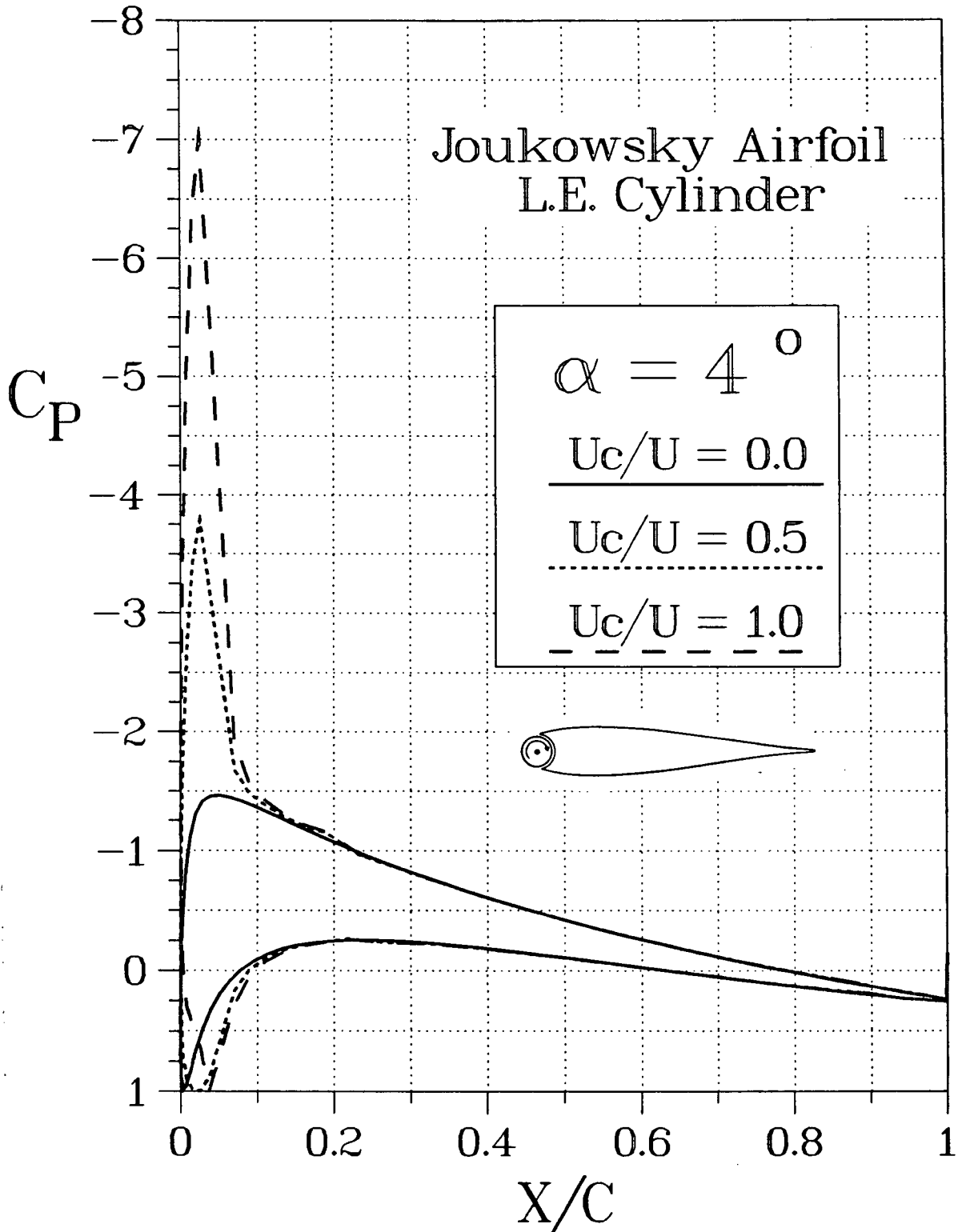


Figure 4-9 Numerically obtained pressure distributions around a Joukowsky airfoil with a rotating cylinder forming its nose.

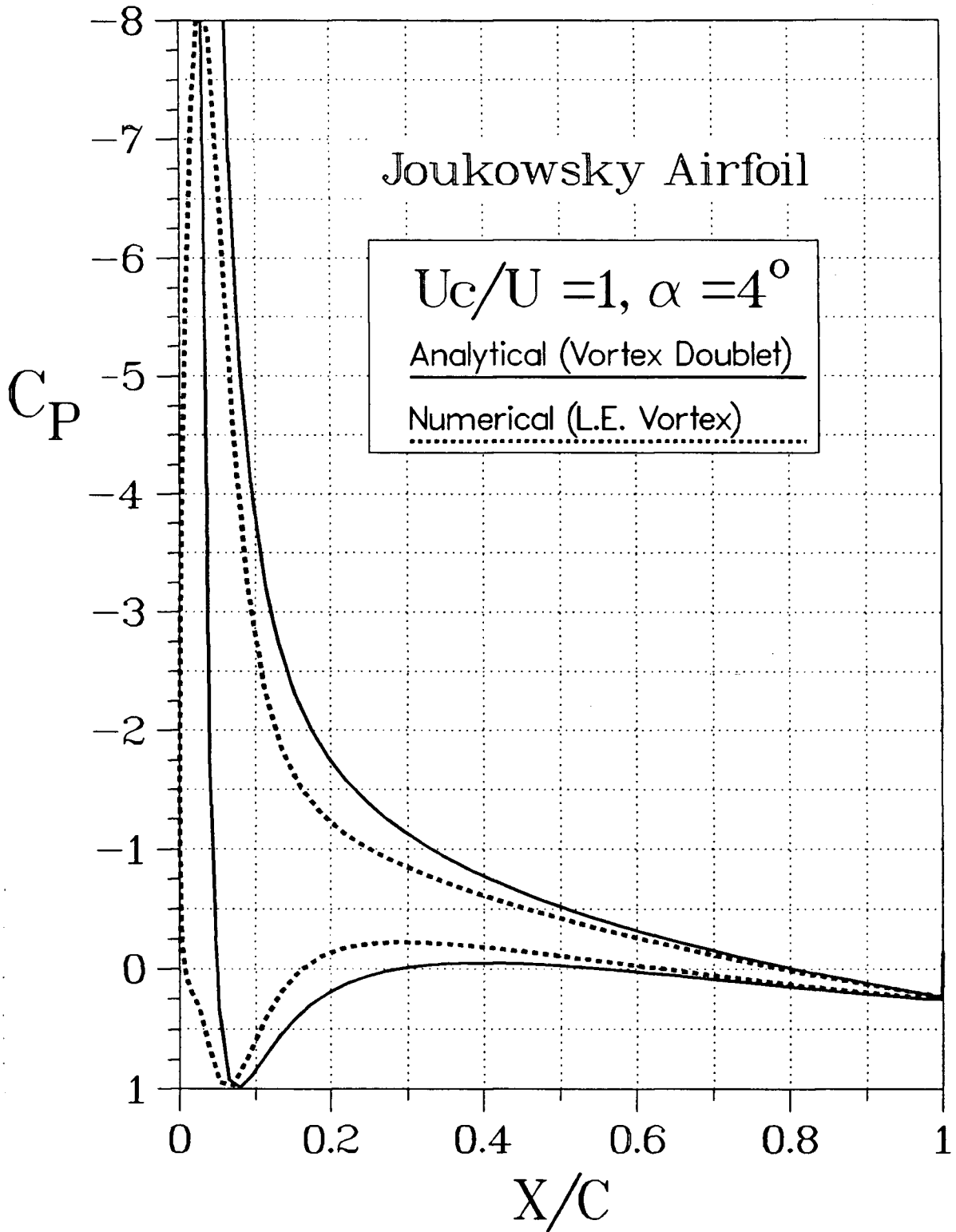


Figure 4-10 A comparison between the analytical and numerical (potential flow) methods used in modelling the leading-edge cylinder.

as their strength.

Figure 4-11 examines the effect of the vertical position of the vortices below the leading edge. The downstream location of the vortices is measured from the leading edge with the first vortex located below the center of the leading-edge-cylinder. The second vortex is placed at the quarter-chord position, an average position based on a study of the stagnation point location as affected by the circulation.

As the vortex pair moves closer to the airfoil surface, the negative pressure peak over the leading edge is reduced (Figure 4-11a). However, the suction over the rest of the upper surface increases. The overall effect is, therefore, a decrease in the adverse pressure gradient over the suction surface behind the nose. The individual contribution of the vortices can be clearly seen in Figure 4-11 (b) and (c). The front vortex, or the vortex right below the leading edge, is responsible for decreasing the magnitude of the pressure peak at the leading edge while the rear vortex increases the suction behind the leading edge keeping the overall circulation of the airfoil the same.

Figure 4-12 shows the effect of changing the relative streamwise position of the two vortices. With the front vortex located directly below the center of the leading edge cylinder ($X/C = 0.05$), several positions of the rear vortex corresponding to increasing distance between the cores of the two vortices, are considered. Obviously, when the vortices are at the same location, their effect cancel and the pressure distribution remains unchanged. As the vortices are moved apart, however, the interference between the two decreases and their individual effects reappear.

Effect of the strength of the vortices, corresponding to increasing the cylinder speed, is considered in Figure 4-13. The pressure plots with the counter-rotating vortices of equal strengths are presented in Figure 4-13(a). In absence of the vortices, a large adverse pressure gradient is present behind the leading edge at, in this

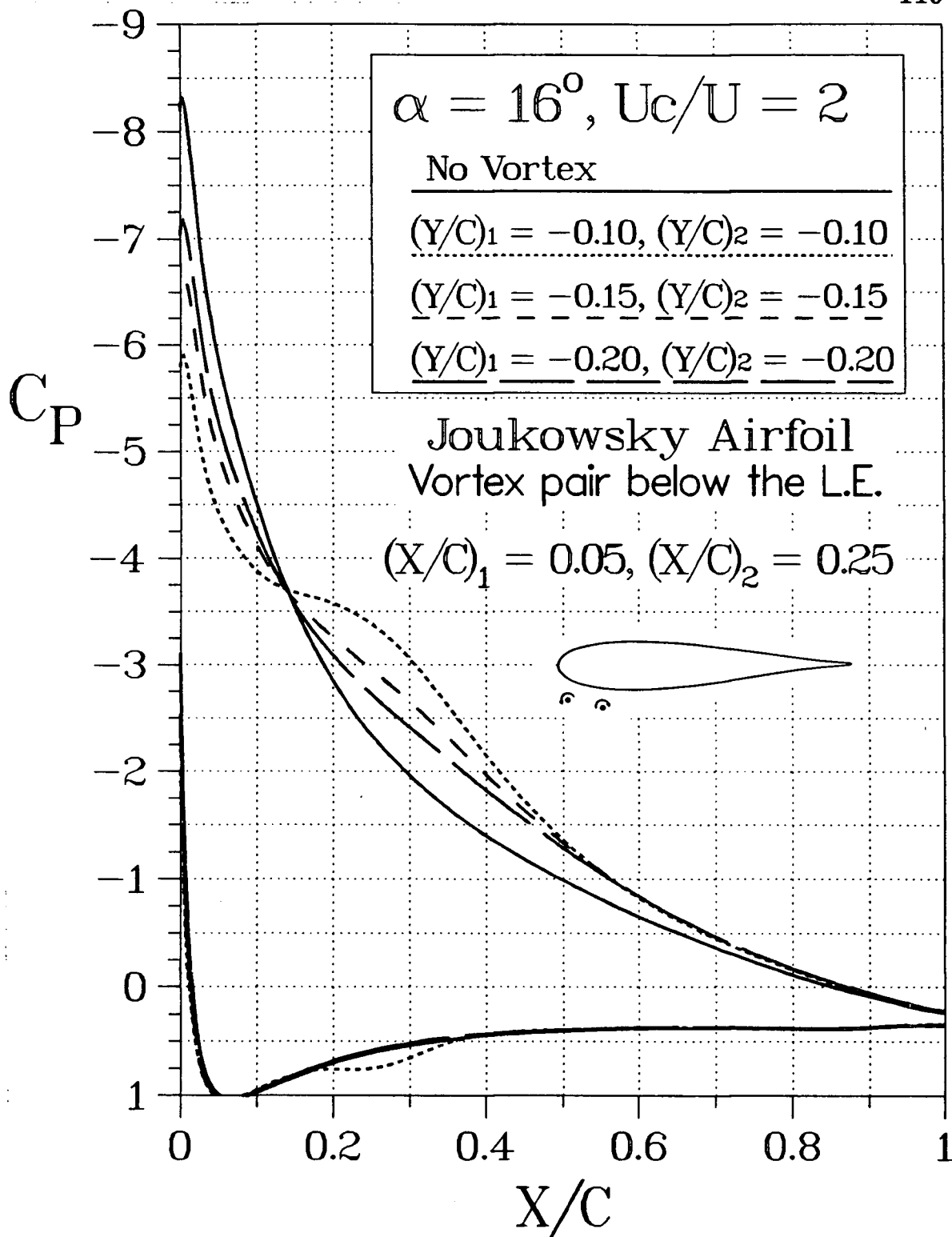


Figure 4-11 Effect of a vortex pair, located below the leading edge, on the pressure distribution of a Joukowski airfoil: (a) effect of the location of the pair below the nose;

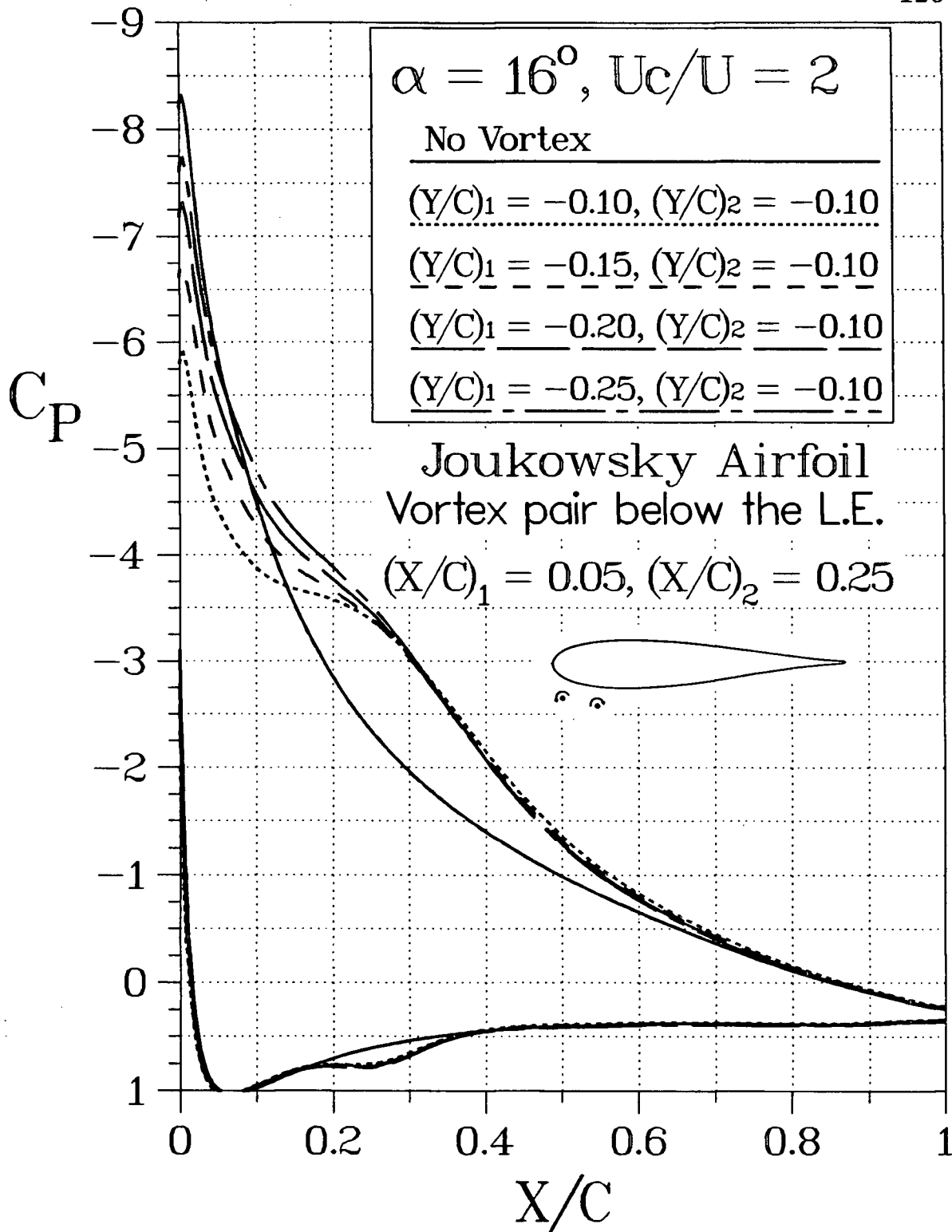


Figure 4-11 Effect of a vortex pair, located below the leading edge, on the pressure distribution of a Joukowski airfoil: (b) individual effect of the front vortex;

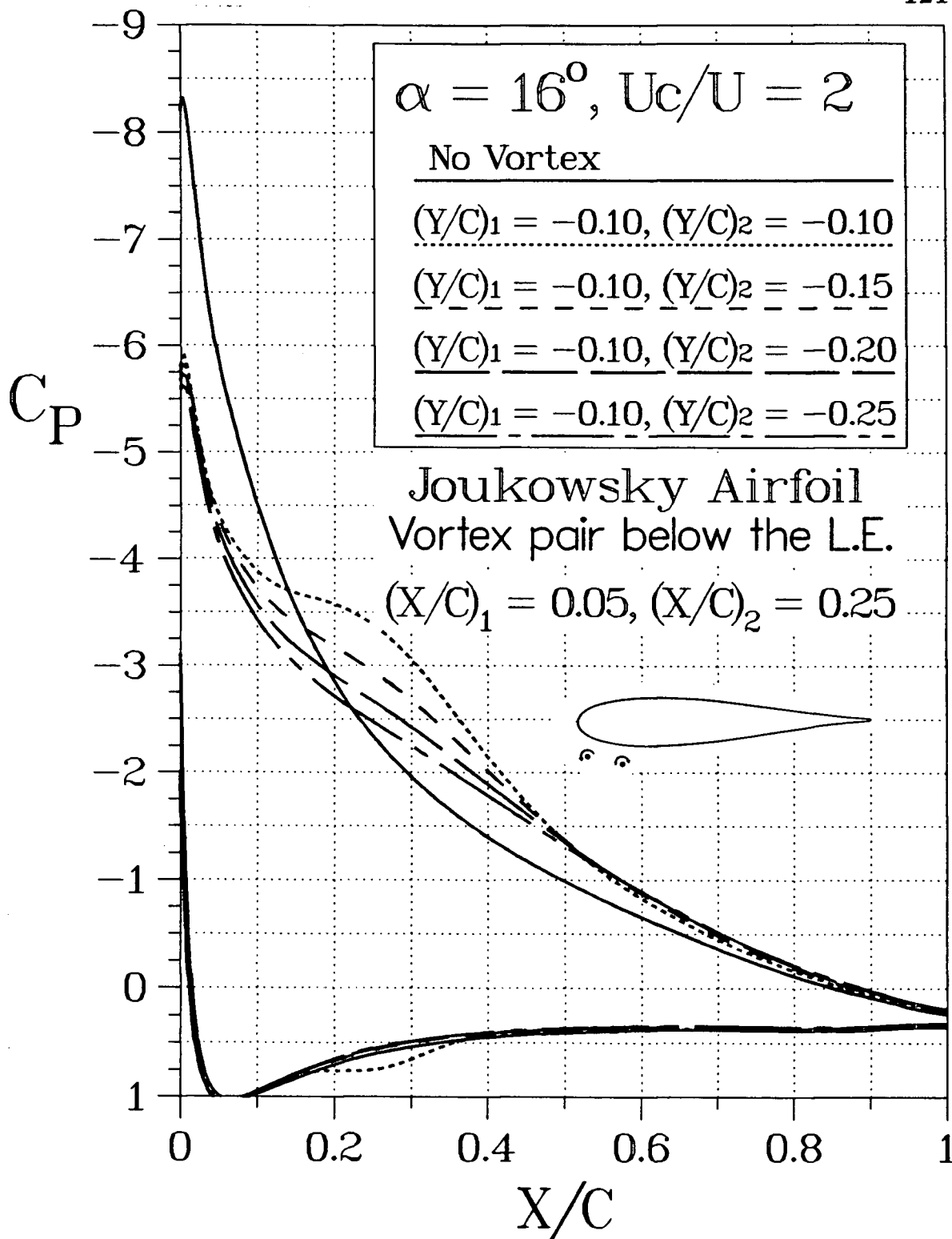


Figure 4-11 Effect of a vortex pair, located below the leading edge, on the pressure distribution of a Joukowski airfoil: (c) individual effect of the rear vortex.

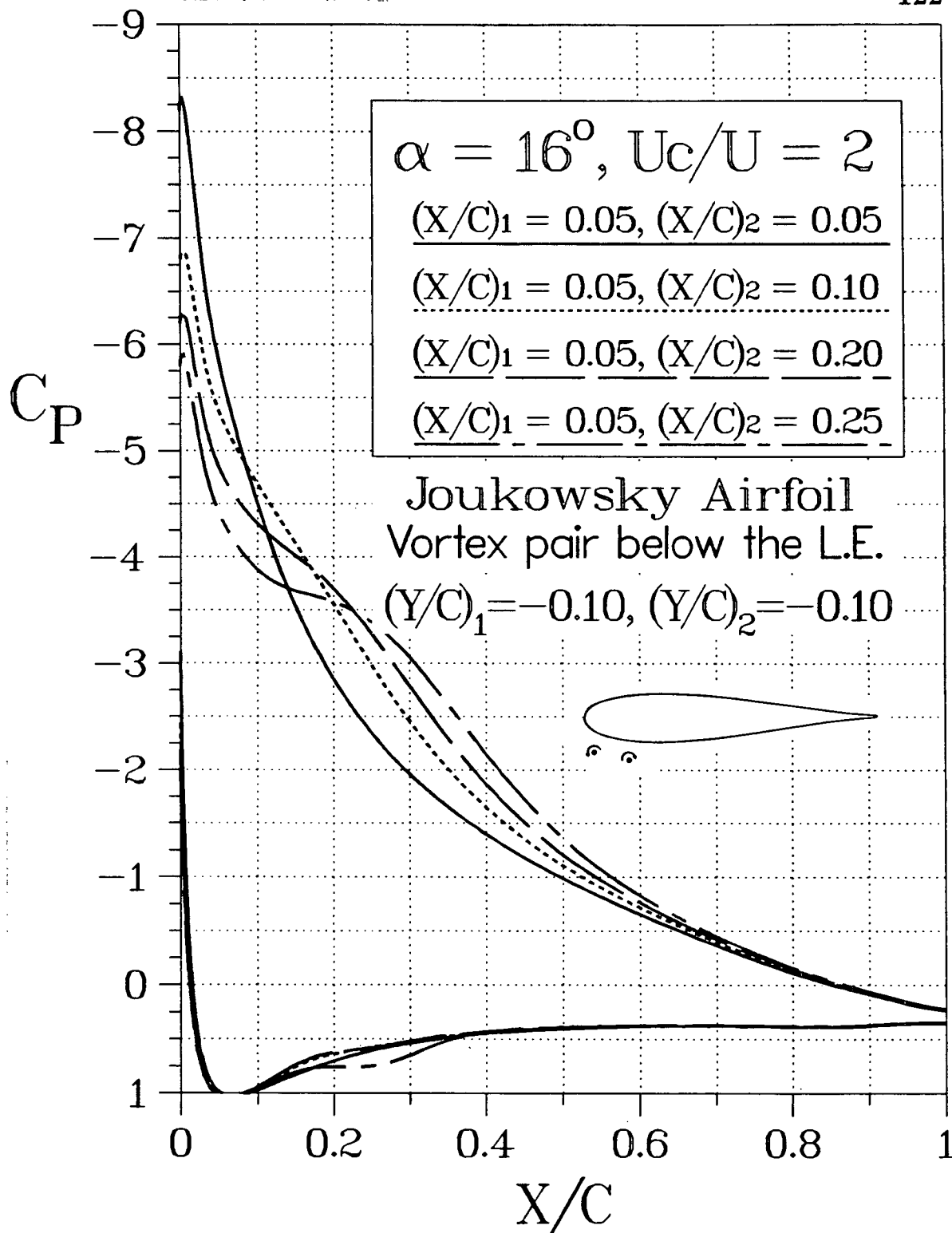


Figure 4-12 Effect of the relative streamwise position of the vortices on the pressure distribution around a Joukowski airfoil.

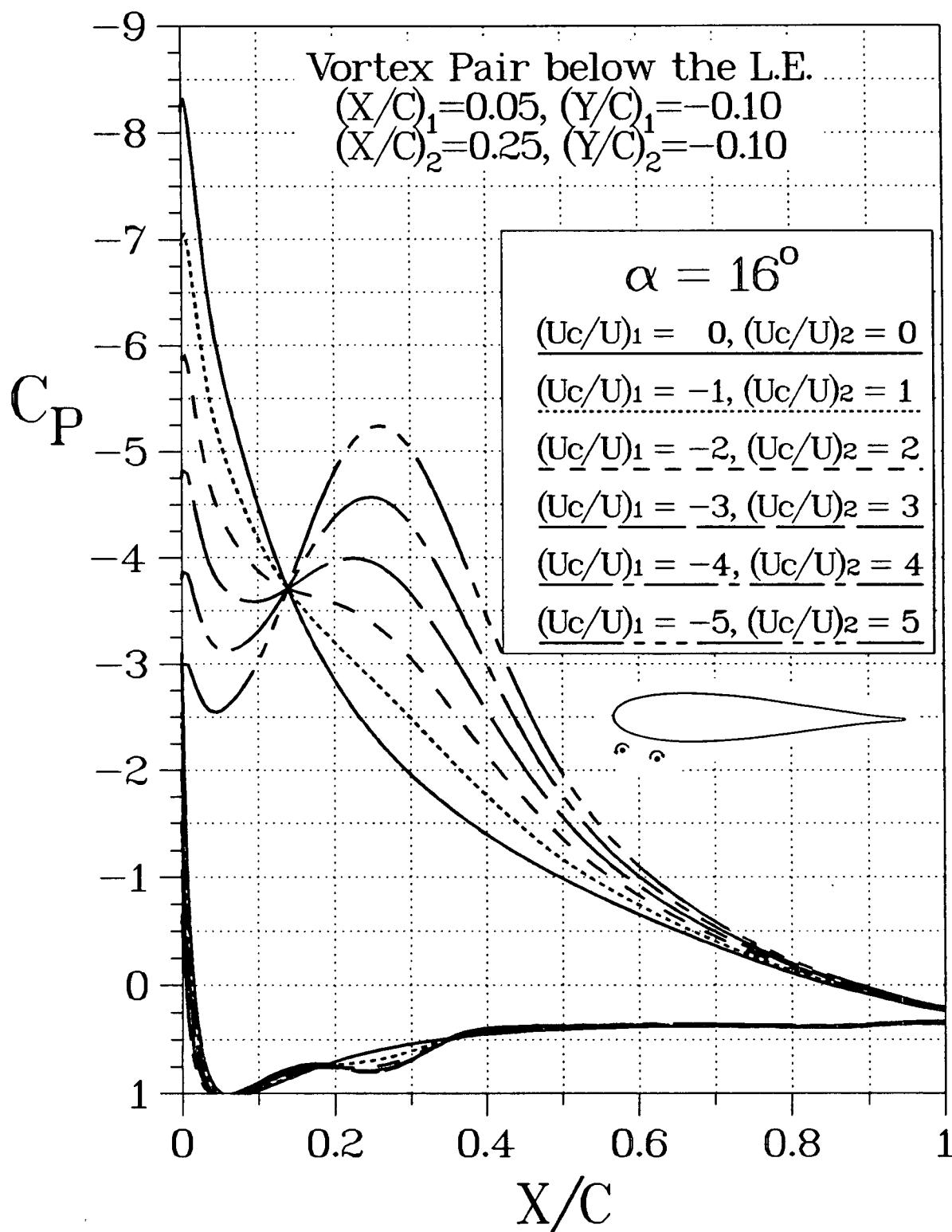


Figure 4-13 Effect of increasing the strength of the vortex pair, located below the leading edge, on the pressure distribution of the Joukowski airfoil:
 (a) vortices with the same strength;

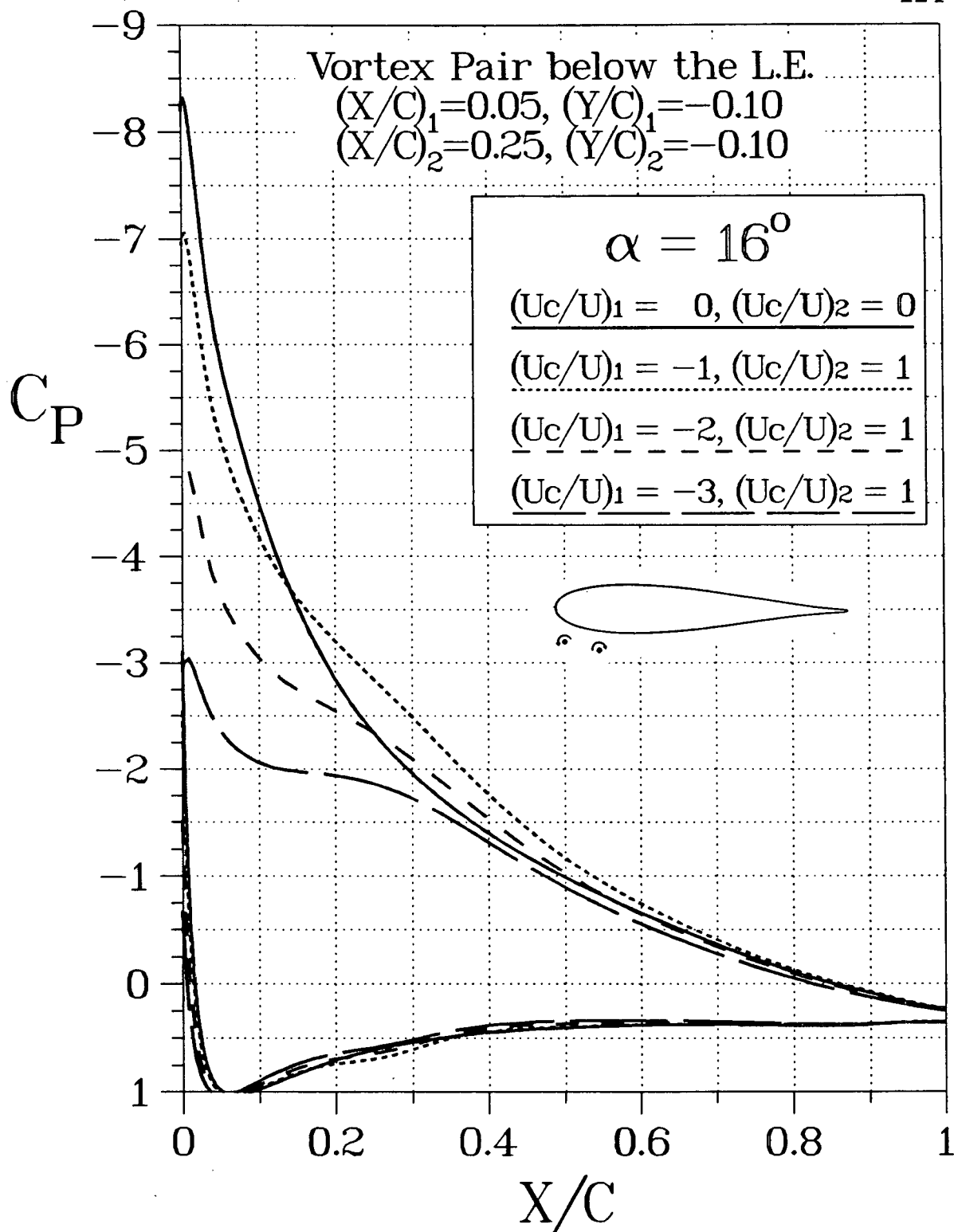


Figure 4-13 Effect of increasing the strength of the vortex pair, located below the leading edge, on the pressure distribution of the Joukowski airfoil: (b) front vortex of higher strength;

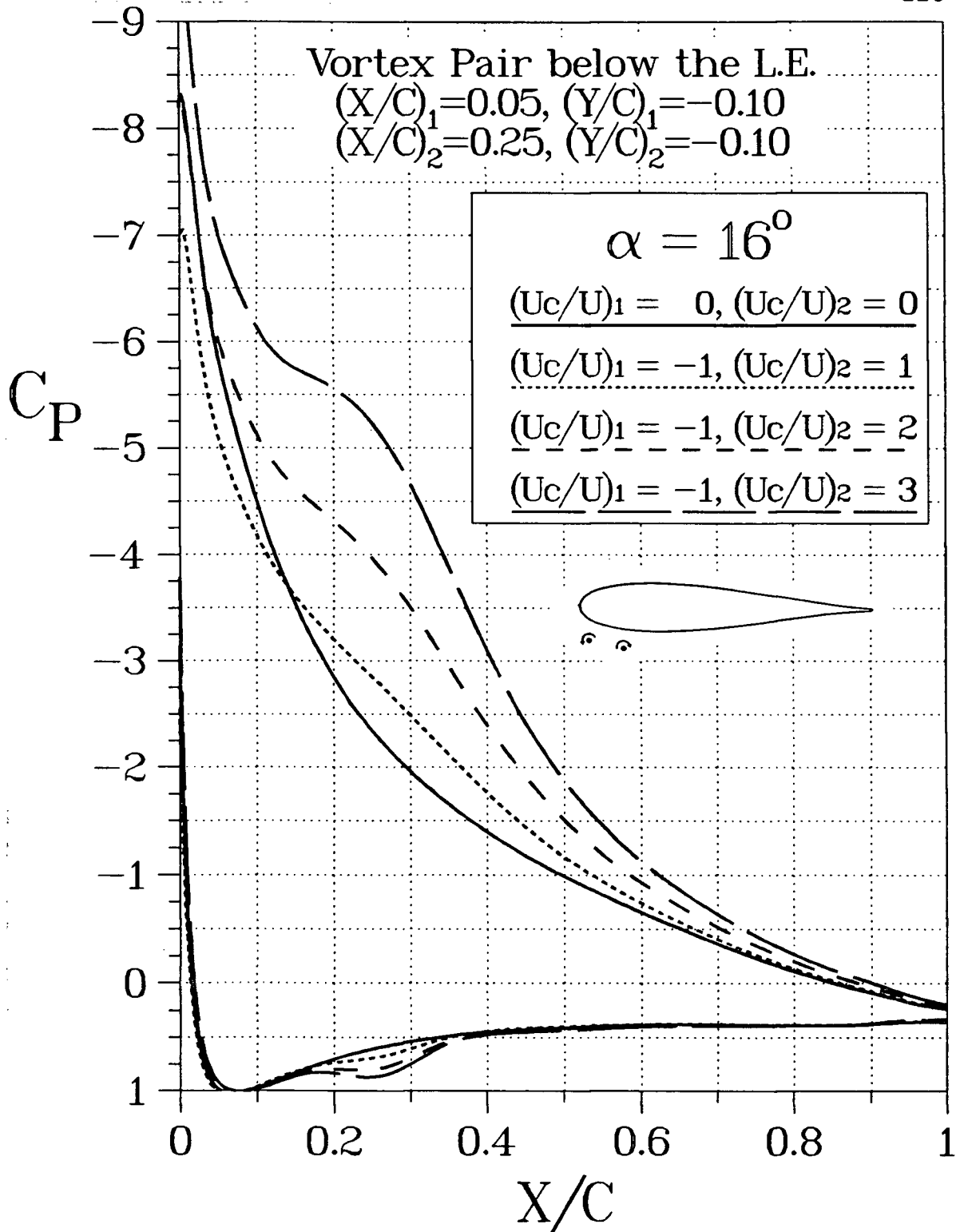


Figure 4-13 Effect of increasing the strength of the vortex pair, located below the leading edge, on the pressure distribution of the Joukowski airfoil: (c) rear vortex of higher strength.

case, $\alpha = 16^\circ$. Increasing the strength of the vortex pair decreases the negative pressure peak at the leading edge, at the same time increasing the suction over the rest of the upper surface. Large values of U_c/U , therefore, greatly decrease the unfavorable pressure gradient and beyond a certain point, make it favorable. The vortex below the leading edge is clearly responsible for decreasing the pressure peak over the nose as shown in Figure 4-13(b). Higher strength of this vortex tends to reduce the pressure gradient over the upper surface as well as decrease the overall circulation around the airfoil. Note, the rear vortex strength is kept constant while the circulation of the front vortex, counterclockwise in sense, is increased. Similarly the rear vortex is shown to cause an increase in suction behind the nose (Figure 4-13c). Higher strengths of this vortex increase the circulation around the airfoil. In all the cases, effect of the vortex pair on the pressure at the bottom surface is minimal.

Thus, modelling the effects of the leading-edge rotating cylinder on the flow field, rather than the cylinder itself, using a vortex pair below the nose seems rather promising. It decreases the adverse pressure gradient on the upper surface of the airfoil. This is consistent with the desired effect of a boundary layer control device in avoiding or at least delaying the separation from the upper surface.

The vortex pair model has some similarity with the flow pattern near the stagnation point, S, detached from the surface of a rotating cylinder at high circulation. Typical streamline pattern for $U_c/U = 3$ is shown in Figure 4-14. The flow pattern suggests the presence of four local circulating regions. The regions labelled (1) and (3) are closer to the cylinder and more stable. On the other hand, vortices (2) and (4) are located farther away and relatively unstable. A part of the vorticity associated with regions (2) and (4) is convected downstream with the main flow at a rate so as to maintain balance between the vorticity generation and its dissipation. Thus vortices (1) and (3) seem to play a dominant role. The counter-rotating vortex-pair model attempts to simulate their effect.

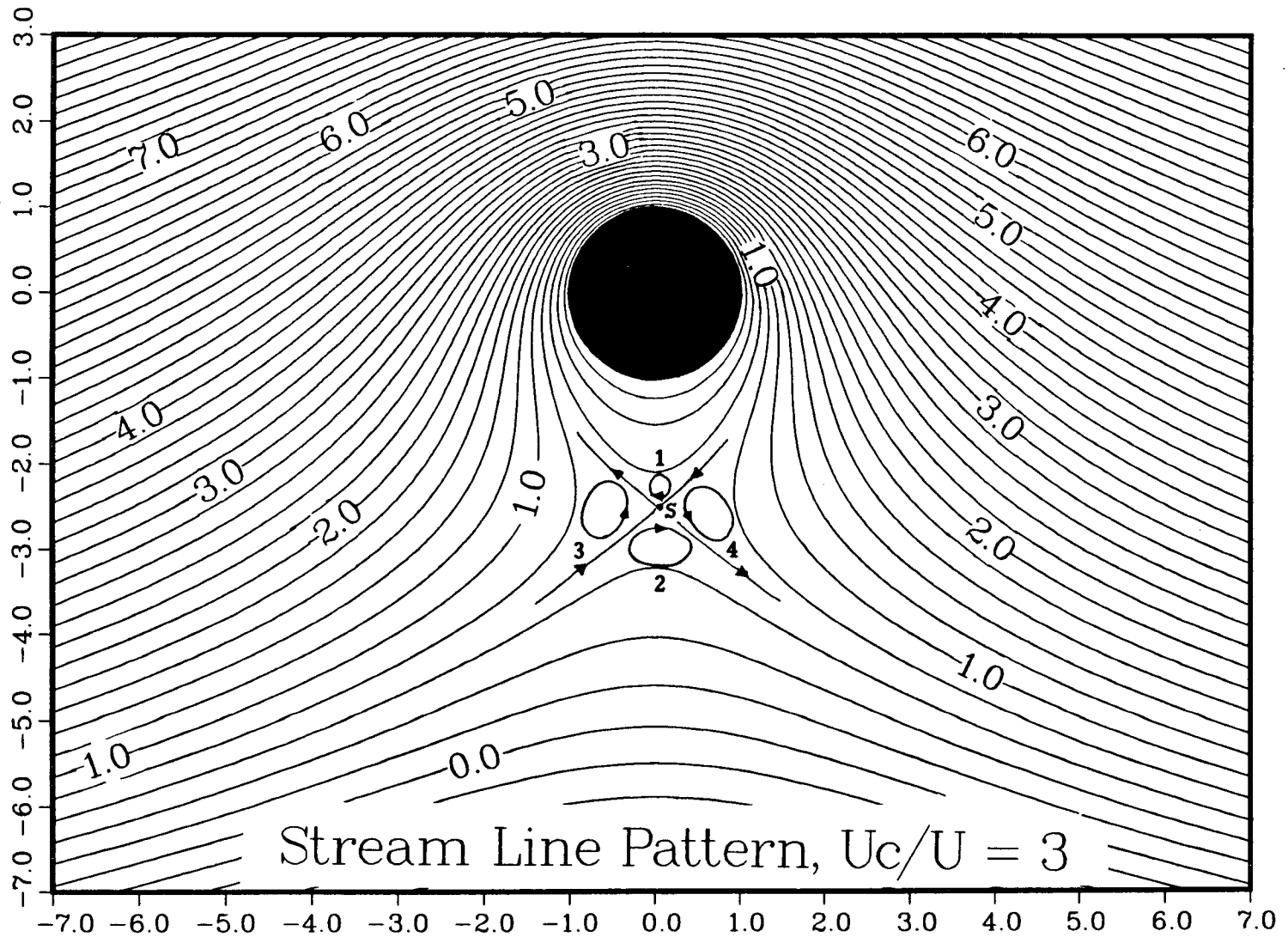


Figure 4-14 Streamline patterns for flow around a circular cylinder with circulation, corresponding to $U_c/U = 3$, showing the detached stagnation point and the associated recirculation regions.

5. VISCOUS CORRECTION SCHEME

5.1 Boundary Layer Calculations

Although the potential flow approximation proved useful qualitatively, it suffers from a major restriction. It is not satisfactory for flow conditions where viscous effects are significant.

In order to model the flow over an airfoil section with boundary-layer control, effects of viscosity must be accounted for. These are confined to the boundary layer and its separated region. One approach is to shift the surface by a distance conventionally referred to as the “displacement thickness” of the boundary layer. Thus variation of the static pressure along the surface within the shear layer depends on the shape of the surface as well as the displacement effect of the boundary layer. The flow over the displaced surface is again taken to be potential.

A practical method of solving this problem, therefore, matches the outer potential flow solution with the inner boundary layer solution. The thin shear layer approximations of the Navier–Stokes equations for steady two-dimensional, incompressible flow are used. The thin shear layer equations with negligible $\partial P/\partial y$ are:

$$\frac{\partial u}{\partial x} + \frac{\partial v}{\partial y} = 0 ;$$
$$u \frac{\partial u}{\partial x} + v \frac{\partial u}{\partial y} = -\frac{1}{\rho} \frac{dP}{dx} + (\nu + \epsilon) \frac{\partial^2 u}{\partial y^2} ;$$

along with the boundary conditions:

$$y = 0, \quad u = 0, \quad v = v_w(x) ;$$
$$y \rightarrow \infty, \quad u = U_e(x) ;$$

v_w being the transpiration velocity, zero on a solid surface. The pressure, P , is a known function of x , assumed independent of y , given by Bernoulli’s equation along

a streamline,

$$\frac{dP}{dx} = -\rho U_e \frac{dU_e}{dx} ,$$

and is obtained from the local potential flow.

The finite difference method used to solve the boundary-layer problem is due to Keller and Cebeci [34, 35], and is often referred to as the “box” method. The governing equations are written in terms of a first order system of PDEs, using the Falkner–Skan transformation,

$$\eta = \left(\frac{U_e}{\nu x} \right)^{1/2} y ,$$

and the dimensionless stream function $f(x, \eta)$ defined as

$$\Psi(x, y) = (U_e \nu x)^{1/2} f(x, \eta) .$$

By the definition of the stream function:

$$u = \frac{\partial \Psi}{\partial y} ; \quad v = -\frac{\partial \Psi}{\partial x} ;$$

the transformed momentum equation becomes

$$\left[\left(1 + \frac{\epsilon}{\nu} \right) f'' \right]' + \frac{m+1}{2} f f'' + m (1 - f'^2) = x \left(f' \frac{\partial f'}{\partial x} - f'' \frac{\partial f}{\partial x} \right) ,$$

where a prime denotes differentiation with respect to η , and the quantity m is a dimensionless pressure gradient parameter defined by

$$m = \frac{x}{U_e} \frac{dU_e}{dx} .$$

The boundary conditions in terms of the transformed variables, including mass transfer at the wall, that is $v = v_w$ when $y = 0$, become:

$$\begin{aligned} \eta = 0, \quad f' = 0, \quad f(x, 0) = f_w = -\frac{1}{(U_e \nu x)^{1/2}} \int_0^x v_w dx ; \\ \eta = \eta_\infty, \quad f' = 1 . \end{aligned}$$

Here, η_∞ corresponds to the transformed boundary layer thickness. In physical coordinates, the boundary layer thickness $\delta(x)$ usually increases in the downstream direction for both laminar and turbulent flows. In transformed coordinates, η_∞ is nearly constant for most laminar flows and increases with increasing streamwise Reynolds number for turbulent flows.

The boundary layer parameters of interest, written in terms of transformed coordinates, include:

boundary-layer displacement thickness

$$\delta^* = \frac{x}{(Re_x)^{1/2}} \int_0^{\eta_\infty} (1 - f') d\eta ;$$

boundary-layer momentum thickness

$$\theta = \frac{x}{(Re_x)^{1/2}} \int_0^{\eta_\infty} f'(1 - f') d\eta ;$$

and the local skin-friction coefficient

$$C_f \equiv \frac{\tau_w}{1/2\rho U_e^2} = \frac{2f_w''}{(Re_x)^{1/2}} ;$$

where

$$Re_x = \frac{U_e x}{\nu}$$

is the streamwise Reynolds number.

Before the above equations can be solved, however, it is necessary to express the eddy viscosity term, $\epsilon^+ = \epsilon/\nu$. The formulation by Cebeci and Smith [36] treats the turbulent boundary layer as a composite layer consisting of inner and outer regions with separate expressions for eddy viscosity in each region. The analytic functions, given below, are based on experimental results.

In the inner region, the eddy-viscosity is defined by

$$(\epsilon^+)_i = L^2 \frac{\partial u}{\partial y} \gamma_{tran} ,$$

where L , for two-dimensional flows, is the mixing length taken as

$$L = Ky \left[1 - \exp\left(\frac{-y}{A}\right) \right], \quad K = 0.4 .$$

Here A is a damping constant defined in terms of the shear stress at the wall:

$$A = 26 \frac{\nu}{N} U_\tau^{-1}; \quad U_\tau = \left(\frac{\tau_w}{\rho} \right)^{1/2} .$$

For flows with no mass transfer, N can be written as

$$N = (1 - 11.8p^+)^{1/2}, \quad \text{where } p^+ = \frac{\nu U_e}{U_\tau^3} \frac{\delta U_e}{\partial x} .$$

In the inner region, γ_{tran} represents an intermittency factor accounting for the transition region that exists between laminar and turbulent regimes. It is defined by

$$\gamma_{tran} = 1 - \exp \left[-G(x - x_{tr}) \int_{x_{tr}}^x \frac{dx}{U_e} \right] .$$

Here, x_{tr} locates the start of transition and the empirical factor G , which has the dimensions of *velocity/(length)²*, is given by

$$G = 8.35 \times 10^{-4} \left(\frac{U_e^3}{\nu^2} \right) Re_x^{-1.34} .$$

In the outer region, the eddy-viscosity is defined by

$$(\epsilon^+)_o = \alpha \left| \int_0^\infty (U_e - u) dy \right| \gamma_{tran}, \quad (\epsilon_m)_o \geq (\epsilon_m)_i ,$$

where α is a universal constant equal to 0.0168 when $Re_\theta \geq 5000$.

The condition used to define the inner and outer regions is the continuity of the eddy viscosity — from the wall outward the expression for the inner eddy viscosity is applied until $(\epsilon^+)_i = (\epsilon^+)_o$.

The details of the formulation and the finite difference procedure followed are those given by Cebeci and Bradshaw [37].

5.2 Equivalent–Airfoil Technique

The method is based on obtaining a viscous solution for a given high lift airfoil through the analysis of an equivalent system in potential flow [38]. The iterative cycle is depicted schematically in Figure 5-1. The first step in the procedure is to calculate the potential–flow pressure distribution. The computed pressure distribution is then used to determine laminar and turbulent displacement thickness, transition location, and separation points through the use of the boundary layer calculation scheme of the previous section. With the boundary–layer characteristics known, an equivalent–airfoil configuration is arrived at by superposing the boundary layer displacement thicknesses on the original airfoil contour. The equivalent system is now analyzed in the potential flow.

Obviously, the definition of the equivalent–airfoil geometry that simulates the viscous contribution constitutes a critical step in the iterative solution cycle. Two distinct cases occur, depending on the attached or separated boundary layer.

5.2.1 Attached–flow case

In most practical boundary–layer calculations, it is necessary to solve for the complete flow. That is, for a given external (potential flow) velocity distribution and for a specified (natural) transition point it is necessary to calculate laminar, transitional, and turbulent boundary layers by starting the calculations at the leading edge or at the forward stagnation point of the body. However, most boundary layer prediction methods avoid the calculation of transitional boundary layers by assuming the transition region to be a switching point between laminar and turbulent regions. With the intermittency factor, defined in the previous section, the transitional region can be accounted for more satisfactorily. For incompressible two–dimensional flows the start of transition can be calculated using, for example, an empirical relation between the transition location and the momentum–thickness

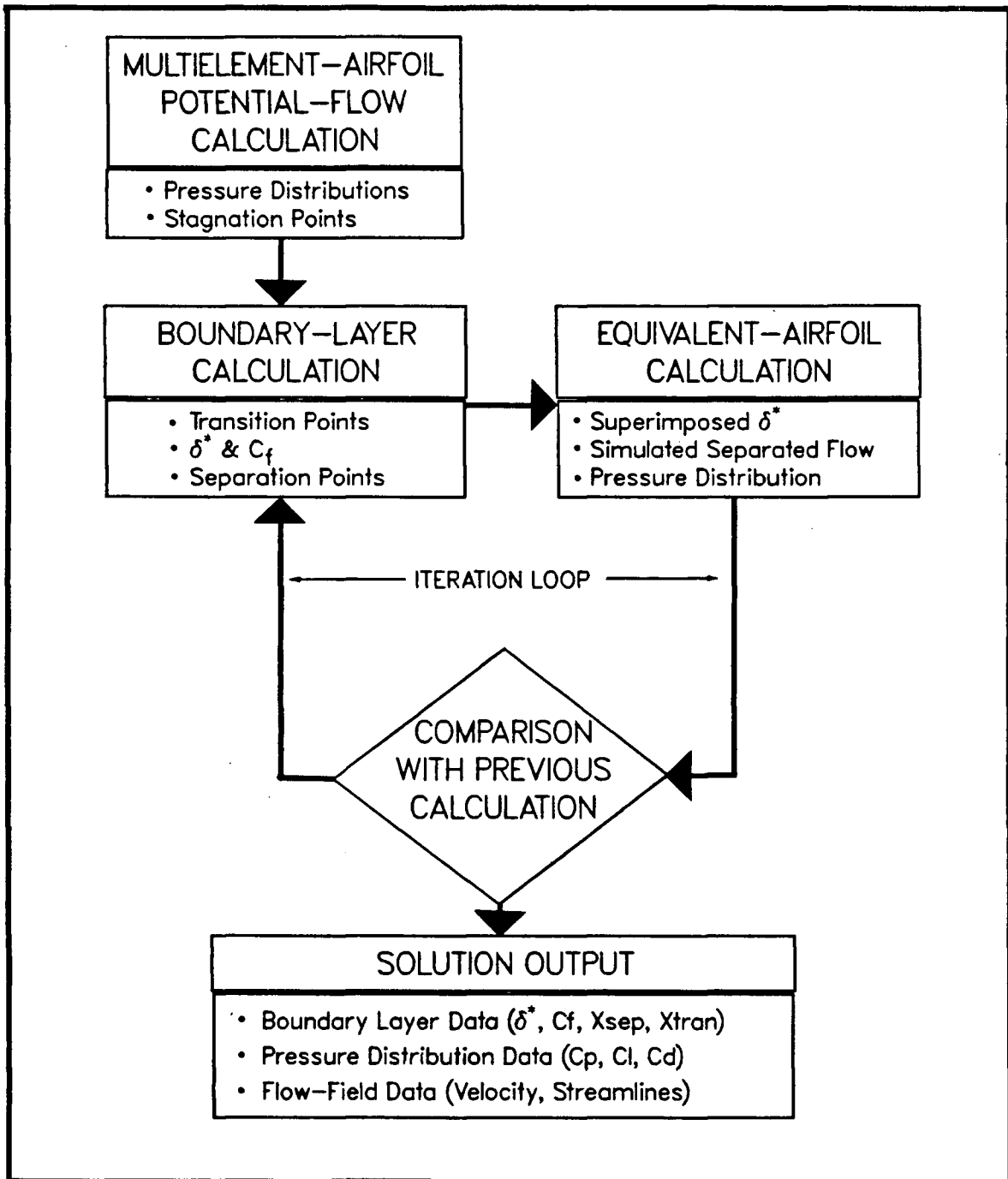


Figure 5-1 Numerical analysis procedure.

Reynolds number [4]. Sometimes, however, the laminar flow calculations indicate flow separation before the transition point can be calculated (laminar separation bubble). In those cases the wall shear becomes negative and prevents the solutions from converging. The transition is then assumed to occur at the laminar separation point and the boundary-layer calculations continued. The point of final turbulent separation is simply the point of vanishing shear stress at the wall.

For the case where no boundary layer separation occurs, the equivalent-airfoil surface is defined by superimposing the computed boundary layer displacement thickness normal to the airfoil contour (Figure 5-2a). Since the displacement thickness is not zero at the trailing edge, the resulting equivalent body is analogous to an airfoil with a finite-thickness trailing edge. Thus the extensions to the basic formulation, described in section 4.2, are directly applicable.

5.2.2 Separated-flow case

The boundary-layer calculations described above predict the separation point but do not carry out calculations beyond the point of separation. Therefore, an equivalent displaced surface past the separation point is not readily available.

One way to solve this problem is to allow the separation streamline to remain a free boundary and fix its position by specifying a constant pressure condition along the streamline, from the separation point to the trailing edge. Experimental data tend to support a nearly constant pressure, separated wake condition. The approach, however, requires the solution of a nonlinear system of equations within the framework of the distributed singularity theory. The undesirability of an iterative approach to the solution led to the search for a simpler method.

The streamline emanating from the separation point can also be approximated by an analytical function [38]. A linear streamline assumption aligns it with the freestream direction while a parabolic streamline assumption orients it so

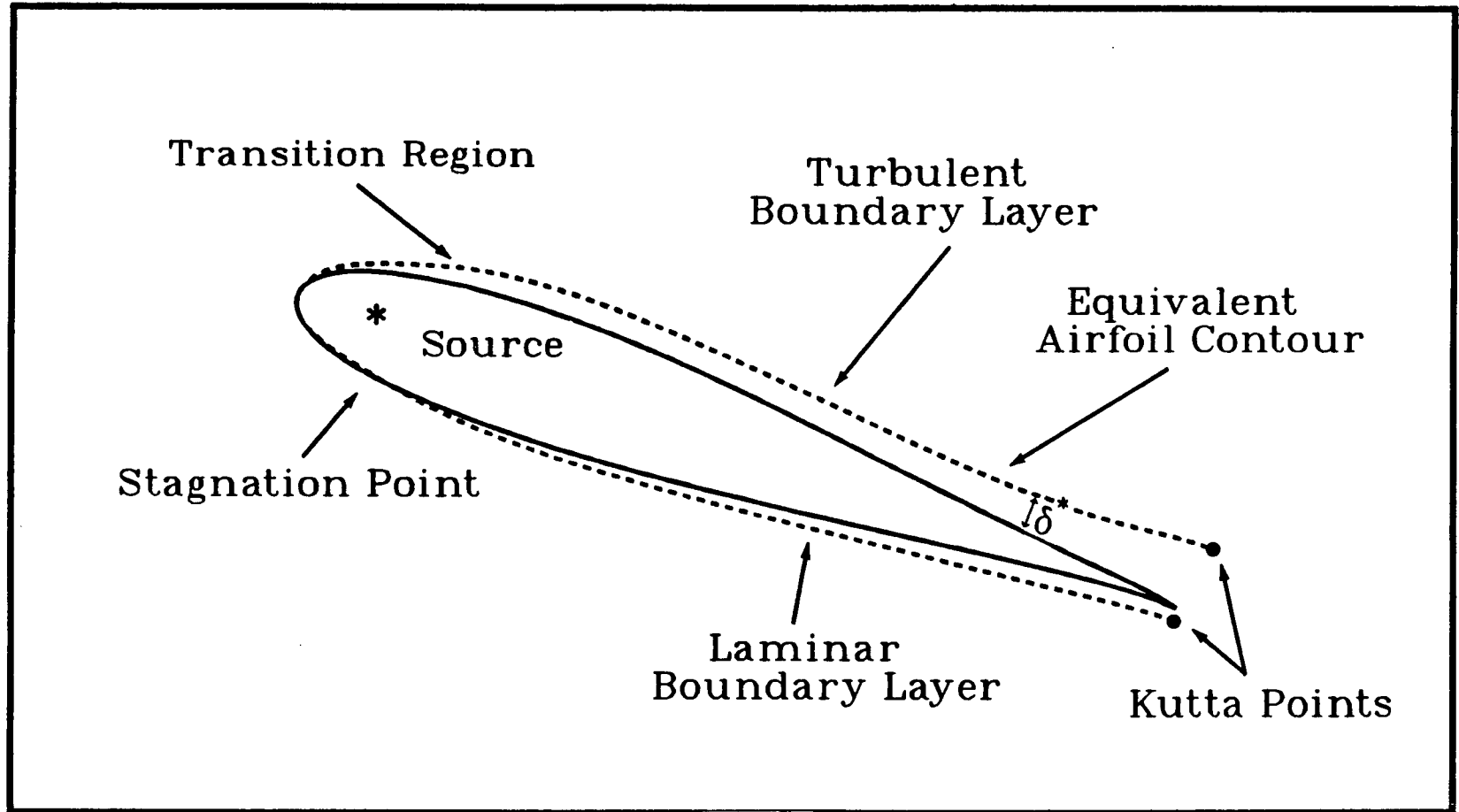


Figure 5-2 Equivalent-airfoil models: (a) attached flow;

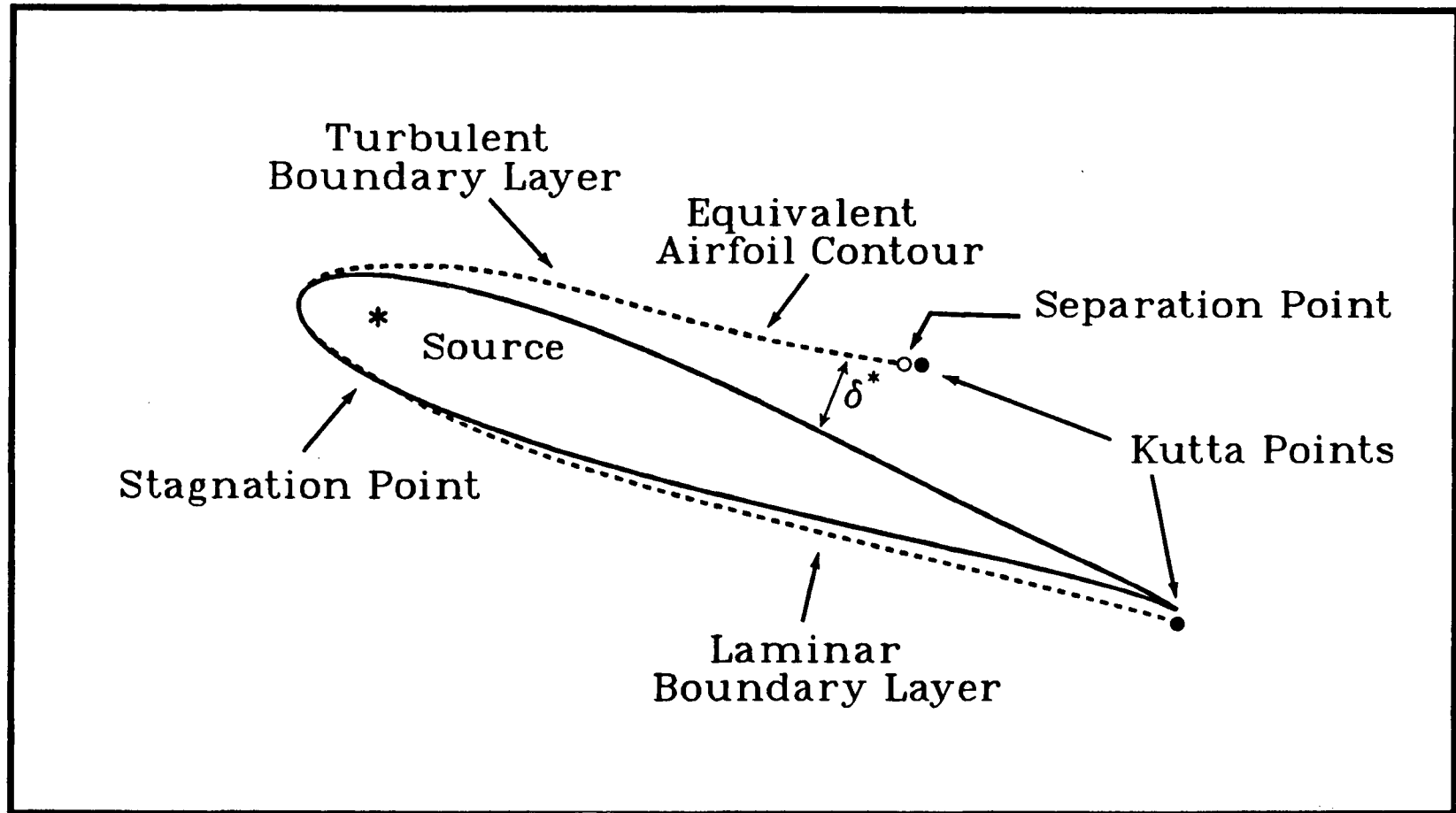


Figure 5-2 Equivalent-airfoil models: (b) separated flow.

that it is tangential to the local surface at the separation point and parallel to the freestream direction at the trailing edge. Alternatively, a satisfactory analytical definition for the separation streamline can be obtained by trial and error for the configuration under investigation. However, it should remain valid for a variety of airfoil configurations and locations of the separation point.

To avoid empiricism, it was decided to adopt a free separation-streamline approach. The model is shown schematically in Figure 5-2(b). The free separation-streamline model is defined by satisfying the boundary conditions of tangential flow on only that part of the airfoil having attached flow. The tangential flow condition is also satisfied at the separation point and the trailing edge. Since no flow control is exercised at points downstream of the separation point, the streamline develops freely from the separation point. The resulting model is mathematically identical to that used to analyze airfoils with finite-thickness trailing edges. In this case, the total separated region of the airfoil is considered as a finite-thickness base. The Kutta point just downstream of the trailing edge on the upper surface in the finite trailing edge airfoil analysis is moved to just downstream of the separation point. The pressure distribution downstream of the separation is assumed to remain constant at a value corresponding to that at the point of separation.

A detailed listing of the computer program used in the numerical computations is given in the Appendix.

5.3 Results and Discussion

The symmetrical Joukowski airfoil model was also analyzed using the numerical surface singularity approach accounting for the viscous correction. The actual measured coordinates of the experimental model, rather than the analytical shape, served as input to the program to facilitate comparison with experimental results and avoid unreal cusp character of the theoretical Joukowski section. Note, the results corrected for boundary layer effects also account for blockage.

Typical pressure plots as obtained using the numerical models are compared with the experimental data in Figure 5-3. The numerical potential flow model predicts considerably higher suction over most of the upper surface. However, the effect due to wall confinement is relatively small. The correction scheme uses these potential flow data (with wall confinement effects) to calculate the displacement effect of the boundary layer, as well as the point of separation, to obtain the "corrected" pressure data.

Considering the relatively simple character of the numerical scheme, the correlation may be considered quite good. The discrepancy between the predicted and experimental results near the trailing edge is believed to be mainly due to the nature of the boundary layer scheme and its simplifying assumptions. Obviously, assuming the pressure to remain constant across the shear layer is no longer valid after the shear layer has separated. More accurate prediction of the pressure in a separated boundary layer with flow reversal would require the use of a sophisticated numerical scheme in conjunction with the full Navier–Stokes equations.

These results, along with the corresponding data at other angles of attack, are summarized in the form of C_L vs. α plots in Figure 5-4. Improvement in correlation with the experimental results due to inclusion of the boundary layer effects is strikingly apparent.

Next, the Joukowski airfoil with a rotating cylinder forming its nose is considered. A typical pressure distribution for this two-component airfoil, as predicted by the potential flow surface singularity method, is compared with the experimental results in Figure 5-5. Since the result of the cylinder rotation, in effect, is to minimize the adverse effects of the boundary layer, the correlation between the inviscid results and experiment remains reasonable, even at an angle of attack as high as $\alpha = 16^\circ$.

However, with a further increase in the angle of attack, at some point it is

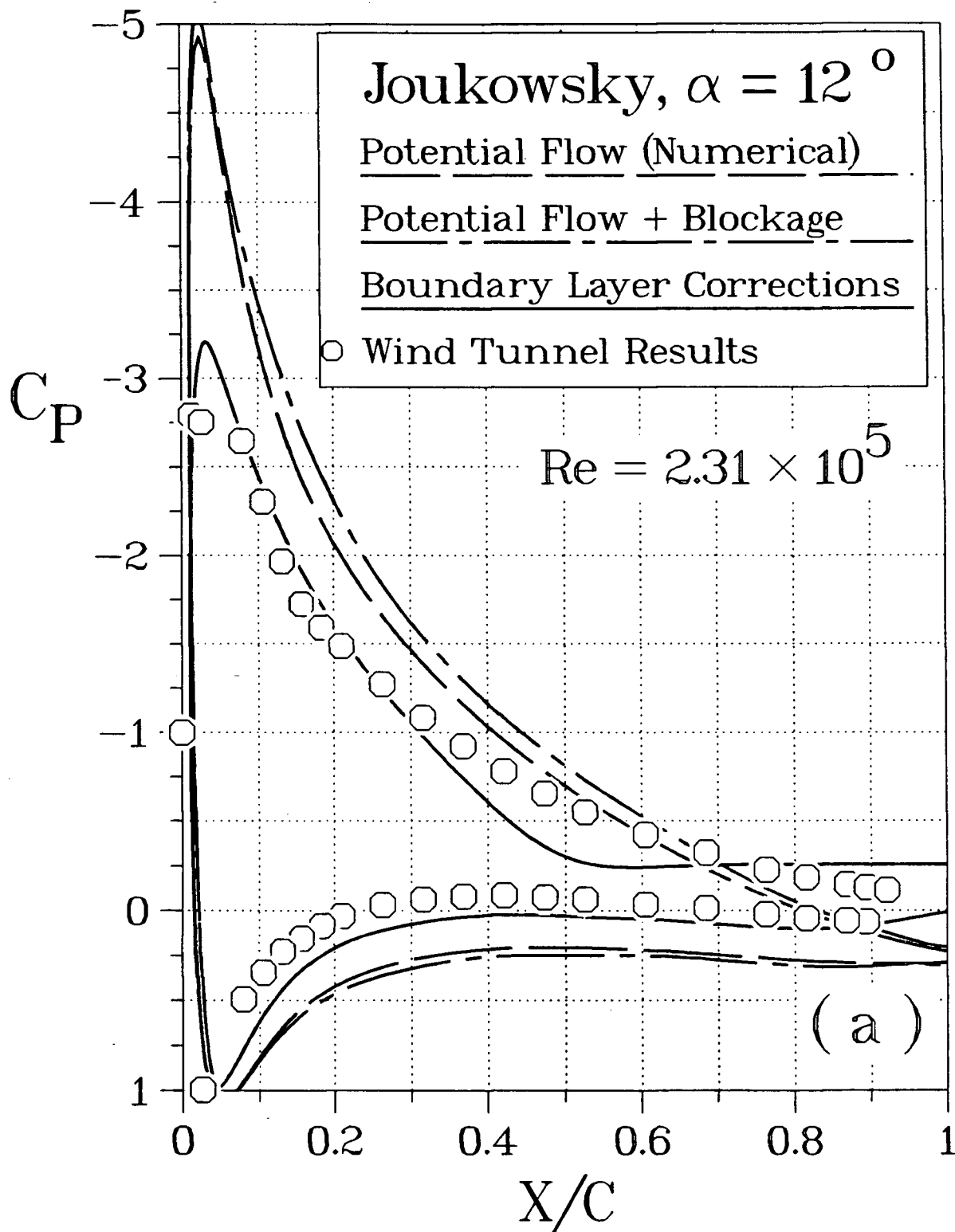


Figure 5-3 Effectiveness of the numerical modelling procedures and their comparison with experimental data.

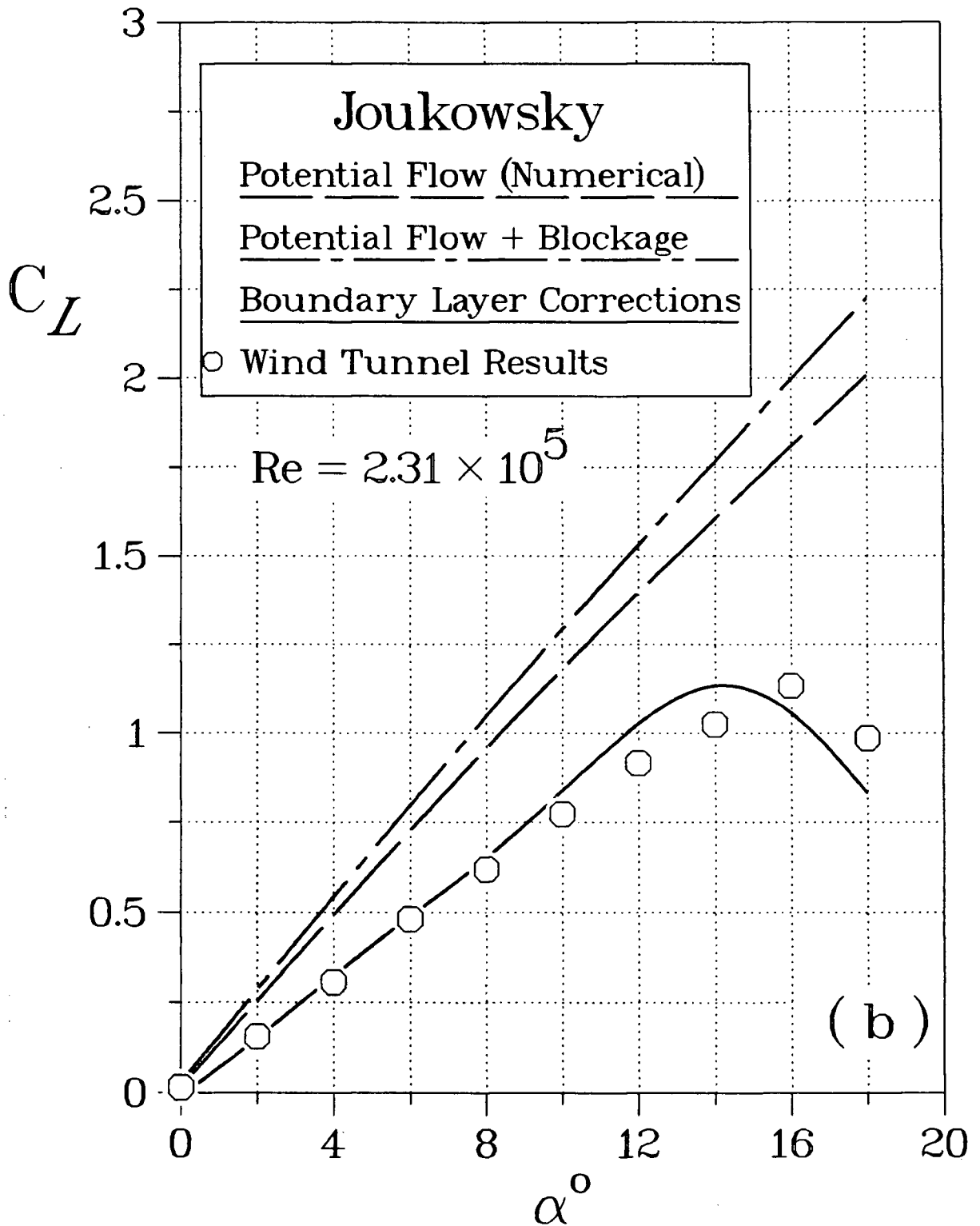


Figure 5-4 Variation of the lift coefficient with angle of attack as predicted by the different models.

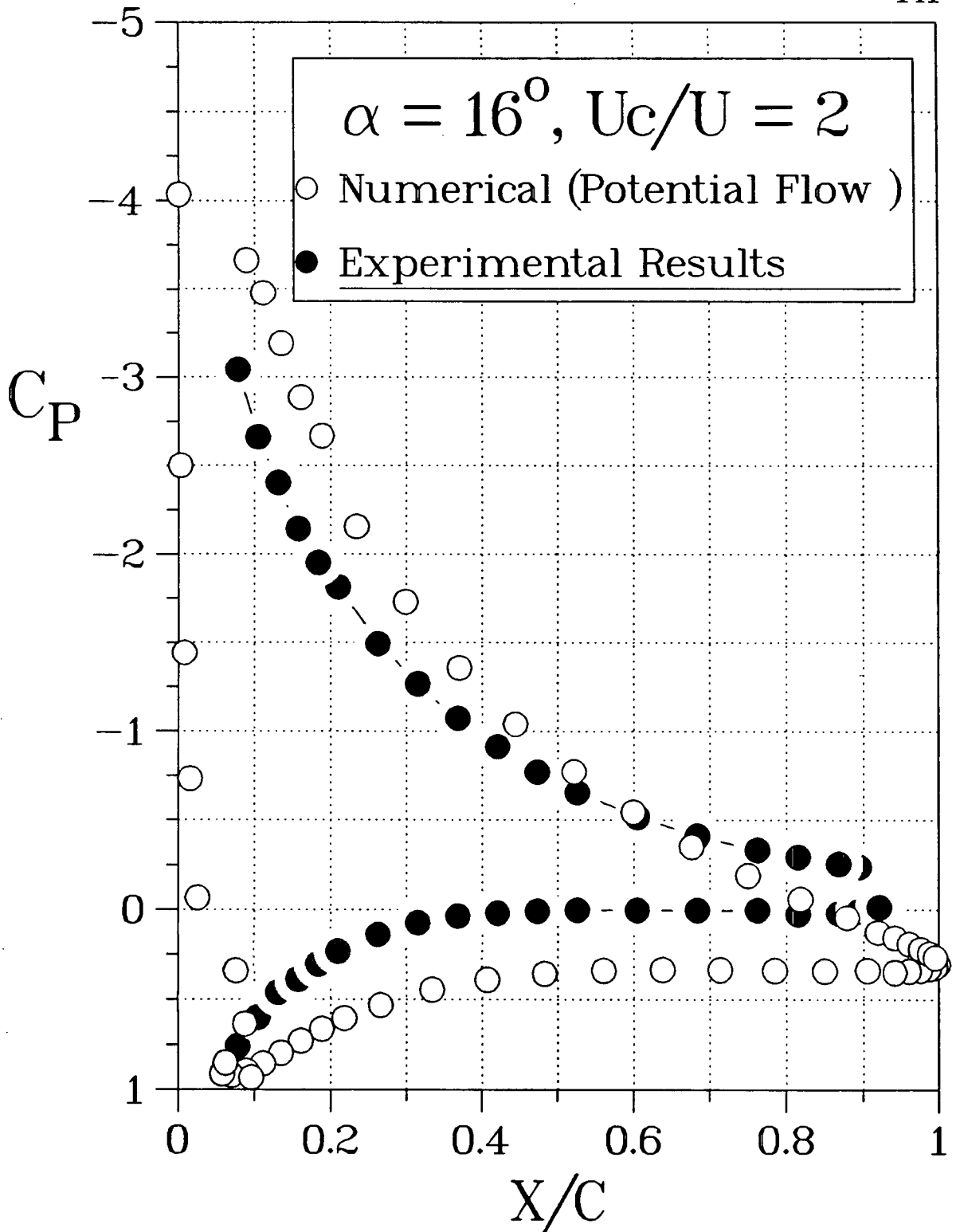


Figure 5-5 Comparison between typical potential flow and experimentally obtained pressure data for a Joukowski airfoil.

no longer possible to keep the flow attached over the entire upper surface. As the size of the separation region grows, the suction over the airfoil decreases and the consideration of the viscous character of the flow becomes essential. The pressure peak at the leading edge, predicted by the potential flow solution, and a large adverse pressure gradient immediately downstream of it cause the boundary layer to separate quite readily. This suggested that to incorporate the boundary-layer corrections effectively, it is essential to model also the cylinder rotation.

The effect of the cylinder rotation is considered in two ways:

- (i) through the boundary layer scheme by setting the appropriate wall velocity conditions at the location of the leading-edge-cylinder; or
- (ii) through initial modification of the external flow using a pair of counter-rotating vortices below the leading edge.

The models used are shown in Figure 5-6.

5.3.1 Modelling the effect of cylinder rotation through boundary-layer modification

The boundary layer which starts at the location of the stagnation point below the nose of an airfoil at a relatively high angle of attack grows considerably around the leading edge, due to the large adverse pressure gradient present in this region, and separates shortly downstream. Rotation of the leading-edge-cylinder, however, can delay separation of the boundary layer by:

- reducing the growth of the boundary layer, particularly near the leading edge; and by
- injecting momentum into the growing boundary layer.

These effects are illustrated in Figure 5-7 and modelled by imposing appropriate boundary conditions on the surface of the airfoil at the location of the cylinder as

CORRECTED NUMERICAL APPROACH

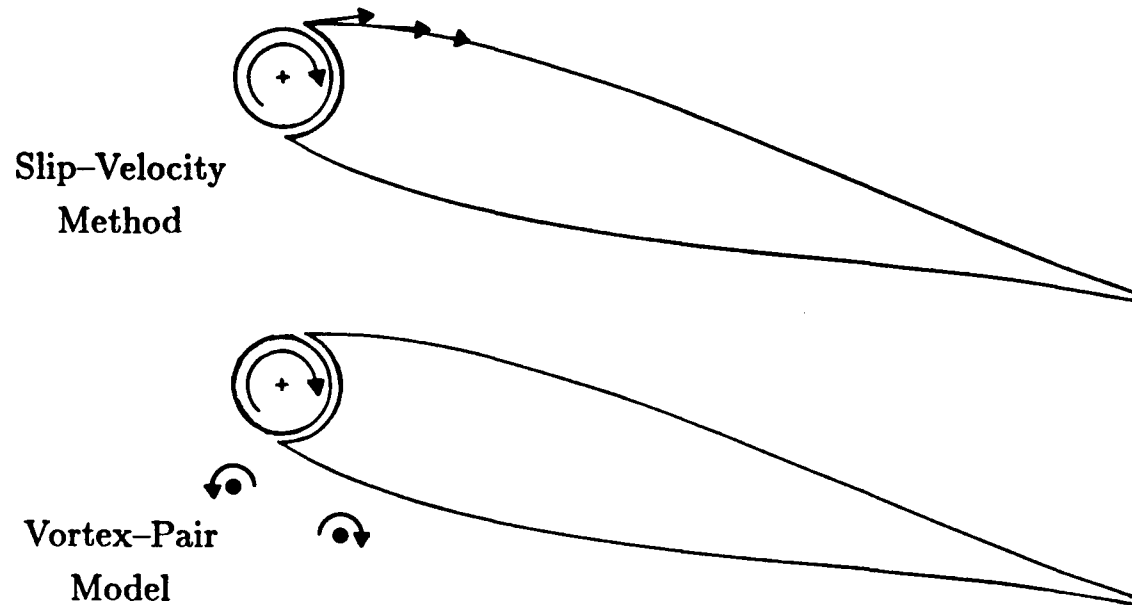


Figure 5-6 Models for the effect of cylinder rotation.

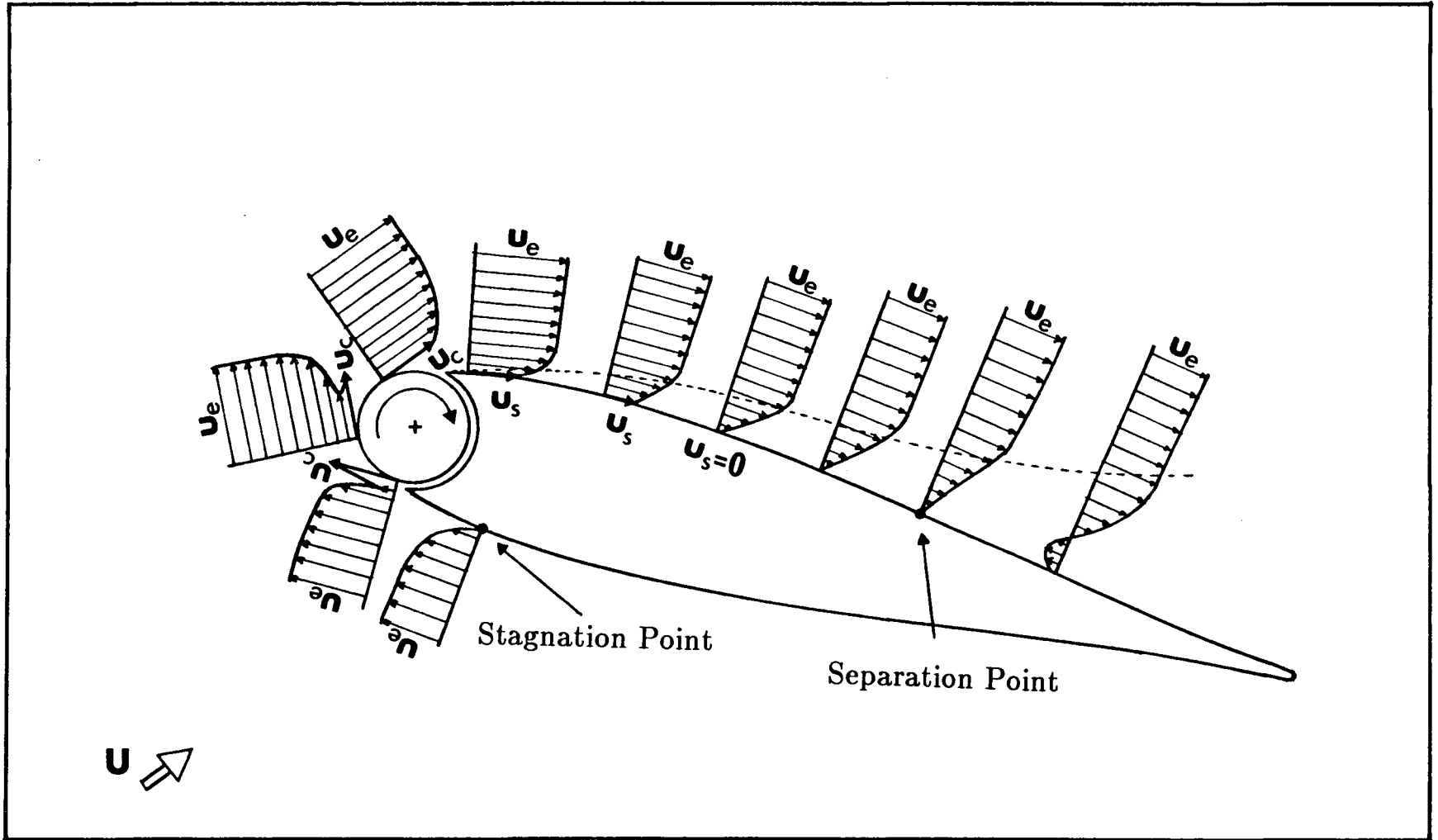


Figure 5-7 Schematic diagram of the velocity profiles around the leading edge of an airfoil illustrating the momentum injection effect due to the rotation of the cylinder.

described below.

Beginning at the location of the “lower gap”, the existing boundary condition on the surface is changed. The new condition sets the fluid velocity at the wall equal to the surface speed of the cylinder, and remains in effect until the “upper gap” is reached. Beyond this point, a “slip velocity” is introduced to model the momentum injection. The initial magnitude of this velocity is equal to the cylinder surface speed but exponentially decreases to zero at the point of maximum thickness of the airfoil. The normal “no-slip” boundary condition takes effect at this point.

The slowly decreasing slip velocity attempts to represent effect of the cylinder rotation. It progressively diminishes and virtually disappears a short distance downstream. The region over which the momentum injection effect persists was qualitatively arrived at through flow visualization using tufts. This compares with the experimentally observed separation, at very large angles of attack ($\alpha > 36^\circ$), near the quarter-chord point (Figure 3-4d).

It is important to emphasize that the above procedure does not specify a point of separation for the upper-surface flow. In fact, depending on the pressure gradient, the flow may remain attached over the entire surface or separate even before the “slip velocity” condition is terminated.

A few representative numerical results accounting for cylinder rotation and the airfoil angle of attack are compared with the experimental data in Figure 5.8 (a) and (b) at $\alpha = 12^\circ$. Considering the highly complex character of the flow due to moving surface momentum injection, the correlation is indeed satisfactory. The lack of pressure taps at the leading edge (on the rotating cylinder) prevents comparison in this region. However, increasing the cylinder speed does predict higher suction over the leading edge as suggested by the experiments (the first pressure tap on the upper surface). Although not quite evident from the experimental data, the theory also shows the point of separation on the upper surface (clearly it moves

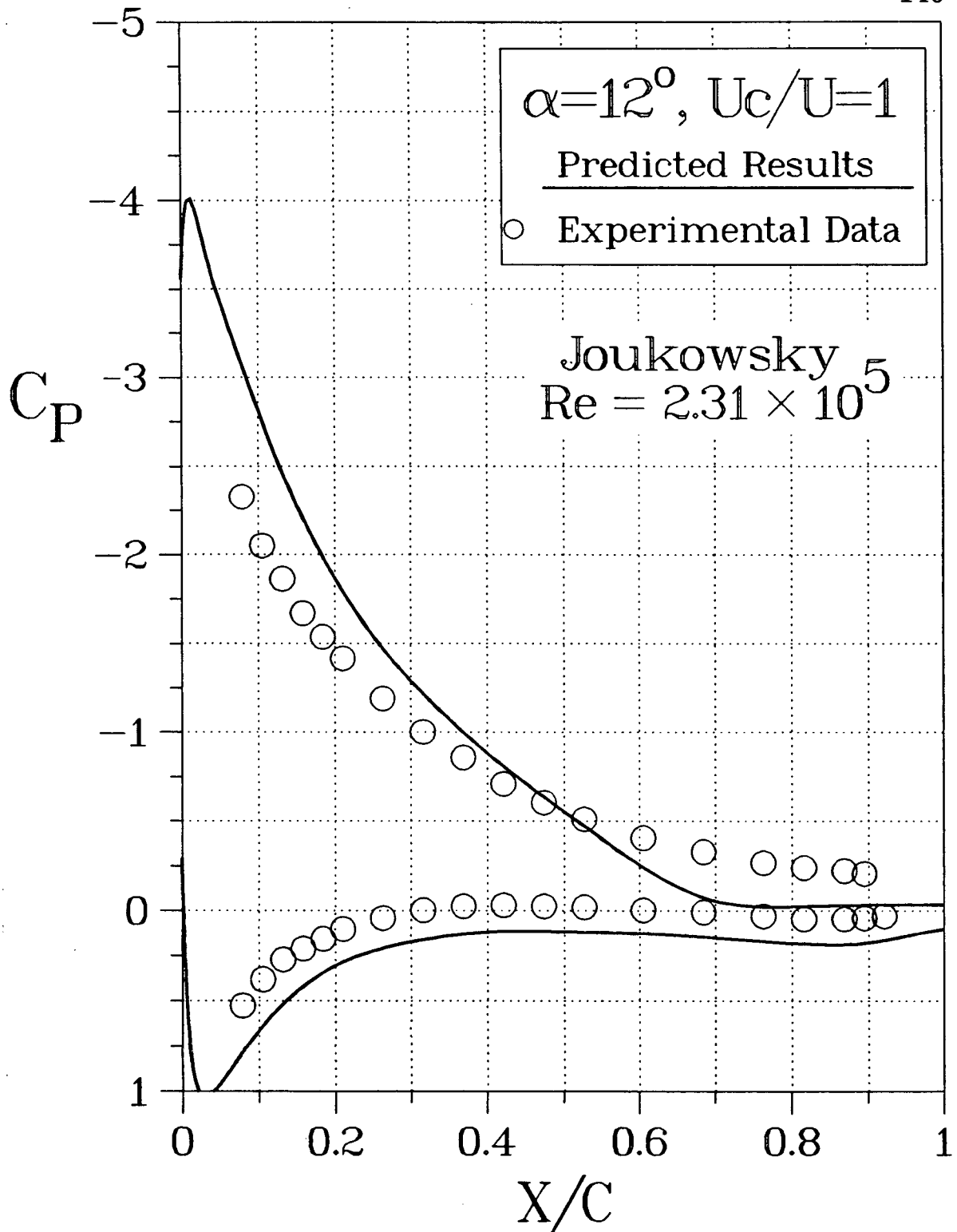


Figure 5-8 Typical numerical predictions of the pressure distribution using boundary-layer modification to model the cylinder rotation and their comparison with experiment: (a) $\alpha = 12^\circ, U_c/U = 1$;

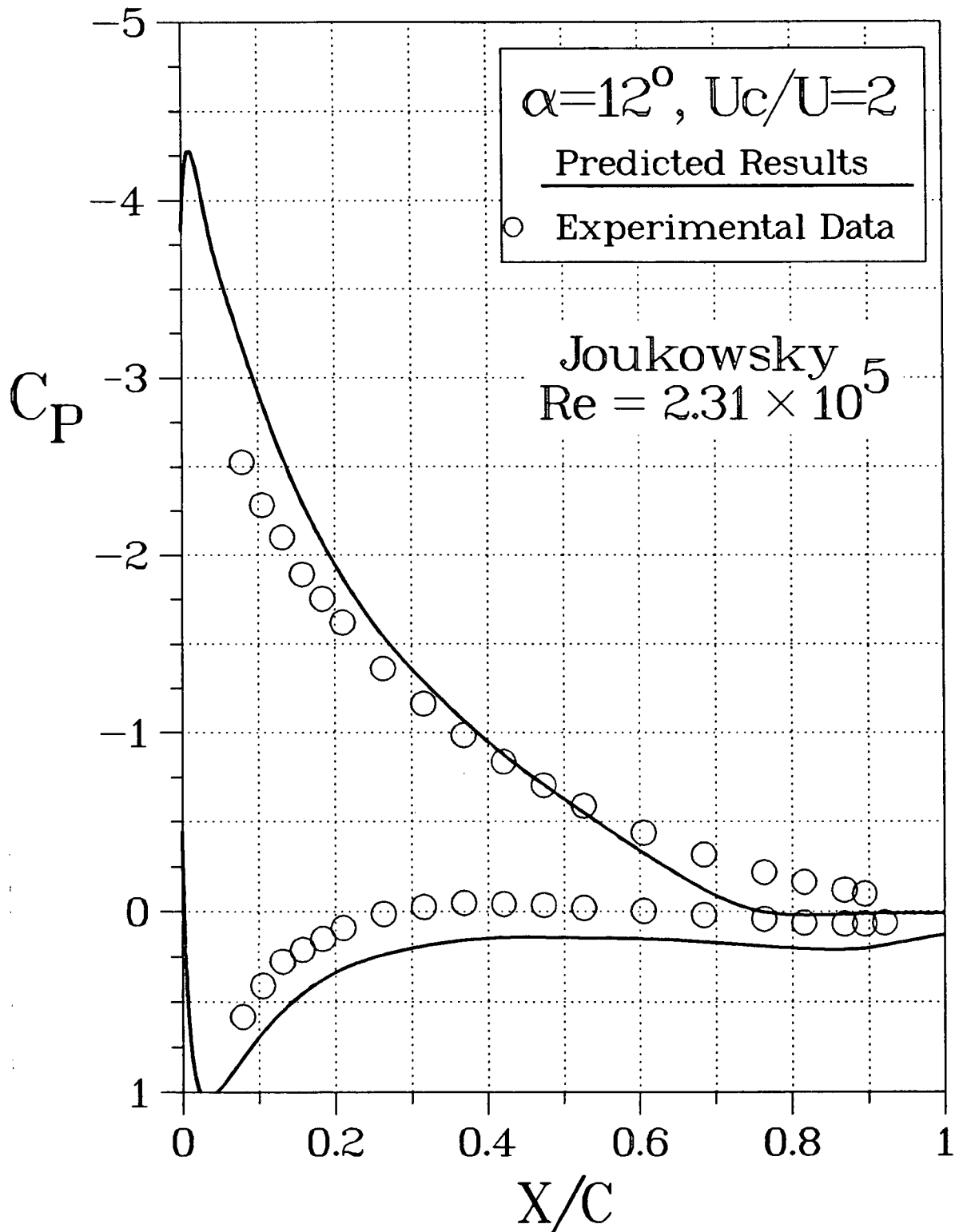


Figure 5-8 Typical numerical predictions of the pressure distribution using boundary-layer modification to model the cylinder rotation and their comparison with experiment: (b) $\alpha = 12^\circ, U_c/U = 2$;

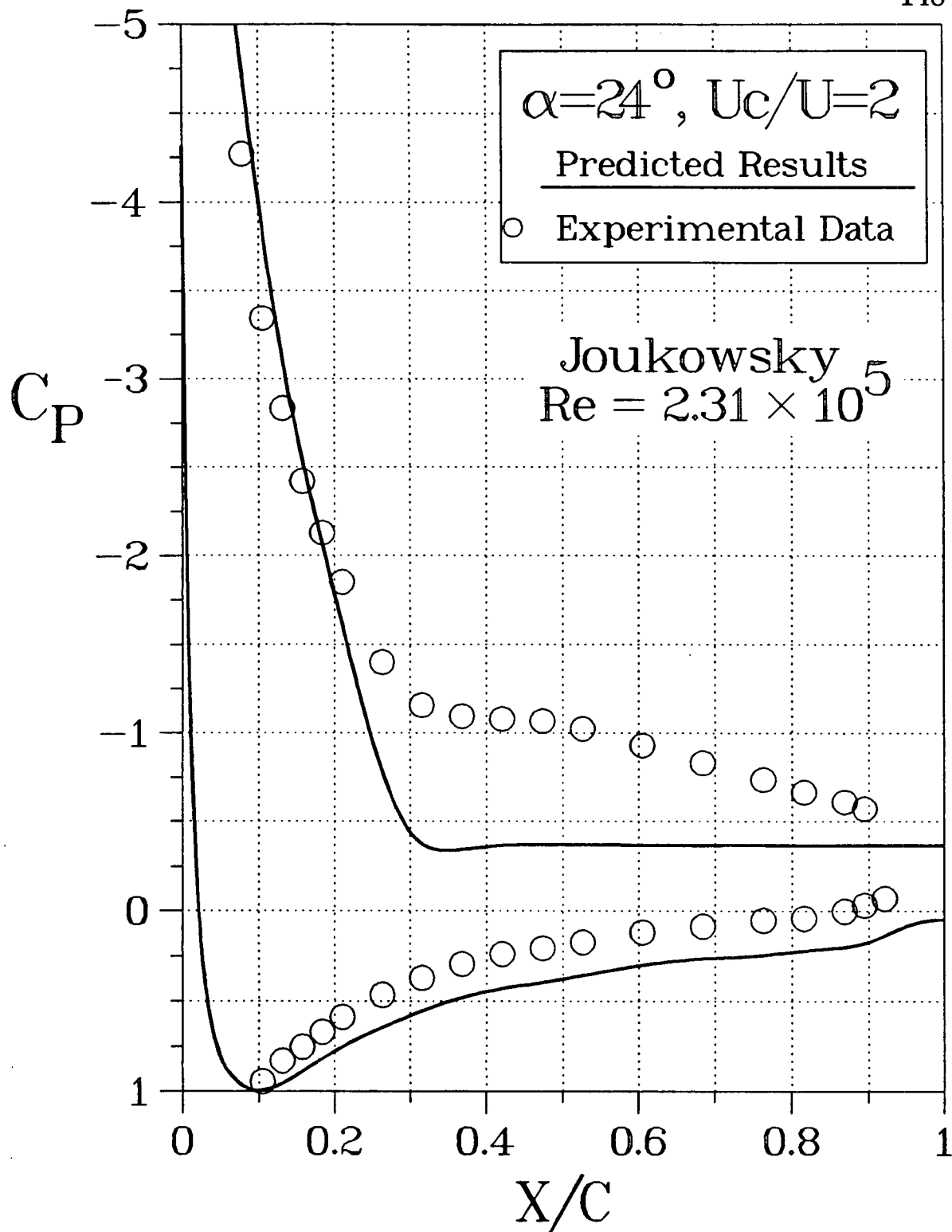


Figure 5-8 Typical numerical predictions of the pressure distribution using boundary-layer modification to model the cylinder rotation and their comparison with experiment: (c) $\alpha = 24^\circ, U_c/U = 2$;

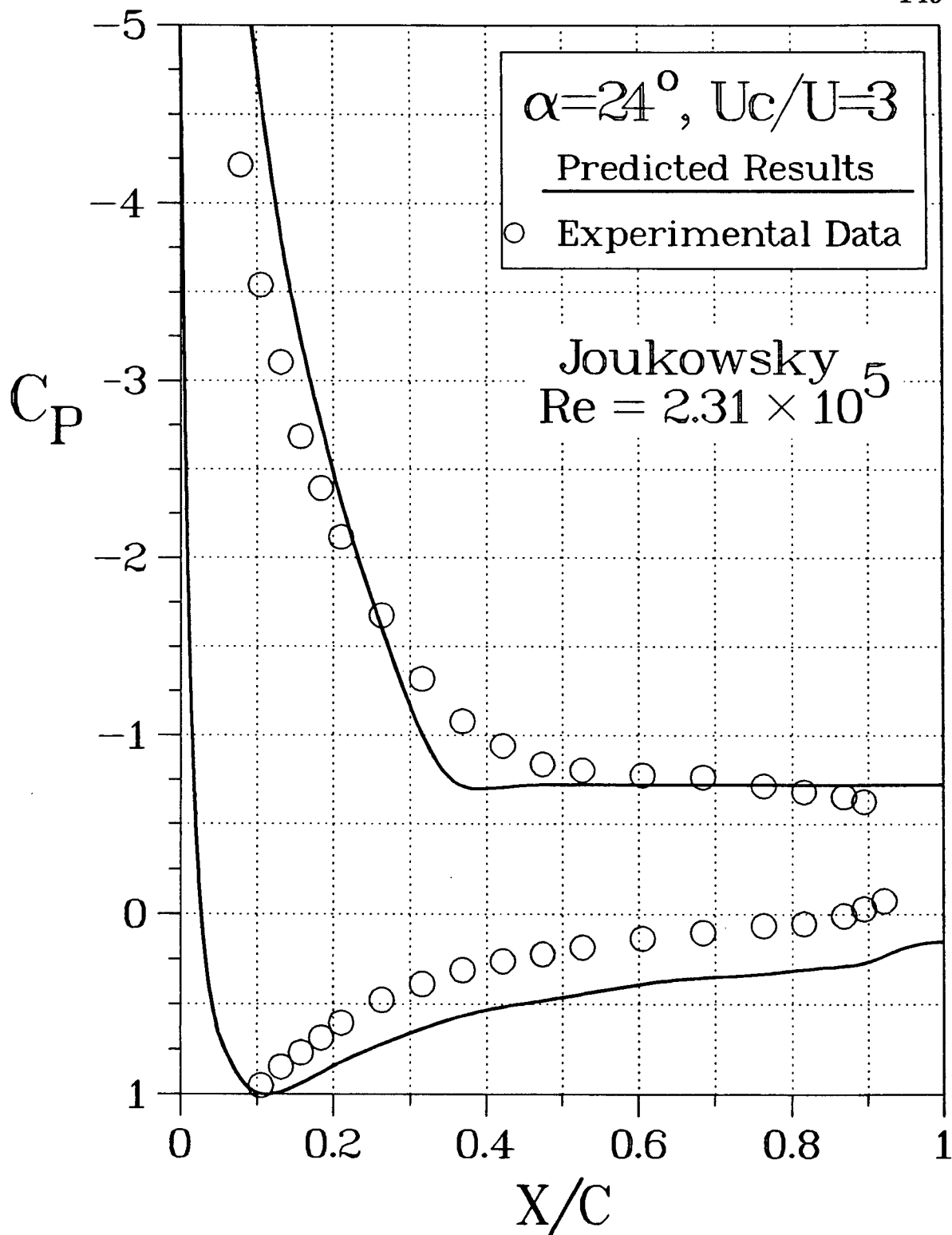


Figure 5-8 Typical numerical prediction of the pressure distribution using boundary-layer modification to model the cylinder rotation and their comparison with experiment: (d) $\alpha = 24^\circ, U_c/U = 3$;

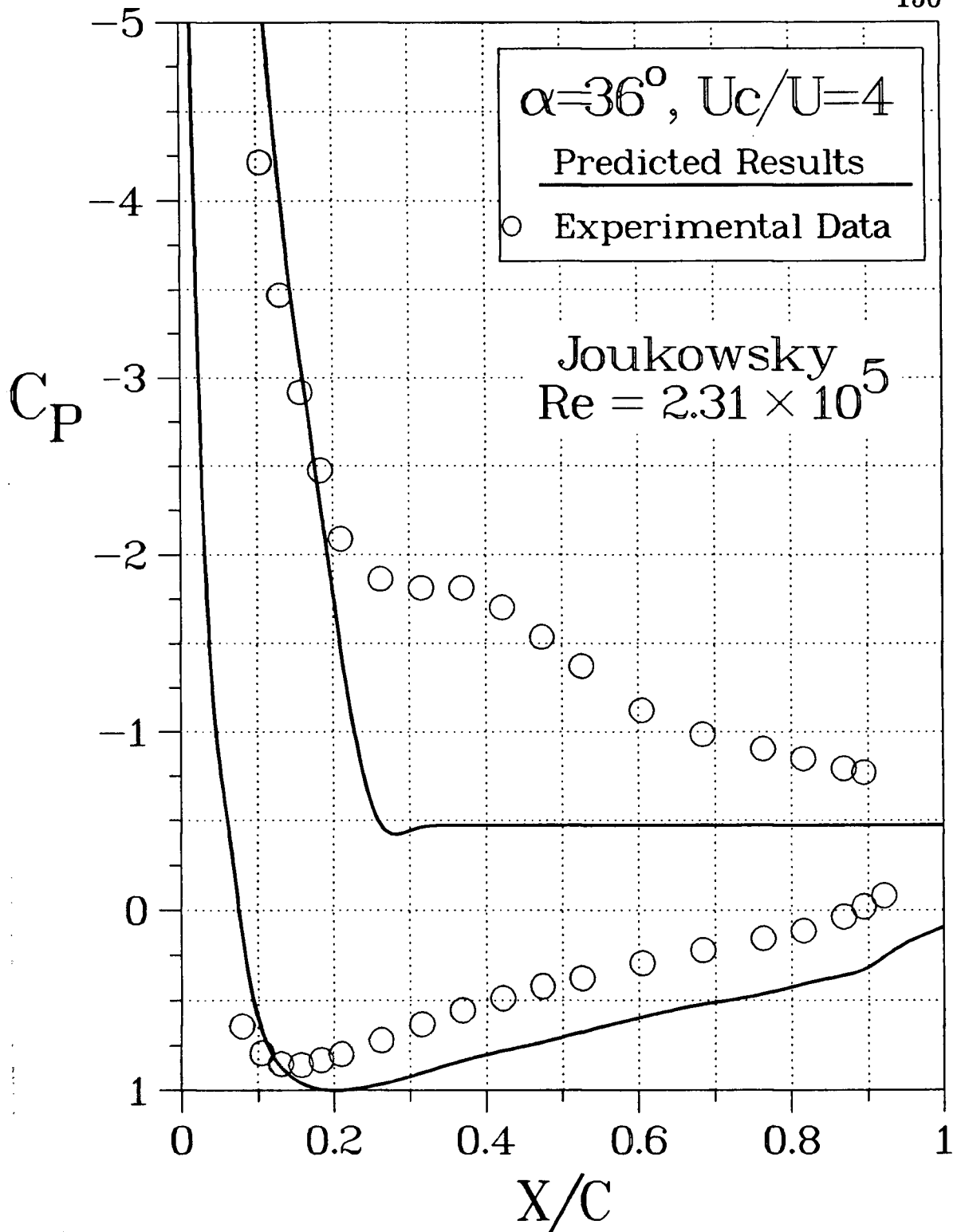


Figure 5-8 Typical numerical prediction of the pressure distribution using boundary-layer modification to model the cylinder rotation and their comparison with experiment: (e) $\alpha = 36^\circ, U_c/U = 4$.

downstream with an increase in cylinder speed).

Similar results at $\alpha = 24^\circ$ are also shown (Figure 5-8 c, d). Note the existence of a rather large separation bubble on the upper surface with $U_c/U = 2$. This region is identified by an essentially constant pressure from $X/C \approx 0.3$ to 0.5 and its recovery towards the trailing edge. Obviously, the present model does not account for reattachment and treats the region downstream of separation as having a constant pressure, leading to the discrepancy. The model “sees” any separation as the final one (here at $X/C \approx 0.35$) and does not calculate the flow beyond this point. At a higher rate of rotation (Figure 5-8d), however, the early separation and reattachment (separation bubble) is avoided and the theory is in much better agreement with the experiment in this case.

At a very large angle of attack of $\alpha = 36^\circ$, the flow separates rather early (at $X/C \approx 0.2$) even in the presence of a high rate of cylinder rotation ($U_c/U = 4$, Figure 5-8e). The pressure recovery fluctuates as the separated boundary layer moves closer to the airfoil surface and intermittently attaches to it (as shown by the video movie taken during the flow visualization). Obviously, the theoretical model is not sophisticated enough to account for such transient behavior and a large discrepancy in this region is apparent.

The experimental lift data are plotted (Figure 5-9a) along with the numerical predictions obtained through integration of the pressure. The experimental results in absence of cylinder rotation are also shown for comparison. Although the theory successfully predicts correct trends and is reasonably close in estimating the $C_{L,max}$ values (1.85 vs. 1.65 at $U_c/U = 2$, 1.93 vs. 1.8 at $U_c/U = 3$) it seems to grossly underestimate the stall angle. The analysis, therefore, overpredicts the slope of the lift curve (6.28/*rad* against 5/*rad*) and hence gives high C_L values for a given α . This is partly due to the presence of gaps, between the test model and the wind tunnel walls, necessary to provide connections to the balance at one end and cylinder drive mechanism, located outside the tunnel, at the other. Thus the

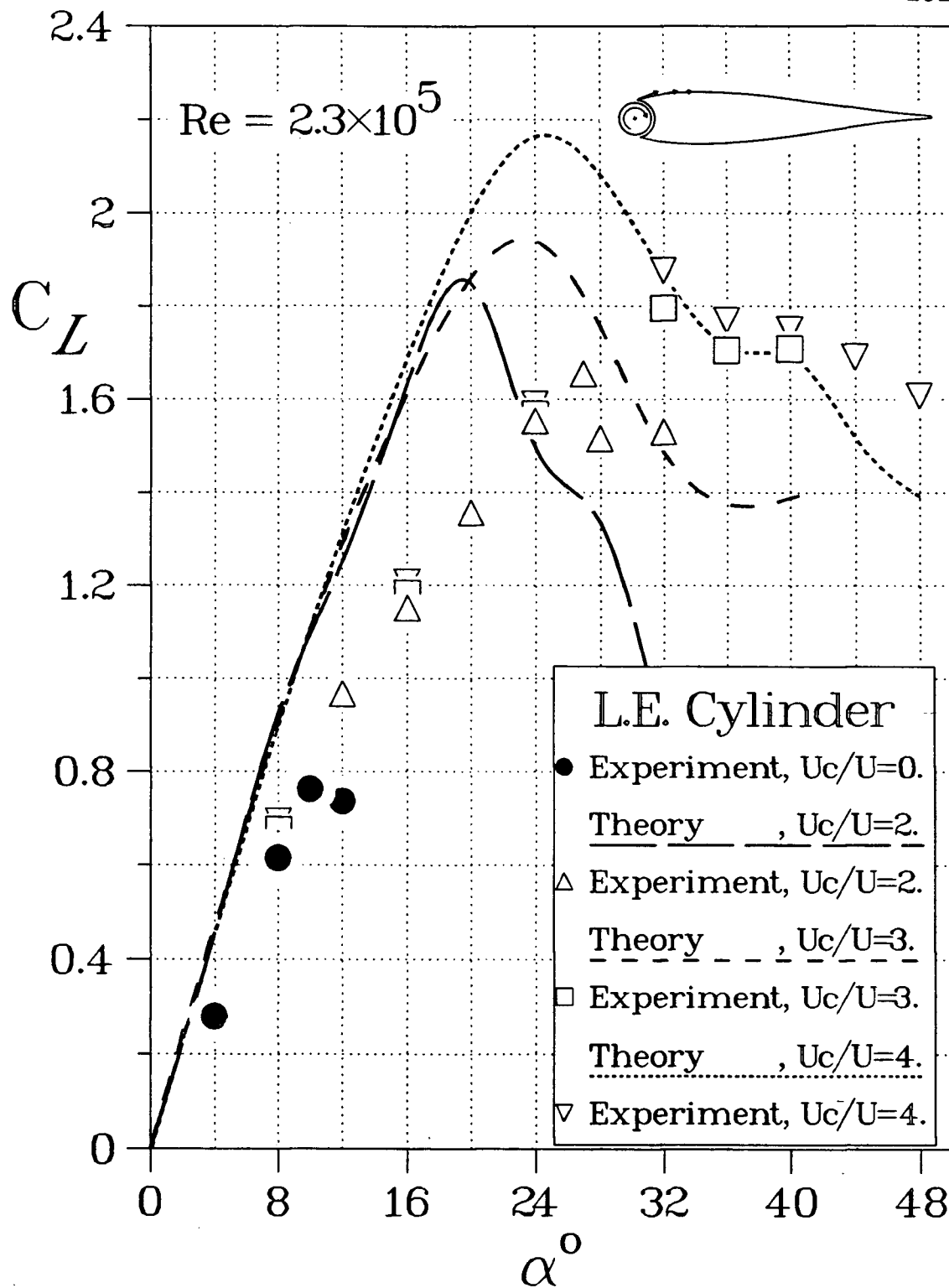


Figure 5-9 Variation of the lift coefficient with angle of attack using boundary-layer modification to model the cylinder rotation - a comparison with experimental data: (a) integrated pressure data;

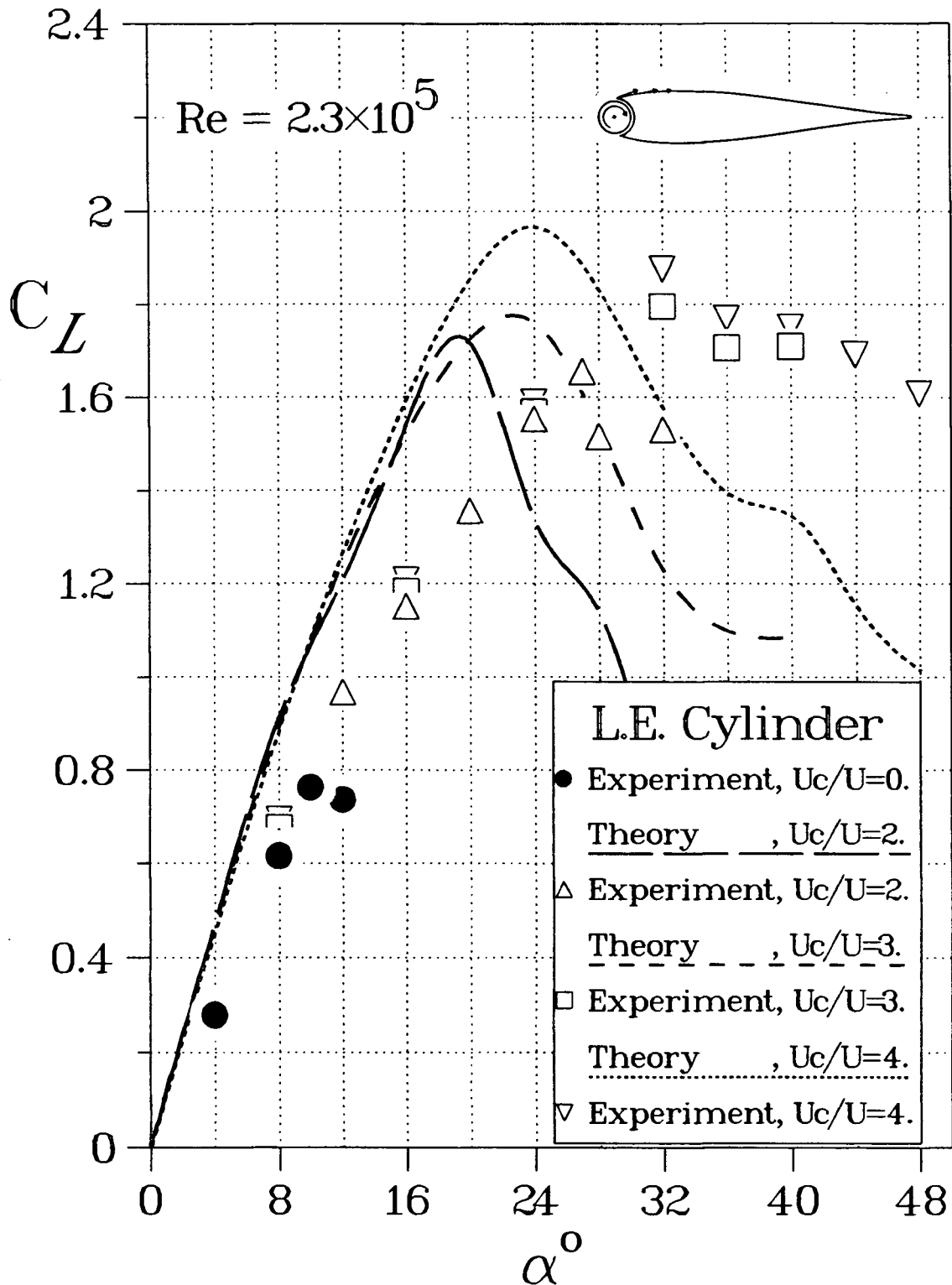


Figure 5-9 Variation of the lift coefficient with angle of attack using boundary-layer modification to model the cylinder rotation - a comparison with experimental data: (b) integrated pressure data with theoretical results modified at the leading edge.

test arrangement does not represent an ideal two-dimensional condition. However, inadequacy of the theory to model such a complex separated flow with possible transient reattachment of the boundary layer (in the presence of cylinder rotation) is the major cause of discrepancy. On the other hand, relatively simple numerical procedure based on potential flow analysis with viscous correction has sufficient accuracy for preliminary engineering analyses.

Due to the lack of pressure taps in the nose section of the experimental model, the integrated pressure distribution results do not include the contribution due to the high suction peak over the leading edge. This partly explains the significantly higher numerical predictions of lift at the larger angles of attack. It is, however, possible to make a better comparison between the results if the theoretical values are modified to exclude the information that is missing from the experimental observations.

Figure 5-9(b) shows the results of integrating the numerical pressure plots with the leading-edge suction peak “flattened” to correspond to the same approximation as used in integration of the experimental results. The maximum lift coefficients predicted by the theory now match the experimental values more closely.

5.3.2 Cylinder rotation modelled through a pair of counter-rotating vortices

The potential flow model, represented by a pair of counter-rotating vortices below the leading edge was described in section 4.2.2. It was shown to effectively decrease the adverse pressure gradient, behind the suction peak, which is responsible for separation at large angles of attack. Combined with the boundary-layer correction scheme, it should provide a way of modelling the momentum injection into the boundary layer. It also takes into account the effect of the gap to some degree because of the inherent discontinuity in the boundary condition from the

rotating cylinder to the airfoil surface.

Results obtained using this approach are compared with the corresponding experimental data in Figure 5-10. The predicted pressure plots are similar to those discussed in the previous section up to the point of stall. There is some improvement in correlation due to a reduction in suction peak, as predicted by the present model, and the corresponding change in compression on the lower surface (compare to Figure 5-8b). The coefficients of lift, therefore, also show better agreement with the experimental values at lower angles of attack ($\alpha \leq 16^\circ$, Figure 5-11). Note, unlike the previous model, the present method predicts complete separation of the upper-surface flow at the point of stall resulting in a large drop in lift. The experiments show relatively gradual onset of stall.

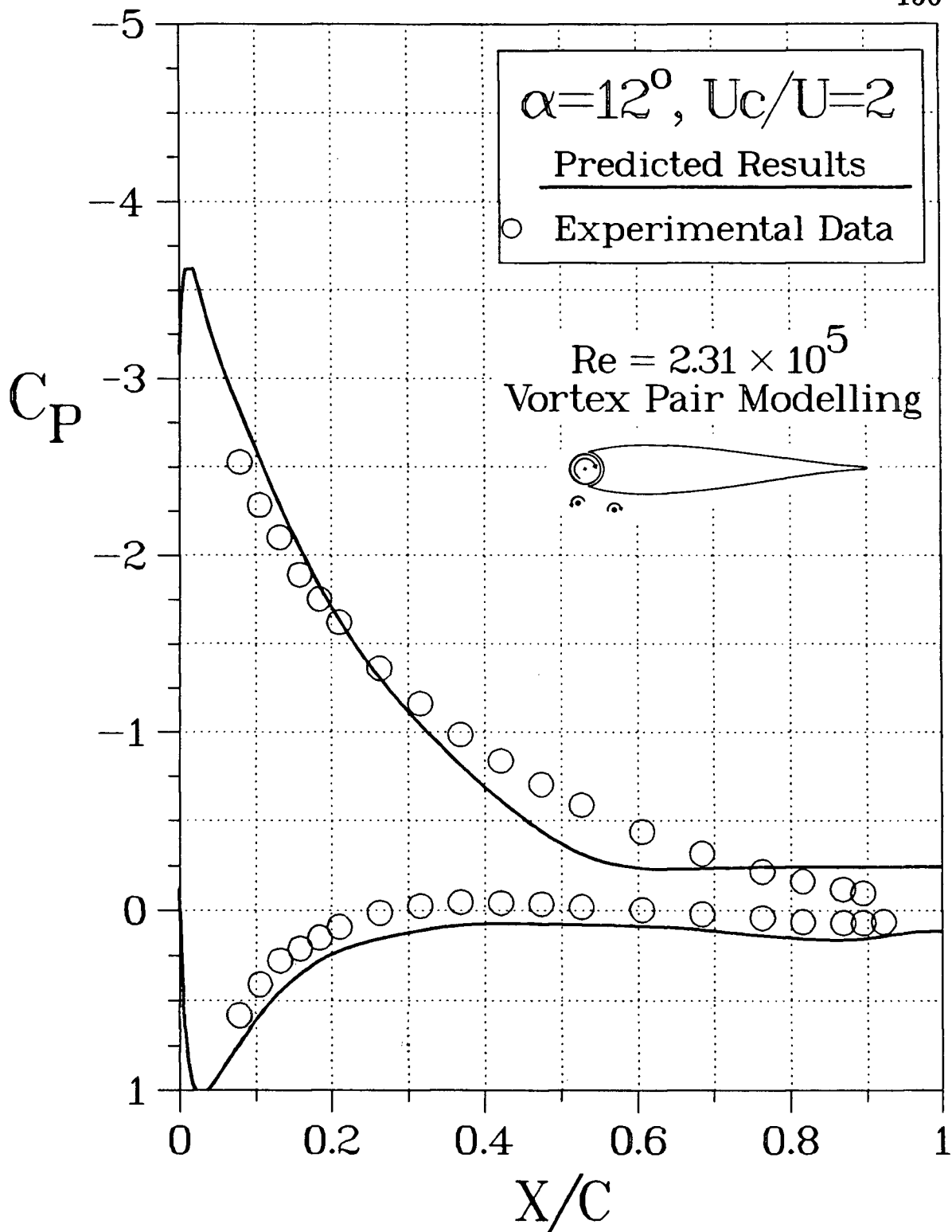


Figure 5-10 Predicted pressure distribution using the vortex-pair modelling of the cylinder rotation and its comparison with the experimental data.

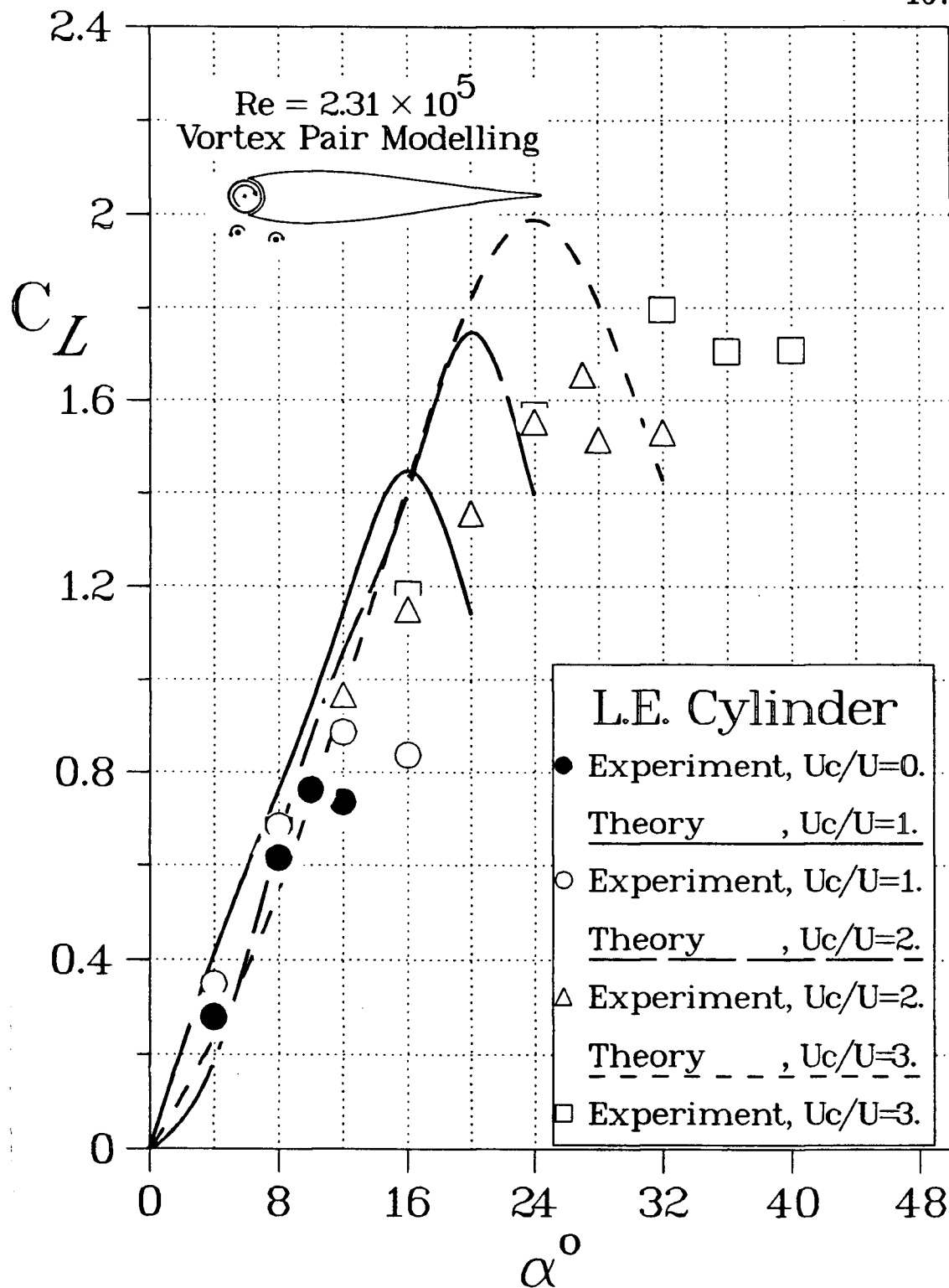


Figure 5-11 Variation of the lift coefficient with angle of attack as predicted using the vortex-pair modelling of cylinder rotation and its comparison with the experimental data.

6. FLOW VISUALIZATION STUDY

A preliminary flow visualization study, undertaken at the beginning of the research program to help appreciate important parameters affecting this form of moving surface boundary layer control, was described earlier (Chapter 2). Conducted in a glycerol-water solution tunnel with dye injection, the study proved useful in planning the design of aerodynamic models.

After conducting an extensive wind tunnel test program, extending over three years, and complimenting it with analytical and numerical studies, it was thought appropriate to undertake a flow visualization study again. The wind tunnel test results indicated rather impressive lift and stall characteristics suggesting remarkable effectiveness for this form of boundary layer control. Furthermore, detailed pressure distribution data implied rather complex character of the flow, on the top surface, with separation and reattachment regions. Of course, their transient character would add to the complexity making even elaborate numerical models of the flow merely approximate.

With experimental and numerical results in hand, and some appreciation as to the challenging character of the associated fluid dynamics, a flow visualization study at this stage should prove more meaningful. In spite of its qualitative character, the study would at least tend to attest the effectiveness of the concept as the experiments have suggested. Furthermore, it would give visual confirmation of the complex flow implied by the pressure data. Thus the main objective of the flow visualization study was to corroborate, at least in a preliminary fashion, potential of the moving surface boundary layer control and have some visual appreciation as to the associated flow field.

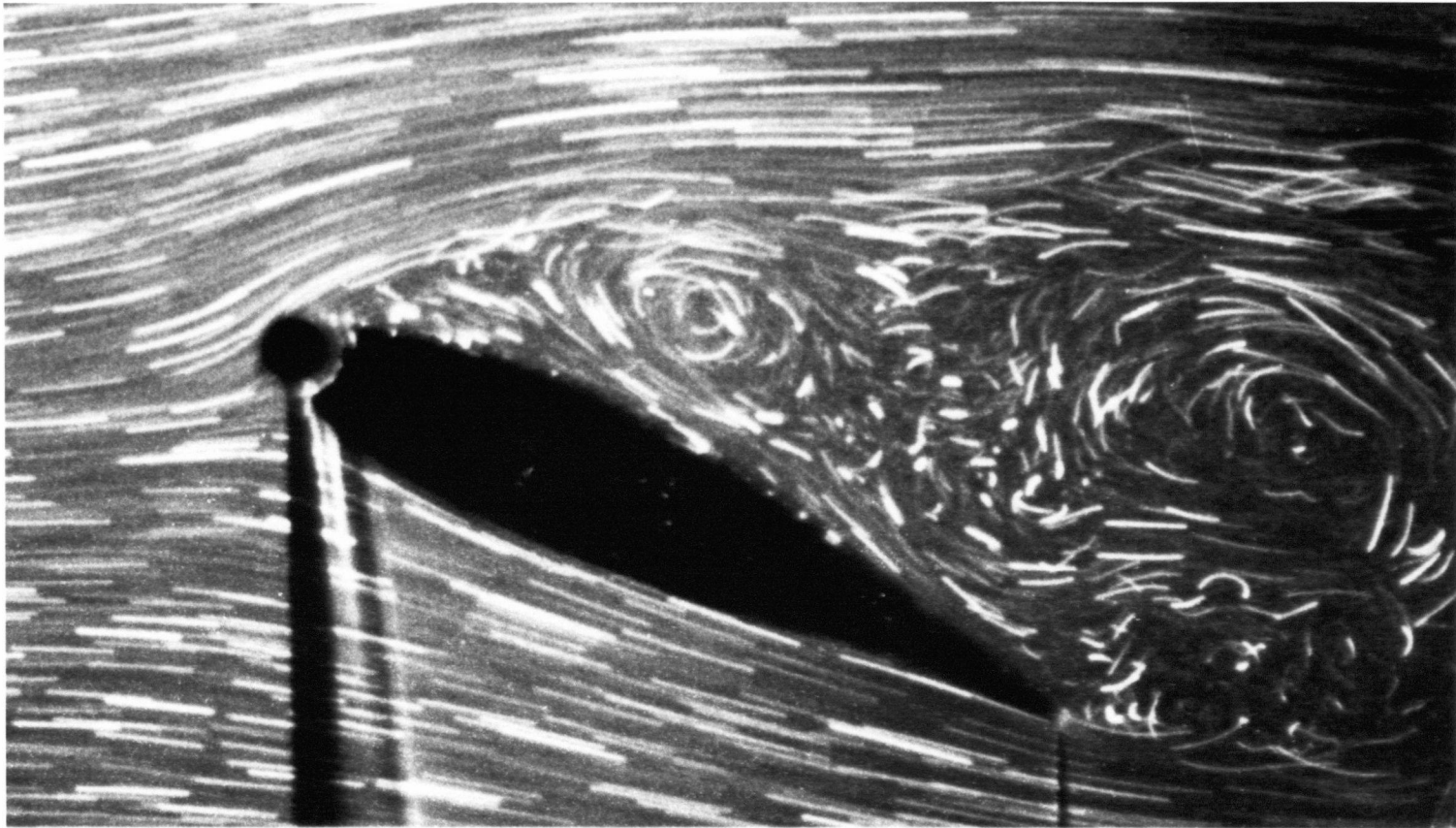
The flow visualization study was carried out in the excellent closed circuit water channel facility in the laboratory of Professor T. Yokomizo at the Kanto

Gakuin University, Yokohama, Japan. A two dimensional model of the NACA 63-218 (modified) airfoil was constructed from plexiglas and fitted with a leading edge cylinder, driven by a compressed-air motor. A suspension of fine aluminum powder was used in conjunction with slit lighting to visualize streaklines. Both angle of attack and cylinder speeds were systematically changed and still photographs as well as a video movie taken.

The study showed, rather dramatically, effectiveness of this form of boundary layer control (Figure 6-1). Presented in Figure 6-2 are a few of the steady state pictures, taken at several angles of attack, with and without the cylinder rotation. In absence of the cylinder rotation, a well defined separation bubble is quite apparent, particularly at higher angles of attack, with large scale vortices sweeping away downstream. However, with the cylinder rotating at $U_c/U \geq 8$, an essentially attached flow is established over most of the upper surface of the airfoil.

At relatively lower rates of cylinder rotation (say $U_c/U = 2, 3, 4$) the flow character was found to be similar to that observed at $U_c/U = 0$ with the separation and reattachment regions progressively shifting downstream as the rotation rate increased. This is apparent through the transient flow patterns depicted in Figure 6-3 where the cylinder rotation quickly increases from $U_c/U = 0$ to 6.

In fact, the flow pattern was found to be quite unsteady with the vortex layer separating and forming a bubble on reattachment, the whole structure drifting downstream, diffusing and regrouping as different scales of vortices. The video movie shows this transient behavior quite vividly. Ultimately the flow sheds large as well as small scales of vorticity. Thus the flow character suggested by the experimentally obtained time average pressure plots appears to be quite accurate. Furthermore, this also explains why the numerical procedure adopted can predict such highly complex and transient flow only in an approximate fashion. In fact, considering the formidable character of the flow, it represents a good approximation.



$Re = 4 \times 10^4$

$\alpha = 25^\circ, U_c/U = 0$

Figure 6-1 Typical photographs taken during the flow visualization study showing remarkable effectiveness of the moving surface boundary-layer control procedure: (a) highly separated flow, at a high angle of attack, in absence of the boundary-layer control;



$Re = 4 \times 10^4$

$\alpha = 25^\circ, U_c/U = 10$

Figure 6-1 Typical photographs taken during the flow visualization study showing remarkable effectiveness of the moving surface boundary-layer control procedure: (b) essentially attached flow established through cylinder rotation.

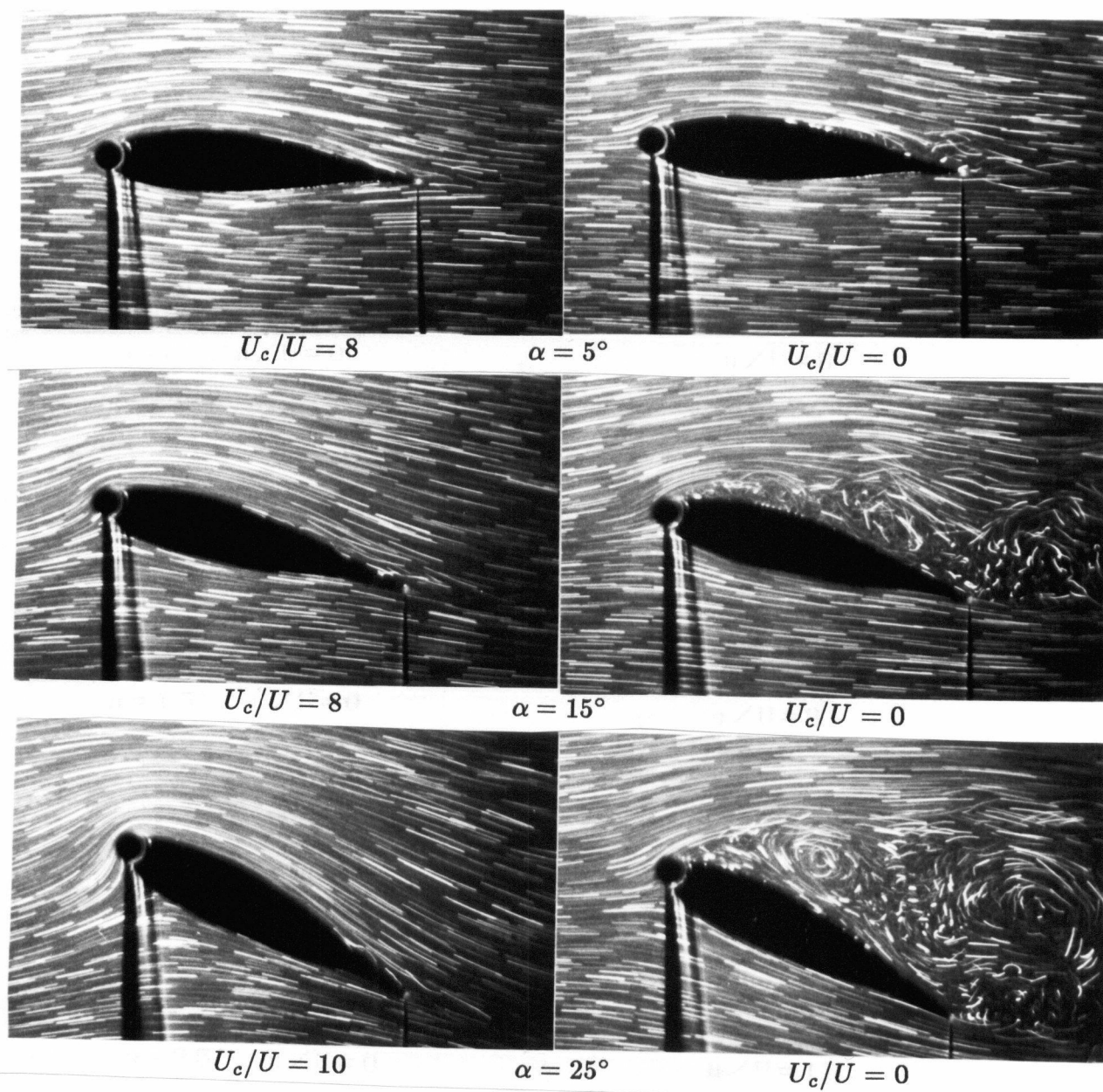


Figure 6-2 Flow visualization photographs showing the steady flow over the airfoil at various angles of attack with and without the rotation of the leading edge.

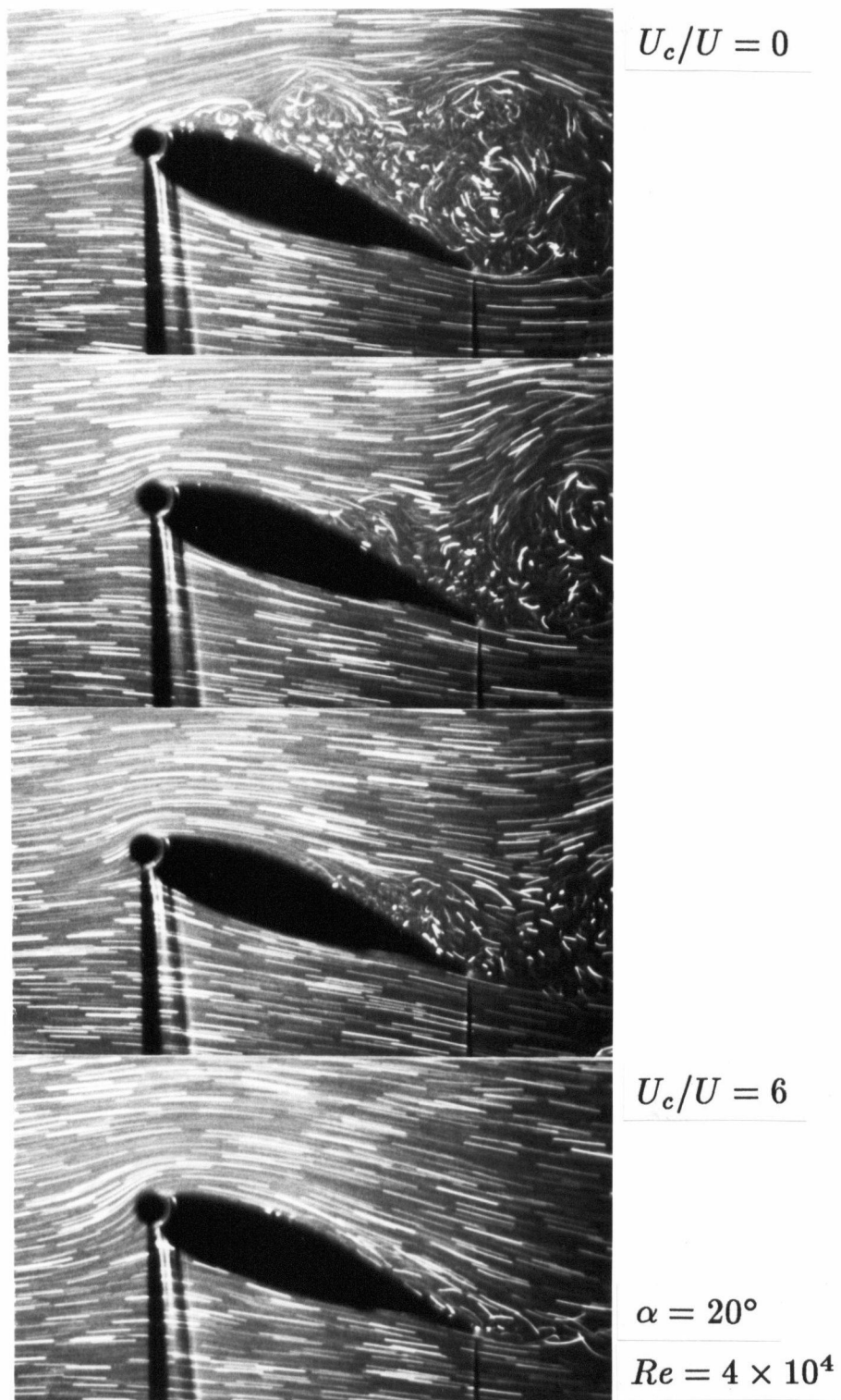


Figure 6-3 Flow visualization photographs showing the transition from the highly separated flow in the absence of cylinder rotation to the essentially reattached flow at $U_c/U = 6$.

7. CLOSING COMMENTS

7.1 Concluding Remarks

The well organized comprehensive experimental program, complemented by analytical, numerical, and flow visualization studies, has provided a considerable amount of useful information of fundamental importance. Only more important conclusions based on results obtained with different configurations are summarized here.

Leading-edge-cylinder

The experimental results with a symmetrical Joukowsky and NACA 63-218 (modified) airfoils using a leading edge rotating cylinder bring to light several interesting points of information:

- In general, rotation of the cylinder results in increased suction over the leading edge. It is the propagation of this lower pressure downstream, however, that determines the effectiveness of the rotation. This depends mainly on the geometry of the nose and smoothness of transition from the cylinder to the airfoil surface. A gap size greater than 3 *mm* substantially decreases beneficial effect of the cylinder rotation.
- The increased momentum injection into the boundary layer, with an increase in speed of rotation, delays the separation of flow from the upper surface (stall) resulting in a higher $C_{L,max}$. The existence of a critical speed is also evident beyond which momentum injection through a moving surface appears to have relatively less effect.
- With the rotation of the cylinder the onset of flow separation occurs at relatively higher angles of attack. The upper surface flow remains attached up to

a distance downstream of the leading edge at which point it separates, leading to a large separation bubble, with reattachment towards the trailing edge. The flow, therefore, is not completely separated from the airfoil, thus resulting in a flatter stall peak.

- The use of a leading-edge-cylinder extends the lift curve without substantially changing its slope thus considerably increasing the maximum lift coefficient and stall angle. For example, in the case of Joukowsky model I, the $C_{L,max}$ increased by around 68% with the stall delayed from 16° to 32° (based on the unmodified reference configuration). For model II and the NACA airfoil the improvement in performance was even better. The Joukowsky model II showed an increase in $C_{L,max}$ by around 110% with the stall delayed from 10° to 28° . The corresponding results for NACA 63-218 (modified) airfoil indicated a $C_{L,max}$ increase of 108% with a delay in stall from 12° to 45° .
- The configuration with a rotating cylinder on the upper side of the leading edge appears to be quite promising. Although the peak $C_{L,max}$ realized with the cylinder rotation was slightly less (1.95 against 2.22) compared to the two-cylinder configuration, it does have a major advantage in being mechanically simple in terms of design and application. The increase in $C_{L,max}$ at $U_c/U = 4$ by around 130% and the delay in stall from 10° to 48° is quite impressive.
- The tests using the NACA 63-218 model showed substantial improvement in lift to drag ratio at all angles of attack.

Scooped cylinder at the leading edge

Effectiveness of the leading-edge-cylinder can be improved at lower speeds of rotation by using a scooped configuration. The rotating air scoop appears to, in effect, slow down the flow over the lower surface and redirect more air over the upper surface. However, at high rates of rotation it appears to the flow effectively as a solid cylinder and there is no particular advantage in using the scoop configuration.

Trailing-edge-cylinder

In contrast to the leading-edge-cylinder, the use of a trailing-edge-cylinder substantially increases the lift *before* stall. The rotating trailing-edge-cylinder acts like a flap shifting the C_L vs. α plots to the left. A high rate of rotation of this cylinder results in a dramatic increase in suction, over the airfoil upper surface, thus giving a larger lift. Furthermore, it can be used in conjunction with the leading-edge-cylinder resulting in impressive values of lift over the whole range of low to moderately high angles of incidence ($\alpha \leq 18^\circ$).

Upper-surface-cylinders

- Presence of a steep positive pressure gradient near the leading edge of the airfoil at large angles of attack requires the rotation of the nose to avoid separation at that point. But depending on the angle of attack, the adverse pressure gradient may still cause flow separation further downstream. Since the flow remains attached at the leading edge, the lift continues to increase with the angle of attack, while the flow remains separated over most of the upper surface, resulting in an increase in pressure drag (as evident from a reduced pressure recovery at the trailing edge). The use of a second cylinder is now required to further improve the lift and stall characteristics.
- Protrusion of the upper-surface-cylinders in the flow has an adverse effect on the aerodynamic characteristics of the airfoil at low angles of attack (Joukowski model II). In absence of the cylinder rotation, the flow separates at the location of the cylinder resulting in a decrease in lift and an increase in drag. However, their rotation increases the $C_{L,max}$ and delays stall. The forward upper-surface-cylinder is particularly effective in this respect. This is, in fact, expected since the adverse pressure gradient is highest close to the leading edge. Further improvements in the $C_{L,max}$ and stall angle are possible when the forward upper-

surface-cylinder is used in conjunction with the leading-edge-cylinder. This configuration is expected to result in lower drag due to almost complete recovery of pressure at the trailing edge at even moderately high angles of attack. The increase in $C_{L,max}$ was observed to be around 160% with the stall delayed to 36° ($U_c/U = 4$ for both cylinders).

Analytical and numerical models

- As expected, the analytical potential flow model, based on the Joukowski transformation, is limited in scope. It does predict trends quite accurately, particularly when the leading-edge-cylinder configuration operates at a relatively small angle of attack.
- The numerical surface singularity approach with viscous correction and accounting for wind tunnel wall confinement significantly improves correlation. However, discrepancies between experimental and numerical results do remain. Partly this is contributed by the experimental results themselves as the flow is not entirely two-dimensional due to presence of gaps in the tunnel walls (necessary to support the model on an externally located balance and drive the cylinder(s) through the motor(s) mounted outside the tunnel). The communication thus created between the internal flow field and the outside atmosphere will tend to lower the slope of the lift curve.
- The numerical model generally predicts $C_{L,max}$ value with reasonable accuracy. Discrepancy in the stall angle is primarily due to an error in the slope of the lift curve as explained above. The assumption of constant pressure across the shear layer is no longer valid after it has separated and will lead to inaccuracies. Obviously, more accurate prediction of the pressure in a separated boundary layer with flow reversal would require the solution of the full Navier-Stokes equations at an enormous effort and cost.

- Considering the highly complex character of the flow, with large separated regions and reattachment, the numerical model has performed remarkably well. Besides other parameters, its effectiveness substantially depends on the successful modelling of the cylinder rotation. The two procedures used here, the concept of slip-velocity and counter-rotating vortex pair, are, at best, approximate and amenable to further sophistication.

Flow visualization

The flow visualization study confirmed effectiveness of the concept in a spectacular fashion. It gave better appreciation of the complex flow with a separation bubble and large turbulent wake. The unsteady flow field is not stable but oscillates in the streamwise direction. Furthermore, it substantiated the flow features revealed by the measured pressure profiles in a qualitative fashion.

7.2 Recommendations for Future Research

The investigation reported here has provided considerable insight into the operation and effectiveness of the moving surface boundary-layer control. Perhaps its most important contribution lies in laying a sound foundation for further study of this challenging problem. Only a small step has been taken, however, and there is considerable scope for further exploration and innovation. A few of the promising avenues are indicated below:

- (i) Results suggest existence of an optimum location for the upper leading-edge cylinder. Efforts aimed at identifying that location are particularly necessary, because of the mechanical simplicity of the single-cylinder configuration, and are likely to be rewarding.
- (ii) The leading-edge-scooped-cylinder study should be pursued further particularly with different scoop geometries and a systematic variation of the cylinder

rotation at lower spectrum of the speed. With the optimum scoop configuration and speed range established, its effectiveness at the optimum location as arrived in (i) should be assessed. The scoop geometry appears particularly attractive due to its favorable performance at relatively lower speeds of rotation and partial flap effect. However, it also requires more precise balancing procedure.

- (iii) Effectiveness of the scooped-cylinder geometry at the trailing edge of the airfoil should be explored. It may lead to a more efficient flap.
- (iv) Effect of roughness of the rotating cylinder needs to be studied in a systematic fashion.
- (v) It appears that further improvement in $C_{L,max}$ can be achieved through the use of twin-cylinder configurations involving combinations of schemes suggested in (i)–(iv).
- (vi) The effect of gaps in the wind tunnel walls must be established precisely through a systematic study to assess contribution of the spanwise flow on the slope of the lift curve.
- (vii) In practical application, the rotating cylinder may be located on a tapered aerodynamic surface of a finite aspect ratio. Hence, it would be useful to study performance of the cylinder in yawed as well as three-dimensional conditions.
- (viii) Considerable scope exists to improve the mathematical model used in the numerical analysis. However, application of the complete Navier–Stokes equations at an enormous effort and cost may not be necessary. The focus should be on further refinement of the approaches developed in the thesis, with emphasis on improvement in the boundary-layer and momentum-injection models. Several procedures are available here:
 - (a) solve for the shape of the separated streamline and use it to arrive at a modified airfoil profile for use with the equivalent airfoil scheme.
 - (b) application of sources and sinks to model separation bubbles.

- (c) incorporation of the experimentally measured information to model the separated boundary layer geometry.
- (d) modelling of the cylinder rotation through slip velocity accounting for its functional dependence on dissipation, rotation, and angle of attack.

All of these promise to improve correlation between the measured and predicted pressure plots and hence the lift characteristics.

REFERENCES

- [1] Goldstein, S., *Modern Developments in Fluid Mechanics*, Vols. I and II, Oxford University Press, 1938.
- [2] Lachmann, G.V., *Boundary Layer and Flow Control*, Vols. I and II, Pergamon Press, 1961.
- [3] Rosenhead, L., *Laminar Boundary Layers*, Oxford University press, 1966.
- [4] Schlichting, H., *Boundary Layer Theory*, McGraw-Hill Book Company, 1968.
- [5] Chang, P.K., *Separation of Flow*, Pergamon Press, 1970.
- [6] Thwaites, B., *Incompressible Aerodynamics*, Clarendon Press, 1960, p. 215.
- [7] Magnus, G., "Ueber die Verdichtung der Gase an der Oberflache Glatte Körper," *Poggendorfs Annalen der Physik und Chemie*, Vol. 88, No. 1, 1853, pp. 604-610.
- [8] Swanson, W.M., "The Magnus Effect: A Summary of Investigation to Date," *Transactions of the ASME, Journal of Basic Engineering*, Vol. 83, September 1961, pp. 461-470.
- [9] Iverson, J.D., "Correlation of Magnus Force Data for Slender Spinning Cylinders," AIAA 2nd Atmospheric Flight Mechanics Conference, Palo Alto, California, September 11-13, 1972, Paper No. 72-966.
- [10] Betz, A., "History of Boundary Layer Control in Germany," *Boundary Layer and Flow Control*, Editor: G.V. Lachmann, Pergamon Press, Vol. I, pp. 1-20.
- [11] Flettner, A., "The Flettner Rotor Ship," *Engineering*, Vol. 19, January 1925, pp. 117-120.
- [12] Favre, A., "Contribution a l'Etude Experimentale des Mouvements Hydrodynamiques a Deux Dimensions," Thesis presented to the University of Paris, 1938.
- [13] Alvarez-Calderon, A., and Arnold, F.R., "A Study of the Aerodynamic Char-

- acteristics of a High Lift Device Based on Rotating Cylinder Flap," Stanford University Technical Report RCF-1, 1961.
- [14] Brown, D.A., "Peruvians Study Rotating-Cylinder Flap," *Aviation Week and Technology*, Vol. 88, No. 23, December 1964, pp. 70-76.
- [15] Brooks, J.D., "Effect of a Rotating Cylinder at the Leading and Trailing Edges of a Hydrofoil," U.S. Naval Ordnance Test Station, Department of the Navy, NAVWEPS Report 8042, April 1963.
- [16] Steele, B.N., and Harding, M.H., "Applications of Rotating Cylinders for Ship Maneuvering," *Journal of Naval Architecture*, July 1971, pp. 27-29.
- [17] Cichy, D.R., Harris, J.W., and MacKay, J.K., "Flight Tests of a Rotating Cylinder Flap on a North American Rockwell YOY-10A Aircraft," NASA CR-2135, November 1972.
- [18] Weiberg, J.A., Giulianettij, D., Gambucci, B., and Innis, R.C., "Takeoff and Landing Performance and Noise Characteristics of a Deflected STOL Airplane with Interconnected Propellers and Rotating Cylinder Flaps," NASA TM X-62, 320, December 1973.
- [19] Cook, W.L., Mickey, D.M., and Quigley, H.G., "Aerodynamics of Jet Flap and Rotating Cylinder Flap STOL Concepts," AGARD Fluid Dynamics Panel on V/STOL Aerodynamics, Delft, Netherlands, April 1974, Paper No. 10.
- [20] "Rotating Cylinder Flaps Tested on OV-10A," *Aviation Week and Space Technology*, Vol. 95, No. 16, October 1971, p. 19, and No. 24, December 1971, cover page.
- [21] Tennant, J.S., "The Theory of Moving Wall Boundary Layer Control and its Experimental Application to Subsonic Diffusers," Ph.D. dissertation, Clemson University, May 1971.
- [22] Tennant, J.S., "A Subsonic Diffuser with Moving Walls for Boundary-Layer Control," *AIAA Journal*, Vol. 11, No. 2, February 1973, pp. 240-242.
- [23] Johnson, W.S., Tennant, J.S., and Stamps, R.E., "Leading Edge Rotating Cylinder for Boundary-Layer control on Lifting Surfaces," *Journal of Hydro-*

- dynamics*, Vol. 9, No. 2, April 1975, pp. 76–78.
- [24] Tennant, J.S., Johnson, W.S., and Krothapalli, A., “Rotating Cylinder for Circulation Control on an Airfoil,” *Journal of Hydronautics*, Vol. 11, No. 3, July 1976, pp. 102–105.
- [25] Tennent, J.S., Johnson, W.S., and Keaton, D.D., “On the Circulation of Boundary Layers along Rotating Cylinders,” *Journal of Hydronautics*, Vol. 11, No. 2, April 1977, pp. 61–63.
- [26] Tennant, J.S., Johnson, W.S., and Keaton, D.D., “Boundary Layer Flow from Fixed to Moving Surfaces including Gap Effects,” *Journal of Hydronautics*, Vol. 12, No. 2, April 1978, pp. 81–84.
- [27] Modi, V.J., Sun, J.L.C., Akutsu, T., Lake, P., McMillian, K., Swinton, P.G., and Mullins, D., “Moving Surface Boundary Layer Control for Aircraft Operation at High Incidence,” *Journal of Aircraft*, AIAA, Vol. 18, No. 11, November 1981, pp. 963–968.
- [28] Huang, M. K., and Chow, C. Y., “Trapping of a Free Vortex by Joukowski Airfoils,” *AIAA Journal*, Vol. 20, No. 3, March 1982, pp. 292–298.
- [29] Chow, C. Y., Huang, M. K., and Yan, C. Z., “Unsteady Flows About a Joukowski Airfoil in the Presence of Moving Vortices,” *AIAA Journal*, Vol. 23, No. 5, May 1985, pp. 657–658.
- [30] Theodorsen, T., “Theory of Wing Sections of Arbitrary Shape,” NACA Report No. 411, 1931.
- [31] Halsey, N.D., “Potential Flow Analysis of Multi-element Airfoils Using Conformal Mapping,” *AIAA Journal*, Vol. 17, No. 12, December 1979, pp. 1281–1288.
- [32] Kennedy, J.L., “The design and Analysis of Airfoil Sections,” Ph.D. dissertation, The University of Alberta, Spring 1977.
- [33] Mavriplis, F., “Aerodynamic Research on High Lift Systems,” *Canadian Aeronautics and Space Journal*, May 1971, pp. 175–183.
- [34] Keller, H.B., and Cebeci, T., “Accurate Numerical Methods for Boundary-Layer Flows, part 1, Two-Dimensional Laminar Flows,” *Lecture Notes in*

Physics, 8, Proceedings of the Second International Conference on Numerical Methods in Fluid Dynamics, p. 92, Springer-Verlag, New York, 1971.

- [35] Keller, H.B., and Cebeci, T., "Accurate Numerical Methods for Boundary-Layer Flows, part 2, Two-Dimensional Turbulent Flows," *AIAA Journal*, Vol. 10, p. 1193, 1972.
- [36] Cebeci, T., and Smith, A.M.O., *Analysis of Turbulent Boundary Layers*, Academic Press, New York, 1974.
- [37] Cebeci, T., and Bradshaw, P., *Momentum Transfer in Boundary Layers*, Hemisphere-McGraw Hill, Washington, 1977.
- [38] Bhatel, I.C., and Bradley, R.G., "A Simplified Model for the Analysis of Multi-Element Airfoils Near Stall," General Dynamics, Corvair Aerospace Division, Forth Worth, Texas, USA, 1972.
- [39] Mokhtarian, F., and Modi, V.J., "Fluid Dynamics of Airfoils with Circulation Control for V/STOL Application," *AIAA Atmospheric Flight Mechanics Conference*, August 1984, paper No. AIAA-84-2090.
- [40] Mokhtarian, F., and Modi, V.J., "Joukowsky Airfoil with Circulation Control," *AIAA Atmospheric Flight Mechanics Conference*, August 1985, paper No. 85-1772-CP.
- [41] Mokhtarian, F., and Modi, V.J., "Fluid Dynamics of Airfoils with Moving Surface Boundary Layer Control," *AIAA Atmospheric Flight Mechanics Conference*, August 1986, paper No. 86-2184-CP; also *Journal of Aircraft*, in press.

APPENDIX: THE COMPUTER PROGRAM

Fortran program to calculate the complete flow field over an airfoil. Given the external potential flow solution, the program uses the Thin Shear Layer approximations to calculate the boundary-layer displacement thickness distribution for two-dimensional laminar and turbulent boundary layers and construct an equivalent airfoil shape which is then used to recalculate the the outer velocity distribution.

```

.   COMMON/BLC0/NP,NX,NXT,NTR,NSEP,NFLOW,ETA,E,VGP,VISC,UINF,
.   1   DETA(111),A(111),ETA(111),NGAP(2),UC
.   COMMON/BLCC/X(99),UE(99),P1(99),P2(99),ALFA(99),RX(99),
.   1   CF,ALFA1,ALFA2,RTHETA(99),USURF(99)
.   COMMON/BLCP/DELV(111),F(111,2),U(111,2),V(111,2),B(111,2)
.   COMMON/BLCT/DELSX(2,99),CFX(99)
.   COMMON/IDEN/NUMX(2,99)
.   COMMON/SCTN/AOA,NUM,NE,XORIG(99),YSCTN(99),XOLD(50)
.   DIMENSION  XSCTN(99),YORIG(99),GAMMA(99)
-----
.   PI=4.*ATAN(1.)
.   VISC=1.6E-04
.   RCHORD=2.31E+05
.   UINF=RCHORD*VISC
-----
.   Input the potential flow velocity distribution
-
.   NUM=65
.   READ(50,1000) (XSCTN(I),YSCTN(I),GAMMA(I),I=1,NUM)
-
00010 NFLAG=0
.   DO 15 I=1,NUM
.   XORIG(I)=XSCTN(I)
.   YORIG(I)=YSCTN(I)
00015 CONTINUE
-----
.   Input Angle of Attack
-
.   WRITE(6,1100)
.   READ (5,1200)AOA
-
.   Point of Effectiveness of Cylinder
-
.   XSEP=0.30
.   XS1 =XSEP-.03
.   XS2 =XSEP+.03
-
.   Locate the leading edge stagnation point
-
.   DO 20 I=1,NUM

```

```

.   IF(GAMMA(I)*GAMMA(I+1) .GT. 0.) GOTO 20
.   ISTAG=I+1
.   GOTO 25
00020 CONTINUE
.   WRITE(6,3000)
.   STOP
-----
.   Transform the coordinates for use in B.L. calculations.
.   For the upper surface;
-
00025 NXT=ISTAG
-
.   X0=XSCTN(ISTAG)
.   IF(YSCTN(ISTAG) .GT. 0.) X0=-X0
.   J=ISTAG
.   NGAP(1)=0
.   NGAP(2)=0
.   NSEP = 99
-
.   DO 30 I=1,NXT
.   X(I)=XSCTN(J)+X0
.   NUMX(1,I)=J
.   IF(YSCTN(J) .GT. 0.) GOTO 26
.   X(I)=-X(I)+2.*X0
.   IF(X(I) .LT. 0.) X(I)=-X(I)+2.*X0
.   IF(NGAP(1) .NE. 0) GOTO 29
.   IF(INT(100.*XSCTN(J)) .EQ. 5) NGAP(1)=I
.   GOTO 29
00026 IF(INT(100.*XSCTN(J)) .EQ. 5) NGAP(2)=I
.   IF(XSCTN(J) .GE. XS1 .AND. XSCTN(J) .LE. XS2) NSEP=I
00029 UE(I)=ABS(GAMMA(J))*UINF
.   USURF(I)=0.0
.   J=J-1
00030 CONTINUE
.   NFLOW=1
.   IF(NGAP(1) .LE. 2) NGAP(1)=3
.   NTR =99
.   GOTO 45
-
.   For the lower surface:
-
00035 ISTAG=ISTAG-1
.   NXT=NUM+1-(ISTAG)
.   X0=XSCTN(ISTAG)
.   IF(YSCTN(ISTAG) .LT. 0.) X0=-X0
.   J=ISTAG
-
.   DO 40 I=1,NXT
.   X(I)=XSCTN(J)+X0

```

```

.     NUMX(2,I)=J
.     IF(YSCFN(J) .LT. 0.) GOTO 36
.     X(I)=-X(I)+2.*X0
.     IF(X(I) .LT. 0.) X(I)=-X(I)+2.*X0
00036 UE(I)=ABS(GAMMA(J))*UINF
.     USURF(I)=0.0
.     J=J+1
00040 CONTINUE
.     NFLOW=2
.     NGAP(1)=0
.     NGAP(2)=0
.     NTR =99
.     NSEP=99
00045 UE(1)=0.

```

The program consists of a MAIN routine, which contains the logic of the computations and construction of the Equivalent Airfoil shape, and ten subroutines: INPUT, GRID, IVPL, GROWTH, EDDY, GAP, CMOM, SOLVE, OUTPUT, and UEDIST. The function of each subroutine is as follows:

INPUT: Reads ν and η_∞ at $x = 0$ and U_e , and m as functions of x .

GRID: Generates the initial-velocity profile for a laminar flow.

GROWTH: Controls the growth of the boundary layer.

EDDY: Contains the eddy-viscosity formulas.

GAP: Accounts for the boundary conditions on the moving surface.

CMOM: Contains the coefficients of the differenced momentum equation.

SOLVE: Contains the recursion formulas that arise in the block elimination method.

OUTPUT: Prints out the desired boundary-layer parameters and profiles. This subroutine also contains the checks for transition to turbulence and final separation.

UEDIST: Calculates the potential flow over the displacement surface, accounting for separated flow and wall confinement effects. A slightly different version of this same routine is used to obtain the starting potential flow pressure distribution. Reference [37] contains the detail derivation and finite-difference formulation of the TSL equations as well as the logic of most of the subroutines used in the program.

```

.     Iteration count
-
.     ITMAX=6
-----
.     ALFA(1)=0.0
.     NX=1
-
.     CALL INPUT
.     CALL GRID
.     CALL IVPL
-----
00050 IF(NFLOW .EQ. 1) WRITE(7,9100)
.     IF(NFLOW .EQ. 2) WRITE(7,9200)

```

```

.   WRITE(7,9500) NX,X(NX)
.   RX(NX)=UE(NX)*X(NX)/VISC
.   IF(NX .GT. 1) ALFA(NX)=0.5*(X(NX)+X(NX-1))/(X(NX)-X(NX-1))
.   ALFA1=P1(NX)+ALFA(NX)
.   ALFA2=P2(NX)+ALFA(NX)
.   IT=0
.   IF(NX .EQ. NGAP(1)) CALL GAP
.   IF(NX .GE. NTR )   CALL EDDY
00060 IT=IT+1
.   IF(IT .LE. ITMAX) GOTO 70
.   WRITE(7,8100)
.   WRITE(8,8100)
.   GOTO 80
-----
00070 CALL CMOM
.   CALL SOLVE
-----
.   Check for convergence
-
00061 IF(NX .GE. NTR) GOTO 62
-----
.   Laminar flow
-
.   IF(ABS(DELV(1)) .GT. 1.0E-05) GOTO 60
.   GOTO 75
-----
.   Turbulent flow
-
00062 IF(V(1,2) .EQ. 0.) GOTO 75
.   IF(ABS(DELV(1)/(V(1,2)+0.5*DELV(1))) .GT. 0.02) GOTO 60
-----
.   Check for GROWTH
-
00075 IF(NX .EQ. 1) GOTO 90
.   IF(NP .EQ. 111) GOTO 90
.   IF(ABS(V(NP,2)) .LE. 1.0E-03) GOTO 90
.   CALL GROWTH
.   IT=0
.   GOTO 60
00080 IF(NX .LE. NGAP(2)) GOTO 90
.   NX=NX-1
.   NSEP=NX
00090 CALL OUTPUT
.   IF(NX .LE. NXT) GOTO 50
-----
.   Modify the airfoil surfaces using the calculated displacement thicknesses
.   at each station.
-
.   IF(NSEP .GT. NXT) NSEP=NXT
.   DO 150 I=2,NSEP
.   J=NUMX(NFLOW,I)

```

```

.   IF(I .EQ. NSEP) GOTO 110
.   Y2=0.5*(YORIG(J+1)+YORIG(J))
.   X2=0.5*(XORIG(J+1)+XORIG(J))
.   GOTO 120
00110 Y2=YORIG(J)
.   X2=XORIG(J)
00120 Y1=0.5*(YORIG(J)+YORIG(J-1))
.   X1=0.5*(XORIG(J)+XORIG(J-1))
.   TETA=ATAN2(Y2-Y1,X2-X1)
.   DELTA=DELSX(NFLOW,I)
.   DELY=-COS(TETA)*DELTA
.   DELX= SIN(TETA)*DELTA
.   IF(NFLOW .EQ. 1 .AND. DELY .LT. 0.) DELY=-DELY
.   IF(NFLOW .EQ. 2 .AND. DELY .GT. 0.) DELY=-DELY
.   YSCTN(J)=YORIG(J)+DELY
.   XSCTN(J)=XORIG(J)+DELX
00150 CONTINUE
-
.   IF(NFLOW .NE. 1) GOTO 200
.   IF(NSEP .EQ. NXT) NFLAG=1
.   NDIFF=NUMX(1,NSEP)-1
.   GOTO 35
-----
00200 NE=NUM-NDIFF
-
.   DO 225 I=1,NDIFF
.   XOLD(I)=XORIG(I)
00225 CONTINUE
-
.   DO 250 I=1,NE
.   IE=I+NDIFF
.   XORIG(I)=XORIG(IE)
.   XSCTN(I)=XSCTN(IE)
.   YSCTN(I)=YSCTN(IE)
00250 CONTINUE
.   WRITE(9,2000) (XSCTN(I),YSCTN(I),I=1,NE)
-----
.   Smooth the airfoil surfaces;
-
.   CALL INTRPL(0,NE,XSCTN,YSCTN,XORIG,YSCTN)
-
.   IF(NFLAG .EQ. 1) WRITE(6,9900)
-
.   Compute the external velocity distribution on the new equivalent airfoil;
-
.   CALL UEDIST
-
.   STOP
-----

```

```

01000 FORMAT(3(2X,F9.6))
01100 FORMAT('INPUT ANGLE OF ATTACK')
01200 FORMAT(F6.2)
02000 FORMAT(1X,F9.6,2X,F9.6)
03000 FORMAT(37H ERROR : NO STAGNATION POINT FOUND !!)
08100 FORMAT(1H ,16X,25HITERATIONS EXCEEDED ITMAX)
09100 FORMAT(16H UPPER SURFACE :)
09200 FORMAT(16H LOWER SURFACE :)
09500 FORMAT(1H ,4HNX =,I3,5X,3HX =,F10.5)
09900 FORMAT(40H NO SEPARATION FROM THE AIRFOIL SURFACE!)
.      END

```

This subroutine defines ν and specifies initial η_∞ at $x = 0$. If the boundary layer wants to grow (see GROWTH), the program computes its own η_∞ at the subsequent stations. Here we read U_e a function of x . Parameter m (Fortran name P2) is computed from the given external-velocity distribution, $U_e(x)$, and from the definition of m . The derivative of dU_e/dx (Fortran name DUDX) is obtained by using three-point Lagrange interpolation formulas.

```

.      SUBROUTINE INPUT
.      COMMON/BLC0/NP,NX,NXT,NTR,NSEP,NFLOW,ETA,E,VGP,VISC,UINF,
.      1      DETA(111),A(111),ETA(111),NGAP(2),UC
.      COMMON/BLCC/X(99),UE(99),P1(99),P2(99),ALFA(99),RX(99),
.      1      CF,ALFA1,ALFA2,RTHETA(99),USURF(99)
-----
.      ETAE =8.0
.      DETA(1)=0.01
.      VGP =1.05
-----
.      WRITE(7,9000) NXT,NTR,NSEP,VISC,UINF,ETAE,DETA(1),VGP
-----
.      Calculations based on Stagnation Flow conditions at X=0.
-
.      P2(1)=1.0
.      P1(1)=1.0
-
.      Calculation of Pressure-Gradient Parameter P2 (=m)
-
00050 DO 80 I=2,NXT
.      IF(I.EQ. NXT) GOTO 60
.      A1=(X(I)-X(I-1))*(X(I+1)-X(I-1))
.      A2=(X(I)-X(I-1))*(X(I+1)-X(I))
.      A3=(X(I+1)-X(I))*(X(I+1)-X(I-1))
.      DUDX=-(X(I+1)-X(I))/A1*UE(I-1)+(X(I+1)-2.0*X(I)+X(I-1))/
.      1      A2*UE(I)+(X(I)-X(I-1))/A3*UE(I+1)
.      GOTO 70
00060 A1=(X(I-1)-X(I-2))*(X(I)-X(I-2))
.      A2=(X(I-1)-X(I-2))*(X(I)-X(I-1))
.      A3=(X(I)-X(I-1))*(X(I)-X(I-2))

```

```

.      DUDX=(X(I)-X(I-1))/A1*UE(I-2)-(X(I)-X(I-2))/A2*UE(I-1)+
.      1  (2.0*X(I)-X(I-2)-X(I-1))/A3*UE(I)
00070 P2(I)=X(I)/UE(I)*DUDX
.      P1(I)=0.5*(P2(I)+1.0)
00080 CONTINUE
.      RETURN
_____
08000 FORMAT(3I3,2F10.6)
08100 FORMAT(3F10.6)
09000 FORMAT(1H ,6HNXT =,I3,11X,6HNTR =,I3,11X,6HNSEP =,I3/
.      1  1H ,6HVISC =,E11.6,3X,6HUINF =,F8.3/
.      2  1H ,6HETAE =,E11.6,3X,6HDETA1=,E11.6,3X,6HVGP =,
.      3  E11.6/)
.      END

```

This subroutine generates the grid normal to the flow. It requires the first initial $\Delta\eta$ -spacing and the variable grid parameter (VGP).

```

.      SUBROUTINE GRID
.      COMMON/BLC0/NP,NX,NXT,NTR,NSEP,NFLOW,ETA,E,VGP,VISC,UINF,
.      1  DETA(111),A(111),ETA(111),NGAP(2),UC
_____
.      IF((VGP-1.0) .LE. 0.001) GOTO 5
_____
.      Total number of grid points (normal to the flow)
.      NP=ALOG((ETA/E/DETA(1))*(VGP-1.0)+1.0)/ALOG(VGP)+1.0001
-
.      GOTO 10
00005 NP=ETA/E/DETA(1)+1.0001
00010 IF(NP .LE. 111) GOTO 15
.      WRITE(6,9000)
.      STOP
00015 ETA(1)=0.0
.      DO 20 J=2,NP
.      DETA(J)=VGP*DETA(J-1)
.      A(J)=0.5*DETA(J-1)
00020 ETA(J)=ETA(J-1)+DETA(J-1)
.      RETURN
_____
09000 FORMAT(1H ,37HNP EXCEEDED 111 - PROGRAM TERMINATED)
.      END

```

This subroutine generates initial-velocity profiles for laminar boundary layers at $x = 0$. The initial profiles for f (F), f' (U), and f'' (V) are given by:

$$f = \frac{\eta_{\infty}}{4} \left(\frac{\eta}{\eta_{\infty}} \right)^2 \left[3 - \frac{1}{2} \left(\frac{\eta}{\eta_{\infty}} \right)^2 \right]$$


```

.      DO 35 J=NP1,NP
.      F(J,1)=U(NP0,1)*(ETA(J)-ETA(NP0))+F(NP0,1)
.      U(J,1)=U(NP0,1)
.      V(J,1)=0.0
.      B(J,1)=B(NP0,1)
.      F(J,2)=U(NP0,2)*(ETA(J)-ETA(NP0))+F(NP0,2)
.      U(J,2)=U(NP0,2)
.      V(J,2)=V(J,1)
.      B(J,2)=B(NP0,2)
00035 CONTINUE
.      NNP=NP-(NP1-1)
.      WRITE(7,6000) NNP
.      RETURN
-----
06000 FORMAT(1H ,5X,13HETAE GROWTH -,I3,13H-POINTS ADDED)
09000 FORMAT(1H ,37HNP EXCEEDED 111 - PROGRAM TERMINATED)
.      END

```

For simplicity, an eddy-viscosity formulation that does not include the low Reynolds number effect and the mass transfer effect is used. These capabilities, if desired, can easily be incorporated into the formulas defined in the subroutine. The formulas for inner and outer eddy-viscosity expressions are given in section 5.1.

```

.      SUBROUTINE EDDY
.      COMMON/BLC0/NP,NX,NXT,NTR,NSEP,NFLOW,ETA,E,VGP,VISC,UINF,
.      1      DETA(111),A(111),ETA(111),NGAP(2),UC
.      COMMON/BLCP/DELV(111),F(111,2),U(111,2),V(111,2),B(111,2)
.      COMMON/BLCC/X(99),UE(99),P1(99),P2(99),ALFA(99),RX(99),
.      1      CF,ALFA1,ALFA2,RTHETA(99),USURF(99)
.      DIMENSION EDVIS(111)
-----
.      GAMTR=1.0
.      UEINTG=0.0
.      U1=1.0/UE(NTR-1)
.      DO 10 I=NTR,NX
.      U2=1.0/UE(I)
.      UEINTG=UEINTG+(U1+U2)*(X(I)-X(I-1))*0.5
00010 U1=U2
.      GG=8.35E-04*UE(NX)**3/(RX(NTR-1)**1.34*VISC**2)
.      EXPTM=GG*(X(NX)-X(NTR-1))*UEINTG
.      IF(EXPTM .LE. 10.0) GOTO 15
C      WRITE(7,9100) GG,UEINTG,EXPTM
.      GOTO 20
00015 GAMTR=1.0-EXP(-EXPTM)
00020 CONTINUE
.      IFLGD=0
.      RX2=SQRT(RX(NX))
.      RX4=SQRT(RX2)

```

```

. PPLUS=0.
. IF(V(1,2) .GE. 0.) PPLUS=P2(NX)/(RX4*(ABS(V(1,2)))**1.5)
. RX216=RX2*0.16
. EN=SQRT(1.0-11.8*PPLUS)
. CRSQV=EN*RX4*SQRT(ABS(V(1,2)))/26.
. J=1
. EDVISO=0.0168*RX2*(ETA(NP)-F(NP,2)+F(1,2))*GAMTR
00050 IF(IFLGD .EQ. 1) GOTO 100
. YOA=CRSQV*ETA(J)
. EDVISI=RX216*ETA(J)**2*V(J,2)*(1.0-EXP(-YOA))**2*GAMTR
. IF(EDVISI .LT. EDVISO) GOTO 200
-----
. IFLGD=1
00100 EDVIS(J)=EDVISO
. GOTO 300
00200 EDVIS(J)=EDVISI
. IF(J .LE. 2) GOTO 300
. IF(EDVIS(J) .GT. EDVIS(J-1)) GOTO 300
. EDVIS(J)=EDVIS(J-1)+(EDVIS(J-1)-EDVIS(J-2))*VGP
00300 B(J,2)=1.0+EDVIS(J)
. IF(B(J,2) .LT. 1.0) B(J,2)=1.0
. J=J+1
. IF(J .LE. NP) GOTO 50
. RETURN
-----
09100 FORMAT(1H ,2X,3HGG=,E14.6,3X,7HUEINTG=,E14.6,3X,6HEXPTM=,
. 1 E14.6)
. END

```

Once the location of the "lower gap" (start of the moving surface) is reached in the calculations, this subroutine is called to assign new boundary conditions. Velocities at the wall are also calculated for the airfoil surface after the location of the "upper gap" (end of the moving surface) in cases where slip-velocity is considered.

```

. SUBROUTINE GAP
. COMMON/BLC0/NP,NX,NXT,NTR,NSEP,NFLOW,ETA,E,VGP,VISC,UINF,
. 1 DETA(111),A(111),ETA(111),NGAP(2),UC
. COMMON/BLCP/DELV(111),F(111,2),U(111,2),V(111,2),B(111,2)
. COMMON/BLCC/X(99),UE(99),P1(99),P2(99),ALFA(99),RX(99),
. 1 CF,ALFA1,ALFA2,RTHETA(99),USURF(99)

```

Physical size of the gap in terms of the dimensionless variables;

```

. ETAGAP=ETA/E/4.

```

```

. JGAP=ALOG((ETAGAP/DETA(1))*(VGP-1.)+1.)/ALOG(VGP)+1.0001

```

Couette Flow profile of form $U=a+b(ETA)$ assumed for the flow in the gap and added to the B.L. profile at the edge of the gap.

```

.   WRITE(6,5000)
.   READ (5,5500) UC
-
.   IF=NX
.   IF(UE(IF) .EQ. 0.0) IF=IF+1
.   USURF(NX)=UINF/UE(IF)*UC
.   DO 100 J=1,JGAP
.   UGAP=USURF(NX)*(1.-ETA(J)/ETAGAP)
.   IF(U(J,2) .LT. UGAP) U(J,2)=UGAP
00100 CONTINUE
-
.   A description and variable definition for the following cubic spline fitting
.   routine can be found in the subroutine INTERPL at the end of the program.
-
.   REAL*8 W(1015)
.   DIMENSION YSPLN(91),DY(91)
.   DIMENSION YY1(91),YY2(91)
-
.   The amount of smoothing :
-
.   DYMIN=0.01
.   DO 200 J=1,JGAP
.   DY(J)=DYMIN+ETA(J)
00200 CONTINUE
.   DYMAX=DYMIN+2.*ETAGAP
.   JGAPP=JGAP+1
.   DO 225 J=JGAPP,NP
.   DY(J)=DYMAX-ETA(J)
.   IF(DY(J) .LT. DYMIN) DY(J)=DYMIN
00225 CONTINUE
.   S=0.1
-
.   Set up the fit parameters :
-
.   DO 250 J=1,NP
.   YSPLN(J)=U(J,2)
00250 CONTINUE
-
.   CALL SPLNFT(ETA, YSPLN,DY,S,NP,W,&991)
-
.   Find the fitted values :
-
.   CALL SPLN (ETA, YSPLN,YY1,YY2,NP,&992)
-
.   DO 275 J=1,NP
.   U(J,2)=YSPLN(J)
.   V(J,2)=YY1(J)
00275 CONTINUE
-
.   WRITE(6,4400)
.   WRITE(6,4500)(J,ETA(J),F(J,2),U(J,2),V(J,2),B(J,2),J=1,NP)

```

```

.   WRITE(7,1000)
-
.   Assign Boundary Conditions in the gap region ;
-
.   IS=NX+1
.   IE=NGAP(2)
.   DO 325 I=IS,IE
.   USURF(I)=UINF/UE(I)*UC
00325 CONTINUE
-
.   And Slip Velocity after the gap:
-
.   ESEP=EXP(-X(NSEP))
.   U0=USURF(IE)/(EXP(-X(IE))-ESEP)
.   IS=IE+1
-
.   DO 350 I=IS,NSEP
.   USURF(I)=U0*(EXP(-X(I))-ESEP)
00350 CONTINUE
-
.   NSEP=99
.   NTR =NGAP(2)
-
.   RETURN
-----
00991 WRITE(7,9001)
.   STOP
-
00992 WRITE(7,9002)
.   STOP
-----
01000 FORMAT('START GAP CALCULATIONS')
04400 FORMAT(1H ,2X,1HJ,3X,4H ETA,6X,1HF,12X,1HU,12X,1HV,10X,1HB)
04500 FORMAT(1H ,I3,F8.3,4E12.4)
05000 FORMAT('INPUT CYLINDER SURFACE VELOCITY')
05500 FORMAT(F5.2)
09001 FORMAT('ERROR : N<=2 OR X-VALUES OUT OF ORDER. ')
09002 FORMAT('ERROR : VARIABLE OUT OF FITTED RANGE. ')
.   END

```

This is one of the most important subroutines of the computer program. It defines the coefficients of the linearized momentum equations [37].

```

.   SUBROUTINE CMOM
.   COMMON/BLC0/NP,NX,NXT,NTR,NSEP,NFLOW,ETA,E,VGP,VISC,UINF,
.   1      DETA(111),A(111),ETA(111),NGAP(2),UC
.   COMMON/BLCC/X(99),UE(99),P1(99),P2(99),ALFA(99),RX(99),
.   1      CF,ALFA1,ALFA2,RTHETA(99),USURF(99)
.   COMMON/BLCP/DELV(111),F(111,2),U(111,2),V(111,2),B(111,2)
.   COMMON/BLC6/S1(111),S2(111),S3(111),S4(111),S5(111),S6(111),

```

```

. 1          R1(111),R2(111),R3(111)
.
. DO 100 J=2,NP
.
. Present station
.
. U2B =0.5*(U(J,2)**2+U(J-1,2)**2)
. FVB =0.5*(F(J,2)*V(J,2)+F(J-1,2)*V(J-1,2))
. FB =0.5*(F(J,2)+F(J-1,2))
. UB =0.5*(U(J,2)+U(J-1,2))
. VB =0.5*(V(J,2)+V(J-1,2))
. DERBV=(B(J,2)*V(J,2)-B(J-1,2)*V(J-1,2))/DETA(J-1)
. IF(NX .GT. 1) GOTO 10
.
. Previous station
.
. CFB =0.0
. CVB =0.0
. CFVB =0.0
. CU2B =0.0
. CDERBV=0.0
. GOTO 20
00010 CFB =0.5*(F(J,1)+F(J-1,1))
. CVB =0.5*(V(J,1)+V(J-1,1))
. CFVB =0.5*(F(J,1)*V(J,1)+F(J-1,1)*V(J-1,1))
. CU2B =0.5*(U(J,1)**2+U(J-1,1)**2)
. CDERBV=(B(J,1)*V(J,1)-B(J-1,1)*V(J-1,1))/DETA(J-1)
.
. Coefficients of the Differenced Momentum Equation
.
. 00020 S1(J)=B(J,2)/DETA(J-1)+(ALFA1*F(J,2)-ALFA(NX)*CFB)*0.5
. S2(J)=-B(J-1,2)/DETA(J-1)+(ALFA1*F(J-1,2)-ALFA(NX)*CFB)*0.5
. S3(J)=0.5*(ALFA1*V(J,2)+ALFA(NX)*CVB)
. S4(J)=0.5*(ALFA1*V(J-1,2)+ALFA(NX)*CVB)
. S5(J)=-ALFA2*U(J,2)
. S6(J)=-ALFA2*U(J-1,2)
.
. Definitions of Rj
.
. IF(NX .EQ. 1) GOTO 30
. CLB=CDERBV+P1(NX-1)*CFVB+P2(NX-1)*(1.0-CU2B)
. CRB=-P2(NX)+ALFA(NX)*(CFVB-CU2B)-CLB
. GOTO 35
00030 CRB=-P2(NX)
00035 R2(J)=CRB-(DERBV+ALFA1*FVB-ALFA2*U2B-ALFA(NX)*(CFB*VB-CVB*FB))
. R1(J) =F(J-1,2)-F(J,2)+DETA(J-1)*UB
. R3(J-1)=U(J-1,2)-U(J,2)+DETA(J-1)*VB
00100 CONTINUE
. R1(1) =0.0

```

```

.   R2(1) =0.0
.   R3(NP)=0.0
.   RETURN
.   END

```

This is the key subroutine that contains the recursion formulas that arise in the block elimination method [37].

```

.   SUBROUTINE SOLVE
.   COMMON/BLC0/NP,NX,NXT,NTR,NSEP,NFLOW,ETA,E,VGP,VISC,UINF,
1   DETA(111),A(111),ETA(111),NGAP(2),UC
.   COMMON/BLCC/X(99),UE(99),P1(99),P2(99),ALFA(99),RX(99),
1   CF,ALFA1,ALFA2,RTHETA(99),USURF(99)
.   COMMON/BLCP/DELV(111),F(111,2),U(111,2),V(111,2),B(111,2)
.   COMMON/BLC6/S1(111),S2(111),S3(111),S4(111),S5(111),S6(111),
1   R1(111),R2(111),R3(111)
.   DIMENSION W1(111),W2(111),W3(111),
1   A11(111),A12(111),A13(111),A21(111),A22(111),A23(111),
2   G11(111),G12(111),G13(111),G21(111),G22(111),G23(111),
3   DELU(111),DELF(111)

```

```

.   W-elements for J=1
-

```

```

.   W1(1)=R1(1)
.   W2(1)=R2(1)
.   W3(1)=R3(1)
-

```

```

.   Alfa elements for J=1
-

```

```

.   A11(1)=1.0
.   A12(1)=0.0
.   A13(1)=0.0
.   A21(1)=0.0
.   A22(1)=1.0
.   A23(1)=0.0
-

```

```

.   Gamma elements for J=2
-

```

```

.   G11(2)=-1.0
.   G12(2)=-0.5*DETA(1)
.   G13(2)= 0.0
.   G21(2)= S4(2)
.   G23(2)=-2.0*S2(2)/DETA(1)
.   G22(2)= G23(2)+S6(2)
-

```

```

.   Forward Sweep
-

```

```

.   DO 500 J=2,NP
.   IF(J .EQ. 2) GOTO 100

```

```

-
.   DEN=(A13(J-1)*A21(J-1)-A23(J-1)*A11(J-1)-A(J)*
1   (A12(J-1)*A21(J-1)-A22(J-1)*A11(J-1)))
.   DEN1=A22(J-1)*A(J)-A23(J-1)
.   G11(J)=(A23(J-1)+A(J)*(A(J)*A21(J-1)-A22(J-1)))/DEN
.   G12(J)=-A(J)*A(J)+G11(J)*(A12(J-1)*A(J)-A13(J-1))/DEN1
.   G13(J)=(G11(J)*A13(J-1)+G12(J)*A23(J-1))/A(J)
.   G21(J)=(S2(J)*A21(J-1)-S4(J)*A23(J-1)+A(J)*
1   (S4(J)*A22(J-1)-S6(J)*A21(J-1)))/DEN
.   G22(J)=(-S2(J)+S6(J)*A(J)-G21(J)*(A(J)*A12(J-1)-A13(J-1)))
1   /DEN1
.   G23(J)=G21(J)*A12(J-1)+G22(J)*A22(J-1)-S6(J)
-
00100 A11(J)= 1.0
.   A12(J)=-A(J)-G13(J)
.   A13(J)= A(J)*G13(J)
.   A21(J)= S3(J)
.   A22(J)= S5(J)-G23(J)
.   A23(J)= S1(J)+A(J)*G23(J)
-
.   W1(J)=R1(J)-G11(J)*W1(J-1)-G12(J)*W2(J-1)-G13(J)*W3(J-1)
.   W2(J)=R2(J)-G21(J)*W1(J-1)-G22(J)*W2(J-1)-G23(J)*W3(J-1)
.   W3(J)=R3(J)
00500 CONTINUE
-----
.   Backward sweep
-
.   DELU(NP)=W3(NP)
.   E1=W1(NP)-A12(NP)*DELU(NP)
.   E2=W2(NP)-A22(NP)*DELU(NP)
.   DELV(NP)=(E2*A11(NP)-E1*A21(NP))/(A23(NP)*A11(NP)-
1   A13(NP)*A21(NP))
.   DELF(NP)=(E1-A13(NP)*DELV(NP))/A11(NP)
.   J=NP
00600 J=J-1
.   E3=W3(J)-DELU(J+1)+A(J+1)*DELV(J+1)
.   DEN2=A21(J)*A12(J)*A(J+1)-A21(J)*A13(J)-A(J+1)*A22(J)*A11(J)+
1   A23(J)*A11(J)
.   DELV(J)=(A11(J)*(W2(J)+E3*A22(J))-A21(J)*W1(J)-
1   E3*A21(J)*A12(J))/DEN2
.   DELU(J)=-A(J+1)*DELV(J)-E3
.   DELF(J)=(W1(J)-A12(J)*DELU(J)-A13(J)*DELV(J))/A11(J)
.   IF(J .GT. 1) GOTO 600
-----
.   WRITE(7,9100) V(1,2),DELV(1)
.   DO 700 J=1,NP
.   F(J,2)=F(J,2)+DELF(J)

```

```

.      U(J,2)=U(J,2)+DELU(J)
00700 V(J,2)=V(J,2)+DELV(J)
.      U(1,2)=USURF(NX)
.      RETURN
-----
09100 FORMAT(1H ,5X,8HV(WALL)=,E14 6,5X,6HDELVW=,E14.6)
.      END

```

This subroutine prints out the desired profiles such as f , f' , and f'' as functions of η and computes the boundary-layer parameters of interest. Integration is done using the trapezoidal rule. The prediction of transition to turbulence and final separation are also made in this subroutine.

```

.      SUBROUTINE OUTPUT
.      COMMON/BLC0/NP,NX,NXT,NTR,NSEP,NFLOW,ETA,E,VGP,VISC,UINF,
.      1      DETA(111),A(111),ETA(111),NGAP(2),UC
.      COMMON/BLCC/X(99),UE(99),P1(99),P2(99),ALFA(99),RX(99),
.      1      CF,ALFA1,ALFA2,RTHETA(99),USURF(99)
.      COMMON/BLCP/DELV(111),F(111,2),U(111,2),V(111,2),B(111,2)
.      COMMON/BLCT/DELSX(2,99),CFX(99)
.      COMMON/IDEN/NUMX(2,99)
-----
.      WRITE(7,4400)
.      WRITE(7,4500) (J,ETA(J),F(J,2),U(J,2),V(J,2),B(J,2),J=1,NP,8)
.      WRITE(7,4500) NP,ETA(NP),F(NP,2),U(NP,2),V(NP,2),B(NP,2)
.      IF(NX .EQ. 1) GOTO 210
.      F1=0.0
.      THETA1=0.0
.      DO 100 J=2,NP
.      F2=U(J,2)*(1 0-U(J,2))
.      THETA1=THETA1+(F1+F2)*0.5*DETA(J-1)
00100 F1=F2
.      THETA=THETA1*X(NX)/SQRT(RX(NX))
.      IF(THETA .LT. 0.0) THETA=0.0
.      DELS=(ETA(NP)-F(NP,2))*X(NX)/SQRT(RX(NX))
.      IF(DELS .LT. 0.0) DELS=0.0
.      H=0.0
.      IF(THETA .NE. 0.) H=DELS/THETA
.      CF=2.0*V(1,2)/SQRT(RX(NX))
.      IF(CF .LT. 0.0) CF=0.0
.      RTHETA(NX)=UE(NX)*THETA/VISC
.      RDELS=UE(NX)*DELS/VISC
.      WRITE(7,9000) X(NX),THETA,DELS,H,CF,RX(NX),RTHETA(NX),
.      1      RDELS,UE(NX),P2(NX)
-----
.      Check for separation;
.
.      IF(NX .EQ. NSEP) GOTO 165

```

```

-
.   IF(NTR .LT. 99) GOTO 195
.   IF(NX .GE. NTR) GOTO 195
.   IF(P2(NX).GT. 0.) GOTO 195
-
.   Laminar separation is taken as point of transition to turbulent flow
-
.   WRITE(8,5000) NX,X(NX)
.   NTR=NX
.   IF(CF .LT. 0.0) CF=0.0
.   GOTO 195
-
.   Final turbulent separation;
-
00165 WRITE(8,6000) NSEP,X(NSEP)
.   DO 175 I=NX,NXT
.   CFX(I)=0.0
00175 CONTINUE
.   NX=NXT
.   GOTO 210
-----
00195 CFX(NX)=CF
.   DELSX(NFLOW,NX)=DELS
.   WRITE(8,9100) X(NX),DELS,CFX(NX)
.   IF(NX .EQ. NSEP) NX=NXT
-----
00210 NX=NX+1
.   IF(NX .LE. NXT) GOTO 400
-----
.   RETURN
-----
00400 CONTINUE
-----
.   Shift profiles
-
.   DO 425 J=1,NP
.   F(J,1)=F(J,2)
.   U(J,1)=U(J,2)
.   V(J,1)=V(J,2)
00425 B(J,1)=B(J,2)
.   RETURN
-----
01000 FORMAT(2(2X,F14 6))
04400 FORMAT(1H ,2X,1HJ,3X,3HETA,6X,1HF,12X,1HU,12X,1HV,10X,1HB)
04500 FORMAT(1H ,I3,F8 3,4E12 4)
05000 FORMAT(1H ,18HTRANSITION AT NX =,I3,5H X =,E14 6)
06000 FORMAT(1H ,18HSEPARATION AT NX =,I3,5H X =,E14 6)
09000 FORMAT(1H ,4X,1HX,11X,5HTHETA,9X,4HDELS,9X,1HH,12X,2HCF/
.   1   1H ,4X,2HRX,10X,6HRTHETA,7X,5HRDELS,9X,2HUE,11X,2HP2/
.   2   1H ,5E12 4/1H ,5E12.4)

```

09100 FORMAT(1H ,E14 6,6X,E14.6,2X,E14.6)

END

A numerical surface singularity method for the calculation of the pressure distribution on an open airfoil (finite- thickness trailing edge) shape for a given test section wall configuration.

- The airfoil shape is supplied by an odd number of section coordinates (XSCTN,YSCTN), the last XSCTN coordinate being the same as the first, from which the surface elements are determined.
- The test section wall coordinates are supplied in the same "sense" (clockwise or anti-clockwise) as the airfoil.
- The Kutta points(two) are calculated from the trailing edge coordinates. The first one assigns a value to the stream function whereas the second one determines the strength of the source.
- The vorticity distributions and tangential velocities are calculated at the centre of each element, denoted by (XCNTRL, YCNTRL).

SUBROUTINE UEDIST

COMMON/SCTN/ AOA,NUM,NE,XORIG(99),YSCTN(99),XOLD(50)

DIMENSION XTRNS(110),YTRNS(110),

1 XCNTRL(110),YCNTRL(110),

2 COST(110),SINT(110),

3 RRATIO(110,110),EPSILN(110,110),

4 THETAS(110),RADS(110),

5 RK(110,110),RHS(110),

6 GAMMA(110),TVEL(110),VEL(110)

INTEGER NPTS(3)

PI=4 *ATAN(1)

TWOPI =2 *PI

FOURPI=4 *PI

The number of components considered (one airfoil section plus two walls) is:

NC=3

The number of the airfoil control points is:

NPTS(1)=NE-1

NEM=NE-1

NEP=NE+1

The angle of attack of the airfoil;

ALFA=AOA*PI/180.

COSA=COS(ALFA)

SINA=SIN(ALFA)

Transform the coordinates (the transformation consists of a translation and a rotation about the pivot point of the section according to the angle of attack.

```

-
.   XPIVOT=0.368421
-
.   DO 20 I=1,NE
.   XTRNS(I)= COSA*(XORIG(I)-XPIVOT)+SINA*YSCTN(I)
.   YTRNS(I)=-SINA*(XORIG(I)-XPIVOT)+COSA*YSCTN(I)
00020 CONTINUE
-----
.   Calculation of the control points for the airfoil section
-
.   DO 30 I=1,NEM
.   XCNTL(I)=(XTRNS(I)+XTRNS(I+1))/2.
.   YCNTL(I)=(YTRNS(I)+YTRNS(I+1))/2.
00030 CONTINUE
-
.   Construct the Kutta Points;
-
.   XCNTL(NE)=1.01*XTRNS(NE)
.   SLOPE=(YTRNS(NE)-YTRNS(NEM))/(XTRNS(NE)-XTRNS(NEM))
.   YCNTL(NE)=YTRNS(NE)+SLOPE*(XCNTL(NE)-XTRNS(NE))
.   XCNTL(NEP)=1.01*XTRNS(1)
.   SLOPE=(YTRNS(1)-YTRNS(2))/(XTRNS(1)-XTRNS(2))
.   YCNTL(NEP)=YTRNS(1)+SLOPE*(XCNTL(NEP)-XTRNS(1))
-
.   NTOTAL=NEP
.   IF(NC .EQ. 1) GOTO 85
-----
.   Read the test section wall coordinates;
-
.   NPTS(2)=22
.   NPTS(3)=22
.   NWPTS=NPTS(2)+NPTS(3)
-
.   DO 50 I=1,NWPTS
.   NW=NE+I
.   READ(51,1000) XTRNS(NW),YTRNS(NW)
00050 CONTINUE
-----
.   Calculation of the control points for the walls;
-
.   NW1=NE+2
.   NWN=NE
.   DO 80 JC=2,3
.   NWN=NWN+NPTS(JC)
.   DO 70 I=NW1,NWN
.   XCNTL(I)=(XTRNS(I-1)+XTRNS(I))/2.
.   YCNTL(I)=(YTRNS(I-1)+YTRNS(I))/2.
00070 CONTINUE
.   NW1=NWN+2
00080 CONTINUE

```

```

.   NTOTAL=NPTS(1)+2+NPTS(2)-1+NPTS(3)-1
00085 CONTINUE

```

```

.   Calculation of the influence coefficients, RK(I,J)
-

```

```

.   NN1=1
.   NNN=0
.   DO 150 JC=1,NC
.   NNN=NNN+NPTS(JC)
.   JJ=NN1-1
.   IF(JC .EQ. 3) JJ=JJ-1
.   DO 140 J=NN1,NNN
.   JJ=JJ+1
.   JE=J
.   XMID=XCNTRL(J)
.   YMID=YNTRL(J)
.   IF(JC .NE. 1) JE=J-1
.   X1=XTRNS(JE)
.   Y1=YTRNS(JE)
.   X2=XTRNS(JE+1)
.   Y2=YTRNS(JE+1)

```

```

.   Calculate the half length of each element
-

```

```

.   DELTA=SQRT((XMID-X1)**2+(YMID-Y1)**2)

```

```

.   The local angle between an element and the X-axis is denoted by TETA
.   and is obtained from the local slope of the element.
-

```

```

.   TETA=ATAN2((Y2-Y1),(X2-X1))
.   COST(J)=COS(TETA)
.   SINT(J)=SIN(TETA)

```

```

.   for each element, consider all control points
-

```

```

.   NP1=1
.   NPN=2
.   DO 120 IC=1,NC
.   NPN=NPN+NPTS(IC)
.   II=NP1-1
.   IF(IC .EQ. 3) II=II-1
.   DO 110 I=NP1,NPN
.   II=II+1
.   BB= COST(J)*(XCNTRL(I)-XMID)+SINT(J)*(YNTRL(I)-YMID)
.   AA=-SINT(J)*(XCNTRL(I)-XMID)+COST(J)*(YNTRL(I)-YMID)
.   R1=AA**2+(BB+DELTA)**2
.   R2=AA**2+(BB-DELTA)**2
.   RRATIO(I,J)=SQRT(R1/R2)
.   CC=AA**2+BB**2-DELTA**2

```

```

.   IF(CC .LE. 0.) GOTO 90
.   EPSILN(I,J)=ATAN2(2 *AA*DELTA,CC)
.   GOTO 95
00090 EPSILN(I,J)=ATAN2((BB+DELTA),AA)-ATAN2((BB-DELTA),AA)
00095 RK(II,JJ)=(BB+DELTA)*ALOG(R1)-(BB-DELTA)*ALOG(R2)-4.*DELTA
.   RK(II,JJ)=RK(II,JJ)+2.*AA*EPSILN(I,J)
00100 RK(II,JJ)=RK(II,JJ)/FOURPI
00110 CONTINUE
.   NP1=NPN+1
.   IF(IC .EQ. 1) NPN=NPN-1
.   IF(IC .EQ. 2) NP1=NP1+1
00120 CONTINUE
00140 CONTINUE
.   IF(JC .EQ. 1) NNN=NNN+1
.   NN1=NNN+2
00150 CONTINUE

```

```

.   The (N+1)st column of the RK(I,J) matrix is ONE for the airfoil section
.   and ZERO for the wall components.
.   The (N+2)nd column is the influence coefficients of the internal source
.   on the control points.
-

```

```

.   NP1=1
.   NPN=2
.   ZERONE=1
.   DO 200 IC=1,NC
.   NPN=NPN+NPTS(IC)
.   II=NP1-1
.   IF(IC .EQ. 3) II=II-1
.   DO 175 I=NP1,NPN
.   II=II+1
.   RK(II,NE)=ZERONE
.   THETAS(I)=ATAN2(YCNTRL(I),XCNTRL(I))
.   RADS(I)=SQRT(YCNTRL(I)**2+XCNTRL(I)**2)
.   TETAS=THETAS(I)+ALFA
.   IF(TETAS .LT. 0.0) TETAS=TWOPI+TETAS
.   RK(II,NEP)=- (TETAS-PI)/TWOPI
00175 CONTINUE
.   NP1=NPN+1
.   IF(IC .EQ. 1) NPN=NPN-1
.   IF(IC .EQ. 2) NP1=NP1+1
.   ZERONE=0.
00200 CONTINUE

```

```

.   Calculation of the RHS(I) column vector
-
.   for the airfoil section;
-
.   DO 225 I=1,NEP

```

```

.   RHS(I)=YCNTRL(I)
00225 CONTINUE
-
.   IF(NC .EQ. 1) GOTO 275
-
.   for the tunnel walls;
-
.   NP1=NE+2
.   NPN=NEP+NPTS(2)-1
.   DO 240 I=NP1,NPN
.   RHS(I)=0.
00240 CONTINUE
.   NP1=NPN+2
.   NPN=NPN+NPTS(3)
.   DO 260 I=NP1,NPN
.   RHS(I-1)=0.
00260 CONTINUE
-
00275 CONTINUE

```

To solve the system of linear equations of the form $AX=B$, the matrix subroutine **MATRIX** is used. The form of the matrices is

$$RK(NTOTAL,NTOTAL) \times GAMMA(NTOTAL) = RHS(NTOTAL)$$

A real two-dimensional array, **T**, provides temporary storage.

A real one-dimensional array, **RZ**, will, on exit, contain the vector of residuals.

An integer one-dimensional array, **IPERM**, dimensioned at least $2 \times (NTOTAL)$ is used by the routine to keep track of row permutations during the computations.

A real variable, **EPS**, is used in the convergence criterion for iterative improvement.

A real and an integer variable, **DET** and **JEXP**, are used to represent the determinant of the matrix of coefficients in the form $DET \times 10^{JEXP}$.

If the solution of the linear equations has failed, $DET=0$.

```

-
.   DIMENSION T(110,110),RZ(110),IPERM(220)
.   COMMON/ZD/DET,JEXP
.   EPS=5.E-7
.   NITER=0
-
.   CALL MATRIX(RK,T,RHS,GAMMA,RZ,IPERM,NTOTAL,110,EPS,1,NITER)
.   IF (DET .NE. 0.) GOTO 299
00295 WRITE(6,9000)
STOP
-
00299 CONTINUE

```

The solution matrix, **GAMMA**, contains the vorticity distribution at the control points plus the values of the stream function and the source strength.

```

-
.   NSUM=NTOTAL+1
.   DO 300 I=1,NSUM
.   WRITE(6,2000) XCNTRL(I),YCNTRL(I),GAMMA(I)

```

00300 CONTINUE

. Calculate the tangential velocity distribution around the airfoil using
 . the above vorticity distribution and the effects of the source and the
 . uniform stream.

. For each control point

. DO 375 I=1,NEM

. Find the effect of vorticity distribution of all elements;

. VORTEX=0.

. NP1=1

. NPN=0

. DO 350 JC=1,NC

. NPN=NPN+NPTS(JC)

. JJ=NP1-1

. IF(JC .EQ. 3) JJ=JJ-1

. DO 325 J=NP1,NPN

. JJ=JJ+1

. IF(I .EQ. J) EPSILN(I,J)=-PI

. VT=-GAMMA(JJ)*EPSILN(I,J)/TWOPI

. VN=-GAMMA(JJ)*ALOG(RRATIO(I,J))/TWOPI

. VTAN=(VT*COST(J)+VN*SINT(J))*COST(I)

. 1 -(-VT*SINT(J)+VN*COST(J))*SINT(I)

. VORTEX=VORTEX+VTAN

00325 CONTINUE

. IF(JC .EQ. 1) NPN=NPN+1

. NP1=NPN+2

00350 CONTINUE

. to this add the effect due to the source;

. UR=GAMMA(NEP)/(TWOPI*RADS(I))

. SOURCE=UR*(COS(THETAS(I))*COST(I)+SIN(THETAS(I))*SINT(I))

. and the effect of the free stream;

. STREAM=COST(I)

. TVEL(I)=VORTEX+SOURCE+STREAM

00375 CONTINUE

. WRITE(6,1500)(XCNTRL(I),YCNTRL(I),GAMMA(I),TVEL(I),I=1,NEP)

. Transform the coordinates back according to the original airfoil configuration;

. DO 400 I=1,NEP

. XRT=COSA*XCNTRL(I)-SINA*YCNTRL(I)+XPIVOT

. YRT=SINA*XCNTRL(I)+COSA*YCNTRL(I)

```

.   XCNTL(I)=XRT
.   YCNTL(I)=YRT
00400 CONTINUE

```

```

.   From the values of the tangential velocities calculated at the control points,
.   interpolate the corresponding values at the ORIGINAL section points;
-

```

```

.   CALL INTRPL(1,NE,XCNTL,TVEL,XORIG,VEL)
.   WRITE(6,2000)(XORIG(I),YSCTN(I),VEL(I),I=1,NE)
-

```

```

.   NDIFF=NUM-NE
.   IE=1+NDIFF
.   XTRNS(IE)=XORIG(1)
.   YTRNS(IE)=YSCTN(1)
.   TVEL(IE) =VEL(1)
.   DO 500 I=2,NE
.   IE=I+NDIFF
.   XTRNS(IE)=XORIG(I)
.   YTRNS(IE)=YSCTN(I)
.   TVEL(IE) =VEL(I)

```

```
00500 CONTINUE
```

```

.   DO 525 I=1,NDIFF
.   XTRNS(I)=XOLD(I)
.   YTRNS(I)=YSCTN(1)
.   TVEL(I) =VEL(1)

```

```
00525 CONTINUE
```

```

-   WRITE(10,2000)(XTRNS(I),YTRNS(I),TVEL(I),I=1,NUM)

```

```

.   RETURN

```

```
01000 FORMAT(1X,F9.6,2X,F9.6)
```

```
01500 FORMAT(4(2X,F9.6))
```

```
02000 FORMAT(3(2X,F9.6))
```

```
09000 FORMAT(1H ,36H SOLUTION OF THE EQUATIONS FAILED !!)
```

```

.   END

```

```

.   SUBROUTINE INTRPL(IFLAG,N1,XSARG,YSARG,XIARG,YIARG)
-

```

```

.   The value of IFLAG determines whether the input coordinates are section
.   points (IFLAG=0) or control points (IFLAG=1).
-

```

```

.   DIMENSION XSARG(N1),YSARG(N1),XIARG(N1),YIARG(N1)
.   DIMENSION XSPLN(110),YSPLN(110)

```

```

.   N=N1-1
.   DO 100 I=1,N
.   IF(XIARG(I+1) .GE. XIARG(I)) GOTO 110

```

```
00100 CONTINUE
```

```
00110 NDIV=I
```

. For interpolation of the upper surface

.
 . NT=(NDIV-IFLAG)+4
 . NTM=NT-1
 . COUNT=NT
 . INCR=1
 . I1=1
 . I2=NDIV
 . M=I2-I1+1
 . GOTO 150

. For interpolation of the lower surface

.
 . 00120 NT=(N1-NDIV-IFLAG)+5
 . NTM=NT-1
 . COUNT=NDIV-4
 . INCR=-1
 . I1=I2+1
 . I2=N1
 . M=I2-I1+1

00150 J=COUNT-INCR

. XSPLN(1)=-XSARG(J)
 . YSPLN(1)=YSARG(J)
 . J=J-INCR
 . XSPLN(2)=-XSARG(J)
 . YSPLN(2)=YSARG(J)
 . J=J-INCR
 . XSPLN(3)=-XSARG(J)
 . YSPLN(3)=YSARG(J)
 . DO 200 I=4,NTM
 . J=J-INCR
 . XSPLN(I)=XSARG(J)
 . YSPLN(I)=YSARG(J)

00200 CONTINUE

. XSPLN(NT)=XSPLN(NTM)+0 1
 . IF(INCR .EQ. -1) XSPLN(NT)=1 01
 . YSPLN(NT)=YSARG(J)

To fit a cubic spline function to the set of data points, the spline fitting subroutine SPLNFT is used. The routine will try to achieve

$$\sum [(g(x_i) - y_i)/dy_i]^2 = S, \quad i = 1, \dots, n,$$

where $dy_i > 0$ and $S \geq 0$ are given numbers, and $g(x)$ is a cubic spline

$$g(x) = a_i + b_i(x - x_i) + c_i(x - x_i)^2 + d_i(x - x_i)^3$$

There are two entry points to the subroutine : To calculate the parameters for the cubic spline:

CALL SPLNFT(X,Y,DY,S,N,W,&nn)

X: real one-dimensional array, dimensioned at least N, containing the abscissae of the given data points. the restriction $X(1) < X(2) < \dots < X(N)$.

Y: real one-dimensional array, dimensioned at least N, containing the ordinates of the data points.

DY: real one-dimensional array, dimensioned at least N. On entry each DY(I) must be set to a value indicating the amount of smoothing to be done at each abscissa X(I). The smaller DY(I) is, the more closely Y(I) will be fitted. If available, an estimate of the standard deviation of Y(I) should be used for DY(I).

S: real variable or constant used to control the implicit rescaling of the DY's. If DY contains the standard deviations of Y, values of S in the range $N - (2N)^{-5} \leq S \leq N + (2N)^{-5}$ give the most natural looking results. If S=0, the result will be an INTERPOLATING CUBIC SPLINE. As S decreases, the amount of smoothing decreases and the data points are fit more exactly.

N: number of data points. $N > 2$

W: REAL*8 one dimensional array, dimensioned at least $11 \times N + 14$ used internally for working storage.

nn: line number to which control will be returned if a restriction on the parameters has been violated.

To calculate ordinates and first and second derivatives for a set of abscissae:

CALL SPLN(XX,YY,YY1,YY2,M,&nn)

XX: real one-dimensional array, dimensioned at least M, containing the abscissae at which the fitted curve is to be evaluated. Note the restriction:
 $X(1) \leq XX(I) \leq X(N)$ for $I=1, \dots, M$

YY: real one-dimensional array, dimensioned at least M. On exit YY contains the estimated ordinate of the function at XX(I).

YY1: real one-dimensional array, dimensioned at least M. On exit YY1 contains the first derivative of the function at XX(I).

YY2: real one-dimensional array, dimensioned at least M. On exit YY2 contains the second derivative of the function at XX(I).

M: number of abscissae, XX(I).

```

_____
.   REAL*8 W(1224)
.   DIMENSION XX(110),YY(110),YY1(110),YY2(110),DY(110)
_____

```

The amount of smoothing :

```

-
.   STDEV=1.0
.   DO 300 I=1,NT
.   DY(I)=STDEV
00300 CONTINUE

```

S=0

Do the fit :

```

-
.   CALL SPLNFT(XSPLN,YSPLN,DY,S,NT,W,&991)
_____

```

```

.   Interpolate;
-
.   J=0
.   DO 325 I=I1,I2
.   J=J+1
.   XX(J)=XIARG(I)
00325 CONTINUE
-
.   CALL SPLN(XX,YY,YY1,YY2,M,&992)
-
.   J=0
.   DO 350 I=I1,I2
.   J=J+1
.   YIARG(I)=YY(J)
00350 CONTINUE
-
.   IF(I2 .NE. N1) GOTO 120
.   RETURN
-----
00991 WRITE(6,9001)
.   STOP
-----
00992 WRITE(6,9002)
.   STOP
-----
09001 FORMAT('ERROR : N<2 OR X VALUES OUT OF ORDER.')
09002 FORMAT('ERROR : VARIABLE OUTSIDE FITTED RANGE.')
.   END

.   SUBROUTINE SPLNFT(X,Y,DY,S,N,W,*)
.   IMPLICIT REAL*8 (A-H,O-Z)
.   REAL*4 X,Y,DY,S,XX,YY,YY1,YY2
.   COMMON /SPLN$/ NCOUNT
.   DIMENSION X(N),Y(N),DY(N),W(1)
.   DIMENSION XX(1),YY(1),YY1(1),YY2(1)
.   INTEGER A,B,C,D,R,R1,R2,T,T1,U,V
.   IF (N.LT.3) RETURN 1
.   NCOUNT=1
.   SS=S
.   DS=SS
.   IF(S.LE.0.0) SS=1.0D-8
.   EE=DS*0.5D-6
.   IF (S.LE.0.0) EE=0.5D-6
.   NM=N-1
.   N2=N+2
.   NB=N
.   NC=NB+N
.   ND=NC+N
.   NR=ND+N
.   NR1=NR+N2
.   NR2=NR1+N2

```

```

.   NT=NR2+N2
.   NT1=NT+N2
.   NU=NT1+N2
.   NV=NU+N2
-
.   W(NR+1)=0.0D0
.   W(NR+2)=0.0D0
.   W(NR2-1)=0.0D0
.   W(NR2)=0.0D0
.   W(NT-1)=0.0D0
.   W(NT)=0.0D0
.   W(NU+1)=0.0D0
.   W(NU+2)=0.0D0
.   W(NV-1)=0.0D0
.   W(NV)=0.0D0
-
.   P=0.0D0
-----
.   Set A to QT*Y
.   Set R,R1,R2 to D*Q
-
.   H=X(2)-X(1)
.   IF (H .LE. 0.D0) RETURN 1
.   F=(Y(2)-Y(1))/H
.   DO 1 I=2,NM
.   A=I
.   G=H
.   H=X(I+1)-X(I)
.   IF(H .LE. 0.D0) RETURN 1
.   E=F
.   F=(Y(I+1)-Y(I))/H
.   W(I)=F-E
.   T=NT+I
.   W(T+1)=.6666667D0*(G+H)
.   T1=NT1+I
.   W(T1+1)=.3333333D0*H
.   R2=NR2+I
.   W(R2+1)=DY(I-1)/G
.   R=NR+I
.   W(R+1)=DY(I+1)/H
.   R1=NR1+I
00001 W(R1+1)=-DY(I)/G-DY(I)/H
-----
.   Set B,C, and D to QT*D*D*Q
-
.   DO 2 I=2,NM
.   B=NB+I
.   R=NR+I
.   R1=NR1+I

```

```

.      R2=NR2+I
.      W(B)=W(R+1)*W(R+1)+W(R1+1)*W(R1+1)+W(R2+1)*W(R2+1)
.      C=NC+I
.      W(C)=W(R+1)*W(R1+2)+W(R1+1)*W(R2+2)
.      D=ND+I
00002 W(D)=W(R+1)*W(R2+3)

```

```

00003 CONTINUE

```

```

.      Do a LDU decomposition of  $QT^*D^*D^*Q+P^*T$ 
-
.      DO 4 I=2,NM
.      A=I
.      R1=NR1+I
.      R=NR+I
.      R2=NR2+I
.      U=NU+I
.      T1=NT1+I
.      B=NB+I
.      C=NC+I
.      D=ND+I
.      T=NT+I
.      W(R1)=F*W(R)
.      W(R2-1)=G*W(R-1)
.      W(R+1)=1 0D0/(W(B)+P*W(T+1)-F*W(R1)-G*W(R2-1))
.      W(U+1)=W(A)-W(R1)*W(U)-W(R2-1)*W(U-1)
.      F=W(C)+P*W(T1+1)-H*W(R1)
.      G=H
00004 H=W(D)

```

```

.      Do back substitution
-
.      DO 5 I=2,NM
.      II=N2-I
.      U=NU+II
.      R=NR+II
.      R1=NR1+II
.      R2=NR2+II
00005 W(U)=W(R)*W(U)-W(R1)*W(U+1)-W(R2)*W(U+2)
.      E=0 0D0
.      H=0 0D0

```

```

.      The V is really  $D^*D^*Q^*U$ 
-
.      DO 6 I=1,NM
.      U=NU+I
.      V=NV+I
.      G=H
.      H=(W(U+2)-W(U+1))/(X(I+1)-X(I))
.      W(V+1)=(H-G)*DY(I)*DY(I)
00006 E=E+W(V+1)*(H-G)
.      G=-H*DY(N)*DY(N)

```

```

.      V=NV+N
.      W(V+1)=G
.      E=E-G*H
.      IF (E .LE. DS .OR. DABS(E-DS) .LE. EE) GO TO 8
_____
.      Calculate F and G
.      For G consider ... A*X=I ; A*(X*Y)=I*Y=Y
-
.      F=0.0D0
.      G=0.0D0
.      DO 7 I=2,NM
.      R=NR+I
.      R1=NR1+I
.      R2=NR2+I
.      U=NU+I
.      T=NT+I
.      T1=NT1+I
.      H=W(U)*W(T1)+W(U+1)*W(T+1)+W(U+2)*W(T1+1)
.      F=F+W(U+1)*H
.      H=H-W(R1)*W(R)-W(R2-1)*W(R-1)
.      G=G+H*W(R+1)*H
00007 W(R+1)=H
.      H=F-P*G
.      IF (H.LE.0.0D0) GO TO 8
.      NCOUNT=NCOUNT+1
.      IF (NCOUNT .GT. 100) RETURN 1
-
.      P=P+DSQRT(E/SS)*(E-DSQRT(DS*E))/H
-
.      GO TO 3
00008 CONTINUE
.      DO 9 I=1,N
.      C=NC+I
.      V=NV+I
.      U=NU+I
.      A=I
.      W(A)=Y(I)-W(V+1)
00009 W(C)=P*W(U+1)
.      DO 10 I=1,NM
.      D=ND+I
.      A=I
.      C=NC+I
.      B=NB+I
.      H=X(I+1)-X(I)
.      W(D)=(W(C+1)-W(C))/(3.0D0*H)
00010 W(B)=(W(A+1)-W(A))/H-(H*W(D)+W(C))*H
.      RETURN
_____
.      ENTRY SPLN(XX,YY,YY1,YY2,M,*)
-

```

```

.      IF (M .LE. 0) RETURN
.      J=1
.      A=1
.      B=A+N
.      C=B+N
.      D=C+N
.      DO 15 I=1,M
00011 IF (XX(I) .LT. X(J)) GO TO 14
.      IF (XX(I) .LT. X(J+1)) GO TO 13
.      IF (J .LT. NM) GO TO 12
.      IF (XX(I) .EQ. X(J+1)) GO TO 13
.      RETURN 1
00012 J=J+1
.      A=J
.      B=A+N
.      C=B+N
.      D=C+N
.      GO TO 11
00013 DIFF=XX(I)-X(J)
.      YY(I)=W(A)+DIFF*(W(B)+DIFF*(W(C)+DIFF*W(D)))
.      YY1(I)=W(B)+DIFF*(2.0D0*W(C)+3.0D0*DIFF*W(D))
.      YY2(I)=2.0D0*W(C)+6.0D0*W(D)*DIFF
.      GO TO 15
00014 IF(J .EQ. 1) RETURN 1
.      J=1
.      A=J
.      B=A+N
.      C=B+N
.      D=C+N
.      GO TO 11
00015 CONTINUE
-----
.      RETURN
.      END

.      SUBROUTINE MATRIX(A,T,B,X,RZ,IPS,N,L,EPS,LT,ITMAX)
.      COMMON /ZD/ DET,JEXP /SLIMP$/ NITER
.      DIMENSION A(L,L),T(L,L),B(1),X(1),RZ(1),IPS(1)
.      DOUBLE PRECISION DSUMM,DA,DX
.      IF(LT .NE. 1) GO TO 10
-
.      CALL FLRD(N,N,L,A,IPS,L,T)
.      CALL FDETM(N,IPS,L,T,DET,JEXP)
00010 CALL FDBS(N,1,L,B,X,IPS,L,T)
-
.      IF(ITMAX .EQ. 0) GO TO 60
.      XNORM=0.0
.      DO 1 I=1,N
00001 XNORM=AMAX1(XNORM,ABS(X(I)))
.      IF(XNORM .LE. 0.0) RETURN

```

```

.     EPS=EPS*XNORM
.     ZX=1.E+60
.     LD=0
.     DO 2 LL=1,ITMAX
.     DO 3 I=1,N
.     DSUMM=0.0
.     DO 4 K=1,N
.     DA=A(I,K)
.     DX=X(K)
00004 DSUMM=DSUMM+DA*DX
.     DSUMM=B(I)-DSUMM
00003 RZ(I)=DSUMM
-
.     CALL FDBS(N,1,L,RZ,RZ,IPS,L,T)
-
.     ZNORM=0.0
.     DO 5 I=1,N
.     ZNORM=AMAX1(ZNORM,ABS(RZ(I)))
00005 X(I)=X(I)+RZ(I)
.     IF(ZNORM .GT. ZX) GO TO 50
.     IF((ZNORM-EPS) .LT. 0.0) GO TO 60
.     ZX=ZNORM
.     GO TO 2
00050 IF(ZNORM .GT. 10.0*ZX) GO TO 70
.     LD=LD+1
.     IF(LD .GE. 3) GO TO 70
00002 CONTINUE
.     LL=LL-1
.     WRITE(6,250)
.     GO TO 71
00070 WRITE(6,247)
00071 EPS=-ZNORM
.     NITER=LL
.     RETURN
-----
00060 EPS=ZNORM
.     NITER=LL
.     RETURN
-----
00250 FORMAT(/'0***ITERATIVE IMPROVEMENT DID NOT CONVERGE'/)
00247 FORMAT(/'0***ITERATIVE IMPROVEMENT IS DIVERGING'/)
.     END

.     SUBROUTINE FLRD(N,N1,NDIMA,A,IP,NDIMT,T)
.     DIMENSION A(NDIMA,1),T(NDIMT,1),IP(1)
-----

```

Matrix triangularization by Gaussian elimination

Input:

N: order of matrix

NDIMA: 1st dimension of A

A: array containing matrix to be triangularized

N1: dummy argument

Output:

A(I,J) ($I \leq J$): upper triangular factor, U

A(I,J) ($I > J$): lower triangular factor, I-L

IP(K) ($K < N$): index of Kth pivot

IP(N): $(-1)^{(\text{no. of interchanges})}$ or 0

```

.   If IP(N)=0 matrix is singular
.   Interchanges finished in U, only partly in L
-----
.   DO 7 J=1,N
.   DO 7 I=1,N
00007 T(I,J)=A(I,J)
.   IP(N)=1
.   DO 6 K=1,N
.   IF(K .EQ. N) GO TO 5
.   KP1=K+1
.   M=K
.   DO 1 I=KP1,N
.   IF(ABS(T(I,K)) .GT. ABS(T(M,K))) M=I
00001 CONTINUE
.   IP(K)=M
.   IF(M .NE. K) IP(N)=-IP(N)
.   TEMP=T(M,K)
.   T(M,K)=T(K,K)
.   T(K,K)=TEMP
.   IF(TEMP .EQ. 0) GO TO 5
.   DO 2 I=KP1,N
00002 T(I,K)=-T(I,K)/TEMP
.   DO 4 J=KP1,N
.   TEMP=T(M,J)
.   T(M,J)=T(K,J)
.   T(K,J)=TEMP
.   IF(TEMP .EQ. 0) GO TO 4
.   DO 3 I=KP1,N
00003 T(I,J)=T(I,J)+T(I,K)*TEMP
00004 CONTINUE
00005 IF(T(K,K) .EQ. 0) IP(N)=0
00006 CONTINUE
-----
.   RETURN
.   END

.   SUBROUTINE FDETM(N,IP,NDIMT,T,DET,JEXP)

```

DETERMINANT.OF TRIANGULAR MATRIX

Input:

N: order of matrix

IP: vector of interchanges; $IP(N)=(-1)^{(\text{no. of interchanges})}$

If matrix produced by FLRD

NDIMT: 1st dimension of T

T: 2×2 array containing matrixDETERMINANT: $DET \times 10^{JEXP}$

```

.   DIMENSION T(NDIMT,1),IP(1)
.   DET=IP(N)
.   JEXP=0
.   DO 1 I=1,N
.     TEMP=T(I,I)
.     IF(ABS(DET) .LE. 1.E15) GO TO 2
.     DET=DET*1.E-15
.     JEXP=JEXP+15
.     GO TO 3
00002 IF(ABS(DET) .GE. 1.E-15) GO TO 3
.     DET=DET*1.E+15
.     JEXP=JEXP-15
00003 DET=DET*TEMP
00001 CONTINUE
.
.   RETURN
.   END
.
.   SUBROUTINE FDDBS(N,NSOL,NDIMBX,B,X,IP,NDIMT,T)

```

BACK AND FORWARD SUBSTITUTION

Input:

N: order of system

NSOL: no. of R.H.S.

NDIMBX: 1st dimension of B and X

T: 2×2 array containing triangularized matrix produced by FLRDB: 2×2 array containing R.H.S.

NDIMT: 1st dimension of T

Output:

X: 2×2 array contains the solution vectors

```

.   DIMENSION T(NDIMT,1),X(NDIMBX,1),B(NDIMBX,1),IP(1)

```

```
.      NM1=N-1
.      DO 1 L=1,NSOL
.      DO 2 I=1,N
00002 X(I,L)=B(I,L)
.      IF(N .EQ. 1) GO TO 9
.      DO 7 K=1,NM1
.      KP1=K+1
.      M=IP(K)
.      TEMP=X(M,L)
.      X(M,L)=X(K,L)
.      X(K,L)=TEMP
.      DO 7 I=KP1,N
00007 X(I,L)=X(I,L)+T(I,K)*TEMP
.      DO 8 KB=1,NM1
.      KM1=N-KB
.      K=KM1+1
.      X(K,L)=X(K,L)/T(K,K)
.      TEMP=-X(K,L)
.      DO 8 I=1,KM1
00008 X(I,L)=X(I,L)+T(I,K)*TEMP
00009 X(1,L)=X(1,L)/T(1,1)
00001 CONTINUE
-----
.      RETURN
.      END
```

LIST OF PUBLICATIONS

- Mokhtarian, F. and Erwin, L., "Computer Analysis of Mixing in Single-Screw Extruders," *Society of Plastics Engineers*, Technical Papers, vol. 28, 1982, pp. 476-480.
- Mokhtarian, F. and Erwin, L., "Analysis of Mixing in Modified Single-Screw Extruders," *Polymer Engineering and Science*, February 1983, vol. 23, No. 2, pp. 49-61.
- Mokhtarian, F. and Modi, V.J., "Fluid Dynamics of Airfoils with Circulation control for V/STOL Application," AIAA Atmospheric Flight Mechanics Conference, Seattle, Washington, USA, August 1984, paper No. AIAA-84-2090; also Proceedings of the conference, AIAA Publisher, New York, USA, pp. 167-175.
- Mokhtarian, F. and Modi, V.J., "Joukowsky Airfoil with Circulation Control," AIAA Atmospheric Flight Mechanics Conference, Snowmass, Colorado, USA, August 1985, paper No. 85-1772-CP.
- Mokhtarian, F. and Modi, V.J., "Fluid Dynamics of Airfoils with Moving Surface Boundary-Layer Control," AIAA Atmospheric Flight Mechanics Conference, Williamsburg, Virginia, USA, August 1986, paper No. AIAA-86-2184-CP; also Proceedings of the conference, AIAA Publisher, New York, USA, pp. 322-330; *Journal of Aircraft*, in press.
- Modi, V.J., Mokhtarian, F., Yokomizo, T., Ohta, G. and Oinuma, T., "Fluid Dynamics of Airfoils with Moving Surface Boundary Layer Control," Proceedings of the 11th Canadian Congress of Applied Mechanics, Edmonton, Alberta, Canada, May-June 1987, pp. B102-103; also as "Bound Vortex Boundary Layer Control with Application to V/STOL Airplanes," Proceedings of the IUTAM Symposium on Fundamental Aspects of Vortex Motion, Tokyo, Japan, August 31-September 4, 1987, in press.
- Mokhtarian, F. and Modi, V.J. "On the Effect of Moving Surfaces on Airfoil Boundary-Layer Control," to be presented at the AIAA Atmospheric Flight Mechanics Conference, Minneapolis, Minnesota, U.S.A., August 1988.
- Mokhtarian, F. and Modi, V.J. "Rotating Air Scoop as Airfoil Boundary-Layer Control," submitted for publication, *Journal of Aircraft*, AIAA.